THESIS FOR THE DEGREE OF DOCTOR OF PHILOSOPHY

Gate tunability and nonlinearity in hybrid superconductor-semiconductor resonators

VITTORIO BUCCHERI

Department of Microtechnology and Nanoscience (MC2)
Quantum Device Physics Laboratory
CHALMERS UNIVERSITY OF TECHNOLOGY

Göteborg, Sweden 2026

Gate tunability and nonlinearity in hybrid superconductor-semiconductor resonators

VITTORIO BUCCHERI
ISBN 978-91-8103-512-4
DOI 10.63959/chalmers.dt/5969
Göteborg, Sweden 2026

COPYRIGHT© VITTORIO BUCCHERI, 2026
All rights reserved.

Doktorsavhandlingar vid Chalmers tekniska högskola
Ny serie Nr 5969
ISSN 0346-718X

Quantum Device Physics Laboratory
Department of Microtechnology and Nanoscience (MC2)
Chalmers University of Technology
SE-412 96 Göteborg, Sweden
Telephone: +46 (0)31-772 1000
www.chalmers.se

Cover
False-colored scanning electron micrograph of a device that didn't work.

Printed by Chalmers Digital tryck
Göteborg, Sweden 2026

Gate tunability and nonlinearity in hybrid superconductor-semiconductor resonators

VITTORIO BUCCHERI
Quantum Device Physics Laboratory
Department of Microtechnology and Nanoscience (MC2)
Chalmers University of Technology

Abstract

Superconducting microwave resonators and Josephson elements form the basis of a broad range of quantum information technologies, including circuit quantum electrodynamics, Josephson parametric amplification, bosonic quantum computing, and engineered interactions between microwave modes. The properties of these circuits are largely determined by material parameters and design geometry, while magnetic flux often provides a means of in situ control. Electrostatic gating offers an additional degree of freedom, motivating the investigation of gate-tunable superconducting circuits, particularly through the integration of superconductors with semiconductor elements.

In this thesis, we investigate the gate tunability and nonlinear response of superconducting microwave resonators incorporating indium arsenide (InAs) nanowires with epitaxial aluminum (Al) shells. We explore two distinct forms of gate control in this platform: the modification of the superconducting properties of the Al shell and the electrostatic tuning of Andreev bound states (ABSs) in Josephson weak links defined in the InAs core.

We characterize the first form of gate control by measuring the gate-induced changes in resonator frequency and internal losses. We demonstrate that the observed response is well described by the Mattis–Bardeen model using an effective-temperature approach, consistent with an increase in quasiparticle population. Time-domain and modulation measurements further reveal characteristic response times down to a few tens of nanoseconds, highlighting the potential of this mechanism for applications in cryogenic switching and superconducting electronics.

We then investigate the ABS–resonator interaction in both the linear and nonlinear regimes, demonstrating coupling strengths approaching the ultrastrong-coupling regime and, most notably, gate and flux control over the ABS-induced Kerr and cubic nonlinearities. In particular, we show that the Kerr contribution can be tuned through zero while maintaining a finite cubic nonlinearity, and observe three-wave-mixing parametric amplification. These findings are particularly

relevant for applications requiring three-wave mixing with suppressed Kerr effects, such as Josephson parametric amplification.

Together, these results demonstrate the potential of hybrid superconductor–semiconductor devices for engineering gate-tunable microwave circuits and controlling their linear and nonlinear response.

Keywords: Superconducting resonators, InAs nanowires, Josephson junctions, gate-tunability, Kerr nonlinearity, cubic nonlinearity

Acknowledgements

Many months later, as I faced the results of my measurements, I was to remember that distant afternoon when Simone Gasparinetti told me to check the phase dependence of the Kerr nonlinearity. Back then, Simone was not yet my supervisor, and I didn't know what the Kerr nonlinearity was. Moreover, I was soon to discover that most of the fancy-looking features in my data were caused by the magnetic-field sweeps of the PPMS recently installed in the lab next door. Anyway, as it turned out, that dependence was indeed there, and nonlinearities in superconducting resonators are one of the main topics of my thesis. This is then one of the reasons why I am grateful to my now-supervisor. Another one, among many others, is that he adopted me halfway through my PhD and welcomed me into the 202Q-Lab: thank you, Simone!

I would also like to thank Attila Geresdi, who trusted me enough to hire me in the first place, my second supervisor, Thilo Bauch, and examiner, Mikael Fogelström, for their support throughout these years.

The D1ungeon. A large part of my PhD was dedicated to setting up a measurement lab in room D1, on the ground floor of the MC2 building. From day one, or actually even earlier, since they took me out for dinner the evening before, I shared this adventure with Nermin and Ivo. Thank you, guys, for both the dinner and everything that followed! And thank you also to Oleg and Ankit, and to Theresa, Bekmurat, and Rodrigo.

The 202Q-Lab. A special thanks to Linus and Thomas, with whom I shared the longest run in the group. I really hope that next time there won't be any nanowires standing between us!

Although our projects didn't overlap much, I'm also grateful for the chance to have collaborated with many other members of the lab. Thank you, Ingrid, Kazi, François, Aamir, Axel, Kunal, Simon, Claudia, Claire, Vyom, Ludvig, Niranjan, Kiwmann, Lukas, Saba, and Nora.

The Department. I would like to thank all the master's students, fellow PhD students, postdocs, researchers, and professors, especially at QDP, QT, and AQP, for the collaborations, discussions, and everything I've learned from them, as well as for every cappuccino, spritz, cappuccino & banana bread, beer, and fika we've shared over nearly six years!

I'm also grateful to all the staff at MC2 and Chalmers who made sure I had access to laboratories, infrastructure, and even a salary. A special thanks to Annika from the administration, and to Henrik, Niclas, Marcus, and Mattias from Myfab, who I believe are the ones I bothered the most. And of course, almost none

of the measurements presented in this thesis would have been possible without the support of Lars Jönsson and his workshop: thank you, Lars!

Collaborators. I'm happy to have been part of two large European projects: AndQC and SuperGate. I would like to thank all the people involved in these projects, especially those who also became coauthors of my publications: Jesper Nygård and Thomas Kanne in Copenhagen, and Péter Makk, Szabolcs Csonka, and their group in Budapest.

Finally, I am grateful to my family and friends for their support during this adventure, and even more for everything we share that has nothing to do with it.

Vittorio Buccheri
Göteborg, November 2026

This thesis was written in LaTeX using Overleaf. Affinity Designer was used to create schematics, apply false coloring, and arrange data plots into figures. Data analysis and plotting were performed using Python. Generative AI tools were used to assist with the writing process and coding. Any AI-assisted material was reviewed and verified by the author, who takes full responsibility for the content of this thesis.

List of Publications

This thesis is based on the following publications:

- **PAPER I**

  Vittorio Buccheri, François Joint, Kazi Rafsanjani Amin, Tosson Elalaily, Olivér Kürtössy, Zoltán Scherübl, Gergő Fülöp, Thomas Kanne, Jesper Nygård, Péter Makk, Szabolcs Csonka, and Simone Gasparinetti.

  Microwave dynamics of gated Al/InAs superconducting nanowires.

  Applied Physics Letters **126**, 232602 (2025).

- **PAPER II**

  Ivo P. C. Cools, Rodrigo M. López-Báez, **Vittorio Buccheri**, Oleg Shvetsov, Nermin Trnjanin, Emil Hogedal, and Saroj P. Dash.

  Losses in magnetic field resilient coplanar stripline resonators.

  Journal of Physics D: Applied Physics **58**, 255102 (2025).

- **PAPER III**

  Oleg O. Shvetsov, Ankit Khola, **Vittorio Buccheri**, Ivo P. C. Cools, Nermin Trnjanin, Attila Geresdi, Thomas Kanne, and Jesper Nygård.

  Approaching the ultrastrong-coupling regime between an Andreev level and a microwave resonator.

  Physical Review Applied **24**, 044015 (2025).

- **PAPER IV**

  Vittorio Buccheri, Ivo P. C. Cools, Nermin Trnjanin, Ankit Khola, Oleg Shvetsov, Thomas Kanne, Jesper Nygård, Attila Geresdi, and Simone Gasparinetti.

  Kerr nonlinearity and three-wave mixing in superconducting resonators hosting Al-InAs weak links.

  Manuscript under review. arXiv:2608.28428

Contents

Abstract iii

Acknowledgements v

List of Publications vii

Contents ix

List of Abbreviations xi

Introduction 1

1 Background 5
- 1.1 Superconducting microwave resonators . . . 5
- 1.2 Semiconducting nanowires . . . 10
  - 1.2.1 Overview of superconducting-semiconducting heterostructures 10
  - 1.2.2 InAs nanowires with epitaxial Al shell . . . 11
- 1.3 Gate-tunable superconducting properties . . . 13
  - 1.3.1 Gate-tunable supercurrent . . . 13
  - 1.3.2 Microwave counterpart . . . 13
- 1.4 Andreev bound states . . . 16
  - 1.4.1 ABSs in semiconducting nanowires . . . 17
  - 1.4.2 Microwave spectroscopy of ABSs . . . 19
- 1.5 Nonlinearities in superconducting resonators . . . 24
  - 1.5.1 ABS-induced nonlinearities . . . 26

2 Methods 29
- 2.1 Fabrication process . . . 29
  - 2.1.1 Device I: Gate-tunable CPW resonator . . . 29
  - 2.1.2 Device II: NbTiN coplanar stripline resonators . . . 31
  - 2.1.3 Devices III and IV: NbTiN resonators with Josephson weak links . . . 31
- 2.2 Experimental setup . . . 37
  - 2.2.1 Luna . . . 37
  - 2.2.2 Embla . . . 39
  - 2.2.3 Ask . . . 42
  - 2.2.4 Copper-powder filters . . . 43

2.3 Measurements and analysis . . . 48
2.3.1 Single-tone spectroscopy . . . 48
2.3.2 Two-tone spectroscopy . . . 50
2.3.3 Gate-response characterization . . . 51
2.3.4 Preliminary characterization of semiconducting weak-links coupled to resonators . . . 55
2.3.5 Extraction of resonator nonlinearities . . . 59

3 Microwave characterization of Al-capped InAs nanowires 63
3.1 Effective temperature approach . . . 63
3.2 Device dynamics . . . 65

4 Coplanar stripline resonators for hybrid devices 69

5 Probing Andreev bound states 75
5.1 From adiabatic to dispersive readout of ABS . . . 75
5.2 Approaching the ultrastrong-coupling regime between an ABS and a microwave resonator . . . 78

6 Andreev bound state-induced nonlinearities in superconducting resonators 83
6.1 Single-junction configuration . . . 83
6.2 Double-junction configuration . . . 86
6.2.1 Three-wave mixing amplification . . . 88
6.2.2 Towards Andreev molecule devices . . . 90

Conclusion 91

Appendices 93

A Fabrication recipes 95
A.1 Auxiliary recipes . . . 95
A.2 Device fabrication . . . 98

References 103

Appended papers 117

Paper I 119

Paper II 137

Paper III 153

Paper IV 167

List of Abbreviations

3WM	Three-wave mixing
ABS	Andreev bound state
ATS	Asymmetrically threaded SQUID
BCS	Bardeen–Cooper–Schrieffer
CPW	Coplanar waveguide
CPS	Coplanar stripline
cQED	Circuit quantum electrodynamics
CW	Continuous wave
HEMT	High-electron-mobility transistor
JJ	Josephson junction
JOFET	Josephson field-effect transistor
KID	Kinetic-inductance detector
LINC	Linear inductive coupler
SEM	Scanning electron micrograph
SNAIL	Superconducting nonlinear asymmetric inductive element
SNR	Signal-to-noise ratio
SQPT	Single-quasiparticle transition
SQUID	Superconducting quantum interference device
TLS	Two-level system
TMAH	Tetramethylammonium hydroxide
TWPA	Traveling-wave parametric amplifier
VNA	Vector network analyzer

Introduction

Superconducting microwave resonators are among the main building blocks of superconducting electronics and quantum information processing [1]. In their linear-response regime, they are well described as harmonic oscillators with high quality factors, which gives them well-defined resonance frequencies and long photon lifetimes. They are widely employed for qubit readout [2], as quantum buses [3] and memories [4], and in Purcell filters [5].

The other main player in superconducting circuits is the Josephson junction, most commonly implemented as two superconducting electrodes separated by a thin insulating barrier. Such tunnel junctions are described by the nonlinear Josephson potential [6]

$$\varepsilon_{\mathrm{JJ}}(\varphi) = -E_J \cos\varphi,$$

where E_J is the Josephson energy and φ the superconducting phase difference across the junction. This nonlinearity is essential for superconducting qubits such as transmons [7] and fluxoniums [8], whose anharmonic energy spectra allow two levels to be addressed selectively. Furthermore, incorporating one or more junctions into superconducting loops yields more complex nonlinear elements, such as superconducting quantum interference devices (SQUIDs) [9] and superconducting nonlinear asymmetric inductive elements (SNAILs) [10].

Resonators and Josephson elements are combined for two main purposes. Coupling superconducting qubits to microwave resonators gives rise to circuit quantum electrodynamics (QED) [11, 12], the circuit counterpart of cavity QED, where artificial atoms interact with confined microwave photons. Embedding a nonlinear Josephson element in a resonator, on the other hand, allows the latter to inherit the nonlinearity of the former, enabling Josephson parametric amplification [10, 13, 14], bosonic quantum computing [15], and engineered coupling schemes between microwave modes [16].

A common challenge in these applications is to engineer the material properties and circuit geometry to obtain the desired response, which can then be tuned in situ through magnetic-flux bias. For example, in circuit QED architectures, the circuit parameters determine the characteristic energy scales of superconducting qubits, while magnetic flux can be used to tune their transition frequencies relative to the resonator. Similarly, in a SNAIL, the Josephson energies and junction asymmetry are designed to achieve a sizable cubic nonlinearity while suppressing the Kerr contribution, with the relative strength of these terms controlled by magnetic flux. In both cases, the accessible range of tunability remains constrained

by the material properties and circuit design established during fabrication.

Electrostatic gating offers an appealing degree of freedom alongside magnetic-flux biasing, in principle enabling more localized control with reduced cross-talk and allowing high-impedance, strongly filtered bias lines to suppress microwave leakage.

In this thesis, we investigate gate control by integrating indium arsenide (InAs) nanowires with an epitaxial aluminum (Al) shell [17] into superconducting microwave resonators. In particular, these hybrid nanowires provide access to two distinct forms of gate control: the modification of the superconducting properties of the Al shell and the electrostatic tuning of Josephson weak links defined in the InAs core.

In fact, the Al shell offers a rather unexpected route to gate control. In metallic superconductors, the high carrier density leads to strong electrostatic screening, making conventional electrostatic modulation unlikely [6]. Nevertheless, in 2018, De Simoni *et al.* demonstrated the suppression of supercurrent in metallic nanowires through an applied gate voltage [18]. This discovery sparked considerable interest, although the underlying mechanism remains debated, as discussed in the review by Ruf *et al.* [19]. Notably, the suppression of supercurrent is often accompanied by the onset of a finite gate leakage current, suggesting the possible involvement of nonequilibrium processes. In the microwave regime, this gate-induced response has been observed as a shift in the resonance frequency and a reduction of the internal quality factor of superconducting resonators [20, 21], reflecting changes in the reactive and dissipative components of the superconducting impedance, respectively.

The second form of gate tunability is achieved by selectively removing a section of the Al shell, thereby defining a semiconducting Josephson weak link whose properties are governed by Andreev bound states (ABSs) [22, 23]. In the short-junction limit, a single spin-degenerate channel hosts a pair of ABSs with energies

$$\pm\varepsilon_{\mathrm{ABS}}(\varphi) = \pm\Delta\sqrt{1-\tau\sin^2\left(\frac{\varphi}{2}\right)},$$

where Δ is the superconducting gap and τ is the channel transparency. The latter can be controlled electrostatically, introducing an additional degree of freedom alongside the superconducting phase difference φ, which remains adjustable through magnetic flux. The resulting gate- and phase-dependent energy spectrum provides a basis for Andreev qubits [24, 25], as well as for engineering the nonlinear response of superconducting circuits [26].

We investigate the first form of gate tunability in PAPER I, where we show that the gate response in our device is consistent with an increase in quasiparticle population described by an effective-temperature approach. We further investigate the dynamics of this response, measuring characteristic times down to a few tens

of nanoseconds. In PAPER IV, instead, we exploit the gate- and phase-dependent ABS potential to control the nonlinear response of a resonator incorporating two Al/InAs Josephson weak links. We demonstrate that the Kerr nonlinearity can be tuned through zero while maintaining a finite cubic contribution, and observe three-wave-mixing parametric amplification.

Complementing our ABS investigation, PAPER II develops and characterizes NbTiN coplanar stripline resonators designed for experiments with hybrid devices. Finally, PAPER III investigates the ABS–resonator coupling, demonstrating coupling strengths approaching the ultrastrong-coupling regime.

Outline

This thesis is organized into six chapters, followed by the Conclusion and an appendix containing the fabrication recipes. The four papers, each with a short description of the candidate's contribution, are appended at the end.

- **Chapter 1 – Background** introduces the theoretical concepts underlying this work, including superconducting microwave resonators, superconductor–semiconductor heterostructures, gate-controlled superconducting properties, Andreev bound states, and nonlinear superconducting circuits.
- **Chapter 2 – Methods** describes the device fabrication processes, experimental setups, and microwave measurement techniques used throughout this thesis. It also presents the development and characterization of custom-made copper-powder microwave filters.
- **Chapter 3 – Microwave characterization of Al-capped InAs nanowires** investigates the gate-induced changes in the microwave impedance of superconducting nanowires, focusing on their effective-temperature description and characteristic response times (PAPER I).
- **Chapter 4 – Coplanar stripline resonators for hybrid devices** presents the characterization of NbTiN resonators developed for hybrid devices (PAPER II).
- **Chapter 5 – Probing Andreev bound states** discusses the interaction between ABSs and microwave resonators, from adiabatic to dispersive readout (PAPER IV), and presents the experimental investigation of coupling strengths approaching the ultrastrong-coupling regime (PAPER III).
- **Chapter 6 – Andreev bound state-induced nonlinearities in superconducting resonators** investigates the gate- and flux-dependent Kerr and cubic nonlinearities of Al/InAs Josephson weak links, including their application to three-wave-mixing parametric amplification (PAPER IV).

1 Background

In this chapter, we provide the background necessary to follow the work presented later. As mentioned in the introduction, superconducting microwave resonators and Al-capped InAs nanowires are two of the main players of this thesis: the first two sections present these systems and their relevant properties. The remaining sections introduce the three topics this thesis investigates: gate-tunable superconducting properties, Andreev bound states and their microwave spectroscopy, and nonlinearities in superconducting resonators.

1.1 Superconducting microwave resonators

Superconducting microwave resonators are structures that support electromagnetic fields at discrete resonant frequencies. In this sense, they are the circuit analogue of optical cavities: instead of confining light between reflecting mirrors, they confine electromagnetic fields in a portion of the circuit, thanks to its geometry and electrical properties [1].

We first consider resonator structures based on two transmission-line geometries: the coplanar waveguide (CPW) [Fig. 1.1a)] and the coplanar stripline (CPS) [Fig. 1.1b)]. Both consist of a superconducting layer deposited on top of a dielectric substrate with thickness t and relative permittivity ε_r. In a CPW geometry, the conducting layer is divided into a central conductor of width W and two lateral ground planes, separated from the central conductor by gaps of width G. In contrast, a CPS geometry consists of two parallel conductors of width W, separated by a gap G. Both geometries are characterized by a characteristic impedance $Z_0 \approx \sqrt{l/c}$, where l and c are the inductance and capacitance per unit length. The capacitance is set by the geometry (W, G) and by the substrate thickness and permittivity (t, ε_r). The inductance has two contributions: a geometric one, also set by W and G, and a kinetic one, due to the inertia of the Cooper pairs. For our thin superconducting films at low temperature, the sheet kinetic inductance can be estimated as [6, 27]

$$L_\mathrm{k}^\square = \frac{\hbar R_\mathrm{N}^\square}{\pi \Delta_0}, \tag{1.1}$$

where $R_\mathrm{N}^\square$ is the normal-state sheet resistance of the superconductor and Δ_0 is the superconducting gap at $T = 0$, estimated using the BCS relation $\Delta_0 \approx 1.764 k_\mathrm{B} T_\mathrm{c}$, with T_c the critical temperature. More generally, a transmission line is also charac-

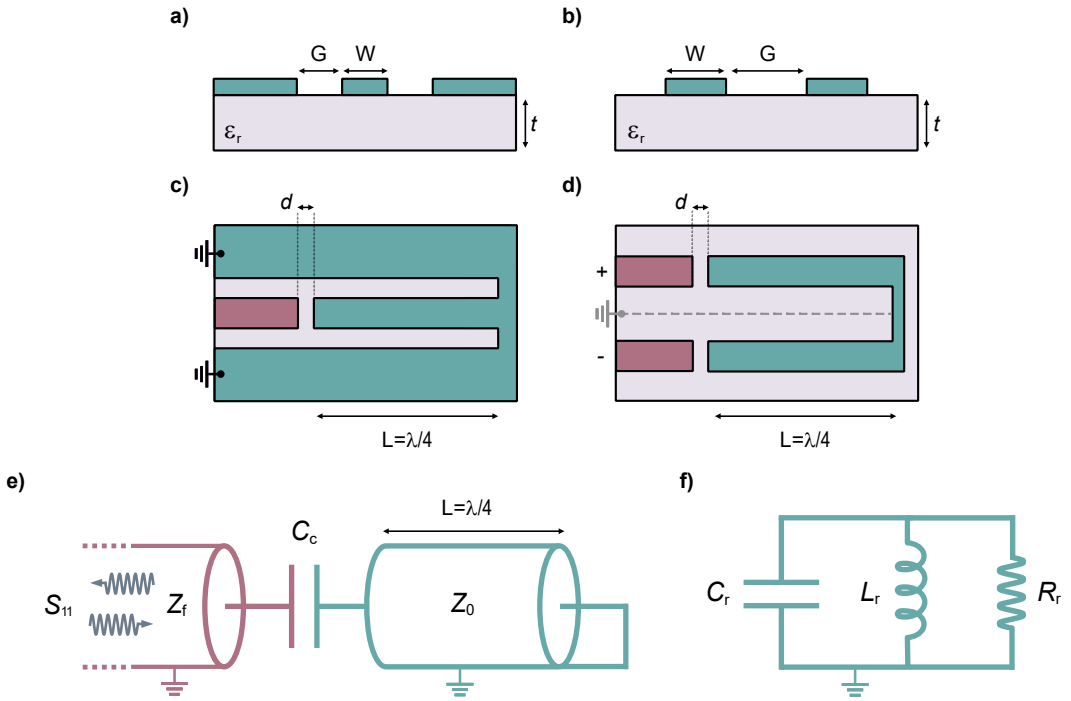


Figure 1.1: Schematic cross-sections of **a)** a coplanar waveguide (CPW), where a central conductor of width W is separated by a gap G from two lateral ground planes, and **b)** a coplanar stripline (CPS), where two conductors of width W are separated by a gap G. In both geometries, the waveguide is made of a superconductor (green) deposited on a substrate of thickness t and relative permittivity ε_r (gray). Schematic top views of a quarter-wavelength **c)** CPW and **d)** CPS resonator. In the CPW resonator, the central conductor is capacitively coupled to a feedline (red) carrying the probing signal on the left, and shorted to the ground plane on the right. In the CPS resonator, the two conductors are capacitively coupled to two feedlines (red) carrying out-of-phase signals on the left, and shorted to each other on the right. For the odd mode, the dashed symmetry line represents a virtual ground. In both cases, L $= \lambda/4$ is the length of the resonator, and d is the distance between the resonator and the feedline. **e)** Transmission-line model of a $\lambda/4$ resonator with characteristic impedance Z_0 coupled to a feedline with characteristic impedance Z_f via a coupling capacitor C_c and probed in reflection through the reflection coefficient S_{11}. **f)** Lumped-equivalent circuit where the resonator is represented as a parallel LCR circuit with effective capacitance C_r, inductance L_r, and resistance R_r. The corresponding effective resonator impedance is $Z_\mathrm{r} = \sqrt{L_\mathrm{r}/C_\mathrm{r}} = 4Z_0/\pi$.

terized by a series resistance and a parallel conductance per unit length, which account for conductor and dielectric losses, respectively. In superconducting coplanar waveguides, however, conductor losses are strongly suppressed, and dissipation at low temperature and low probing power is often dominated by dielectric losses associated with two-level systems located at material surfaces and interfaces [28, 29].

Neglecting spurious modes, in a CPW the potential of the central conductor oscillates with respect to the two ground planes, which sit at a constant value ($V = 0$). A CPS, on the other hand, can support either an even or an odd mode, depending on whether the potentials of the two conductors oscillate in phase or out of phase. In this thesis, we will consider the CPS odd mode, in which the two conductors oscillate out of phase, namely at opposite potentials. By symmetry, then, the potential vanishes at the center of the gap, which acts as a virtual ground.

A resonator can be formed from a transmission line by imposing appropriate boundary conditions at its ends [30]. Here, we discuss quarter-wavelength waveguide resonators, which are waveguide segments of length L that support a fundamental resonance when $L = \lambda/4$, where λ is the mode wavelength. This gives them their name, $\lambda/4$ resonators. In a CPW, this condition can be realized by leaving one end of the central conductor open and short-circuiting the other end to the ground planes [Fig. 1.1c)]. Similarly, in a CPS, the two conductors are left open at one end and short-circuited to each other at the other [Fig. 1.1d)]. In both cases, the open end of the resonator is capacitively coupled to the feedline circuitry via a coupling capacitor C_c, which is defined by geometry (W and the distance d between the resonator and the feedline) and material properties (ε_r). Through this feedline, the resonator becomes part of a microwave network characterized by complex scattering parameters S_{ij}, which describe the interaction of the probing microwave signals with the resonator.

A typical resonator can therefore be modeled as a transmission line of length $L = \lambda/4$ and characteristic impedance Z_0, short-circuited at one end and capacitively coupled at the other to an external microwave feedline, through which probing signals can interact with the resonator [Fig. 1.1e)]. While the same transmission-line formalism applies to both geometries, Z_0 refers to the voltage and current between the central conductor and the ground planes in a CPW, and to the differential voltage and current between the two conductors in a CPS.

The system is then characterized by the angular resonance frequency ω_r, which determines the frequency at which electromagnetic energy can be stored in the resonator; the external quality factor Q_c, which describes the coupling to the feedline through the rate $\kappa_\mathrm{c} = \omega_\mathrm{r}/Q_\mathrm{c}$; and the internal quality factor Q_i, which accounts for energy dissipation within the resonator through the loss rate $\kappa_\mathrm{i} =$

$\omega_\mathrm{r}/Q_\mathrm{i}$. The loaded quality factor Q_l, which is defined as

$$\frac{1}{Q_\mathrm{l}} = \frac{1}{Q_\mathrm{i}} + \frac{1}{Q_\mathrm{c}}, \tag{1.2}$$

accounts for both mechanisms and therefore characterizes the overall rate at which energy leaves the resonator.

In a reflection configuration, we extract ω_r and the quality factors from measurements of $S_{11}(\omega)$, which, close to resonance, can be described by the following simplified[1] expression [31, 32]

$$S_{11} \sim \left[\frac{2Q_l/Q_c}{1 + 2iQ_l\,(\omega/\omega_\mathrm{r} - 1)} - 1\right]. \tag{1.3}$$

In principle, the characteristic impedance Z_0 can be calculated from the transmission-line geometry using conformal mapping techniques, throughout this thesis, however, we obtain it from electromagnetic simulations of the resonator structure. More information about these procedures will be given in Chapter 2.

Close to its fundamental resonance, an ideal, uniform $\lambda/4$ distributed resonator can be represented by an equivalent parallel circuit [Fig. 1.1f)], where the effective capacitance $C_\mathrm{r} = \pi/(4\omega_\mathrm{r}Z_0)$ and inductance $L_\mathrm{r} = 4Z_0/(\pi\omega_\mathrm{r})$ define the resonant frequency and resonator impedance,

$$\omega_\mathrm{r} = \frac{1}{\sqrt{L_\mathrm{r}C_\mathrm{r}}}, \qquad Z_\mathrm{r} = \sqrt{\frac{L_\mathrm{r}}{C_\mathrm{r}}} = \frac{4Z_0}{\pi}, \tag{1.4}$$

whereas the effective resistance R_r accounts for internal losses.

In this thesis, we used a CPW resonator in PAPER I, CPS resonators in PAPER II and PAPER IV, and a lumped-element resonator in PAPER III. In contrast to the distributed transmission-line resonators discussed so far, in a lumped-element resonator the inductive and capacitive contributions are spatially localized and represented directly by an inductance L_r and a capacitance C_r. Within this description, the resonator mode corresponds to the periodic exchange of energy between the electric field of the capacitor and the magnetic field of the inductor. Despite this difference, the resonator is characterized by the same quantities introduced above, in particular ω_r, Q_i, Q_c and Z_r.

In Sec. 1.4, we will introduce Andreev bound states and discuss their coupling to a resonator. It will then be necessary to treat the resonator quantum-mechanically. Neglecting losses, the equivalent LC circuit can be quantized using the node flux $\Phi(t) = \int_{-\infty}^{t} V(t')\,dt'$ as a generalized coordinate, where V is the voltage across the equivalent LC circuit, such that $V = \dot{\Phi}$ [33, 34]. The Lagrangian

[1] Here, we neglect attenuation, cable delay, and impedance mismatch in the measurement environment. Full expressions for both pure-reflection and notch-type setups will be given in Chapter 2.

of the system then reads

$$\mathcal{L} = \frac{C_\mathrm{r}}{2}\dot{\Phi}^2 - \frac{\Phi^2}{2L_\mathrm{r}}. \tag{1.5}$$

The conjugate momentum is the charge on the capacitor,

$$Q = \frac{\partial \mathcal{L}}{\partial \dot{\Phi}} = C_\mathrm{r}\dot{\Phi}, \tag{1.6}$$

and the Legendre transformation $H = Q\dot{\Phi} - \mathcal{L}$ gives the Hamiltonian

$$H = \frac{Q^2}{2C_\mathrm{r}} + \frac{\Phi^2}{2L_\mathrm{r}}. \tag{1.7}$$

The circuit is quantized by promoting Φ and Q to operators satisfying $[\hat{\Phi}, \hat{Q}] = i\hbar$ and introducing the bosonic annihilation and creation operators, $\hat{a}$ and $\hat{a}^\dagger$, which allow us to write

$$\hat{\Phi} = \Phi_\mathrm{zpf}\left(\hat{a} + \hat{a}^\dagger\right), \qquad \hat{Q} = -iQ_\mathrm{zpf}\left(\hat{a} - \hat{a}^\dagger\right), \tag{1.8}$$

where

$$\Phi_\mathrm{zpf} = \sqrt{\frac{\hbar Z_\mathrm{r}}{2}}, \qquad Q_\mathrm{zpf} = \sqrt{\frac{\hbar}{2Z_\mathrm{r}}}. \tag{1.9}$$

Finally, substituting Eqs. 1.8 and 1.9 into the Hamiltonian in Eq. 1.7 gives

$$\hat{H}_\mathrm{r} = \hbar\omega_\mathrm{r}\left(\hat{a}^\dagger\hat{a} + \frac{1}{2}\right), \tag{1.10}$$

which is the Hamiltonian of a quantum harmonic oscillator.

Importantly, the zero-point flux fluctuations of the resonator mode scale as $\Phi_\mathrm{zpf} \propto \sqrt{Z_\mathrm{r}}$ and therefore increase with the resonator impedance. As we will see, larger zero-point flux fluctuations can enhance the interaction with systems coupled to the resonator flux, such as the Andreev bound states considered later in this thesis. The resonator impedance Z_r is therefore a key parameter in determining the coupling strength, together with the fraction of the resonator flux seen by the coupled system.

1.2 Semiconducting nanowires

The resonators discussed in the previous section are fully superconducting devices made from a single metallic layer. Since our goal is to study superconductor-semiconductor hybrid devices, a semiconducting element needs to be embedded into the resonator structures. In our case, this semiconducting element consists of an Al-capped InAs nanowire, which we introduce in this section.

1.2.1 Overview of superconducting-semiconducting heterostructures

Semiconductors typically have a much lower charge-carrier density than metals, which allows their conductivity to be controlled electrostatically, as in field-effect transistors (FETs) [35], or individual electrons to be confined and manipulated through appropriately shaped electrostatic potentials, as in quantum dots [36]. At the same time, in conventional superconductors, a large number of electrons form Cooper pairs that condense into a single macroscopic quantum state [37], resulting in remarkable properties such as dissipationless current flow (supercurrent) and the Josephson effect. Superconductor-semiconductor hybrid structures combine these different properties within a single device. An example of such a system is the Josephson field effect transistor (JOFET), proposed in 1980 [38], where the supercurrent through a semiconducting Josephson junction is controlled by an electrostatic gate. Experimental demonstrations of JOFETs have been achieved in various combinations of superconductor/semiconductor, including Al/InAs [39], Al/SiGe [40], Al/InSb [41], Nb/InAs [42], and NbTiN/InSb [43].

A major limiting factor in realizing these heterostructures is obtaining a good interface between the semiconductor and the superconductor. In fact, the transfer of Cooper-pair correlations from the superconductor to the semiconductor, known as the proximity effect [6], relies on a particular reflection mechanism at the interface, called Andreev reflection, which will be discussed later. Oxide contamination and Schottky barriers reduce the interface transparency, favoring normal reflection over Andreev reflection and thereby weakening the proximity effect in the semiconductor. This limits the choice of materials and motivates the development of fabrication techniques aimed at improving the semiconductor-superconductor interface, including semiconductor doping [44] and the introduction of a thin Si interlayer at the Al/InGaAs interface [45, 46]. Important breakthroughs in this fabrication effort were reported between 2015 and 2016, with the development of epitaxial aluminum growth in two platforms: InAs nanowires [17, 47] and InAs/InGaAs two-dimensional electron gases (2DEGs) [48].

Besides the quality of the interface, another relevant semiconductor property is the spin-orbit coupling, which is a relativistic effect that couples the spin and momentum of an electron moving in an electric field. This interaction can lift the

spin degeneracy of the semiconductor subbands even without an applied magnetic field and, as we will discuss in Sec. 1.4, can also produce spin splitting of Andreev bound states in finite-length semiconducting Josephson junctions, enabling the realization of spin qubits [25]. On the superconductor side, instead, a large superconducting gap and a high critical field are desirable for maintaining induced superconductivity at elevated temperatures and in large external magnetic fields. Promising alternatives to Al and Nb compounds include Sn [49] and Pb [50].

A broader overview of material challenges and applications of these heterostructures can be found in Ref. [51].

1.2.2 InAs nanowires with epitaxial Al shell

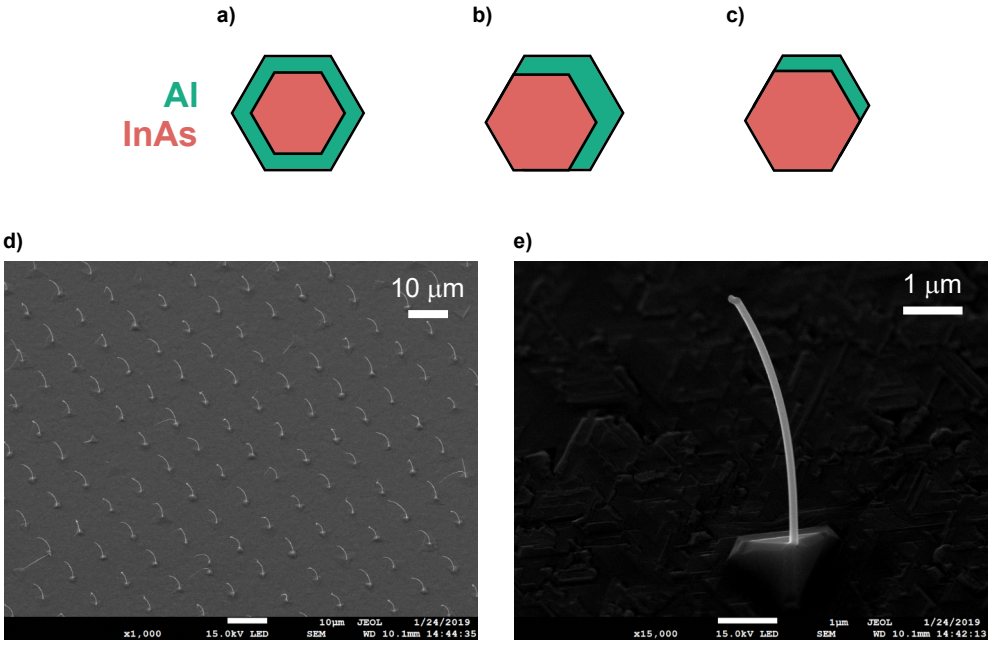


Figure 1.2: Schematic cross-sections of InAs nanowires (red) with an epitaxial Al shell (green) covering **a)** the entire semiconducting core (full-shell), **b)** three facets (half-shell), and **c)** two facets. Tilted scanning electron micrographs (SEMs) of **d)** an array of as-grown half-shell Al/InAs nanowires and **e)** a single nanowire. The SEM images are courtesy of Jesper Nygård and Thomas Kanne.

In this thesis, we investigate InAs nanowires capped with Al [17, 47], which were fabricated at the Center for Quantum Devices of the Niels Bohr Institute (University of Copenhagen).

The nanowires are grown on an InAs substrate in a molecular beam epitaxy system by the Au-catalysed vapour–liquid–solid method [17]. They have a hexagonal cross-section, with dimensions set by the growth conditions. Typical lengths of 5–10 μm and diameters of 60–100 nm are reported in Ref. [17]. The Al shell is epitaxially grown in situ in three different configurations: full-shell [Fig. 1.2a)], half-

shell [Fig. 1.2b)] and two-facet [Fig. 1.2c)]. After growth, the Al/InAs nanowires form a forest-like array extending from the substrate [Fig. 1.2d)], from which individual nanowires [Fig. 1.2e)] can be picked up and transferred to the device substrate (see Chapter 2).

The shell geometry determines, in particular, how much of the InAs surface remains exposed and can therefore be directly coupled to electrostatic gates. In the full-shell geometry, the Al completely surrounds the InAs core and screens it from external electric fields. By contrast, partial-shell geometries leave part of the semiconductor exposed, allowing stronger electrostatic control of its carrier density and confinement potential. The shell geometry and the resulting electrostatic potential can also modify the spin-orbit interaction, including the strength of its Rashba contribution and the orientation of the effective spin-orbit field [52, 53]. These properties, and more generally the shell geometry, are particularly relevant in experiments targeting topological phenomena [54, 55], as well as in studies involving external magnetic fields [56].

In our experiments, however, the main practical distinction between the devices is whether the InAs core is exposed to electrostatic gating through a weak link. In PAPER I, we wanted to investigate the gate response of the superconducting Al shell without directly gating the semiconductor (see Sec. 1.3), making the full-shell geometry the natural choice. In PAPER III and PAPER IV, we investigated Andreev bound states (Sec. 1.4) in semiconducting Josephson junctions, which we fabricated from half-shell nanowires by selectively etching a portion of the Al shell. Nonetheless, we do not expect the main results discussed there to depend qualitatively on the shell geometry. In particular, the phenomena investigated in PAPER III have also been observed in devices with weak links etched in full-shell [23] and two-facet nanowires [57].

1.3 Gate-tunable superconducting properties

Electrostatic gating is a key ingredient of semiconductor technology, where an applied electric field can be used to locally control the carrier density and, consequently, the electrical properties of a device [35]. Extending a similar approach to superconducting circuits would combine the versatility of gate control with the dissipationless transport of superconductors, a particularly attractive prospect for cryoelectronic applications [58].

1.3.1 Gate-tunable supercurrent

This prospect gained new momentum in 2018, when De Simoni et al. demonstrated gate control of the switching current in Ti and Al thin-film devices, originally attributing this behavior to an electrostatic field effect [18]. Following these findings, similar results have been reported in several materials, geometries, and platforms, while alternative explanations have been proposed for the underlying microscopic mechanism, which remains under debate [20, 21, 59–70].

Thorough overviews of the experimental findings, possible applications, and proposed microscopic mechanisms can be found in Andrea Iorio's PhD thesis [71] and in the review by Ruf et al. [19]. Following these references, and for the purposes of this thesis, the phenomenology of gate-controlled supercurrent can be summarized by a few common experimental features:

- The effect is observed in all-metallic superconducting devices.
- The effect occurs above a characteristic gate-voltage onset and is approximately symmetric with respect to gate-voltage polarity. The switching current remains nearly constant below this onset and monotonically decreases above it, eventually being fully suppressed.
- The suppression of the switching current is commonly accompanied by a finite gate leakage current.
- The characteristic gate-voltage onset depends only weakly on temperature.

1.3.2 Microwave counterpart

These features have been predominantly established through DC measurements, by observing the suppression of the switching current in superconducting bridges [59–61, 63–69]. In this thesis, we focus on their microwave counterpart, where the effect manifests itself through gate-induced changes in the resonant frequency and losses of superconducting resonators. To illustrate the connection with the phenomenology discussed above, we use the preliminary characterization of the

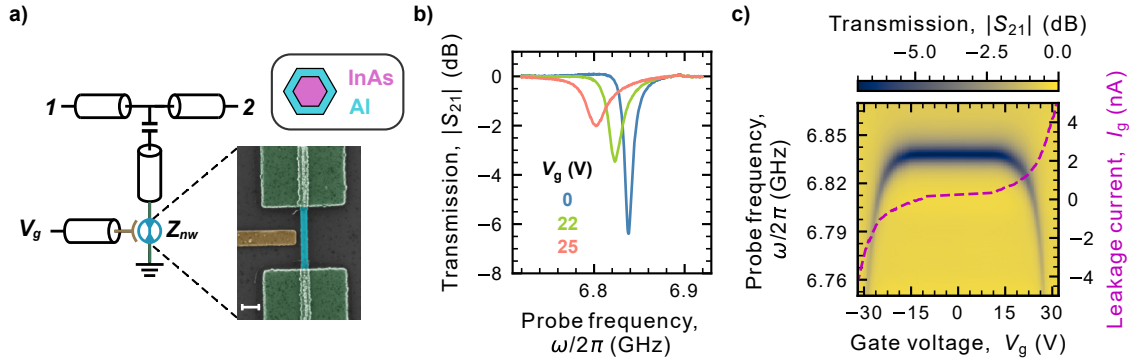


Figure 1.3: a) Simplified schematic of the device. The resonator is capacitively coupled to the feedline in a notch-type configuration and is characterized through the feedline transmission. The scanning electron micrograph shows the nanowire (scale bar: 300 nm) and is courtesy of our collaborators in Budapest. *Inset*: Schematic of the nanowire cross-section. The Al shell and the InAs core have a thickness of 20 nm and a diameter of 150 nm, respectively. **b)** Magnitude of the feedline transmission parameter, $|S_{21}|$, as a function of probe frequency ω for three gate voltages V_g. **c)** Heat map of $|S_{21}|$ vs V_g and ω. The gate leakage current I_g is plotted against the right axis.

device investigated in PAPER I and compare our observations with the existing literature.

The system we investigate consists of a $\lambda/4$ CPW superconducting resonator [72], with an InAs nanowire covered by a full Al shell embedded close to the resonator current antinode [Fig. 1.3a)]. The nanowire is modeled as an impedance Z_{NW}, which can be tuned through a side gate placed next to it. The resonator is capacitively coupled to a transmission line in a notch-type geometry and characterized by measuring the feedline transmission parameter S_{21}. Importantly, the InAs core is screened from the gate-induced electric field by the Al shell, whose thickness is orders of magnitude larger than the Thomas–Fermi screening length [69]. Direct electrostatic modulation of the carrier density in the InAs core is therefore expected to be negligible.

We first measure S_{21} as a function of probe frequency ω at $V_{\mathrm{g}} = 0$ V and identify a resonance dip around $\omega_{\mathrm{r}}/2\pi \approx 6.84$ GHz. Increasing the gate voltage to $V_{\mathrm{g}} = 22$ V and then 25 V produces a progressive shift of the resonant frequency towards lower values, together with a broadening of the resonance [Fig. 1.3b)]. The gate dependence becomes clearer when $|S_{21}|$ is shown as a function of both ω and V_{g} [Fig. 1.3c)]. The response exhibits an onset around $|V_{\mathrm{g}}| \approx 16$ V and is approximately symmetric with respect to gate-voltage polarity. Moreover, the onset of the resonator gate response coincides with a rise in the gate leakage current, which reaches a few nA [Fig. 1.3c), right axis]. We extract (see Chapter 2) the resonant frequency ω_{r} and internal quality factor Q_{i} from the complex transmission coefficient [Fig. 1.4a)-b)]. Both quantities decrease monotonically with

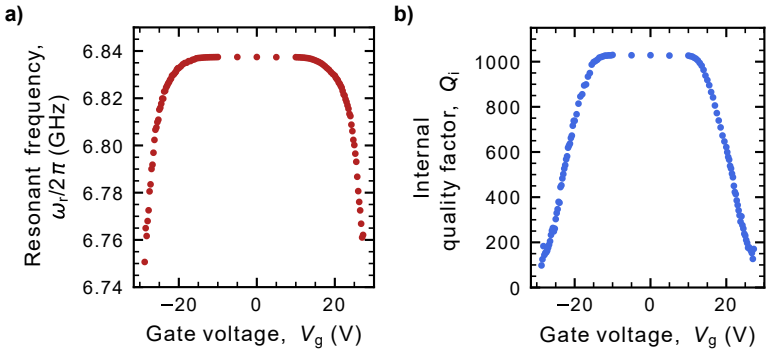


Figure 1.4: a) Resonant frequency ω_r and **b)** internal quality factor Q_i as a function of gate voltage V_g.

increasing $|V_g|$ above the gate onset, going from $\omega_r/2\pi \approx 6.84$ GHz and $Q_i \approx 1000$ at $V_g = 0$ V to $\omega_r/2\pi \approx 6.75$ GHz and $Q_i \approx 100$ around $V_g = \pm 30$ V. Finally, we repeat the measurement at different temperatures [Fig. 1.5]. Increasing the temperature reduces both ω_r and Q_i already at $V_g = 0$ V, consistent with the increase in kinetic inductance and quasiparticle losses. In contrast, the characteristic gate-voltage onset and approximate symmetry of the gate response remain largely unchanged over the investigated temperature range.

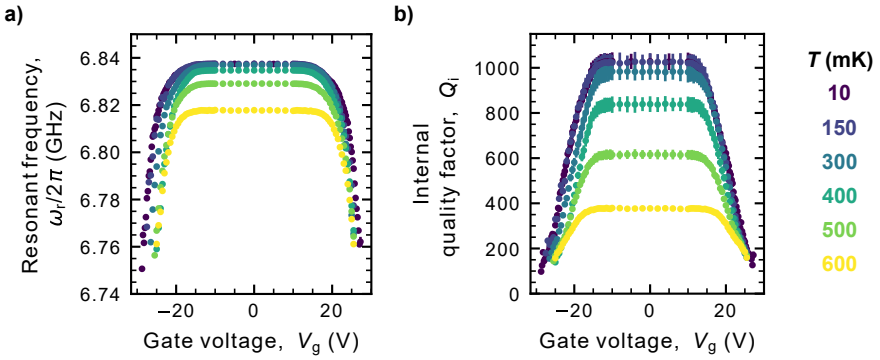


Figure 1.5: a) Resonant frequency ω_r and **b)** internal quality factor Q_i as a function of gate voltage V_g for different mixing-chamber temperatures.

The gate dependence of the resonant frequency and quality factor therefore displays features analogous to those observed in switching-current measurements, consistently with previous reports on similar devices [20, 21, 62, 70]. Furthermore, the simultaneous frequency shift and increase in losses indicate changes in both the reactive and dissipative components of the nanowire impedance. The analysis of these changes, together with the investigation of the gate-response dynamics, is presented in PAPER I and Chapter 3.

1.4 Andreev bound states

In analogy with electronic bound states of an electron trapped in a finite potential well, Andreev bound states (ABSs) are localized fermionic states arising in a weak link through repeated Andreev reflections of electron-like quasiparticles at the interfaces with the superconducting leads [73, 74]. These states underlie the microscopic description of the Josephson effect. However, individual ABSs can be spectroscopically resolved most easily in systems with a small number of highly transmitting conduction channels, such as atomic point contacts [24, 75, 76], carbon nanotubes [77, 78], graphene Josephson junctions [79, 80], and semiconducting Josephson junctions [22, 23, 25, 81–86]. Here, we focus on the latter.

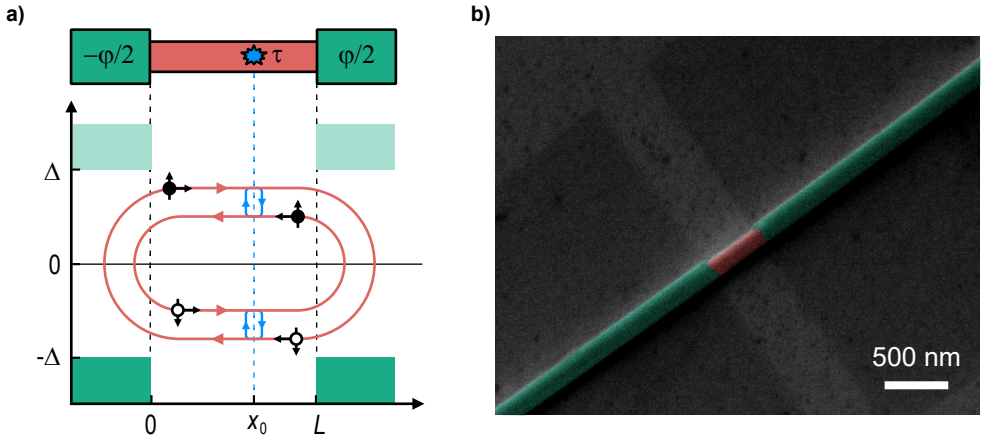


Figure 1.6: a) *Top:* Sketch of a semiconducting weak link. The semiconducting region (red) of length L is sandwiched between two superconducting leads (green) with energy gap Δ and phase difference φ. The weak link hosts a single conduction channel containing a scatterer at x_0 (blue star) with transmission probability τ. *Bottom:* Schematic of the quasiparticle trajectories and the superconducting density of states in the leads (green regions), with an energy gap 2Δ around the Fermi energy; dark and light green indicate occupied and empty states, respectively. Electrons (full circles) and holes (open circles) propagate back and forth through the weak link, undergoing Andreev reflection at the superconductor-semiconductor interfaces (red paths) or normal scattering at x_0 (blue paths). The quasiparticle spin is indicated by the vertical arrows. Only trajectories of spin-up electrons and spin-down holes are shown; an analogous set of trajectories exists for the opposite spin. Image inspired by Refs. [23, 57]. **b)** False-colored scanning electron micrograph of an InAs nanowire with an epitaxial Al shell (green), deposited on a substrate and locally etched to expose the semiconductor core and form a Josephson weak link.

1.4.1 ABSs in semiconducting nanowires

To understand the formation of ABSs in a weak link, consider a semiconducting region of length L sandwiched between two superconducting leads with energy gap Δ and phase difference φ [Fig. 1.6a)]. Following Refs. [22, 23, 57], we describe each conduction channel in the weak link using a single-scatterer model, with a scatterer located at x_0 and transmission probability τ. Electron-like and hole-like quasiparticles propagating through the weak link can undergo Andreev reflection at the semiconductor-superconductor interfaces [red paths in Fig. 1.6a)] or normal scattering at x_0 [blue paths in Fig. 1.6a)]. Experimentally, we realize a semiconducting weak link in our nanowires by selectively etching a portion L of the Al shell, thereby exposing the InAs core [Fig. 1.6b)].

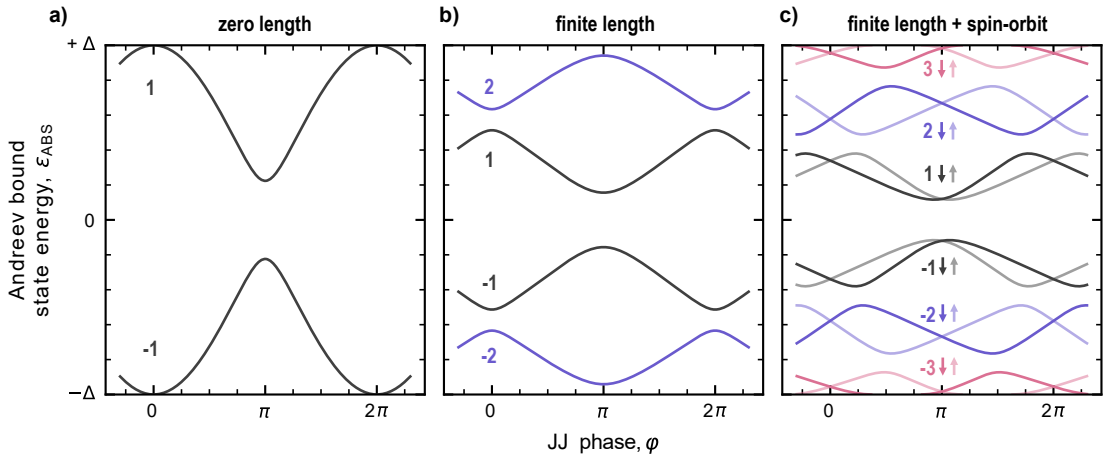


Figure 1.7: Phase-dependent energy spectrum of Andreev bound states in a weak link described by a single effective conduction channel: **a)** in the zero-length limit, **b)** for a finite length junction, and **c)** for a finite length junction with spin-orbit coupling, which lifts the spin degeneracy away from $\varphi = 0$ and π. The spectra are obtained by solving Eq. 1.12 using the parameters listed in Table 1.1. Adapted from Ref. [22].

Depending on the parameter $\Lambda = L/\xi$, where $\xi = \hbar v_F/\Delta$ is the ballistic superconducting coherence length and v_F is the Fermi velocity in the semiconducting region, one can distinguish two regimes [22]:

- **Zero length:** For $\Lambda = 0$, each conduction channel in the weak link hosts a spin-degenerate pair of ABSs [Fig. 1.7a)] with phase-dependent energies given by

$$\pm\varepsilon_{\mathrm{ABS}} = \pm\Delta\sqrt{1 - \tau\sin^2\left(\frac{\varphi}{2}\right)}. \tag{1.11}$$

  This expression also provides a good approximation in the short-junction limit, $\Lambda \ll 1$.

- **Finite length:** As the junction length increases, due to the quantization condition yielding a level spacing $\sim \hbar v_\mathrm{f}/L$, additional spin-degenerate ABS pairs fit inside the superconducting gap [Fig. 1.7b)]. Moreover, spin-orbit coupling can lift the spin degeneracy away from $\varphi = 0$ and π [Fig. 1.7c)]. The minimal model considered here that takes into account both effects includes coupling between two transverse subbands of the semiconductor, giving rise to two characteristic Fermi velocities, v_1 and v_2, associated with spin-orbit-coupled propagating modes [23, 57, 87]. The ABS energies in this case are obtained by solving the transcendental equation

$$\begin{aligned}\tau \cos\left[(\Lambda_1 - \Lambda_2)\,\varepsilon \mp \varphi\right] + (1-\tau)\cos\left[(\Lambda_1 + \Lambda_2)\,\varepsilon x_r\right] \\ = \cos\left[2\arccos\varepsilon - (\Lambda_1 + \Lambda_2)\,\varepsilon\right],\end{aligned} \tag{1.12}$$

  where $\varepsilon = \varepsilon_\mathrm{ABS}/\Delta$, $x_r = 2x_0/L - 1 \in [-1, 1]$, and $\Lambda_i = L\Delta/(\hbar v_i)$, with $i = 1, 2$. Equation 1.12 also describes finite-length junctions without spin-orbit splitting when $\Lambda_1 = \Lambda_2$, and reduces to the zero-length result of Eq. 1.11 when $\Lambda_1 = \Lambda_2 = 0$.

Interestingly, the familiar Josephson potential of a conventional tunnel junction can be recovered from the short-junction expression. In this limit, at zero temperature, each conduction channel contributes $-\varepsilon_\mathrm{ABS}$ to the junction ground-state energy, up to a phase-independent constant. An ideal tunnel Josephson junction with a homogeneous barrier, an area of the order of 1 $\mu\mathrm{m}^2$, and a normal-state resistance of the order of 10 kΩ can be viewed as a set of $n \sim 10^6$ parallel conduction channels with $\tau_i \sim 10^{-6}$ [88]. For such small transparencies, the ground-state energy associated with one channel in Eq. 1.11 becomes

$$\begin{aligned}-\varepsilon_\mathrm{ABS} &= -\Delta\sqrt{1 - \tau\sin^2\left(\frac{\varphi}{2}\right)} \\ &\approx -\Delta\left[1 - \frac{\tau}{2}\sin^2\left(\frac{\varphi}{2}\right)\right] \\ &= -\Delta\left[1 - \frac{\tau}{4}\left(1 - \cos\varphi\right)\right].\end{aligned} \tag{1.13}$$

The total ground-state energy of a junction hosting n conduction channels would then read

$$\begin{aligned}E_\mathrm{tot} &\approx -\Delta\sum_{i=1}^{n}\left[1 - \frac{\tau_i}{4}(1 - \cos\varphi)\right] \\ &= -E_\mathrm{J}\cos\varphi.\end{aligned} \tag{1.14}$$

where $E_\mathrm{J} = (\Delta/4)\sum_{i=1}^{n}\tau_i$, and phase-independent terms have been omitted. Using the Landauer formula, $R_N^{-1} = (2e^2/h)\sum_{i=1}^{n}\tau_i$ [74], we can rewrite the Josephson energy as

$$E_\mathrm{J} = \frac{\Delta\Phi_0}{4eR_\mathrm{N}} \quad\longrightarrow\quad I_\mathrm{c} = \frac{\Delta\pi}{2eR_\mathrm{N}} \tag{1.15}$$

where $\Phi_0 = h/(2e)$ is the superconducting flux quantum, R_N is the normal-state resistance of the junction and $I_c = 2eE_J/\hbar$ is its critical current. Equations 1.14 and 1.15 recover the conventional Josephson potential and the zero-temperature Ambegaokar-Baratoff relation for a tunnel junction with identical superconducting leads [6]. In this limit, the large number of weakly transmitting ABSs lie very close to the superconducting gap edges. They are therefore hardly distinguishable individually from the quasiparticle continuum and cannot generally be individually addressed experimentally.

1.4.2 Microwave spectroscopy of ABSs

As summarized in Ref. [55], there are three main experimental techniques to probe ABS spectra: Josephson spectroscopy [81, 89], tunneling spectroscopy [79, 90], and microwave spectroscopy [22, 23, 91]. Here, we focus on the last one, which consists in coupling ABSs to a superconducting microwave resonator, following the standard cQED approach developed for superconducting qubits [1].

In particular, we consider a system in which the nanowire is embedded in a superconducting loop and galvanically coupled to an LC resonator via a shared inductance L_s [Fig. 1.8a)]. The magnetic flux Φ threading the loop, and consequently φ, is controlled by a current I_f flowing through a nearby flux line. The weak link is also capacitively coupled to an electrostatic gate voltage V_g, which tunes its transparency τ. An additional microwave tone at angular frequency ω_d is used to excite the weak link.

We first assume the short-junction limit with a single conduction channel, which gives one spin-degenerate ABS pair with energies $\pm\varepsilon_{ABS}$. Each spin-degenerate ABS is associated with two quasiparticle states of opposite spin. In the excitation picture, this gives four possible many-body configurations: the ground state, with no quasiparticle excitations; the excited state, with two quasiparticle excitations; and two spin-degenerate odd-parity configurations with a single quasiparticle excitation. In the short-junction limit considered here, the drive can induce a pair transition from the ground to the excited state when $\omega_d = \omega_{ABS}$ [orange arrow in Fig. 1.8b)], where

$$\hbar\omega_{ABS} = 2\varepsilon_{ABS}. \tag{1.16}$$

Importantly, the ABS dispersion, and therefore its excitation energy, depends strongly on the junction transparency τ [Fig. 1.8c)]. As τ increases, the positive- and negative-energy ABS branches approach each other around $\varphi = \pi$, where the minimum pair-excitation energy is $\hbar\omega_{ABS}(\pi) = 2\Delta\sqrt{1-\tau}$. Consequently, τ (and V_g) directly controls the detuning between the ABS transition and the resonator, whose bare frequency is assumed to satisfy $\hbar\omega_r^0 \ll \Delta$ [Fig. 1.8d)]. At low transparency, $\omega_{ABS} \gg \omega_r^0$ over the entire phase range, whereas, as τ increases, the ABS transition approaches the resonator around $\varphi = \pi$ and can eventually cross it.

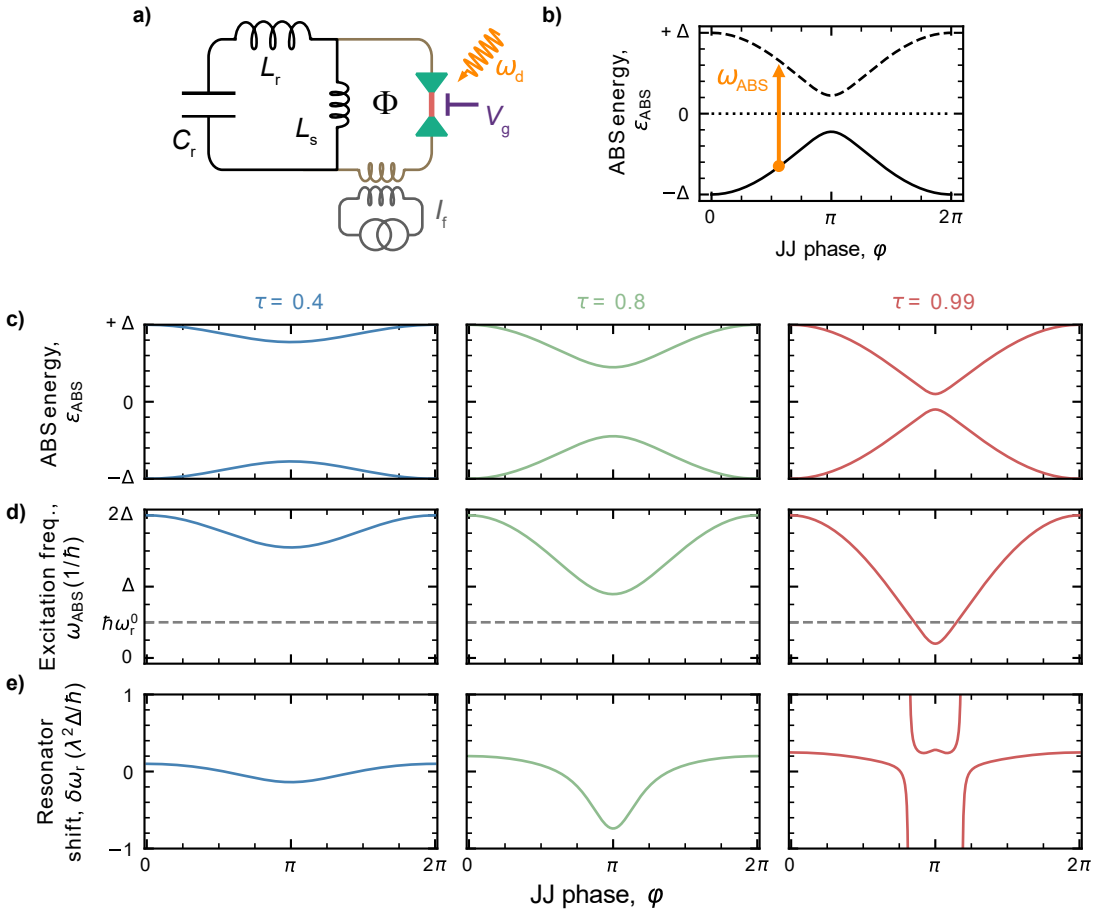


Figure 1.8: a) Schematic of a semiconductor junction embedded in a superconducting loop and coupled to an LC resonator through a shared inductance L_s. The junction phase and transparency are controlled through the magnetic flux Φ threading the loop and the electrostatic gate voltage V_g, respectively. A drive at angular frequency ω_d is used to excite the junction. **b)** Schematic of the many-body energy spectrum associated with a spin-degenerate ABS pair: ground state (solid line), excited state (dashed line), and two spin-degenerate odd-parity states (dotted line). A pair transition between the ground and excited states can be driven at $\omega_d = \omega_{ABS}$, as indicated by the orange arrow. **c)** ABS energies in the short-junction limit for three values of the transparency τ. **d)** Corresponding Andreev excitation frequencies for a pair transition (Eq. 1.16). The horizontal dashed line indicates the resonator frequency ω_r^0. For clarity, we choose $\hbar\omega_r^0 = 0.5\Delta$, whereas in a more realistic Al-based cQED device $\omega_r^0/(2\pi) \sim 5$–10 GHz and $\Delta_{Al}/h \sim 50$ GHz. **e)** Resonator frequency shifts induced by the ground-state ABS (Eq. 1.22).

To quantify the ABS-resonator interaction, we write the Hamiltonian of the uncoupled resonator and ABS system as

$$\begin{aligned}\hat{H}_0 &= \hat{H}_\mathrm{r} + \hat{H}_\mathrm{ABS} \\ &= \hbar\omega_\mathrm{r}^0 \hat{a}^\dagger \hat{a} + \frac{1}{2}\hbar\omega_\mathrm{ABS}\left(\varphi, \tau\right)\hat{\sigma}_\mathrm{z},\end{aligned} \tag{1.17}$$

where $\hat{H}_\mathrm{r}$ and $\hat{H}_\mathrm{ABS}$ are the resonator and ABS contributions, respectively, $\hat{a}$ ($\hat{a}^\dagger$) is the annihilation (creation) operator of the bare resonator mode, and $\hat{\sigma}_\mathrm{z}$ is the Pauli z operator acting on the two even-parity ABS states. The resonator and ABS couple through the resonator zero-point flux fluctuations across the shared inductance, which induce a phase perturbation:

$$\varphi \rightarrow \varphi + \hat{\delta\varphi}, \tag{1.18}$$

with $\hat{\delta\varphi} = \lambda\left(\hat{a} + \hat{a}^\dagger\right)$ [22, 51, 91, 92]. We can write

$$\lambda = p\left(2\pi\frac{\Phi_\mathrm{zpf}}{\Phi_0}\right), \tag{1.19}$$

where $p = L_\mathrm{s}/(L_\mathrm{s}+L_\mathrm{r})$ is the inductive participation ratio for the simplified circuit shown here, and $\Phi_\mathrm{zpf} = \sqrt{\hbar Z_\mathrm{r}/2}$ is the amplitude of the resonator zero-point flux fluctuations, which depends on the resonator impedance Z_r, as introduced in Sec. 1.1.

By expanding the ABS Hamiltonian to second order in λ, accounting for the phase dependence of both the ABS energies and their eigenstates, the coupling Hamiltonian reads [91, 92]

$$\hat{H}_\mathrm{c} = \lambda\hat{H}'_\mathrm{ABS}\left(\hat{a} + \hat{a}^\dagger\right) + \frac{\lambda^2\hat{H}''_\mathrm{ABS}}{2}\left(\hat{a} + \hat{a}^\dagger\right)^2, \tag{1.20}$$

where the operator derivatives with respect to φ are

$$\begin{aligned}\hat{H}'_\mathrm{ABS} &= \frac{d\varepsilon_\mathrm{ABS}}{d\varphi}\left[\hat{\sigma}_\mathrm{z} + \sqrt{1-\tau}\tan\left(\frac{\varphi}{2}\right)\hat{\sigma}_\mathrm{x}\right], \\ \hat{H}''_\mathrm{ABS} &= \frac{d\varepsilon_\mathrm{ABS}}{d\varphi}\left[\frac{\tau + (2-\tau)\cos\varphi}{2\sin\varphi}\hat{\sigma}_\mathrm{z} + \sqrt{1-\tau}\hat{\sigma}_\mathrm{y}\right].\end{aligned} \tag{1.21}$$

Applying perturbation theory up to second order in λ, we obtain the resonator frequency shift when the ABS is in its ground state [22, 91]:

$$\begin{aligned}\delta\omega_\mathrm{r} &= \omega_\mathrm{r}\left(\varphi\right) - \omega_\mathrm{r}^0 \\ &= \frac{\lambda^2 c_2^\mathrm{ABS}}{\hbar} + g_\mathrm{c}^2\left(\frac{2}{\omega_\mathrm{ABS}} - \frac{1}{\delta_-} - \frac{1}{\delta_+}\right),\end{aligned} \tag{1.22}$$

where $c_2^{\mathrm{ABS}} = -d^2\varepsilon_{\mathrm{ABS}}/d\varphi^2$ is the curvature of the ABS ground state, $\delta_\pm = \omega_{\mathrm{ABS}} \pm \omega_{\mathrm{r}}^0$, and

$$g_{\mathrm{c}} = \frac{\lambda}{\hbar}\sqrt{1-\tau}\left(-\frac{d\varepsilon_{\mathrm{ABS}}}{d\varphi}\right)\tan\left(\frac{\varphi}{2}\right) \tag{1.23}$$

is the phase- and transparency-dependent coupling rate. The first term in Eq. 1.22 originates from the curvature of the ABS ground-state energy and dominates when the ABS transition is far detuned, whereas the second term accounts for virtual transitions and becomes important as the ABS transition approaches the resonator. The resonator thus acquires a phase-dependent frequency shift, whose modulation generally increases with τ and can eventually develop in an avoided-crossing pattern [Fig. 1.8e)].

The resonator frequency shift depends on the ABS occupation and is therefore different for its ground and excited states. In the dispersive regime, $|\delta_-| \gg g_{\mathrm{c}}$, and within the rotating-wave approximation, the interaction gives the familiar Jaynes-Cummings dispersive contribution $\pm\chi$, with $\chi \simeq g_{\mathrm{c}}^2/\delta_-$ [1]. Consequently, driving the ABS transition changes the response of the coupled resonator.

This coupling mechanism provides two complementary ways of probing the ABS. In single-tone spectroscopy, the resonator is probed without an additional drive tone, and information about the ABS is inferred from the phase-dependent frequency shift induced by its ground state. In two-tone spectroscopy, an additional drive tone is used to excite the ABS transition, while the resulting change in the resonator response provides an indirect readout of the excitation. By sweeping the drive frequency, the phase-dependent ABS excitation spectrum can therefore be mapped out.

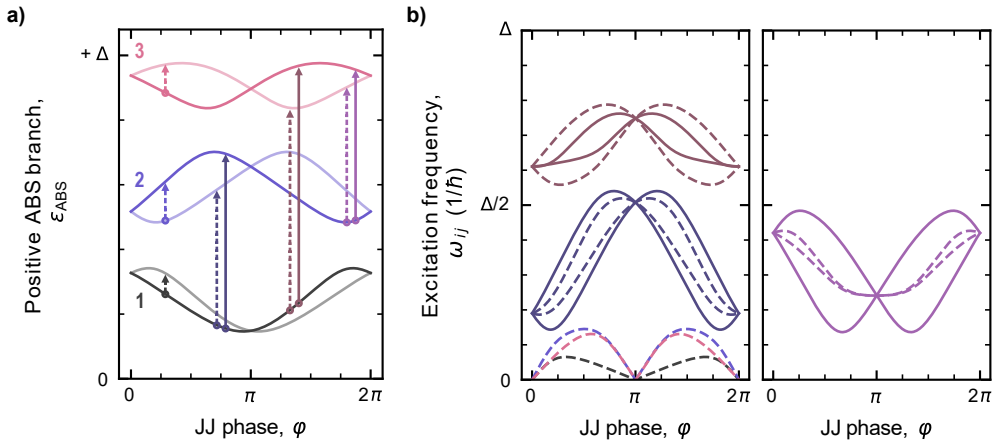


Figure 1.9: a) Positive branches of the Andreev spectrum in the finite-length regime, with spin-orbit coupling lifting the spin degeneracy. Solid and dashed arrows indicate spin-conserving and spin-flipping single-quasiparticle transitions, respectively. The spectra are obtained by solving Eq. 1.12 using the parameters listed in Table 1.1. **b)** Corresponding single-quasiparticle excitation frequencies, $\hbar\omega_{ij} = \varepsilon_j - \varepsilon_i$, separated into two panels to avoid overlapping curves.

Besides the pair transitions discussed so far, the presence of multiple ABSs in finite-length junctions allows a second type of excitation: single-quasiparticle transitions between different ABSs [Fig. 1.9a)]. Since microwave excitation conserves fermion parity, these transitions require a quasiparticle to be already trapped in the weak link, for example through quasiparticle poisoning. In the presence of spin-orbit coupling, the lifting of spin degeneracy allows a richer set of spin-conserving and spin-flipping transitions, giving rise to characteristic bundles in the excitation spectrum [Fig. 1.9b)] [22, 23, 57].

Although the expression for the ABS-induced resonator frequency shift in Eq. 1.22 can be generalized to account for multiple ABSs and the spin-splitting [22], we do not employ this formalism here. For spectra without resolved spin splitting, we adopt an effective short-junction approximation, describing the dominant ABS dispersion as [22, 84, 93–95]

$$\pm\varepsilon_{\mathrm{ABS}}^{\mathrm{eff}} = \pm\Delta_{\mathrm{eff}}\sqrt{1-\tau\sin^2\left(\frac{\varphi}{2}\right)}, \tag{1.24}$$

where[96]

$$\Delta_{\mathrm{eff}} = \frac{\Delta}{\sqrt{(1+\Lambda)^2+(x_r\Lambda\sqrt{1-\tau})^2}} < \Delta. \tag{1.25}$$

This approximation is most justified near $\varphi = \pi$ for the lowest pair transition and does not resolve spin-orbit splitting or the higher ABSs of a finite-length junction. Since our devices are not strictly in the short-junction limit, this expression describes the pair-transition data in PAPER III and provides an effective model for PAPER IV. In PAPER III, excitation spectra with resolved spin splitting are instead fitted using the full transcendental equation (Eq. 1.12).

Plot	Λ_1	Λ_2	x_r	τ
Fig. 1.7a)	0	0	-	0.95
Fig. 1.7b)	1.7	1.7	0.45	0.83
Fig. 1.7c)	1.7	3.56	0.45	0.83
Fig. 1.9	2.2	3.56	0.45	0.7

Table 1.1: Parameters used to plot ABSs in Figs. 1.7 and 1.9 from Eq. 1.12.

1.5 Nonlinearities in superconducting resonators

In Sec. 1.1, we modeled superconducting resonators as harmonic oscillators, which are linear systems in the sense that their dynamics is governed by a linear differential equation of the form $\ddot{x} + \omega_0^2 x = 0$. Indeed, starting from the Lagrangian of an LC resonator, a similar equation of motion follows directly from the Euler–Lagrange equation:

$$\mathcal{L} = \frac{C_r}{2}\dot{\Phi}^2 - \frac{\Phi^2}{2L_r} \quad \xrightarrow{\frac{d}{dt}\frac{\partial \mathcal{L}}{\partial \dot{\Phi}} - \frac{\partial \mathcal{L}}{\partial \Phi} = 0} \quad \ddot{\Phi} + \frac{1}{L_r C_r}\Phi = 0. \tag{1.26}$$

The linearity has also a counterpart in the quantum description. Neglecting the constant term in Eq. 1.10, the Hamiltonian reads

$$H = \hbar\omega_\mathrm{r}\hat{a}^\dagger\hat{a}, \tag{1.27}$$

and is therefore linear in the photon-number operator $\hat{n} = \hat{a}^\dagger\hat{a}$. Consequently, the energy levels are equally spaced, with a transition frequency ω_r that is independent of the photon number.

This linear regime underlies several applications of superconducting resonators, including qubit readout [2] (and also the ABS readout discussed in the previous section), quantum buses [3], memories [4], and Purcell filtering [5]. However, superconducting resonators also inherit a nonlinearity from the kinetic inductance of the superconducting film from which they are fabricated. We neglect this contribution in this thesis, as the discussed systems operate in a regime where it is negligible. In other devices, instead, kinetic-inductance nonlinearity is deliberately exploited, for example in traveling-wave parametric amplifiers (TWPAs) [97], kinetic-inductance detectors (KIDs) operated in the nonlinear regime [98], and gate-tunable kinetic-inductance parametric amplifiers [99].

Josephson junctions, on the other hand, are intrinsically nonlinear elements. For a tunnel junction, this nonlinearity originates from the Josephson potential Eq. 1.14, depending on E_J and φ [6]. More general potential shapes $U(\varphi)$ can be obtained by combining one or several Josephson junctions in superconducting loops. The nonlinear properties of such a potential are identified by expanding it around the equilibrium point φ_min,

$$U(\varphi) = \sum_{n=0}^{\infty} \frac{c_n}{n!}(\varphi - \varphi_\mathrm{min})^n, \qquad c_n = \left.\frac{d^n U}{d\varphi^n}\right|_{\varphi_\mathrm{min}}, \tag{1.28}$$

where φ_min is determined by the equilibrium condition $c_1 = 0$.

When a nonlinear element is embedded in a resonator, the coefficients of its potential modify the properties of the resonator. In particular, after quantization, the resonator Hamiltonian can be written as [100, 101]

$$H = \hbar\tilde{\omega}_\mathrm{r}\hat{a}^\dagger\hat{a} + \hbar g_3(\hat{a} + \hat{a}^\dagger)^3 + \hbar g_4(\hat{a} + \hat{a}^\dagger)^4 + \cdots, \tag{1.29}$$

where $\tilde{\omega}_\mathrm{r}$ includes the linear inductive response associated with the quadratic coefficient c_2. Treating this contribution as a weak perturbation of a bare resonator with frequency ω_r^0, we obtain

$$\tilde{\omega}_\mathrm{r} \simeq \omega_\mathrm{r}^0 + \frac{\lambda^2 c_2}{\hbar}, \tag{1.30}$$

where λ is the zero-point phase fluctuation across the nonlinear element. We already encountered an example of this mechanism in the previous section, where the curvature of the ABS ground-state potential, $-d^2\varepsilon_\mathrm{ABS}/d\varphi^2$, gives the first contribution to the ABS-induced frequency shift in Eq. 1.22.

The higher-order expansion coefficients, instead, give rise to the nonlinear Hamiltonian terms, with

$$\hbar g_n = \frac{\lambda^n}{n!} c_n, \qquad n \geq 3. \tag{1.31}$$

Both the linear and nonlinear properties imparted to the resonator can therefore be related to the expansion coefficients of the potential.

The leading nonlinear contributions are associated with the cubic coefficient c_3, which enables three-wave mixing (3WM), and the quartic coefficient c_4, which contributes to the Kerr nonlinearity. The quartic term also enables four-wave mixing, which we do not discuss here. In a 3WM process, energy is transferred from a pump tone at ω_p to signal and idler tones at ω_s and ω_i, subject to the energy-conservation condition $\omega_\mathrm{p} = \omega_\mathrm{s} + \omega_\mathrm{i}$. The Kerr nonlinearity, instead, manifests as a photon-number-dependent shift of the resonance frequency. To leading order, this shift is written as $\delta\omega_\mathrm{Kerr} \simeq K\bar{n}$, where K is the Kerr coefficient and $\bar{n}$ is the mean photon number in the resonator.

These nonlinearities enable a broad range of applications, including parametric amplification [9, 10, 13, 14, 102–104], bosonic-mode quantum computing [15, 105–108], and both linear [16, 109] and nonlinear [110] coupling schemes. In particular, the cubic nonlinearity can be exploited for 3WM parametric amplification [9, 10, 13, 14], non-Gaussian interactions [15], and beamsplitter interactions between bosonic modes [109]. The Kerr nonlinearity, on the other hand, can often be detrimental, for instance by limiting the dynamic range of parametric amplifiers and degrading the fidelity of bosonic-mode operations. Achieving a sizable cubic nonlinearity while suppressing the Kerr term is therefore an important goal in the design of nonlinear superconducting circuits.

One strategy to address this challenge is to engineer the shape of the effective potential $U(\varphi)$ through the Josephson energies of the individual junctions and tune it in situ using external magnetic fluxes threading superconducting loops. This allows operating points with a sizable cubic interaction and a suppressed effective Kerr term to be reached. Circuit designs based on this principle include the radio-frequency superconducting quantum interference device (rf-SQUID) [9],

the superconducting nonlinear asymmetric inductive element (SNAIL) [10], the asymmetrically threaded SQUID (ATS) [106], and the linear inductive coupler (LINC) [16].

This brings us back to one of the leitmotifs of this thesis. The devices mentioned above rely on tunnel junctions, whose Josephson energies are largely fixed at fabrication, while external magnetic flux provides in situ control of the effective circuit potential. Semiconductor Josephson junctions offer an additional experimental knob: electrostatic gating can modify the channel transparencies and, consequently, the shape of the junction potential.

1.5.1 ABS-induced nonlinearities

We consider again the system introduced in the previous section, in which a semiconductor Josephson junction is coupled to an LC resonator through a shared inductance, and both the superconducting phase φ across the junction and its transparency τ can be controlled [Fig. 1.10a)]. We adopt an effective short-junction description and consider a single spin-degenerate ABS pair, whose even-parity ground- and excited-state energies are $-\varepsilon_{\mathrm{ABS}}^{\mathrm{eff}}$ and $+\varepsilon_{\mathrm{ABS}}^{\mathrm{eff}}$, respectively [Eq. 1.24; Fig. 1.10b)]. Restricting the ABS system to its ground state, the total potential of the superconducting loop is

$$U(\varphi) = \left(\frac{\Phi_0}{2\pi}\right)^2 \frac{(\varphi - \varphi_{\mathrm{ext}})^2}{2L_{\mathrm{s}}} - \Delta_{\mathrm{eff}}\sqrt{1 - \tau \sin^2\left(\frac{\varphi}{2}\right)}, \tag{1.32}$$

where $\varphi_{\mathrm{ext}} = 2\pi\Phi/\Phi_0$ and we have assumed $L_{\mathrm{loop}} \simeq L_{\mathrm{s}}$. The expansion coefficients c_n are evaluated at a stable minimum φ_{min} of this potential.

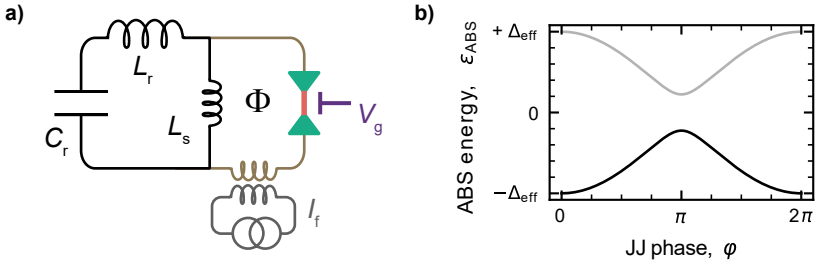


Figure 1.10: a) Schematic of a semiconductor junction embedded in a superconducting loop and coupled to an LC resonator through a shared inductance L_{s}. The junction phase and transparency are controlled through the magnetic flux Φ threading the loop and the electrostatic gate voltage V_{g}, respectively. **b)** Negative (black) and positive (gray) phase-dependent ABS energies.

We now approach the same system from a different perspective. In the previous section, we investigated how the ABS modifies the linear response of the resonator, resulting in a shift of its resonance frequency. Here, instead, we consider the junction and the loop inductance as an effective rf-SQUID nonlinear

element, whose potential can be expanded around its minimum to estimate the nonlinearities imparted to the resonator.

Considering the nonlinear contributions up to fourth order, we approximate the cubic and Kerr nonlinearities associated with the ground-state potential as [26]

$$\hbar g_3 = \frac{\lambda^3}{6} c_3, \tag{1.33}$$

and

$$\hbar K_{\mathrm{GND}} = \frac{\lambda^4}{2}\left(c_4 - \frac{5c_3^2}{3c_2}\right), \tag{1.34}$$

where the second term in Eq. 1.34 accounts for the contribution of the cubic nonlinearity to the effective Kerr coefficient.

This ground-state-potential description neglects dynamical contributions arising from transitions between the ABS states. The approximation is generally more reliable at low transparency and away from $\varphi \simeq \pi$, where the ABS transition is typically far detuned from the resonator. Virtual transitions introduce an additional dispersive contribution, analogous to the second term of the ABS-induced frequency shift in Eq. 1.22. An accurate calculation of the nonlinear coefficients would require expanding the full coupled ABS–resonator Hamiltonian, which is beyond the scope of this thesis. Instead, following a phenomenological approach, we supplement Eq. 1.34 with the leading dispersive Kerr contribution of a transversely coupled two-level system, obtained within the rotating-wave and dispersive approximations [92, 111]:

$$\hbar K = \hbar K_{\mathrm{GND}} + \frac{\hbar g_{\mathrm{c}}^4}{\left(\omega_{\mathrm{ABS}} - \omega_{\mathrm{r}}^0\right)^3}. \tag{1.35}$$

Note that the simplified transverse two-level model used for the dispersive correction does not provide additional contributions to the cubic coefficient. Such contributions may nevertheless arise from a systematic expansion of the full ABS–resonator Hamiltonian.

For the parameters considered in this thesis, at moderate transparency, the Kerr nonlinearity remains weakly negative over most of the phase range and develops a positive maximum around $\varphi = \pi$, resulting in two symmetric zero crossings [Fig. 1.11a)]. As τ increases, the phase dependence becomes progressively sharper and the magnitude of the Kerr nonlinearity increases. At sufficiently high transparency, the ABS transition crosses the resonator frequency, and the dispersive contribution in Eq. 1.35 develops a discontinuous, avoided-crossing-like pattern. At higher transparency, the model also predicts additional zero crossings, suggesting further operating points with suppressed Kerr nonlinearity.

In contrast, the magnitude of the cubic nonlinearity vanishes at $\varphi = 0$, π, and 2π, and develops two symmetric maxima on either side of $\varphi = \pi$ [Fig. 1.11b)].

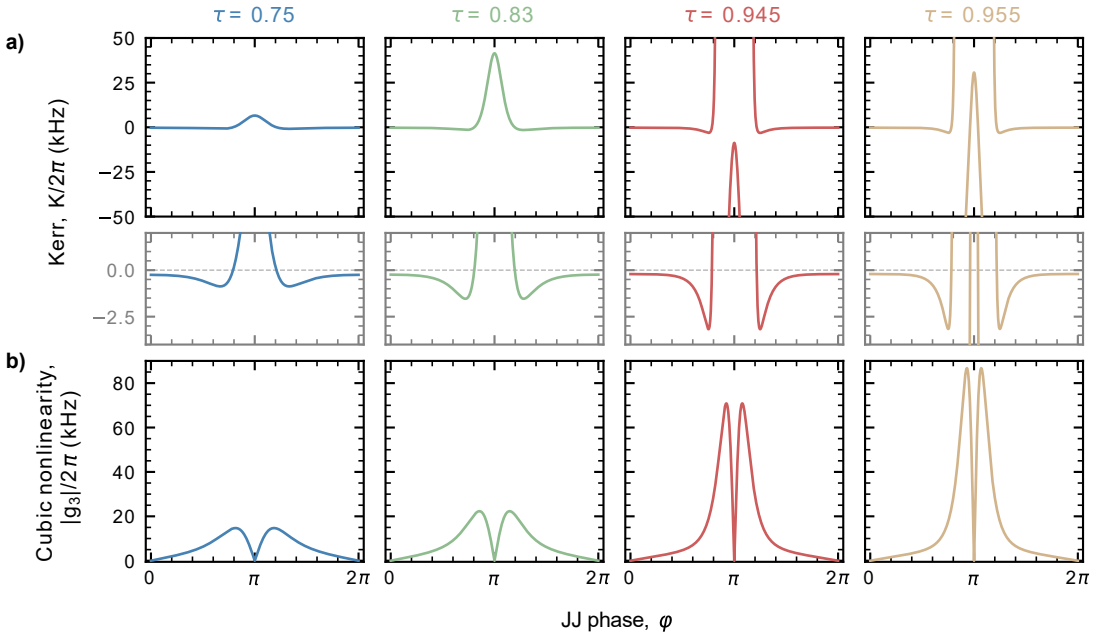


Figure 1.11: a) Phenomenological ABS-induced Kerr curves retained from the PAPER IV model, Eq. 1.35, for four values of the transparency τ, shown over the full range (top row) and around zero (bottom row). Singularities near resonance lie outside the dispersive approximation. **b)** ABS-induced cubic nonlinearity, Eq. 1.33, for the same values of τ. The parameters are close to those of the system investigated in this thesis: $\Delta_{\text{eff}}/h = 10$ GHz, $\lambda = 0.028$, $\omega_{\text{r}}^0/2\pi = 6.5$ GHz, and $L_{\text{s}} = 350$ pH.

Increasing τ enhances $|g_3|$ and shifts these maxima toward π, where the phase dependence of the ABS energy becomes increasingly sharp.

Importantly, at moderate transparencies [see $\tau = 0.75$ and 0.83 in Fig. 1.11], the Kerr zero crossings occur at phases where the cubic nonlinearity remains finite. At higher transparency, the appearance of four zero crossings suggests that operating points combining suppressed Kerr and sizable cubic nonlinearity may also exist in this regime. Such a combination is particularly favorable for three-wave mixing. We use this model to describe the nonlinear response measured in PAPER IV, as discussed in Chapter 6.

2 Methods

In this chapter, we present the experimental methods employed throughout this work. We begin with an overview of the device fabrication processes, followed by a description of the experimental setups. Finally, we introduce the measurement techniques and data-processing procedures used to characterize and analyze our devices.

2.1 Fabrication process

Here, we present an overview of the fabrication processes used for the devices investigated in this thesis. Detailed recipes for the processes developed within this work are reported in Appendix A.

As already mentioned in Sec. 1.2, the Al/InAs nanowires were grown at the Center for Quantum Devices of the Niels Bohr Institute (University of Copenhagen), by the group of Jesper Nygård. The nanowires were provided to us ready for transfer onto our devices, and their growth is therefore not included in the fabrication processes discussed here. The remaining fabrication steps were performed, unless otherwise specified, at the Myfab cleanroom facility at Chalmers University of Technology.

Our fabrication process can be divided into four main steps:

- **Substrate preparation:** Cleaning and preparation of the substrate for thin-film deposition.
- **Base-layer processing:** Deposition and patterning of superconducting thin films to define the resonators, microwave feedlines, and coarse control circuitry.
- **Nanowire transfer:** Placement of the nanowires onto the device chip using a nanomanipulator.
- **Nanowire processing:** Definition of Josephson weak links, when required, and fabrication of electrical contacts and fine control circuitry.

2.1.1 Device I: Gate-tunable CPW resonator

This device was investigated in PAPER I, and discussed in Sec. 1.3 and Chapter 3 of this thesis. Its fabrication was carried out by François Joint, who performed the

substrate preparation and base-layer processing, in collaboration with colleagues at the Budapest University of Technology and Economics, who were responsible for nanowire transfer and processing. The following description is adapted from the Supplementary Material of PAPER I.

The device is part of a 7×7 mm^2 chip [Fig. 2.1a)], hosting four resonator-gate structures, labeled D1, D2, D3, and D4. Device D2 serves as a reference resonator without a nanowire (NW) [Fig. 2.1b)], while in D1, D3, and D4 the resonators are shunted to ground through a NW [Fig. 2.1c) and d)].

The sample was fabricated on a high-resistivity Si substrate [Fig. 2.1e)]. First, a 200-nm-thick oxide layer was thermally grown on a 2-inch Si wafer using a furnace. Next, a 150-nm-thick aluminum film was evaporated across the entire wafer. Using a maskless UV lithography system, the microwave circuitry, including feedlines, gate lines, and resonators, was patterned. The patterns were transferred to the aluminum layer by immersing the wafer in an aluminum etchant solution for approximately two minutes. Subsequently, alignment markers were patterned using electron-beam lithography (EBL), followed by the lift-off of a 25-nm-thick gold layer. This step prepared the wafer for the transfer and integration of the nanowires into the existing circuitry. The NWs were transferred onto the chip using a nanomanipulator and subsequently integrated into the cQED structure through 100-nm-thick Ti/Al contacts. These contacts were patterned by EBL and fabricated by a lift-off process. Before metal evaporation, Ar ion milling was performed to reduce the contact resistance.

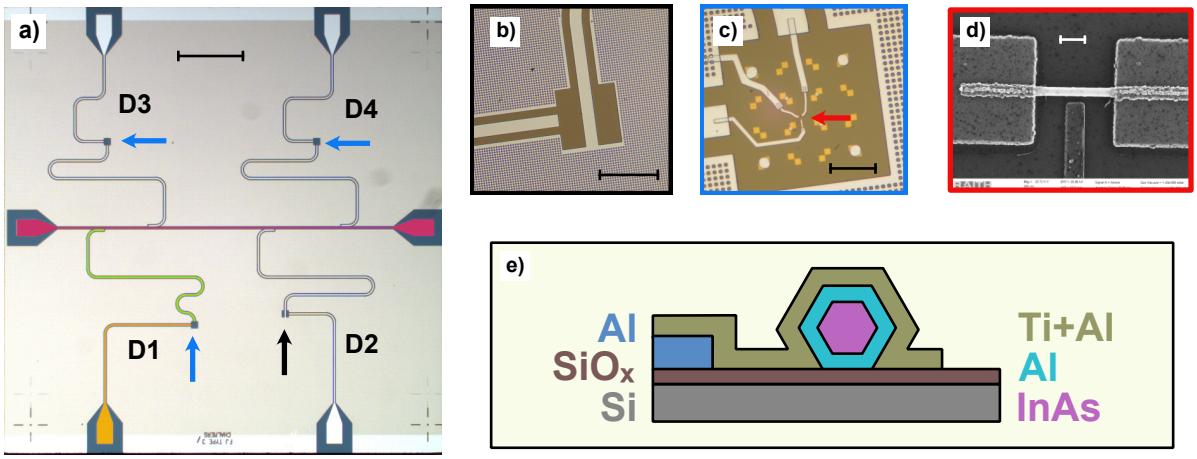


Figure 2.1: Device I. **a)** False-colored optical micrograph of the chip, showing four $\lambda/4$ CPW resonators (D1–D4) coupled to a common feedline (red). The resonator (green) and gate line (yellow) of D1 are highlighted. Blue arrows indicate the nanowire regions, while the black arrow marks the reference (bare) resonator D2. **b)** Optical micrograph of D2's voltage node. **c)** Optical micrograph of the nanowire (red arrow) shunting the resonator to ground, with a nearby gate line. **d)** SEM micrograph of the contacted nanowire. **e)** Schematic cross-section of the material stack.

2.1.2 Device II: NbTiN coplanar stripline resonators

The NbTiN CPS resonators investigated in PAPER II were fabricated by Ivo Cools, who also developed the fabrication recipe during his PhD, with contributions from Rodrigo M. López-Báez's master's thesis project. An overview of the fabrication process is provided in the following subsection on Device IV, which is based on the CPS resonator design investigated in PAPER II. Further details on the development and optimization of the recipe can be found in Ivo's PhD thesis [112].

2.1.3 Devices III and IV: NbTiN resonators with Josephson weak links

Device III refers to the fabrication process used for the three devices investigated in PAPER III, fabricated by Oleg Shvetsov and Ankit Khola, whereas Device IV is the device investigated in PAPER IV. Since their fabrication processes differ mainly in the base-layer processing, we describe them together in this subsection, focusing on Device IV and highlighting the differences with Device III where relevant.

Substrate preparation

Our devices are fabricated on single-side-polished, 430 ± 25 μm-thick C-plane sapphire wafers. The substrates are cleaned using Standard Clean 1 (SC1) of the RCA protocol [113], followed by solvent cleaning. These steps remove organic residues and particulate contamination [114, 115].

Base-layer processing

The base layers of our devices consist of NbTiN, deposited onto the substrates by DC sputtering from a $Nb_{81.9}Ti_{18.1}$ target in an atmosphere of N_2 and Ar. The main parameters used to control the film properties are the deposition time, which determines the film thickness, and the substrate temperature. In particular, we distinguish between *hot sputtering*, where the substrate is maintained at 660 °C during deposition, and *cold sputtering*, where the substrate is water-cooled. Cold sputtering generally produces more disordered films, resulting in a higher kinetic inductance, whereas hot sputtering favors more ordered films with lower kinetic inductance. Similarly, thinner films exhibit a higher sheet kinetic inductance than thicker ones. Regardless of the sputtering process, the NbTiN layers are patterned using either optical or electron-beam lithography, followed by inductively coupled plasma reactive ion etching (ICP-RIE) with an Ar/Cl_2 gas mixture. The only etching parameter adjusted between different samples is the etching time, which depends mainly on the thickness of the NbTiN layer. The process is monitored by

measuring the intensity of a laser beam reflected from the sample surface, allowing us to detect when the NbTiN layer has been fully etched and stop the process accordingly.

- **Device III:** For the devices discussed in PAPER III, the base layer consists of two NbTiN films with different thicknesses. First, a 90-nm-thick NbTiN film was deposited and patterned (optical lithography) to define the ground plane, the coarse gate and flux lines, and the alignment markers. A second, 6-nm-thick NbTiN film was subsequently deposited and patterned (electron-beam lithography) to define the resonator. Both depositions were performed by cold sputtering.
- **Device IV:** For the device discussed in PAPER IV, a single 10-nm-thick NbTiN film was deposited by hot sputtering and patterned (electron-beam lithography) to define the superconducting circuitry. Ti/Au alignment markers were fabricated before patterning the NbTiN using a standard lift-off process.

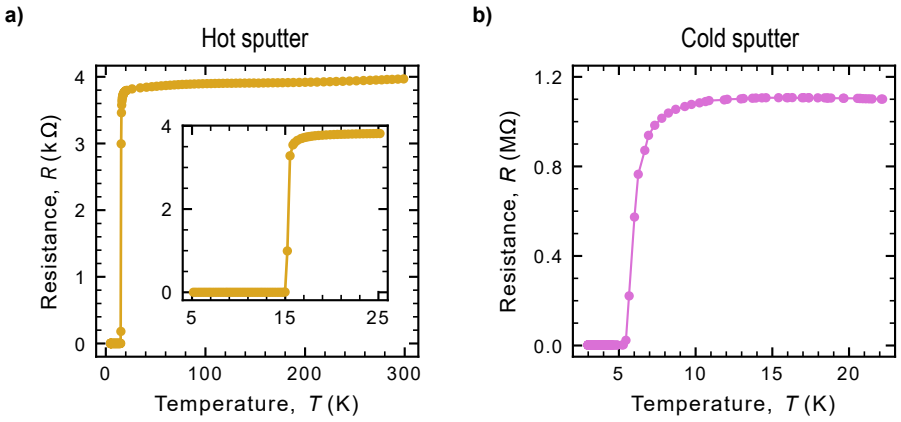


Figure 2.2: Typical electrical resistance R as a function of temperature T, measured on four-point test structures patterned in the NbTiN resonator layers obtained from **a)** hot-sputtering and **b)** cold-sputtering process. The superconducting transitions give critical temperatures of approximately $T_c = 15$ K and 6 K, respectively. These measurements were performed in a Quantum Design Physical Property Measurement System (PPMS) by Ivo Cools and Oleg Shvetsov for hot and cold sputtered film, respectively.

The sheet kinetic inductance of the two resonator layers can be estimated from their sheet resistance and critical temperature T_c. The sheet resistance was measured directly on the NbTiN films using a four-point probe, averaging measurements taken at several positions across the wafer. The critical temperature was instead extracted from temperature-dependent resistance measurements on Hall-bar test structures patterned from reference NbTiN films deposited using the corresponding resonator-layer recipes (Fig. 2.2). Using Eq. 1.1, we estimate sheet

kinetic inductance of approximately 10 pH/□ for the hot-sputtering process and up to 400 pH/□ for the cold one. Assuming that T_c remains unchanged for films deposited using the same recipe, we characterize subsequent resonator layers by measuring only their sheet resistance and use it to estimate their kinetic inductance. These values are then used in electromagnetic simulations to guide the choice of resonator geometry and estimate the resonance frequency and characteristic impedance.

Device IV [Fig. 2.3a)-c)] uses the quarter-wavelength differential CPS resonator design investigated in PAPER II, whereas Device III employs a lumped-element resonator based on a similar differential geometry [Fig. 2.3d)]. Both resonator types were introduced in Sec. 1.1.

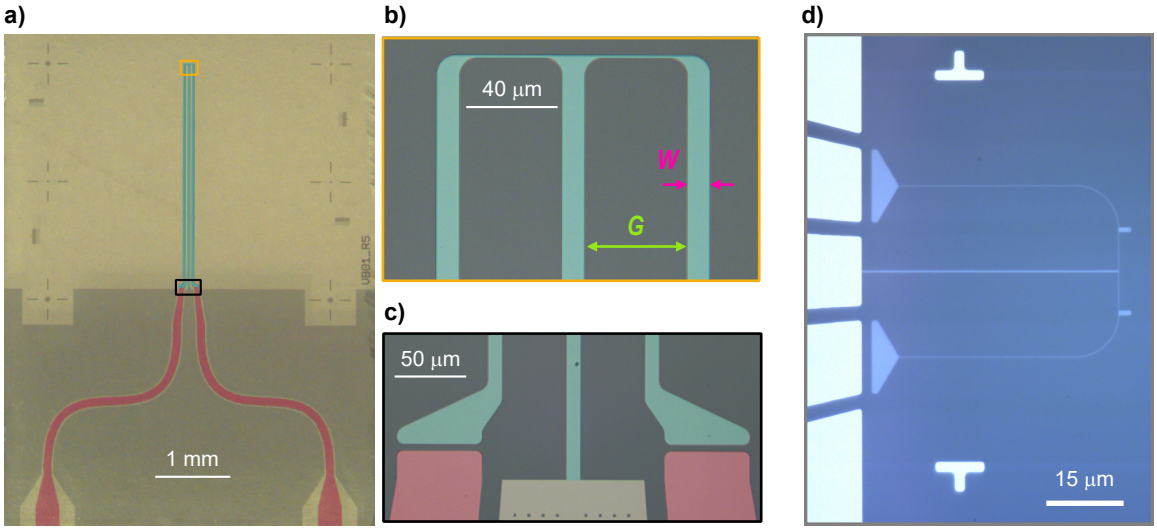


Figure 2.3: Optical micrographs of the NbTiN resonators. **a)** Quarter-wavelength differential CPS resonator (green) coupled to feedlines (red) used in Device IV and based on the design investigated in PAPER II. Yellow and black rectangles are magnified in b) and c), respectively. **b)** Magnified view of the CPS conductors, highlighting their width W and separation G. **c)** Magnified view of the coupling capacitors with the feedlines. **d)** Resonator used in Device III, based on a similar CPS geometry as Device IV but operating in the lumped-element regime.

As a final step of the base-layer processing, the wafer is diced in 10×6 mm^2 chips, which are then ready for nanowire transfer.

Nanowire transfer

The half-shell Al/InAs nanowires are transferred from their growth substrate onto the device chip using a commercial transfer system from HQ Graphene, mounted on an air-suspended optical table. The transfer station consists of an optical microscope and two independently controlled stages: one holding the growth substrate and device chip, and the other holding a needle with a tip size of 100 nm

from American Probe & Technology [Fig. 2.4a) and b)]. The sample stage allows translation along the x, y, and z axes and rotation around the z axis, while the needle stage allows translation along x and y and rotation around all three axes, with an additional independent rotation of the needle around its own axis. Both stages are controlled via joystick with micrometric precision. The microscope is equipped with two cameras, allowing the transfer process to be monitored on separate screens.

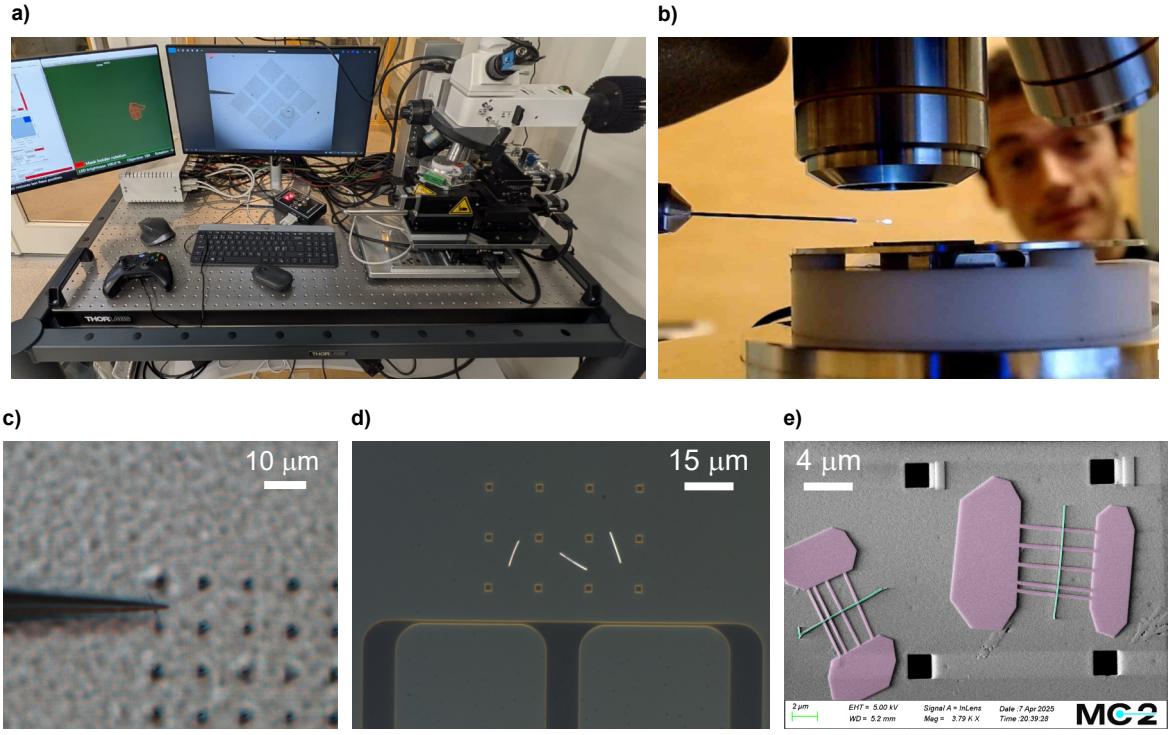


Figure 2.4: a) Photograph of the nanowire transfer station, consisting of an optical microscope and two joystick-controlled stages holding the samples and the manipulation needle. **b)** Photograph of the needle approaching the growth substrate under the microscope, with a slightly out-of-focus PhD candidate in the background. **c)** Optical micrograph showing a nanowire being picked up from the growth substrate by the needle. **d)** Optical micrograph of three nanowires transferred onto the device chip, near a CPS resonator and surrounded by alignment markers. **e)** False-colored scanning electron micrograph of two nanowires (green) after selective etching of the Al shell. The footprint of the etching windows (pink) is still visible and includes drainage areas designed to facilitate the flow of the etchant.

During the transfer, the needle is brought into contact with a nanowire on the growth substrate, which is then picked up and moved onto the device chip [Fig. 2.4c)]. The transfer relies on van der Waals forces, which initially promote adhesion of the nanowire to the needle and subsequently to the device chip. The nanowires are deposited near the resonator, using the lithographically defined

alignment markers as references for positioning [Fig. 2.4d)]. Several nanowires are typically transferred onto each chip, providing multiple candidates for subsequent processing. Their positions are then inspected to determine the alignment of the lithographic patterns used in the following fabrication steps.

Nanowire processing

After transferring the nanowires onto the device chip, we define the Josephson weak links by selectively removing a portion of the epitaxial Al shell. The etching windows are patterned by positive electron-beam lithography, and the exposed Al is removed by wet etching in a TMAH-based solution (MF319), [Fig. 2.4e) and also Fig. 1.6b)]. The nanowires are then inspected by scanning electron microscopy to evaluate the quality of the etched regions and select the most promising candidate for further processing.

Finally, we fabricate the fine circuitry, including the superconducting contacts connecting the nanowire to the resonator, as well as the gate and flux-bias lines. These structures are patterned by EBL and fabricated by lift-off of a Ti/Al bilayer, consisting of 6 nm of Ti and 200 nm of Al. Immediately before metal deposition, we perform Ar ion milling to remove the native oxide from the remaining Al shell of the nanowire, ensuring good electrical contact between the epitaxial shell and the deposited Ti/Al electrodes.

The main differences between the two final devices lie in their resonator geometry and the number of weak links coupled to them. Device III employs a high-impedance lumped-element resonator coupled to a single Josephson weak link [Fig. 2.5d) and e)], whereas Device IV incorporates a differential CPS resonator coupled to two Josephson weak links defined in the same Al/InAs nanowire [Fig. 2.5a)–c)].

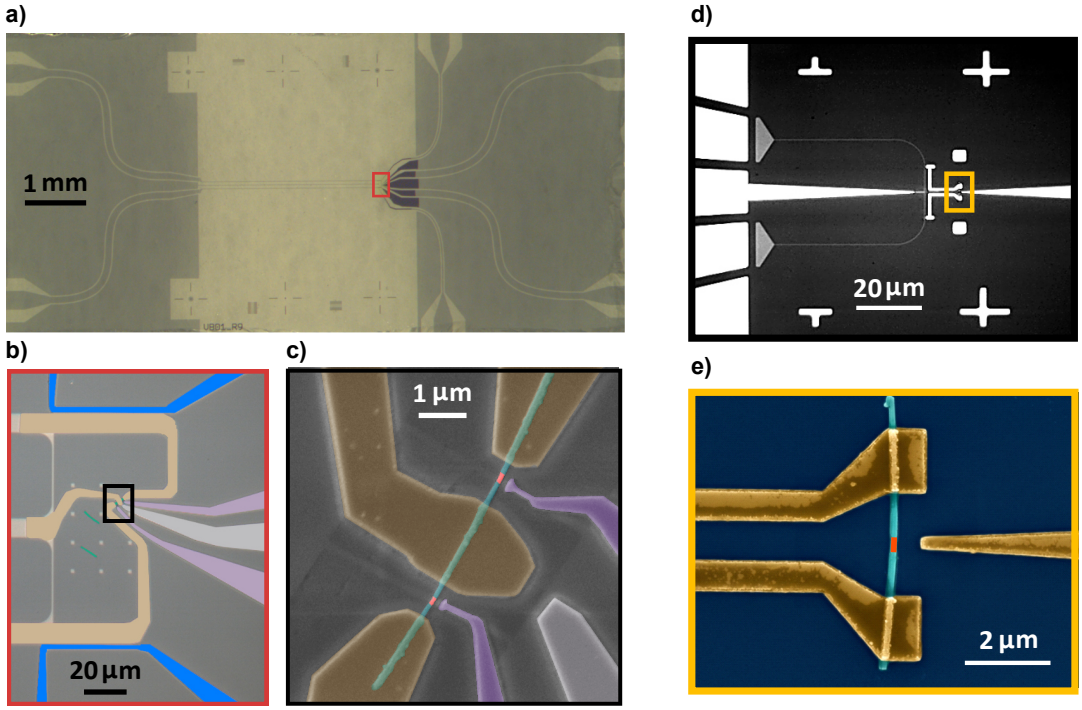


Figure 2.5: Devices III and IV. **a)** Optical micrograph of Device IV, consisting of a differential CPS resonator coupled to two Josephson weak links. The resonator and feedlines, previously highlighted in Fig. 2.3a)–c), are visible in the central and left regions, while the coarse gate and flux lines extend towards the right. The red rectangle indicates the region enlarged in panel b). **b)** False-colored optical micrograph of the nanowire region, showing the superconducting loops (yellow), flux lines (blue), gate lines (purple), and ground shielding (gray). The black rectangle indicates the region enlarged in panel c). **c)** False-colored scanning electron micrograph of the Al/InAs nanowire (cyan), showing the two Josephson weak links (red), Ti/Al contacts (yellow), and gate lines (purple). **d)** Scanning electron micrograph of a representative Device III, consisting of a high-impedance lumped-element resonator coupled to a single Josephson weak link. The yellow rectangle indicates the region enlarged in panel e). **e)** False-colored scanning electron micrograph of the Al/InAs nanowire (cyan), showing the Josephson weak link (red), Ti/Al contacts (yellow), and side gate. The micrographs in panels d) and e) are courtesy of Oleg Shvetsov and Ankit Khola.

2.2 Experimental setup

The measurements presented in this thesis were performed in three different Bluefors dilution refrigerators, named Luna, Embla, and Ask, operating at base temperatures of approximately 10 mK. While Luna was already operational and maintained by our colleagues at the 202Q-Lab [116], Embla and Ask were assembled and configured as part of this thesis project through a collaborative effort within the D1ungeon-Lab (ex Geresdi Lab).

In the following, we describe the cryogenic wiring and room-temperature instrumentation of each experimental setup. The measurement techniques, instead, are discussed in the next section.

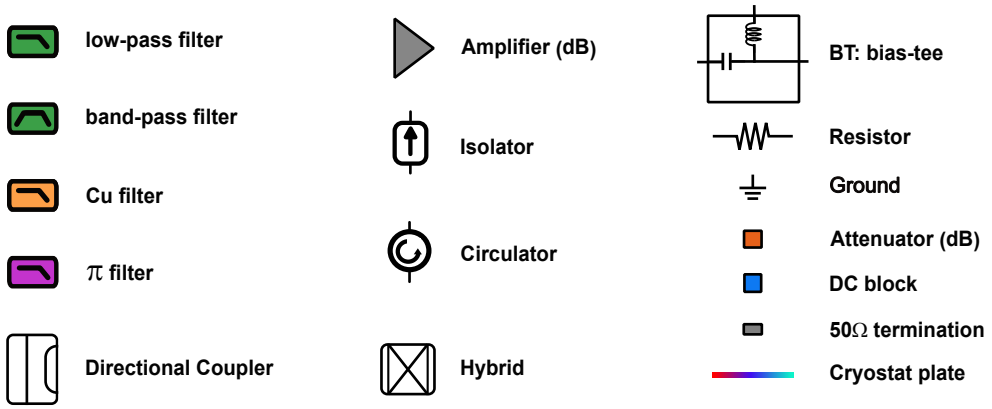


Figure 2.6: Symbols used in the schematics of the three experimental setups.

2.2.1 Luna

The measurements reported in PAPER I were performed in Luna. The microwave input line was attenuated and filtered at different temperature stages, while the output signal had four-stage isolation (LNF-CIISC4_8A plus LNF-ISISC4_8A) and was amplified by a cryogenic HEMT amplifier (LNF-LNC4_8A) at 4 K [Fig. 2.7a)]. An additional amplification stage was added at room-temperature as well. The DC and RF gate signals were combined through a bias tee (Marki BT0018) at the mixing chamber, with a cutoff frequency of 40 kHz. The sample was mounted and wire-bonded in an OQTO sample box [117][Fig. 2.7b) and c)], which was anchored to the mixing-chamber plate of the cryostat.

The DC gate voltage was supplied by a Stanford Research DC205 source, while the leakage current was determined from the voltage drop across a 4.6 kΩ series resistor, measured using a Keithley 2000 multimeter [Fig. 2.8a)]. Frequency-domain spectroscopy was performed using a four-port Keysight P5024A vector network analyzer (VNA), measuring the feedline transmission coefficient S_{21} [Fig. 2.8b)]. Time-domain measurements were performed with a Presto digital transceiver [118]

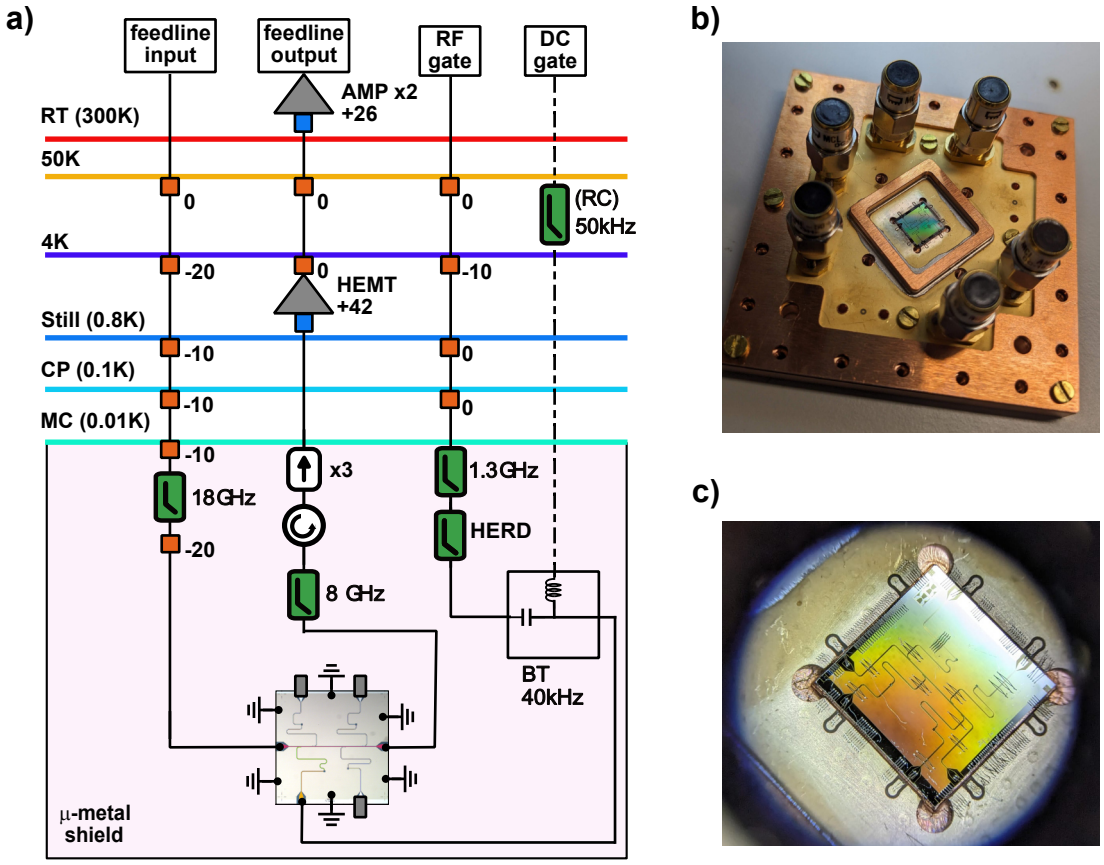


Figure 2.7: a) Schematic of the cryogenic wiring of Luna, showing the microwave input and output lines, gate lines, attenuators, filters, and amplification stages. Solid lines represent SMA coaxial cable, while dash-dotted lines represent twisted pairs. Other symbol definitions are given in Fig. 2.6. **b)** Photograph of the OQTO sample box with the lid removed and the sample mounted inside. Box connectors are SMA. **c)** Optical micrograph of the device chip mounted and wire-bonded inside the OQTO sample box.

by Intermodulation Products, which generated the readout and gate pulses and recorded the output signal [Fig. 2.8c)]. The transceiver operates at a sampling rate of 1 GS/s. The gate pulses were amplified by a room-temperature amplifier, also from Intermodulation Products, with a response time of approximately 2 ns. Finally, sideband spectroscopy was performed using two ports of the VNA in continuous-wave (CW) mode to generate the readout and gate excitation tones, while a third port operated in spectrum-analyzer mode to measure the output signal [Fig. 2.8d)].

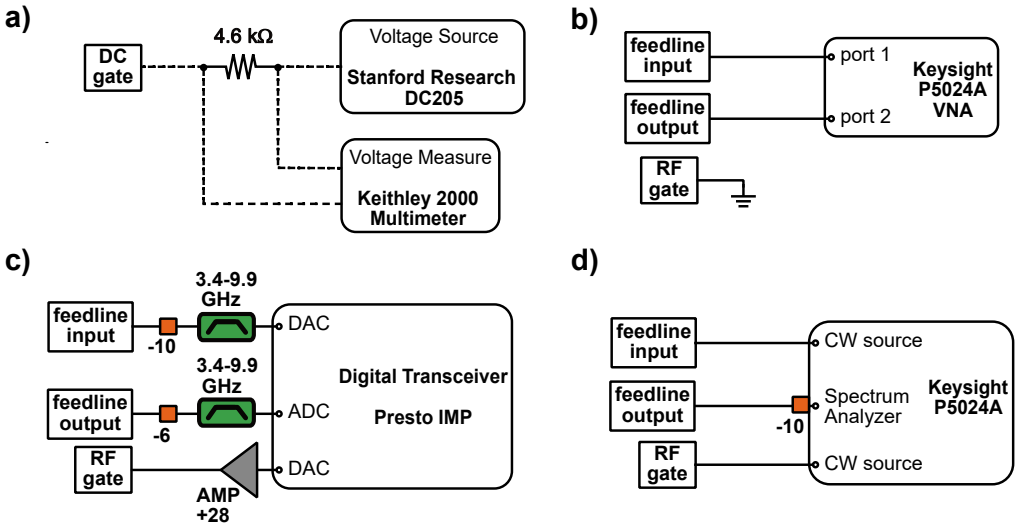


Figure 2.8: Room-temperature instrumentation used in Luna for **a)** DC gate biasing and leakage-current measurements, **b)** frequency-domain spectroscopy, **c)** time-domain spectroscopy, and **d)** sideband spectroscopy. Solid lines represent SMA coaxial cables, while dashed lines represent BNC coaxial cables. Other symbol definitions are given in Fig. 2.6.

2.2.2 Embla

The measurements reported in PAPERS III and IV, as well as part of those in PAPER II, were performed in Embla. Here, we describe the configuration used for PAPER IV, while similar configurations were employed for PAPER II and III. As in Luna, the microwave input line was attenuated and filtered at different temperature stages, while the output line included a circulator-isolator assembly (LNF-CIISC4_12A) and two additional isolators (Raditek RADC4-8-cryo), a HERD2 infrared filter [119], and a HEMT amplifier (LNF-LNC4_16B) at 4 K. An additional microwave line was used to inject pump and drive tones through a directional coupler[1] (Krytar 180120) [Fig. 2.9a)]. Additional information about the filtering will be given in Sec. 2.2.4.

The resonators were driven differentially using a 180° hybrid coupler (Krytar 4060200), which splits the input signal into two components with opposite phases. The hybrid couplers and sample boxes were enclosed in an aluminum shield, thermally anchored to the mixing-chamber plate and covered with μ-metal shielding tape to suppress stray magnetic fields [Fig. 2.9b)].

The space available inside the aluminum shield limits the number of samples that can be investigated in a single cooldown to two devices of the type used in PAPER IV [Fig. 2.10a)]. As discussed earlier, these devices host two Josephson junctions, each requiring independent gate and flux control. For this reason, we

[1] This is the most important difference with the setup used in PAPER III, where the drive tone was combined with the DC gate signal at the mixing chamber level via a bias-tee.

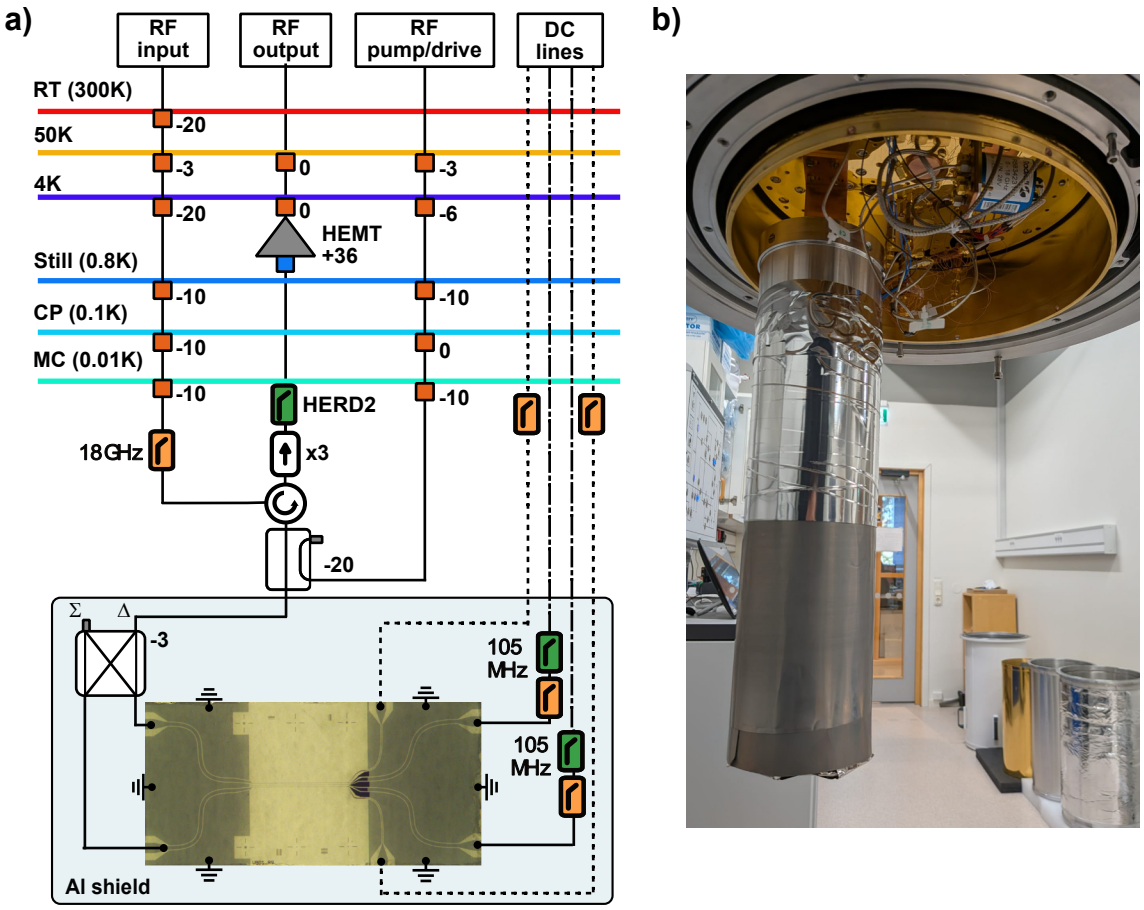


Figure 2.9: a) Schematic of the cryogenic wiring of Embla, showing the microwave input, output, pump/drive, and DC control lines. Solid lines represent SMA coaxial cables, while dashed and dash-dotted lines represent twisted pairs for the flux and gate control lines, respectively. The flux-control twisted pairs are superconducting below the 4 K stage. Other symbol definitions are given in Fig. 2.6. **b)** Photograph of Embla with the cryostat opened, showing the aluminum shield enclosing the samples and hybrid couplers.

developed a six-port sample box, with two RF ports, two gate lines, and two flux lines [Fig. 2.10b)]. SMA connectors were used for the RF and gate lines, while MCX connectors were used for the flux lines. In contrast, the devices investigated in PAPERS II and III hosted either no junction or a single junction, for which a four-port sample box with SMA connectors was sufficient [Fig. 2.10c)]. In addition to the on-chip flux lines, the sample boxes can be equipped with an external coil consisting of several hundred turns of Nb-based superconducting wire to provide magnetic flux bias [red arrow in Fig. 2.10a)].

The resonator reflection coefficient S_{11} was measured using a Keysight P5004A VNA, with additional filtering and two room-temperature amplifiers (2×LNF-LNR4_14B) on the output line [Fig. 2.11a)]. The DC gate voltages and flux-bias currents were controlled by an SPI rack [120], using D5a DAC modules combined

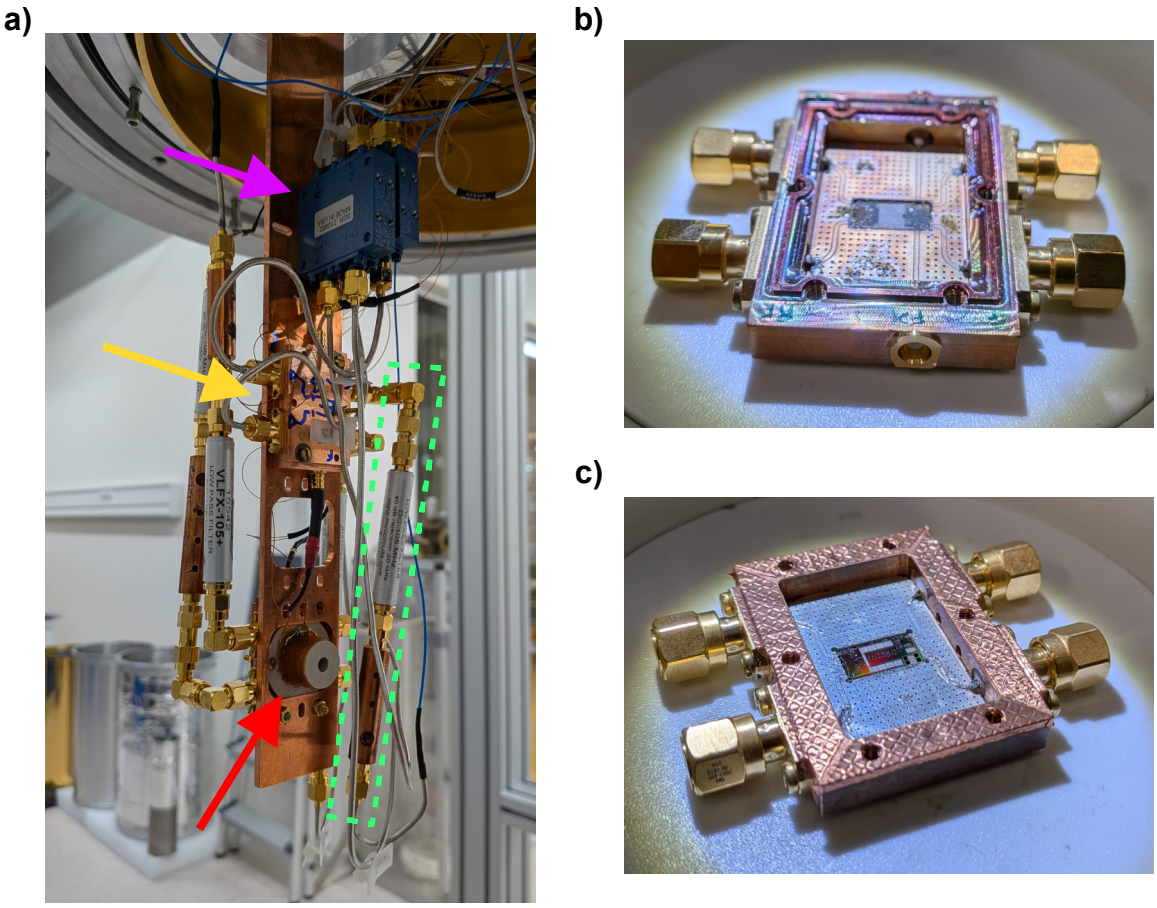


Figure 2.10: a) Photograph of the microwave components mounted at the mixing-chamber stage of Embla, with the aluminum shield removed. Two hybrid couplers (pink arrows) and two sample boxes of the type used in PAPER IV are mounted on opposite sides of a copper bracket. The yellow arrow indicates the sample box facing the camera, while the red arrow indicates the superconducting coil mounted behind the second sample box. The green highlighted region shows the combination of low-pass filters used for a gate line. **b)** Six-port copper sample box used for the device investigated in PAPER IV, with the lid removed. RF and gate lines use SMA connectors, while flux lines use MCX connectors. **c)** Four-port copper sample box used for the devices investigated in PAPERS II and III, with the lid removed.

with S1f and IVd modules, respectively [Fig. 2.11b)]. The DC lines were additionally filtered at room temperature using π filters. The pump and drive tones were generated using a Rohde & Schwarz SGS100A signal generator equipped with an SGU100A frequency upconverter unit [Fig. 2.11c)].

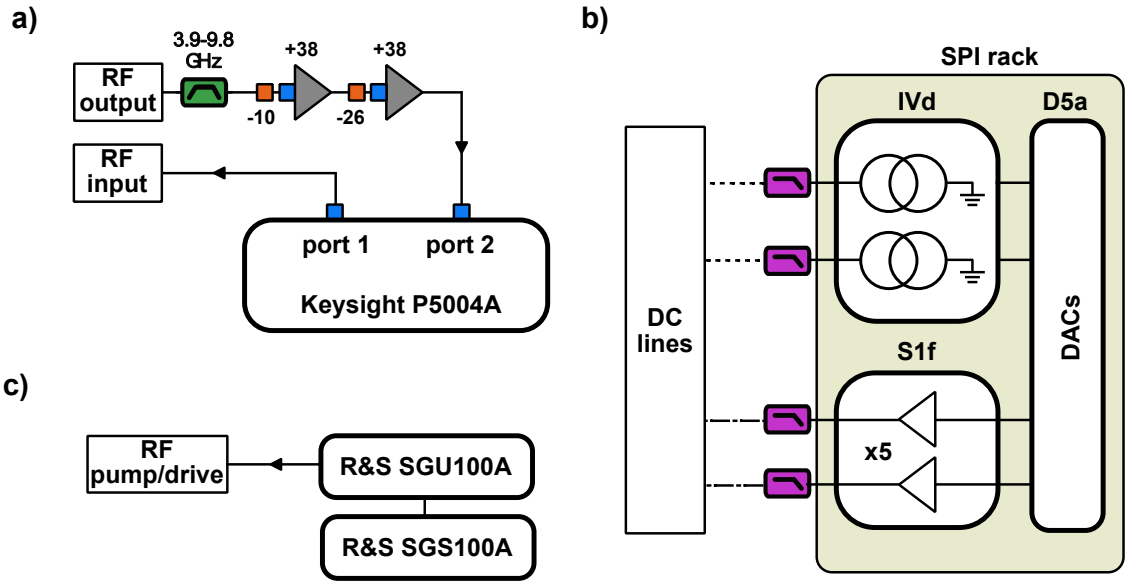


Figure 2.11: Room-temperature instrumentation used in Embla for PAPER IV. For PAPER II and III, there was no band-pass filter and the attenuators were adjusted in order to avoid amplifier compression. **a)** Resonator readout using a VNA with additional filtering and amplification. **b)** SPI rack used to control the gate voltages and flux-bias currents. **c)** Microwave signal generator and frequency extension unit used for pump and drive excitation. Solid lines represent coaxial cables, while dashed and dash-dotted lines represent twisted pairs. Other symbol definitions are given in Fig. 2.6.

2.2.3 Ask

The magnetic-field characterization of the resonators reported in PAPER II was performed in Ask, a dilution refrigerator equipped with a vector magnet from American Magnetics and a bottom-loading system [Fig. 2.12a)–c)]. The vector magnet allows magnetic fields up to 9 T along the z axis and up to 1 T in an arbitrary direction. The bottom-loading system enables rapid sample exchange, requiring approximately 24 hours between successive samples reaching base temperature.

This setup was primarily configured for DC transport and magnetotransport measurements [56]. However, the probe head provides several SMP connectors [Fig. 2.12d)], six of which are connected to standard Bluefors cryogenic coaxial lines, accessible through SMA connectors at the top of the refrigerator. We equipped Ask with microwave wiring for both transmission and reflection measurements, including attenuators, a circulator-isolator assembly (LNF-CIISC4_12A 4-12 GHz), and a HEMT amplifier at 4 K (LNF-LNC0.3_14A). For our measurements, the resonator and a 180° hybrid coupler were mounted inside the bottom-loading probe [Fig. 2.12e)], and the same Keysight P5004A VNA used in Embla was employed for the readout.

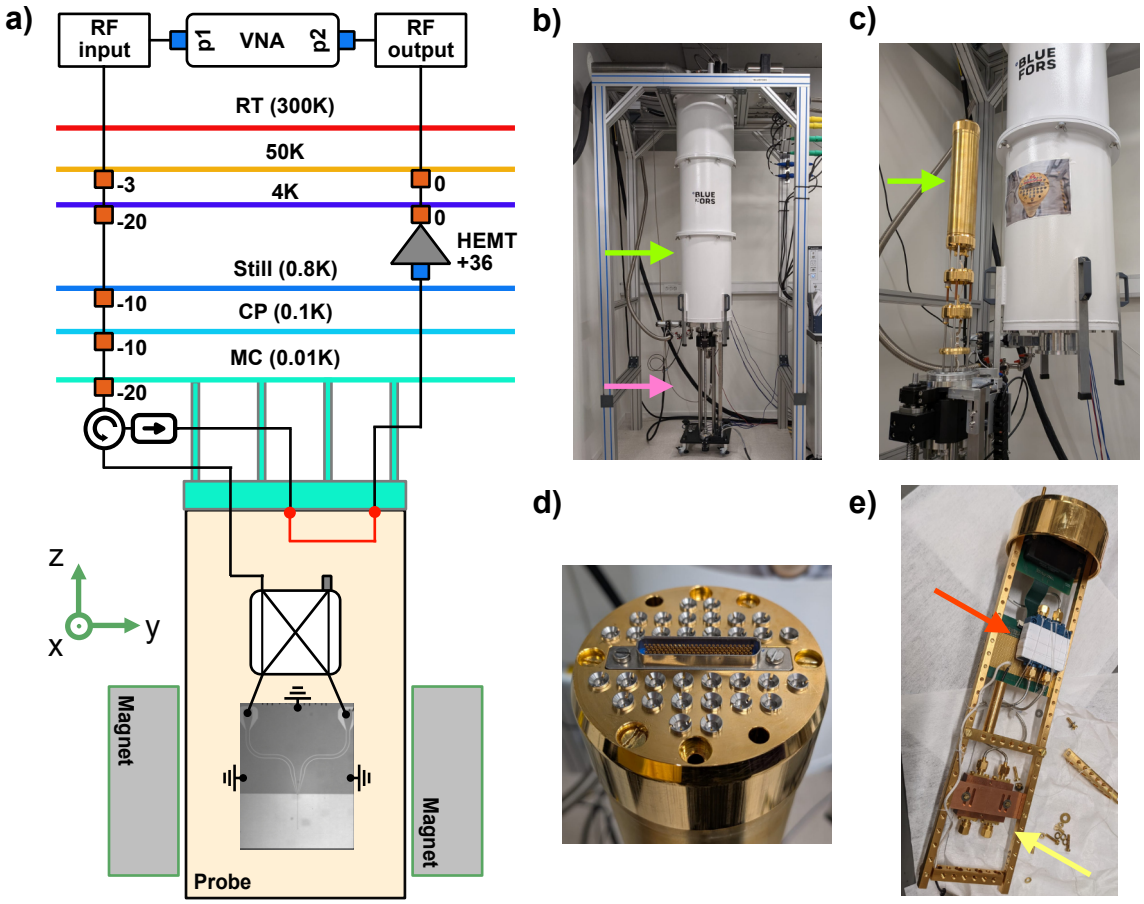


Figure 2.12: a) Schematic of the cryogenic microwave wiring of Ask, showing the input and output lines, attenuation, amplification, and vector magnet configuration. The room temperature measurement configuration for the measurement with the VNA is also shown. Other symbol definitions are given in Fig. 2.6. **b)** Photograph of Ask, showing the dilution refrigerator and the bottom-loading system (pink arrow) attached to it. The green arrow indicates approximately the position of the probe inside the cryostat. **c)** Detail of the bottom-loading probe (green arrow) outside the cryostat. **d)** Probe head with SMP connectors for the microwave lines and a 100-pin connector for DC control. **e)** Interior of the sample probe, showing the 180° hybrid coupler (red arrow) and the copper sample box (yellow arrow).

2.2.4 Copper-powder filters

Filtering is essential in cryogenic microwave experiments to suppress electrical noise and unwanted electromagnetic radiation reaching the device [121–123]. In our setups, the DC lines are filtered in stages. In particular, for the gate lines we use reactive low-pass filters (VLFX-105+, Mini Circuits) to suppress noise starting from relatively low frequencies (the passband is DC-105 MHz), π filters (4209-003, Tusonix) provide attenuation over an intermediate frequency range (approximately 10 MHz–10 GHz), and absorptive Cu-powder filters, which are

used to suppress higher-frequency radiation. The microwave input, output, and drive lines can also incorporate reactive filters to select the desired frequency bands, together with Cu-powder filters for broadband attenuation. Unlike reactive filters, which primarily reflect out-of-band signals and may exhibit leakage at higher frequencies, Cu-powder filters dissipate electromagnetic energy over a broad frequency range. We developed and characterized our own Cu-powder filters, as described below.

We start from hollow cylindrical copper housings (6 mm diameter) with four different lengths: 3, 4, 5, and 6 cm [Fig. 2.13a)]. Each cylinder has a larger opening for soldering and filling, together with a series of smaller holes to release trapped air and monitor the filling process. Female-to-female SMA connectors are screwed into both ends, with their central contacts joined by a 0.8 mm diameter copper wire (Distrelec, 155-50-330) [Fig. 2.13b)]. We first solder the wire to one connector, cut it to the appropriate length, and assemble the filter before soldering the other end through the larger hole. The shortest assembled filter, including the SMA connectors, has a total length of approximately 5 cm [Fig. 2.13c)].

We fill the housing with a mixture of epoxy (3M Scotch-Weld 2216 B/A) and Cu powder (Sigma-Aldrich, 326453), with grain sizes ranging from 10 to 25 μm. We define the Cu mass concentration as the percentage of Cu powder mass relative to the total mass of the mixture. After obtaining a homogeneous mixture, we inject it into the housing through the larger hole using a syringe, and leave it to cure at room temperature. We label the fabricated filters as "FxxYn", where xx indicates the Cu mass concentration in percent (or ZZ for empty filters), Y identifies the cylinder length (A = 3 cm, B = 4 cm, C = 5 cm, D = 6 cm), and n is the serial number of the filter.

To characterize the effective dielectric properties and microwave losses of the filters, we measure their scattering parameters S_{ij} at room temperature using a VNA, calibrated with an SMA connector. As expected for passive, reciprocal elements, the filters exhibit $|S_{12}| \simeq |S_{21}|$. In addition, we find approximately equal reflection magnitudes, $|S_{11}| \simeq |S_{22}|$. Here, port 1 is defined as the connector on the side with the smaller holes, while port 2 corresponds to the connector on the side with the larger opening.

We extract the relative permittivity ε_r from the periodic oscillations in the reflection coefficients S_{ii} [Fig. 2.13d)–f)], whose frequency spacing Δf is given by [30]

$$\Delta f \simeq \frac{c}{2L_\mathrm{eff}\sqrt{\varepsilon_\mathrm{r}}}, \tag{2.1}$$

where c is the speed of light in vacuum and L_eff is the effective propagation length, accounting for the SMA connectors extending into the copper housing. We estimate L_eff from the empty filters, assuming $\varepsilon_\mathrm{r} = 1$, and find it to be approximately 1 cm shorter than the cylinder length. We then use this value to extract ε_r for different Cu concentrations.

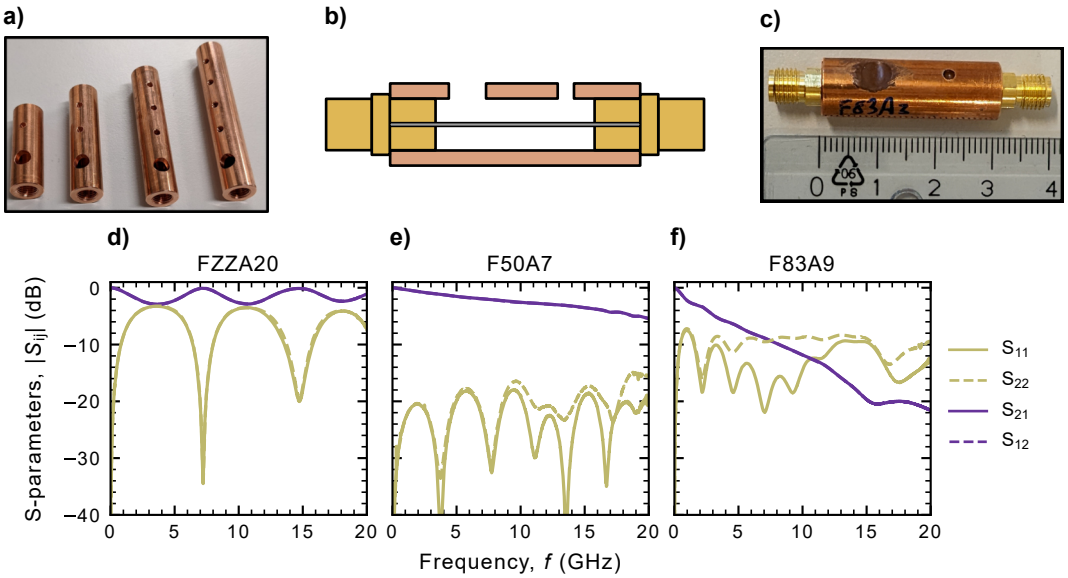


Figure 2.13: a) Copper housings with lengths of 3, 4, 5, and 6 cm. **b)** Schematic cross-section of the Cu-powder filter, showing a 3 cm copper housing, the SMA connectors, and the central copper wire. **c)** Photograph of an assembled filter (F83A2), with a total length of approximately 5 cm. **d)–f)** Room-temperature scattering parameters S_{ij} measured for an empty filter (FZZA20), a filter with 50% Cu concentration (F50A7), and one with 83% Cu concentration (F83A9), respectively.

On the other hand, we estimate the attenuation constant α from the transmission coefficient S_{21}. Approximating the filters as lossy coaxial transmission lines, with propagation constant $\gamma = \alpha + i\beta$, and neglecting impedance-mismatch oscillations, we write [30, 124]

$$S_{21} \propto e^{-\gamma L_{\text{eff}}} \quad \Rightarrow \quad 20 \log_{10} |S_{21}| \simeq -8.686\, \alpha L_{\text{eff}}. \tag{2.2}$$

We then estimate $\alpha(f)$ by fitting the approximately linear frequency dependence of the transmission magnitude in decibels. Assuming a homogeneous, nonmagnetic effective medium and neglecting conductor losses, α is related to the dielectric loss tangent by

$$\begin{aligned} \alpha &= \text{Re}\left\{ \frac{i2\pi f}{c} \sqrt{\varepsilon_{\text{r}}(1 - i \tan\delta)} \right\} \\ &\simeq \frac{\pi f}{c} \sqrt{\varepsilon_{\text{r}}} \tan\delta, \end{aligned} \tag{2.3}$$

where the second expression holds in the low-loss limit, $\tan\delta \ll 1$.

Both ε_{r} and $\tan\delta$ increase significantly at high Cu concentrations [Fig. 2.14a)]. Although the model provides an effective description of the complete filter, including the Cu-epoxy mixture and the conducting structures, rather than the intrinsic dielectric properties of the mixture, the extracted values are consistent with those reported for similar Cu-epoxy composites [125].

The −3 dB cutoff frequency decreases with increasing Cu concentration, from approximately 12 GHz at 50% to 2 GHz at 83%. We further characterize the transmission of filter F83D16 at 3 K, observing a slight shift of the cutoff towards higher frequencies compared to room temperature [Fig. 2.14b)]. This behavior is consistent with the increase in Cu conductivity upon cooling, which reduces microwave dissipation, as previously reported for similar filters [126]. Importantly, measurements at 10 mK reveal no discernible magnetic-field dependence of the filter's attenuation profile up to 9 T. In contrast, an Eccosorb filter exhibits a pronounced magnetic-field dependence, with clear reduced attenuation at few hundreds of mT. This magnetic-field resilience makes Cu-powder filters particularly suitable for cryogenic microwave experiments requiring large external magnetic fields. These measurements were performed in Ask, using a transmission configuration.

We confirm the expected broadband attenuation of Cu-powder filters by extending the room-temperature measurements up to 65 GHz [Fig. 2.14c)]. Both 50% and 83% Cu-powder filters maintain substantial attenuation throughout the measured frequency range, whereas a commercial reactive low-pass filter (Mini-Circuits ZLSS-8G-S+) exhibits significant high-frequency leakage above approximately 25 GHz.

Finally, we investigate the thermal transport properties of the Cu-epoxy mixture to assess the thermalization of the filter's central conductor. We fabricate a cylindrical probe with 83% Cu concentration by casting the mixture in a plastic syringe, which is removed after curing [Fig. 2.14d) left]. One end of the probe is screwed onto the mixing chamber plate of a dilution refrigerator, at temperature T_{cold}, while the other is equipped with a heater and a thermometer to control and measure T_{hot}.

At steady state, assuming negligible parasitic heat leaks and a small temperature difference $\Delta T = T_{\mathrm{hot}} - T_{\mathrm{cold}}$, the applied heater power P_{h} equals the conducted heat flow P_{k} [Fig. 2.14d) right], giving

$$P_{\mathrm{h}} = P_{\mathrm{k}} \simeq G(T_0)(T_{\mathrm{hot}} - T_{\mathrm{cold}}), \qquad G(T_0) = \kappa(T_0)\frac{A_{\mathrm{probe}}}{L_{\mathrm{probe}}}, \tag{2.4}$$

where G is the thermal conductance at the average temperature $T_0 = (T_{\mathrm{hot}} + T_{\mathrm{cold}})/2$, and A_{probe} and L_{probe} are the cross-sectional area and length of the probe, respectively.

By repeating the measurement at different temperatures, we extract the thermal conductivity $\kappa(T)$ [Fig. 2.14e)]. We fit the data with a power law, $\kappa(T) = A \times T^B$, obtaining $A = 143\ \mu\mathrm{W\,cm^{-1}\,K^{-(1+B)}}$ and $B = 2.25 \pm 0.06$. The resulting temperature dependence is consistent with that expected for insulating epoxy resins [127], suggesting that thermal transport remains dominated by the epoxy matrix despite the high Cu concentration. Consequently, although the outer copper housing is in principle well thermalized to the mixing chamber, thermal transport

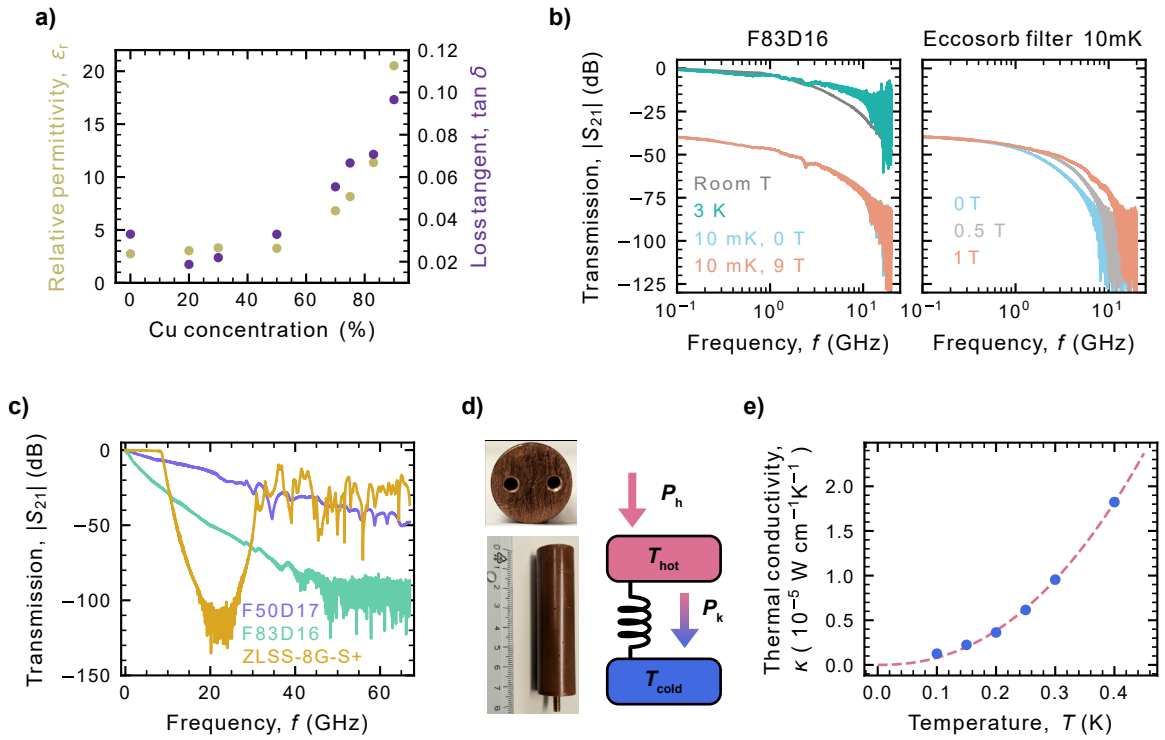


Figure 2.14: a) Effective relative permittivity ε_r (left axis) and loss tangent $\tan\delta$ (right axis), extracted from room-temperature scattering-parameter measurements as a function of Cu mass concentration. **b)** Transmission coefficient $|S_{21}|$ of the Cu-powder filter F83D16 at room temperature, 3 K, and 10 mK with magnetic fields of 0 and 9 T (left), compared with an Eccosorb filter measured at 10 mK under magnetic fields of 0, 0.5, and 1 T (right). The 3 K measurement is de-embedded, whereas the 10 mK measurements include attenuation from the microwave setup. The Eccosorb filter was fabricated by fellow members at 202QLab and Quantum Technology Laboratory. **c)** Room-temperature transmission coefficient $|S_{21}|$ measured up to 65 GHz for two Cu-powder filters (F50D17 and F83D16) and a commercial reactive low-pass filter (Mini-Circuits ZLSS-8G-S+). We thank Robert Rehammar for assisting us during these measurements. **d)** Photographs of the cylindrical Cu-epoxy probe with 83% Cu concentration (left) and schematic of the thermal conductance measurement (right). One end is anchored to the mixing chamber at T_cold, while a heater applies power P_h to the opposite end, whose temperature T_hot is measured. The resulting conducted heat flow is denoted by P_k. **e)** Thermal conductivity κ of the Cu-epoxy mixture with 83% Cu concentration as a function of temperature (blue dots). The dashed line represents a power-law fit, $\kappa(T) \propto T^B$, with $B = 2.25 \pm 0.06$.

through the mixture may limit the thermalization of the central conductor. This is relevant because, according to the fluctuation-dissipation theorem, a dissipative element not only absorbs incoming electromagnetic noise but also emits thermal noise determined by its own temperature [128]. Insufficient thermalization could limit the effective noise suppression of the filter, although our measurements do not directly establish the temperature of the central conductor.

Another design consideration is impedance matching. Since the relative permittivity depends on Cu concentration, the characteristic impedance of the filters also varies [see how S_{ii} level change in Fig. 2.13d)–f)]. In principle, the inner diameter of the copper housing should be adjusted for each concentration to maintain a 50 Ω impedance.

We leave the optimization of the impedance matching and a quantitative investigation of the filter noise temperature for future work. For the experiments discussed here, we selected 50% or lower for the resonator microwave input and output[1], and 83% for the DC gate and flux lines, where stronger high-frequency attenuation is required. Although we have not systematically quantified the improvement introduced by these filters in our measurement setups, Ivo reports in his thesis that their implementation suppressed the quasiparticle-related contribution to the temperature-dependent resonator frequency shift, allowing the TLS response to be resolved and fitted [112].

2.3 Measurements and analysis

2.3.1 Single-tone spectroscopy

Single-tone spectroscopy consists of probing a resonator with a microwave tone swept in frequency and measuring the transmission S_{21} or reflection S_{11} coefficient of the feedline. By repeating the frequency sweep while varying an external parameter, we obtain a map of the resonator response, from which we can extract changes in its resonant frequency and quality factors. The probe power can also be varied to investigate the power dependence of the resonator response. At sufficiently low power, the resonator operates in the small-signal regime, where its response is linear and the scattering parameters are independent of the probe power. Increasing the power can reveal nonlinear effects, such as Kerr-induced frequency shifts and bifurcation, as well as power-dependent losses.

In cQED, single-tone spectroscopy is commonly used to investigate resonators coupled to atomic-like systems, such as Andreev bound states, whose energy spectrum and occupation affect the resonator response. We employ this approach in PAPERS III and IV to study the gate- and flux-dependent response of the hybrid junctions. More generally, single-tone spectroscopy is used throughout this thesis to characterize the resonator response as a function of gate voltage (PAPER I), magnetic field and temperature (PAPER II), and probe power (PAPERS II and IV).

[1] In PAPER IV we use an HERD2 in the output line instead of a Cu-filter.

Resonator parameters extraction

We extract the resonant frequency ω_r and quality factors Q_i and Q_c by fitting the complex resonator response, including both its magnitude and phase, using the circle-fit method [31, 32, 129]. For the notch-type transmission geometry used in PAPER I [Fig. 2.15a)] and the purely reflective configuration used in PAPER II–IV [Fig. 2.15b)], the scattering coefficient is described by

$$S_{ij}(\omega) = Ae^{i\alpha}e^{-i\omega t_\mathrm{d}}\left[1 - \frac{\eta_{ij}Q_\mathrm{l}e^{i\phi}}{|Q_\mathrm{c}|\left(1 + 2iQ_\mathrm{l}\frac{\omega-\omega_\mathrm{r}}{\omega_\mathrm{r}}\right)}\right], \tag{2.5}$$

where $\eta_{21} = 1$ for S_{21} and $\eta_{11} = 2$ for S_{11}. The parameters A, α, and t_d account for the attenuation, phase offset, and electrical delay introduced by the measurement setup, while ϕ accounts for asymmetries in the resonance line shape.

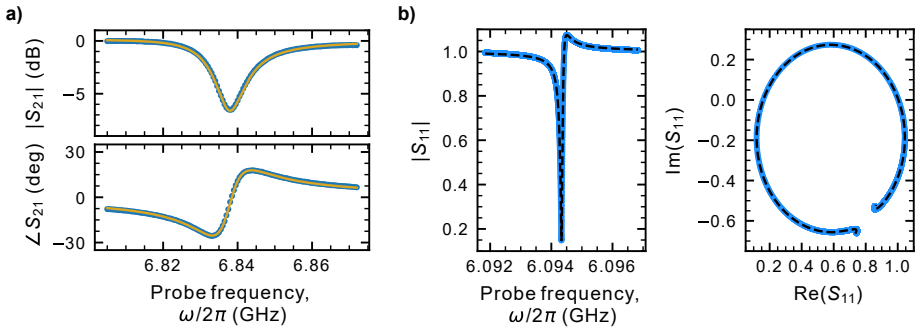


Figure 2.15: Representative resonator fits. **a)** Magnitude (top) and phase (bottom) of the transmission coefficient S_{21} for the notch-type resonator used in PAPER I. **b)** Magnitude of the reflection coefficient S_{11} (left) and corresponding representation in the IQ plane (right) for a CPS resonator used in PAPER II. Experimental data are shown in blue, with circle-fit models represented by solid [a)] or dashed [b)] lines.

For our CPS resonators, an important parameter is the resonator impedance Z_r, which determines the amplitude of the zero-point fluctuations and therefore affects the coupling strength to the ABSs investigated in PAPERS III and IV. The relevant impedance depends on the resonator mode, since odd- and even-mode excitations produce different current distributions, as illustrated by the electromagnetic simulations [Fig. 2.16a)–b)]. In our experiments, we exploit the odd mode, and therefore estimate its impedance using Sonnet simulations with a differential excitation, applying opposite polarities to the two conductors [Fig. 2.16c)] [22]. We extract then the differential characteristic impedance $Z_{0,\mathrm{diff}}$, which gives $Z_\mathrm{r} = 4Z_{0,\mathrm{diff}}/\pi$ for our $\lambda/4$ CPS resonators. For the lumped-element resonator of Device III [Fig. 2.16d)], instead, we get directly $Z_\mathrm{r} = 2\sqrt{L_\mathrm{r}/C_\mathrm{r}}$ without requiring any conversion from the transmission-line impedance. The factor 2 here accounts for the differential geometry.

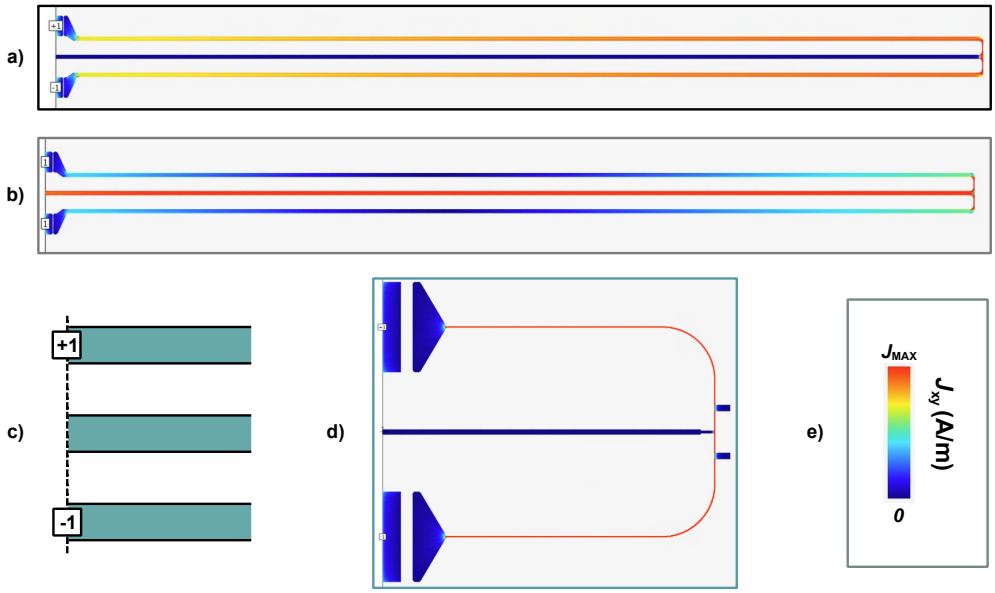


Figure 2.16: Simulated surface current density J_{xy} in the CPS resonators. **a)** Odd-mode excitation of a quarter-wavelength CPS resonator. The central grounding strip carries negligible current, consistent with the virtual-ground symmetry of the differential mode. **b)** Even-mode excitation of the same resonator, showing a substantial current in the central grounding strip. **c)** Differential excitation configuration used to extract the differential characteristic impedance $Z_{0,\mathrm{diff}}$. **d)** Odd-mode excitation of the lumped-element resonator. The nearly uniform current density along the inductive arms is consistent with the lumped-element approximation. **e)** Qualitative color scale of the surface current density, ranging from zero to its maximum value J_{max}. All simulations were performed in Sonnet. Panels a)–b), d)–e) show screenshots of the simulation results.

Finally, the resonator parameters allow us to estimate the average intracavity photon number $\bar{n}$ from the applied microwave power at the device [130],

$$\bar{n} = \frac{4Q_{\mathrm{l}}^2}{Q_{\mathrm{c}}} \frac{P_{\mathrm{in}}}{\hbar\omega_{\mathrm{r}}^2} \frac{Z_{\mathrm{f}}}{Z_{\mathrm{r}}}, \tag{2.6}$$

where P_{in} is the probe power reaching the resonator, Z_{f} is the feedline impedance.

2.3.2 Two-tone spectroscopy

Two-tone spectroscopy introduces an additional microwave drive alongside the resonator readout tone. Typically, the readout frequency is fixed close to the resonator resonance, while the drive frequency is swept. When the drive excites a transition in a coupled atomic-like system, the resulting change in its state population modifies the resonator response, allowing us to identify the transition frequency. We use this technique in PAPERS III and IV to investigate ABS

transitions. More generally, two-tone measurements do not necessarily involve spectroscopy of discrete energy levels. In PAPER I, for instance, we use a second tone as a gate excitation to modulate the resonator response and generate sidebands, while in PAPER IV, we apply a second tone as a pump to induce parametric amplification and characterize the cubic nonlinearity.

2.3.3 Gate-response characterization

In PAPER I, we investigate the dynamics of the gate response using pulsed and continuous microwave excitation. In both cases, the gate excitation is applied on top of a DC working point above the gate-response onset (see Sec. 1.3), with the DC and RF signals combined through a bias-tee at the mixing chamber [Fig. 2.7a)].

As we saw in the fabrication section, the chip hosts four resonators, D1–D4, of which D1, D3, and D4 incorporate Al/InAs nanowires, while D2 serves as a reference without a nanowire. Temperature-dependent spectroscopy reveals a frequency shift in the nanowire-loaded resonators, whereas D2 remains approximately unchanged (Fig. 2.17). This indicates that the kinetic inductance contribution is dominated by the nanowires rather than the thicker Al resonator films. Initially, the gate lines were connected to a common bias-tee through a cryogenic switch, allowing us to investigate the gate response of the different devices. However, only D1 exhibited a reproducible gate response, and in a second cooldown we grounded D2–D4, focusing our measurements on D1.

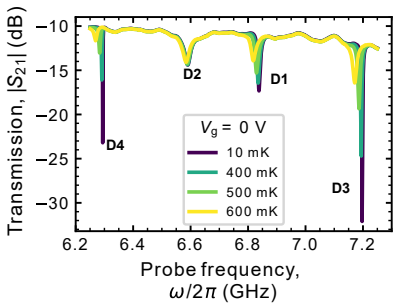


Figure 2.17: Feedline transmission spectra at different temperatures and $V_g = 0$ V. The nanowire-loaded resonators (D1, D3, and D4) shift towards lower frequencies with increasing temperature, whereas the reference resonator D2 remains approximately unchanged.

Time-domain measurements

We first investigate the gate dynamics directly in the time domain. The measurement sequence consists of three pulses: a trigger pulse, a readout pulse, and a gate pulse [Fig. 2.18a)-b)]. All three pulses are generated by Presto, which

also records and processes the output signal. The readout signal is generated through digital up-conversion, while the output signal is acquired through digital down-conversion, both using the same intermediate frequency, in the range 100–125 MHz. The down-converted signal is then demodulated and filtered to suppress unwanted frequency components, resulting in an effective time resolution of approximately 8 ns. During the trigger window, which defines the acquisition period, we apply a readout pulse at frequency ω_{ro} to the feedline and a square pulse of amplitude A_{g} and duration τ_{g} to the gate line. By averaging the output signal s_{out} over 10^5–10^6 repetitions and repeating the measurement for different ω_{ro}, we obtain a two-dimensional map $s_{\mathrm{out}}(t, \omega_{\mathrm{ro}})$ [Fig. 2.18c)].

This representation allows us to examine the resonator response from two complementary perspectives. Vertical line cuts provide the resonator spectrum at a given time, from which we extract the instantaneous resonant frequency ω_{r} and loaded quality factor Q_{l} through Lorentzian fits. By comparing the steady-state frequency shift induced by the gate pulse [Fig. 2.18d), left] with the DC gate response discussed in Sec. 1.3 [Fig. 1.4a)], we calibrate the attenuation of the RF gate line and determine the effective pulse amplitude. Horizontal line cuts, on the other hand, show the time evolution of the resonator response [Fig. 2.18d), right]. Two characteristic features can be distinguished here: the initial resonator ring-up and the subsequent response to the gate pulse. The ring-up transient relaxes exponentially towards its steady-state value, with a characteristic time that limits the temporal resolution of the resonator. From an exponential fit, we obtain $\tau_{\mathrm{res}} \simeq 10$ ns [Fig. 2.18e)].

We then focus on the gate response. We choose pulse durations between 500 and 800 ns, sufficiently long for the response to reach a steady value while limiting distortions associated with the bias-tee [Fig. 2.18f)]. We fix the readout frequency close to resonance and use gate pulses with $|A_{\mathrm{g}}| = 250$ mV, corresponding to a small perturbation around the DC gate working point. At this amplitude, the responses to positive and negative pulses are approximately symmetric, consistent with the linear-response regime [Fig. 2.18g)]. For each working point, we apply both pulse polarities and fit the rising response to the positive pulse and the falling response to the negative pulse with exponential functions. From these fits, we extract the characteristic rising and falling times, τ_{R} and τ_{F}, respectively. The opposite edges of the two pulse polarities are affected by the bias-tee response and are therefore excluded from the analysis.

Sideband spectroscopy

As a complementary approach, we investigate the device dynamics using continuous gate excitation. Unlike the pulsed measurements, this method probes the gate response at frequencies well above the 40 kHz cutoff of the bias-tee, providing an independent estimate of the characteristic response time. The measurement

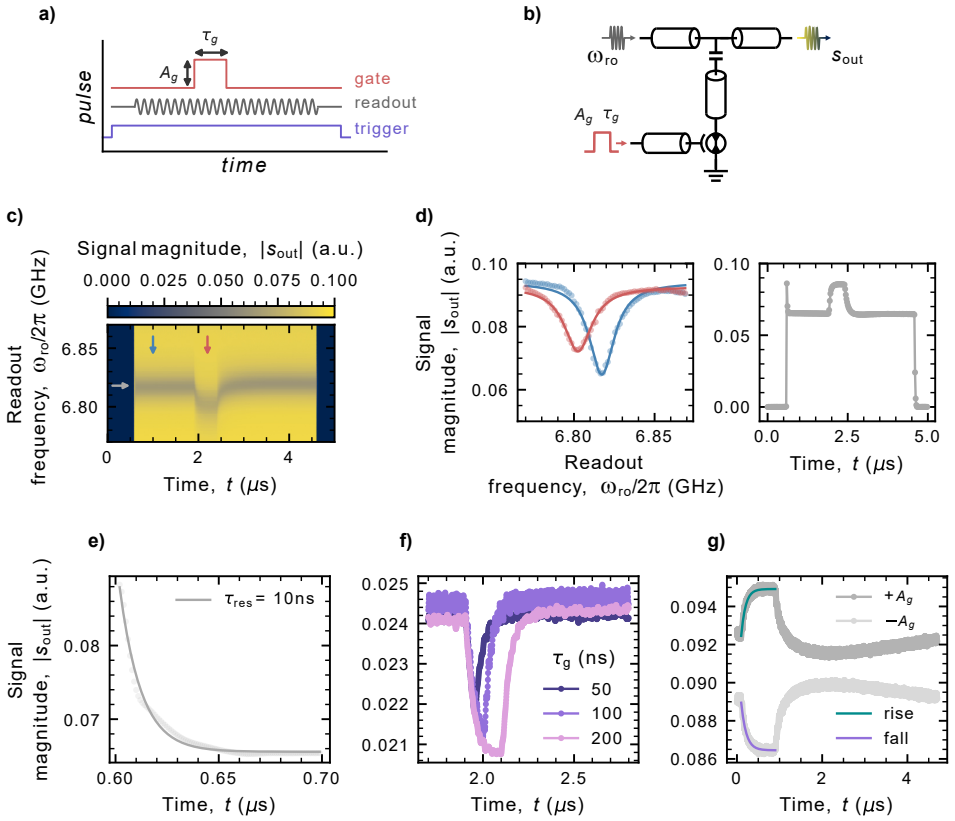


Figure 2.18: a) Pulse sequence used for the time-domain measurements. **b)** Simplified schematic of the measurement setup. **c)** Heat map of resonator time traces recorded for different readout frequencies ω_{ro} at gate voltage $V_{\mathrm{g}} = 23.5$ V. The trigger period is 5 μs, a 4 μs-long readout pulse starts at 0.6 μs, and a gate pulse with $A_{\mathrm{g}} = -1.5$ V and $\tau_{\mathrm{g}} = 500$ ns starts around 2 μs. Arrows indicate the line cuts shown in panel d). **d)** Line cuts from panel c). *Left*: vertical line cuts at 1 μs (blue) and 2.2 μs (red), showing the resonator shift induced by the gate pulse. Lorentzian fits yield $\omega_{\mathrm{r}}/2\pi = 6.82$ GHz and $Q_{\mathrm{l}} = 716$ (blue), and $\omega_{\mathrm{r}}/2\pi = 6.80$ GHz and $Q_{\mathrm{l}} = 652$ (red). *Right*: horizontal line cut at 6.815 GHz, showing the resonator ring-up and gate response in the time domain. **e)** Zoom of the resonator ring-up in panel d), with an exponential fit yielding a characteristic time $\tau_{\mathrm{res}} = 10$ ns. **f)** Gate response for three different pulse durations $\tau_{\mathrm{g}} = 50$, 100, and 200 ns. **g)** Time traces at $V_{\mathrm{g}} = 21$ V showing the resonator response under positive (dark gray) and negative (light gray) gate pulses. Gate parameters are $|A_{\mathrm{g}}| = 250$ mV and $\tau_{\mathrm{g}} = 800$ ns. Exponential fits to the rising (cyan) and falling (purple) responses yield the characteristic times $\tau_{\mathrm{R}} = 103$ ns and $\tau_{\mathrm{F}} = 116$ ns, respectively.

relies on the gate dependence of the resonant frequency: a continuous gate excitation at frequency ω_{g} periodically modulates ω_{r} around the DC working point [Fig. 2.19a)].

To implement this scheme, we apply a continuous tone at ω_{r} to the feedline and a second tone at ω_{g} to the gate. The system can then be viewed as an effective mixer, with ω_{r} and ω_{g} playing the roles of the local oscillator and intermediate

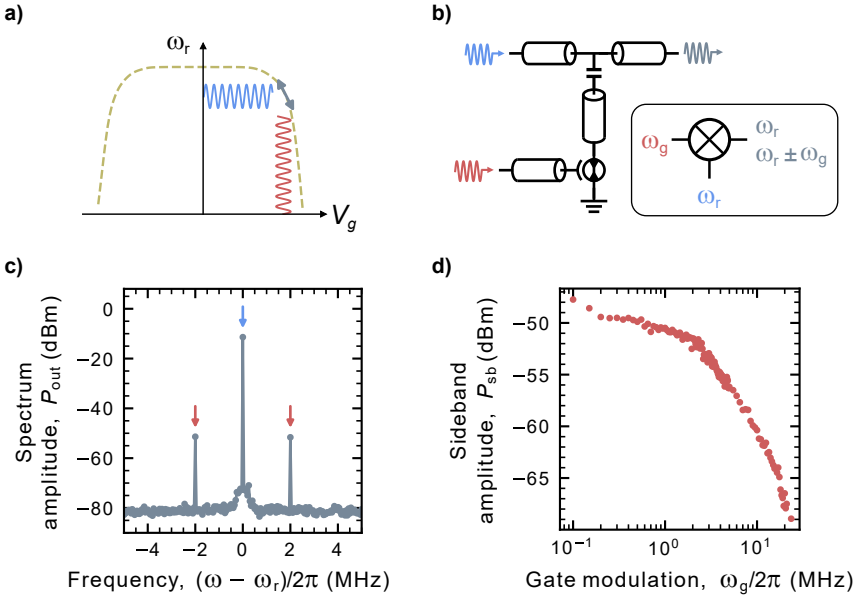


Figure 2.19: a) Schematic of the measurement principle: continuous gate excitation modulates the resonator response due to the gate dependence of the resonant frequency, $\omega_r(V_g)$. **b)** Mixer-equivalent circuit of the system under continuous modulation. **c)** Output spectrum for $V_g = 27$ V, $\omega_g/2\pi = 2$ MHz, and $P_g = -5$ dBm. The readout tone and first-order sidebands are indicated by blue and red arrows, respectively. **d)** Averaged amplitude of the upper and lower first-order sidebands [red arrows in panel c)] as a function of gate modulation frequency ω_g.

frequency, respectively [Fig. 2.19b)]. By measuring the output signal with a spectrum analyzer, we observe the readout tone at ω_r, together with the two first-order sidebands at $\omega_r \pm \omega_g$ [Fig. 2.19c)].

By sweeping ω_g and measuring the average amplitude of the two first-order sidebands, we characterize the frequency dependence of the gate response [Fig. 2.19d)]. The sideband amplitude decreases with increasing ω_g, reflecting the finite response time of the system. Assuming a first-order low-pass response [131], we estimate the characteristic time from the 3-dB cutoff frequency $\omega_{g,3dB}$ as

$$\tau_{sb} = \frac{1}{\omega_{g,3dB}}. \tag{2.7}$$

For $V_g = 27$ V, we obtain $\omega_{g,3dB}/2\pi \simeq 3$ MHz, corresponding to $\tau_{sb} \simeq 50$ ns, in agreement with the time-domain measurements.

For these measurements, the readout and gate powers are chosen to predominantly excite first-order sidebands. By increasing the excitation powers, higher-order sidebands appear at $\omega_r \pm n\omega_g$, with n up to four [Fig. 2.20a)]. Their amplitudes also decrease with increasing modulation frequency [Fig. 2.20b)]. These higher-order sidebands reflect frequency mixing beyond the small-modulation regime and are not considered in our analysis of the characteristic response time.

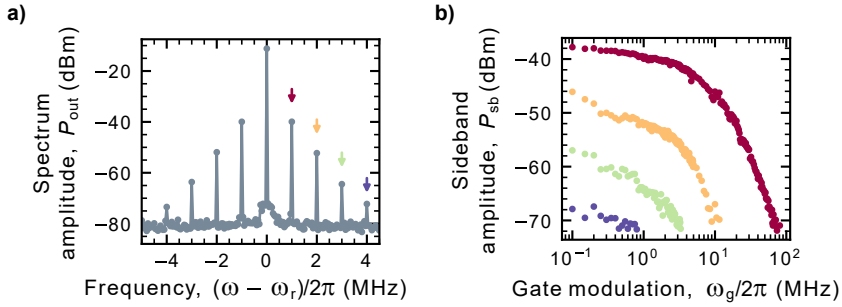


Figure 2.20: a) Higher-order sideband excitation for $V_g = 27$ V, $\omega_g/2\pi = 1$ MHz, $P_g = 10$ dBm, and $P_{ro} = -20$ dBm. Upper sideband peaks from the first to the fourth order are indicated by red, yellow, green, and violet arrows, respectively. **b)** Amplitude of the first- to fourth-order sidebands as a function of gate modulation frequency ω_g, using the same color code as in panel a).

2.3.4 Preliminary characterization of semiconducting weak-links coupled to resonators

In this section, we describe the preliminary single-tone spectroscopy measurements used to characterize the devices investigated in PAPERS III and IV and identify suitable operating points. For convenience, we also reproduce the device micrographs introduced earlier and summarize their measurement configurations schematically [Fig. 2.21a)–c) for PAPER III and Fig. 2.22a)–b) for PAPER IV].

Weak-link pinch-off and gate response

The first step in characterizing our devices is to identify the active and pinched-off regimes of the weak links. In the active regime, a supercurrent flows through the junction, producing a periodic modulation of the resonator response with the applied magnetic flux [Fig. 2.21d)]. Applying increasingly negative gate voltages progressively depletes the InAs weak link, reducing the number and transparency of its conducting channels. Eventually, the junction becomes pinched off, effectively behaving as an open circuit. This regime is identified by the disappearance of the flux modulation and the saturation of the resonant frequency with gate voltage [Fig. 2.21e)]. The corresponding resonator parameters define its bare response, without appreciable loading from the weak link.

The flux-dependent resonance frequency typically exhibits maxima near $\varphi = 2n\pi$ and minima near $\varphi = (2n+1)\pi$, with n an integer. Near the maxima, the ABS pair transitions are generally far detuned from the resonator, and the gate dependence predominantly reflects changes in the inductive loading [Fig. 2.21e)]. Near the minima, the transition energies are reduced and can be tuned through the resonator frequency, producing avoided crossings [Fig. 2.21f)]. The same qualitative behavior is observed in PAPER IV, where the presence of a second weak link introduces an additional degree of control.

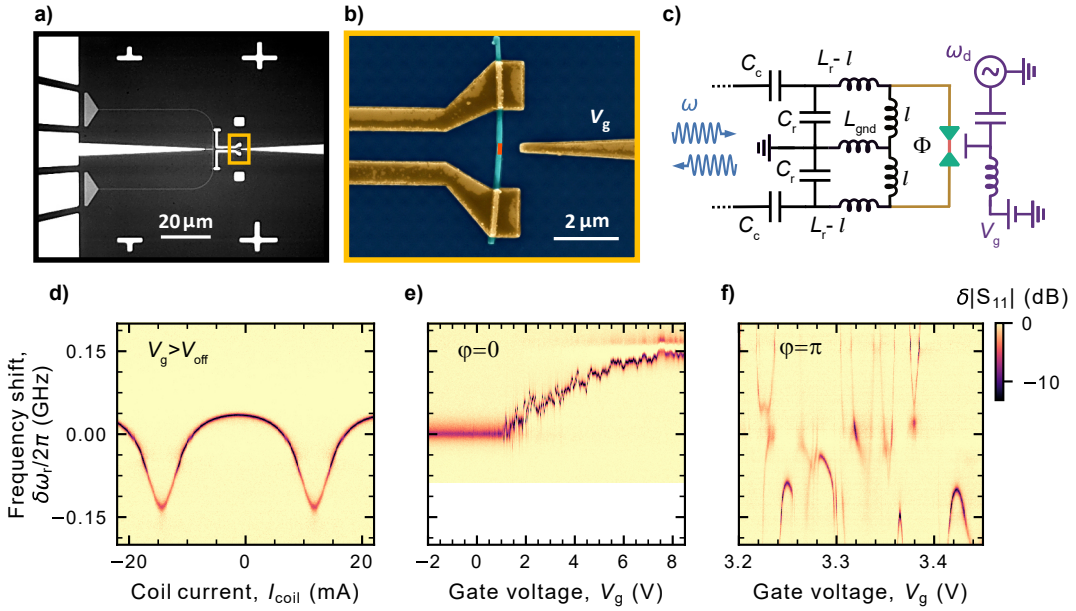


Figure 2.21: Preliminary characterization of the hybrid resonator investigated in PAPER III. **a)** Micrograph of Device III, with the weak-link region highlighted. **b)** False-colored micrograph of the weak link, superconducting contacts, and side gate. The device fabrication is described earlier in this chapter. **c)** Equivalent circuit showing the differential resonator, the shared inductance $2l$, and the flux-biased weak link. The resonator is probed at ω, while an additional drive at ω_d can be applied through the gate. **d)** Single-tone spectroscopy showing the periodic resonance-frequency shift as a function of the applied flux, with the weak link active. **e), f)** Gate-dependent spectra at $\varphi = 0$ and $\varphi = \pi$, respectively. Panel **e)** shows the transition from the pinched-off to the active regime, while panel **f)** reveals several avoided crossings. The color scale represents the background-subtracted reflection response.

Flux and gate crosstalk compensation

Device IV contains two independently gated weak links, each embedded in a superconducting loop [Fig. 2.22a)–b)]. However, each flux line also couples to the neighboring loop, and each gate weakly affects the neighboring junction. We can compensate for this cross-talk by applying the following linear transformations:

$$\begin{pmatrix} I_1^{\mathrm{app}} \\ I_2^{\mathrm{app}} \end{pmatrix} = \begin{pmatrix} 1 & -0.11 \\ -0.22 & 1 \end{pmatrix} \begin{pmatrix} I_1 \\ I_2 \end{pmatrix}, \qquad \begin{pmatrix} V_1^{\mathrm{app}} \\ V_2^{\mathrm{app}} \end{pmatrix} = \begin{pmatrix} 1 & -0.042 \\ -0.03 & 1 \end{pmatrix} \begin{pmatrix} V_1 \\ V_2 \end{pmatrix}. \quad (2.8)$$

Here, the superscript app denotes the settings applied to the physical lines, whereas I_i and V_i denote the compensated coordinates. Sweeping one compensated coordinate therefore generally requires changing both physical source settings. The compensated gates provide access to four configurations: both junctions pinched off, either JJ_1 or JJ_2 active individually, and both junctions active [Fig. 2.22c)–f)].

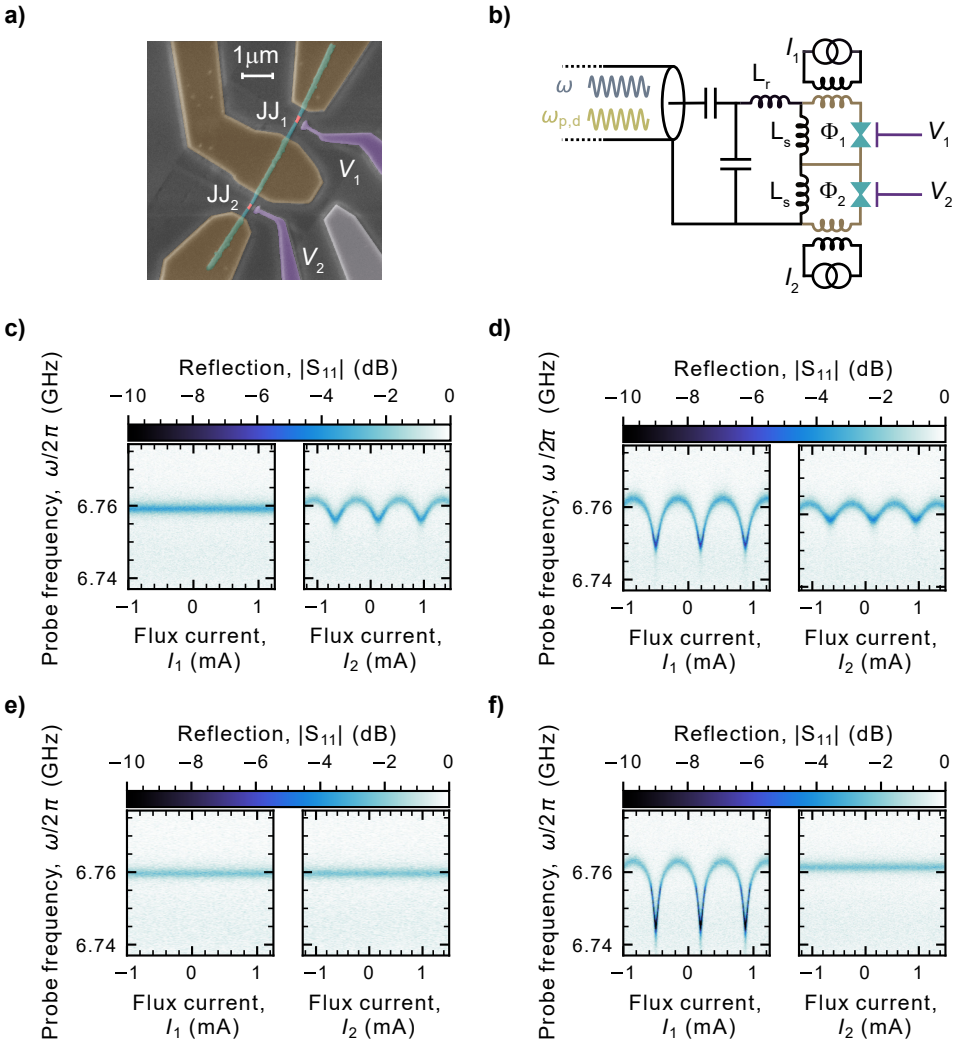


Figure 2.22: Independent control of the two weak links in Device IV. **a)** False-colored scanning electron micrograph showing JJ_1 and JJ_2 and their respective gates. **b)** Equivalent circuit of the resonator coupled to two weak links through shared inductances L_s. The loop fluxes are controlled by two flux lines. **c)**–**f)** Single-tone spectroscopy versus the compensated flux coordinates I_1 (left) and I_2 (right), with **c)** only JJ_2 active, **d)** both junctions active, **e)** both junctions pinched off, and **f)** only JJ_1 active.

Flux-to-phase conversion

In our experiments, the magnetic flux Φ_{ext} through the superconducting loops is controlled by the current applied to a flux line or coil. To compare our measurements with the theoretical models, we therefore need to convert this current into the superconducting phase difference φ across the weak link. The externally imposed phase is given by $\varphi_{\text{ext}} = 2\pi\Phi_{\text{ext}}/\Phi_0$. However, a finite loop inductance can introduce a screening correction, such that φ differs from φ_{ext}. To estimate

this correction, we consider the total potential energy of the loop,

$$U_{\mathrm{tot}}(\varphi) = \frac{1}{2L_{\mathrm{loop}}}\left(\frac{\Phi_0}{2\pi}\right)^2(\varphi-\varphi_{\mathrm{ext}})^2 - \varepsilon_{\mathrm{ABS}}^{\mathrm{eff}}(\varphi), \tag{2.9}$$

where L_{loop} is the loop inductance and $-\varepsilon_{\mathrm{ABS}}^{\mathrm{eff}}$ is the ABS ground-state energy Eq. 1.24. The equilibrium phase φ_{min} is then obtained by solving the minimization condition

$$\left.\frac{\partial U_{\mathrm{tot}}}{\partial\varphi}\right|_{\varphi_{\mathrm{min}}} = \left(\frac{\Phi_0}{2\pi}\right)^2\frac{\varphi_{\mathrm{min}}-\varphi_{\mathrm{ext}}}{L_{\mathrm{loop}}} - \left.\frac{\partial\varepsilon_{\mathrm{ABS}}^{\mathrm{eff}}}{\partial\varphi}\right|_{\varphi_{\mathrm{min}}} = 0. \tag{2.10}$$

In PAPER IV, we assume that the loop inductance is dominated by the shared NbTiN inductance $L_{\mathrm{s}} \simeq 350$ pH. Using representative values of τ and Δ_{eff}, we find that φ_{min} remains close to φ_{ext} [Fig. 2.23a)]. Even considering a scenario where $L_{\mathrm{loop}} = 3L_{\mathrm{s}}$, which would be like assigning to the entire loop the kinetic inductance per square of the NbTiN portion, the maximum phase deviation remains below 3% of π [Fig. 2.23b)]. This supports the approximation $\varphi \simeq \varphi_{\mathrm{ext}}$. A similar conclusion was obtained in Appendix D of PAPER III, where the screening correction was estimated from the weak-link inductance inferred from single-tone spectroscopy.

We therefore convert the flux current into superconducting phase using the measured oscillation period,

$$\varphi \simeq 2\pi\frac{I-I_0}{I_{\Phi_0}}, \tag{2.11}$$

where I_{Φ_0} is the current period corresponding to one flux quantum and I_0 identifies $\varphi = 0$ modulo 2π. Note that neglecting the screening correction in the flux-to-phase conversion does not imply neglecting the shared inductance in the coupling and nonlinearity models.

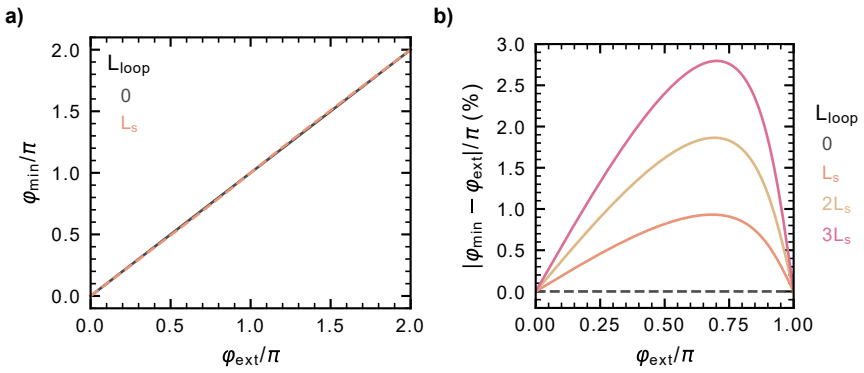


Figure 2.23: Effect of loop inductance on the flux-to-phase conversion. **a)** Equilibrium junction phase φ_{min} obtained from Eq. 2.10, compared for $L_{\mathrm{loop}} = 0$ (gray dashed line) and $L_{\mathrm{loop}} = L_{\mathrm{s}}$ (salmon line). **b)** Absolute phase deviation $|\varphi_{\mathrm{min}} - \varphi_{\mathrm{ext}}|$, normalized to π and expressed as a percentage, for $L_{\mathrm{loop}} = 0$, L_{s}, $2L_{\mathrm{s}}$, and $3L_{\mathrm{s}}$. The calculation uses $\tau = 0.9$, $\Delta_{\mathrm{eff}}/h = 40$ GHz, and $L_{\mathrm{s}} = 350$ pH.

2.3.5 Extraction of resonator nonlinearities

In this section, we describe the measurements and analysis used to extract the resonator nonlinearities investigated in PAPER IV.

Kerr nonlinearity

At a fixed gate and flux configuration, we sweep the probe frequency for increasing probe power P_{in} and track the resonant frequency [Fig. 2.24a)]. The power-induced frequency shift is defined relative to its low-power value,

$$\delta\omega_{\mathrm{kerr}}(P_{\mathrm{in}}) = \omega_{\mathrm{r}}(P_{\mathrm{in}}) - \omega_{\mathrm{r}}(P_{\mathrm{in}} \to 0). \tag{2.12}$$

We convert the probe power into the average intracavity photon number $\bar{n}$ using Eq. 2.6. The input power reaching the device is estimated from the VNA output power and the nominal input-line attenuation, including an additional 6 dB to account for cable losses. The uncertainty in this estimate, of the order of a few dB, introduces a systematic uncertainty in $\bar{n}$ and consequently in the extracted Kerr nonlinearity.

We extract K by fitting the power-induced frequency shift to

$$\delta\omega_{\mathrm{kerr}} = K\bar{n} + K'\bar{n}^2, \tag{2.13}$$

where the quadratic term accounts phenomenologically for higher-order corrections to the initial linear dependence [Fig. 2.24b)]. The fit is restricted to the regime where the resonance can be reliably tracked without strong distortion or bistability.

As a control measurement, we repeat the power sweep with both junctions pinched off. No appreciable frequency shift is observed over the investigated power range [Fig. 2.24c)], indicating that the intrinsic nonlinearity of the bare resonator is below our measurement sensitivity in this regime.

Cubic nonlinearity

As discussed in Chapter 1, 3WM couples the probe signal at ω to an idler at $\omega_{\mathrm{i}} = \omega_{\mathrm{p}} - \omega$, allowing energy from the pump to amplify the probe. At each flux bias, we first locate the low-power resonance and then acquire spectra with the pump off and on, choosing $\omega_{\mathrm{p}} = 2\omega_{\mathrm{r}}$ [Fig. 2.25a)].

We define the on-off power gain as

$$G(\omega) = \frac{|S_{11}^{\mathrm{ON}}(\omega)|^2}{|S_{11}^{\mathrm{OFF}}(\omega)|^2}, \qquad G_{\mathrm{dB}} = 10\log_{10} G. \tag{2.14}$$

The difference between the ON and OFF traces expressed in decibels therefore gives the gain profile. Around its maximum, we fit the gain in linear power units

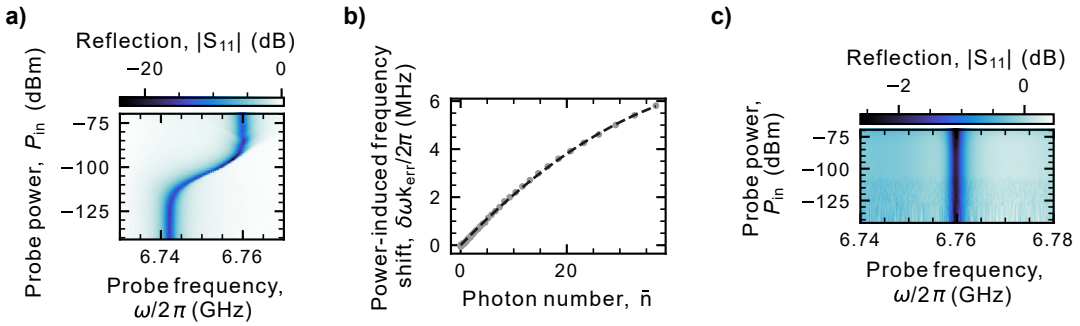


Figure 2.24: Extraction of the Kerr nonlinearity in PAPER IV. **a)** Single-tone spectroscopy versus probe power with both junctions active, showing a power-dependent resonance-frequency shift. **b)** Power-induced frequency shift versus estimated average intracavity photon number $\bar{n}$. The dashed line represents a fit to Eq. 2.13. **c)** Control measurement with both junctions pinched off, showing no appreciable power-dependent frequency shift over the investigated range.

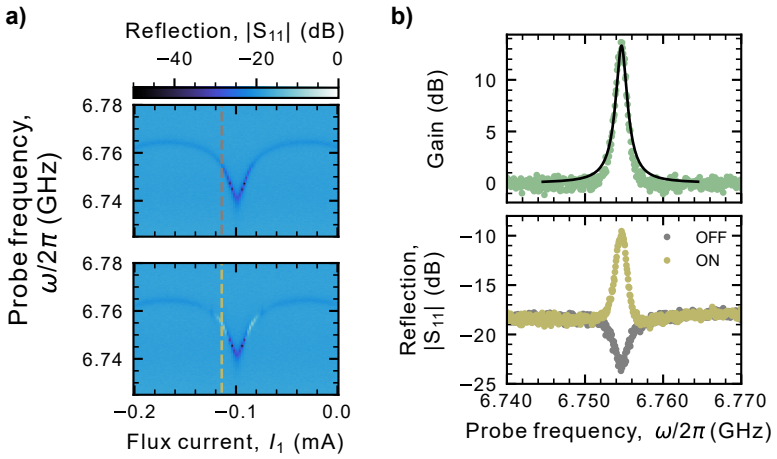


Figure 2.25: Three-wave-mixing measurements used to estimate the cubic nonlinearity. **a)** Resonator spectra versus flux current with the pump off (top) and on (bottom), with the pump frequency following twice the resonator frequency. **b)** Bottom: OFF (gray) and ON (yellow) traces at the flux bias marked in panel **a)**. Top: corresponding on-off gain (green) and Lorentzian fit (black), from which the peak gain G_0 is extracted.

with a Lorentzian function,

$$G(\omega) = 1 + \frac{G_0 - 1}{1 + [(\omega - \omega_0)/\Gamma]^2}, \tag{2.15}$$

where G_0 is the peak gain, ω_0 its center frequency, and Γ the half-width at half-maximum of the excess gain [Fig. 2.25b)].

We then estimate $|g_3|$ from the small-signal gain relation [14],

$$G_0 \simeq 1 + \frac{4\kappa^2|g|^2}{\left[(\delta_\mathrm{p}/2)^2 + \kappa^2/4 - 4|g|^2\right]^2}, \qquad g = 2g_3\sqrt{\bar{n}_\mathrm{p}}, \tag{2.16}$$

where $\delta_\mathrm{p} = \omega_\mathrm{p} - 2\omega_\mathrm{r}$ and $\kappa = \omega_\mathrm{r}/Q_\mathrm{l}$ is the resonator linewidth. The average intracavity pump photon number is estimated using [132]

$$\bar{n}_\mathrm{p} = \frac{\kappa_\mathrm{c}}{(\omega_\mathrm{p} - \omega_\mathrm{r})^2 + (\kappa/2)^2}\frac{P_\mathrm{p}}{\hbar\omega_\mathrm{p}}, \qquad \kappa_\mathrm{c} = \frac{\omega_\mathrm{r}}{Q_\mathrm{c}}, \tag{2.17}$$

where P_p is the estimated pump power reaching the device.

For these measurements, we choose the pump power to obtain gains of approximately 10 dB or lower, limiting corrections associated with stronger pumping. Since the pump power reaching the device is estimated from the nominal line attenuation, the extracted $|g_3|$ is subject to a systematic uncertainty. Furthermore, the extraction relies on an approximate gain model that neglects pump-induced frequency shifts.

3 Microwave characterization of Al-capped InAs nanowires

In this chapter we summarize the results published in PAPER I, starting from the microwave phenomenology of gate-tunable superconducting properties we introduce in Sec. 1.3, where we show that our device exhibits a decrease in both resonant frequency ω_r and internal quality factor Q_i with increasing gate voltage. In the same section, we also show that a qualitatively similar behavior is observed when increasing the temperature at zero gate voltage. These temperature- and gate-driven responses [see data points in Fig. 3.1a)-b)] form the basis of the analysis presented below.

3.1 Effective temperature approach

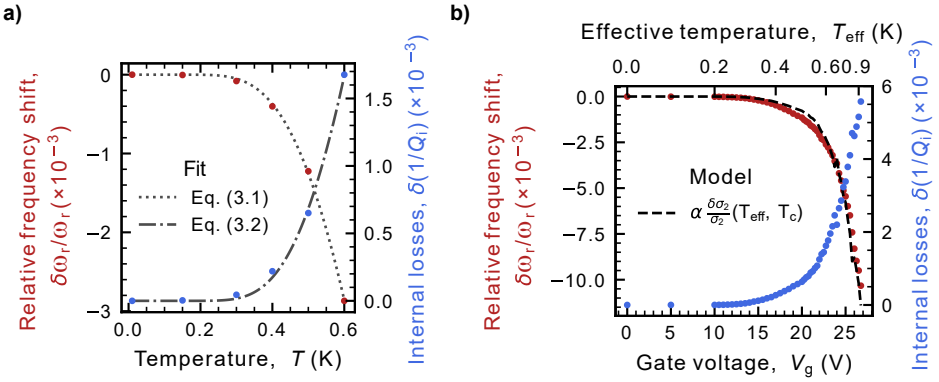


Figure 3.1: a) Temperature-driven data with $V_g = 0$: relative frequency shift $\delta\omega_r/\omega_r$ (left axis) and inverse quality factor $\delta(1/Q_i)$ (right axis) are plotted vs temperature T. Equations 3.1 and 3.2 are globally fitted to the data, according to Mattis–Bardeen model. Fit results: $\alpha = (0.14 \pm 0.04)$ and $T_c = (1.31 \pm 0.05)$ K. **b)** Gate-driven data for $T = 10$ mK: $\delta\omega_r/\omega_r$ (left axis) and $\delta(1/Q_i)$ (right axis) vs V_g (bottom axis). For each data point in $\delta(1/Q_i)$, we obtain an effective temperature T_{eff} (top axis), assuming that the gate effect is equivalent to an increase in temperature and using Eq. 3.2. The predicted $\delta\omega_r/\omega_r$, based on Eq. 3.1, with the parameter obtained from the fit in panel a), and $T = T_{eff}$ is plotted as a dashed line. Figure adapted from PAPER I.

The simultaneous decrease in ω_r and Q_i is consistent with an increase in the

nanowire kinetic inductance and dissipation, respectively, suggesting an increased quasiparticle population. To test this interpretation, we describe the nanowire through its complex conductivity, $\sigma_{\mathrm{NW}} = \sigma_1 + i\sigma_2$. Within the generalized Mattis–Bardeen framework, the relative frequency shift and the variation in internal losses can be written as [133, 134]

$$\frac{\delta\omega_{\mathrm{r}}}{\omega_{\mathrm{r}}} = \frac{\alpha}{2}\frac{\delta\sigma_2}{\sigma_2}, \tag{3.1}$$

and

$$\delta\left(\frac{1}{Q_{\mathrm{i}}}\right) = \alpha\frac{\delta\sigma_1}{\sigma_2}, \tag{3.2}$$

where α is the participation ratio of the gate-affected kinetic inductance to the total resonator inductance [21, 135, 136]. In the limits $k_{\mathrm{B}}T \ll \Delta_0$ and $\hbar\omega \ll \Delta_0$, the conductivity components can be approximated as [21, 133, 134]

$$\frac{\sigma_1}{\sigma_n} = \frac{2\Delta_0}{\hbar\omega}\frac{n_{\mathrm{qp}}}{N_0\sqrt{2\pi k_{\mathrm{B}}T\Delta_0}}\sinh(\xi)K_0(\xi), \tag{3.3}$$

and

$$\frac{\sigma_2}{\sigma_n} = \frac{\pi\Delta_0}{\hbar\omega}\left[1 - \frac{n_{\mathrm{qp}}}{2N_0\Delta_0}\left(1 + \sqrt{\frac{2\Delta_0}{\pi k_{\mathrm{B}}T}}e^{-\xi}I_0(\xi)\right)\right], \tag{3.4}$$

where σ_n is the normal-state conductivity, N_0 is the density of states at the Fermi level, $\Delta_0 = 1.764 k_{\mathrm{B}}T_{\mathrm{c}}$ is the zero-temperature superconducting gap, $\xi = \hbar\omega/(2k_{\mathrm{B}}T)$, and I_0 and K_0 are modified Bessel functions. In thermal equilibrium, the quasiparticle density is

$$n_{\mathrm{qp}}(T) = 2N_0\sqrt{2\pi k_{\mathrm{B}}T\Delta_0}\exp\left(-\frac{\Delta_0}{k_{\mathrm{B}}T}\right). \tag{3.5}$$

We first use the temperature-driven measurements at $V_{\mathrm{g}} = 0$ to determine the two device parameters α and T_{c} independently of the gate response. By simultaneously fitting Eqs. 3.1 and 3.2 to the relative frequency shift and internal losses [Fig. 3.1a)], we obtain $\alpha = 0.14$ and $T_{\mathrm{c}} = 1.31$ K, consistent with the device geometry and the properties of a 20-nm-thick Al film [137, 138]. We assume that the relevant kinetic-inductance contribution originates predominantly from the nanowire, as supported by the characterization of reference resonators without nanowires in Sec. 2.3.3. From the extracted α, and neglecting the nanowire's geometrical inductance, we estimate its kinetic inductance to be on the order of a few hundred pH, consistent with Ref. [139].

With α and T_{c} fixed, we then apply the model to the gate-driven measurements by introducing an effective temperature T_{eff}. This phenomenological parameter is commonly used to characterize nonequilibrium quasiparticle populations [136, 140–143]. For each gate voltage, we extract T_{eff} from the measured increase in internal losses using Eq. 3.2, and then use the resulting $T_{\mathrm{eff}}(V_{\mathrm{g}})$ in Eq. 3.1 to

predict the frequency shift. The prediction agrees well with the measured gate-dependent response without additional fitting parameters [Fig. 3.1b)].

The gate-induced changes in both kinetic inductance and dissipation can therefore be described consistently in terms of an effective quasiparticle temperature. Importantly, this agreement does not establish that the nanowire is in thermal equilibrium: T_{eff} is a parameter describing its effective microwave response, rather than a direct measurement of the quasiparticle energy distribution.

3.2 Device dynamics

Having characterized the steady-state gate response, we now investigate its dynamics using the two techniques introduced in Sec. 2.3.3. Square-pulse gate excitation allows us to extract the rising and falling characteristic times, τ_{R} and τ_{F}, from the time-domain response. Continuous gate modulation, on the other hand, produces sidebands from which we estimate a characteristic time τ_{sb}, assuming a first-order low-pass response.

In the time-domain measurements, we observe no appreciable difference between τ_{R} and τ_{F}. Both decrease with increasing DC gate voltage, from approximately 170 ns at $V_{\mathrm{g}} = 19$ V to 35 ns at $V_{\mathrm{g}} = 27$ V [Fig. 3.2a)]. To compare this behavior with the effective-temperature description, we repeat the measurement as a function of temperature at a fixed gate voltage $V_{\mathrm{g}} = 21$ V. The characteristic times remain approximately constant around 130 ns up to $T \simeq 500$ mK, before decreasing to approximately 50 ns at 800 mK [Fig. 3.2b)]. At this gate voltage, the effective temperature extracted from the steady-state measurements is $T_{\mathrm{eff}} \simeq 510$ mK, which is comparable with the onset in the temperature-driven time-response, $T \sim 500$ mK.

To investigate whether quasiparticle relaxation can account for these timescales, we compare the measurements with the expected quasiparticle recombination time [144],

$$\tau_{\mathrm{qp}} = \frac{\tau_0}{n_{\mathrm{qp}}} \frac{N_0 (k_{\mathrm{B}} T_{\mathrm{c}})^3}{2\Delta_0^2}, \tag{3.6}$$

where τ_0 is the material-dependent electron–phonon interaction time. For a thermal quasiparticle population, substituting Eq. 3.5 into Eq. 3.6 gives

$$\tau_{\mathrm{qp}} = \frac{\tau_0}{\sqrt{\pi}} \left(\frac{k_{\mathrm{B}} T_{\mathrm{c}}}{2\Delta_0} \right)^{5/2} \sqrt{\frac{T_{\mathrm{c}}}{T}} \exp\left(\frac{\Delta_0}{k_{\mathrm{B}} T} \right). \tag{3.7}$$

We convert the gate voltage into T_{eff} using the procedure of the previous section and compare the model with the average response time $(\tau_{\mathrm{R}} + \tau_{\mathrm{F}})/2$. For $\tau_0 = 30$ ns, the recombination time has the same order of magnitude and a similar temperature dependence as the measured response [Fig. 3.2c)]. This agreement is

qualitative, since the measured times characterize the resonator response and are not a direct measurement of the quasiparticle recombination time.

The value $\tau_0 = 30$ ns is smaller than the approximately 440 ns commonly reported for Al [121, 144, 145]. However, shorter times have been observed in Al films with increased impurity concentrations [146], and nonequilibrium quasiparticle or phonon populations may further modify the relaxation dynamics [144, 146, 147]. Moreover, although the InAs core is screened from the gate electric field, it could also provide an additional relaxation channel.

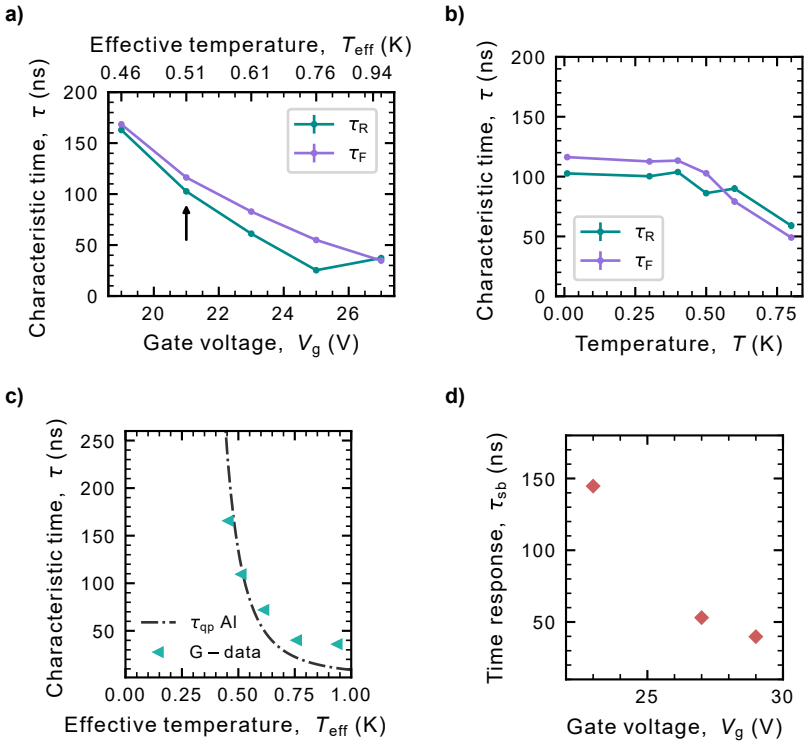


Figure 3.2: a) Rising (τ_R) and falling (τ_F) characteristic times as a function of gate voltage V_g, with the corresponding effective temperature T_{eff} on the top axis. The arrow indicates the working point used in panel b). **b)** Characteristic times as a function of temperature at $V_g = 21$ V. **c)** Average characteristic time $(\tau_R + \tau_F)/2$ as a function of effective temperature, compared with the expected quasiparticle recombination time (dash-dotted line) calculated for $\tau_0 = 30$ ns. **d)** Characteristic response time τ_{sb} extracted from the sideband 3-dB bandwidth as a function of gate voltage.

Finally, sideband spectroscopy provides an independent estimate of the gate-response timescale. We find that τ_{sb} decreases with increasing V_g [Fig. 3.2d)], consistently with the time-domain results. In particular, at $V_g = 27$ V, the measured 3-dB bandwidth of approximately 3 MHz corresponds to $\tau_{sb} \simeq 50$ ns.

In summary, we have investigated the gate response of a full-shell Al/InAs nanowire through its influence on the microwave properties of a superconducting

resonator. We demonstrated a gate-driven frequency tunability exceeding 90 MHz, accompanied by an approximately 85% decrease in the internal quality factor and an increase in the gate leakage current up to 4 nA. Similar behavior has been reported in TiN [21], Nb [20, 70], and V [62] gate-controlled Dayem bridges embedded in resonator structure.

The relation between the frequency shift and the increase in internal losses is well described by the Mattis–Bardeen model using an effective temperature, consistent with a gate-induced increase in the quasiparticle population. Similar descriptions were suggested in Refs. [20, 21], whereas Ref. [62] attributes the response to heating induced by electron field emission, described within the Fowler–Nordheim model.

The pulsed measurements reveal characteristic response times down to 35 ns, while sideband spectroscopy gives a comparable timescale of approximately 50 ns. These results are consistent with quasiparticle relaxation dynamics and comparable to the timescales reported for Nb Dayem bridges in Ref. [70]. Together with local voltage control, they suggest opportunities for RF switches and cryoelectronic applications [19]. However, the associated increase in losses and the possible influence of gate leakage on noise performance remain to be assessed for practical devices.

4 Coplanar stripline resonators for hybrid devices

Investigating ABSs in the microwave regime requires resonator structures that provide strong coupling to semiconducting weak links and allow electrostatic gate control. Magnetic-field resilience is an additional advantage, particularly for studying spin-dependent and topological phenomena. In PAPER II, we investigate NbTiN CPS resonators as a platform for these hybrid devices, focusing on their microwave losses and magnetic-field resilience. Here, we summarize the main results.

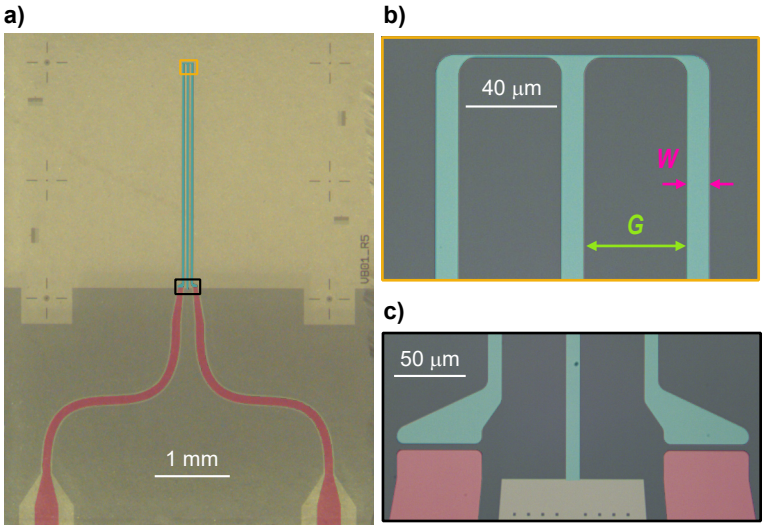


Figure 4.1: Optical micrographs of a representative differentially driven NbTiN CPS resonator. **a)** Overview of the resonator (cyan) and microwave feedlines (red). The colored boxes indicate the regions enlarged in panels b) and c). **b)** Short-circuited end of the CPS, showing the conductor width W and separation G. **c)** Capacitive coupling between the open end of the CPS and the feedlines, with a central DC grounding line.

We fabricate our $\lambda/4$ CPS resonators [Fig. 2.3a)–c) and for convenience Fig. 4.1] from thin NbTiN films, following the process described in Chapter 2. By varying the conductor width W and separation G, we obtain resonator impedances ranging from approximately 80 to 680 Ω. As discussed in Sec. 1.1, increasing the resonator impedance enhances its zero-point phase fluctuations and can therefore strengthen the coupling to the ABSs.

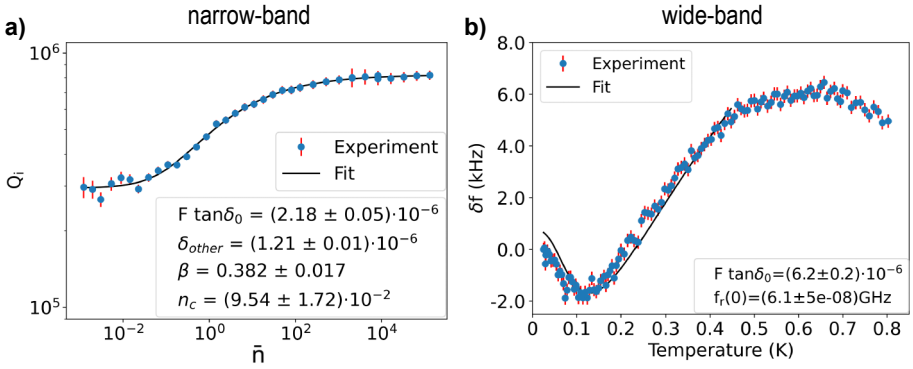


Figure 4.2: Representative microwave loss analysis for a NbTiN CPS resonator with $W = 2$ μm and $G = 2$ μm. **a)** Internal quality factor Q_i as a function of the average photon number $\bar{n}$, fitted using the narrow-band TLS model [Eq. 4.1]. **b)** Resonance frequency shift as a function of temperature, fitted using the wide-band TLS model [Eq. 4.2]. The extracted fit parameters are reported in each panel. Note the different notation between the main text and panel b), where $\delta f = \delta\omega/2\pi$ and $f_\mathrm{r}(0) = \omega_0/2\pi$. Adapted from PAPER II.

We characterize the resonator losses through two complementary measurements. First, we measure the internal quality factor Q_i as a function of the probing power, expressed in terms of the average photon number $\bar{n}$ [Fig. 4.2a)]. The increase in Q_i with $\bar{n}$ is characteristic of the saturation of dielectric two-level systems (TLSs) resonant with the microwave mode, which we refer to as narrow-band (nb) TLSs. At low temperatures, we describe this dependence using the following TLS saturation model [130, 148]:

$$\frac{1}{Q_\mathrm{i}} = \frac{(F\tan\delta_0)_\mathrm{nb}}{\left(1+\frac{\bar{n}}{n_\mathrm{c}}\right)^\beta} + \delta_\mathrm{other}, \tag{4.1}$$

where $(F\tan\delta_0)_\mathrm{nb}$ represents the effective narrow-band TLS loss contribution, n_c is the characteristic photon number for TLS saturation, and β describes the saturation behavior, which can be influenced by interactions between TLSs. Finally, δ_other accounts for additional loss channels.

Second, we measure the temperature-dependent resonance frequency shift, which probes the dispersive response of TLSs over a broader frequency range, referred to as wide-band (wb) TLSs [Fig. 4.2b)]. In this case the TLS model reads [28]:

$$\frac{\delta\omega(T)}{\omega_0} = \frac{(F\tan\delta_0)_\mathrm{wb}}{\pi}\left[\mathrm{Re}\,\Psi\left(\frac{1}{2}+\frac{\hbar\omega_0}{2\pi i k_\mathrm{B}T}\right) - \ln\left(\frac{\hbar\omega_0}{2\pi k_\mathrm{B}T}\right)\right], \tag{4.2}$$

where Ψ is the digamma function, $(F\tan\delta_0)_\mathrm{wb}$ represents the effective wide-band TLS contribution, and $\delta\omega(T) = \omega_\mathrm{r}(T) - \omega_0$ denotes the resonance frequency shift relative to the zero-temperature value $\omega_0 = \omega_\mathrm{r}(0)$. For comparison with the

experimental data, we reference both the measured and modeled frequency shifts to $T_0 = 10$ mK, treating ω_0 as a fitting parameter.

The observed power dependence and non-monotonic temperature response indicate a significant contribution from dielectric TLSs to the resonator losses at zero magnetic field. Across the devices studied in PAPER II, we extract effective narrow-band TLS loss contributions on the order of 10^{-6} and wide-band contributions on the order of 10^{-6}–10^{-5}. Both contributions generally decrease with increasing conductor width W and separation G, consistent with a reduced electric-field participation of lossy interfaces. Together with the measured internal quality factors reaching nearly 10^6 in the single-photon regime, these results demonstrate that CPS resonators can combine relatively high impedance with low microwave losses.

Another important requirement for hybrid devices is compatibility with magnetic fields, which may be needed to lift the spin degeneracy of ABSs or access topological regimes. Compared with Al, NbTiN has a higher critical temperature and upper critical field, making it a suitable material for this purpose. The CPS geometry also avoids the large coplanar ground planes of conventional CPW resonators, which can host vortices and contribute to microwave dissipation under magnetic field, as illustrated by magneto-optical imaging experiments on NbTiN resonators [149].

We assess the magnetic-field response by measuring the relative resonance frequency shift and internal quality factor under in-plane [Fig. 4.3a)] and out-of-plane [Fig. 4.3b)] fields. We compare two resonators with the same conductor separation $G = 2$ μm and different widths, $W = 0.25$ μm and $W = 1$ μm. For in-plane fields, both devices exhibit a similar response, with the magnitude of the relative frequency shift remaining below approximately 3×10^{-4} up to 1 T, while Q_i remains on the order of 10^5. In contrast, out-of-plane fields produce a substantially stronger response, which depends on the conductor width. For the $W = 1$ μm device, the relative frequency shift reaches approximately 5% around 60 mT, accompanied by a reduction in Q_i of more than two orders of magnitude. The narrower device exhibits a weaker frequency shift and maintains a higher Q_i over a wider magnetic-field range. In both orientations, the frequency shift is approximately quadratic in field,

$$\frac{\delta\omega_\mathrm{r}}{\omega_\mathrm{r}} = -k_{\parallel(\perp)} B^2_{\parallel(\perp)} \tag{4.3}$$

with the stronger out-of-plane response consistent with orbital depairing across the conductor width rather than the film thickness.

Besides magnetic-field compatibility, CPS resonators offer practical advantages for integrating hybrid devices. The absence of a coplanar ground plane facilitates the patterning of multiple electrostatic gates without interrupting the resonator

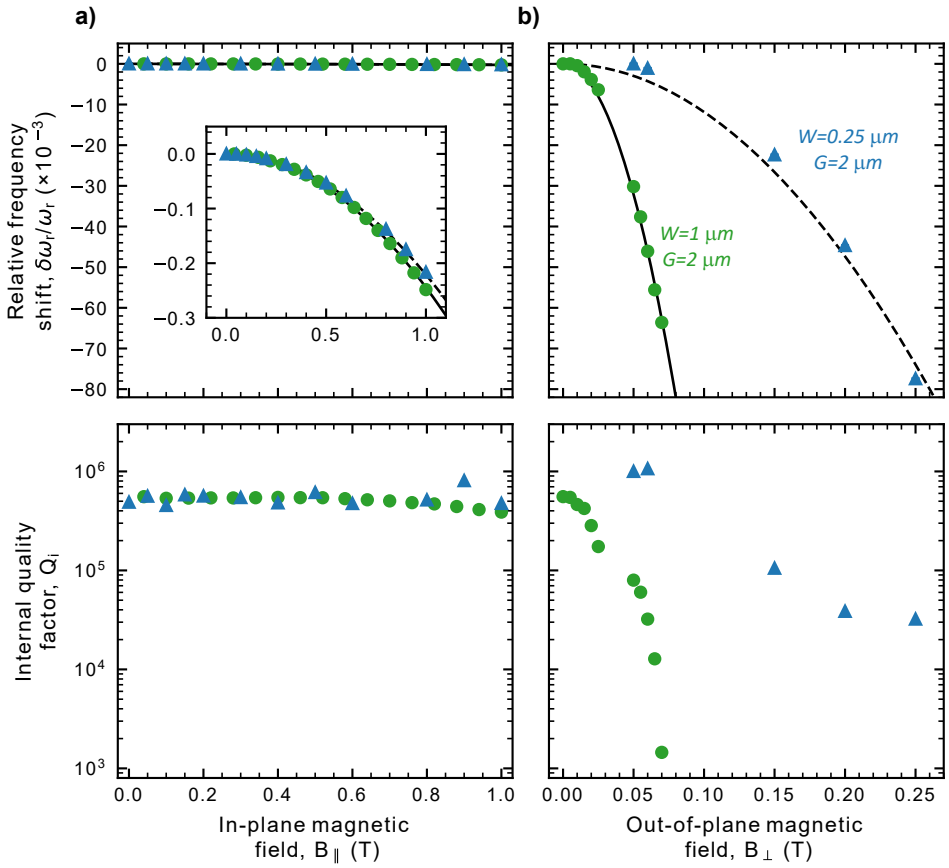


Figure 4.3: Magnetic-field response of NbTiN CPS resonators under **a)** in-plane and **b)** out-of-plane magnetic fields, for conductor widths $W = 0.25$ μm (blue triangles) and $W = 1$ μm (green circles), both with $G = 2$ μm. *Upper panels*: Relative resonance frequency shift $\delta\omega_r/\omega_r$, with solid and dashed lines representing quadratic fits to the data. The inset in panel a) shows the same data on a magnified vertical scale. *Lower panels*: Corresponding internal quality factor Q_i.

current paths[1]. Moreover, in the odd mode, the differential excitation creates a virtual ground along the symmetry line (Sec. 1.1). This allows a physical grounding line to be placed along this line without significantly perturbing the resonator mode, providing a DC ground reference for the nanowire circuit. When a weak link is embedded in a superconducting loop sharing part of the resonator inductance, the differential mode couples to its phase-dependent supercurrent. In principle, this configuration probes only the diagonal current component of the weak-link susceptibility matrix, which should facilitate the resolution of spin-dependent ABS responses [96].

[1] In our devices, we designed the gate and flux lines as CPWs to preserve the possibility of applying microwave excitation directly to the weak links, while facilitating impedance matching to the 50 Ω measurement environment. However, since microwave excitation can also be applied through the resonator, these control lines could, in principle, be designed exclusively for DC operation, further simplifying the layout.

The differential resonator concept investigated in PAPER II was subsequently used in the compact lumped-element design of PAPER III and in the CPS-based device of PAPER IV. These implementations provided the microwave platform for the ABS spectroscopy and nonlinear measurements discussed in the following chapters.

5 Probing Andreev bound states

In this chapter, we investigate the interaction between ABSs and superconducting microwave resonators, building on the devices and measurement techniques introduced in the previous chapters. We first discuss the gate- and phase-dependent resonator response measured in PAPER IV, before presenting the high-impedance devices developed in PAPER III to enhance the ABS–resonator coupling.

5.1 From adiabatic to dispersive readout of ABS

Following the framework introduced by S. Park et al. in *From Adiabatic to Dispersive Readout of Quantum Circuits* [91], we investigate how the ABS–resonator interaction evolves with gate voltage and superconducting phase (Sec. 1.4). We consider the single-junction configuration of PAPER IV, with JJ_1 active and JJ_2 pinched off [Sec. 2.3.4 and Fig. 2.22a)-b)]. These measurements were performed in Embla (Sec. 2.2.2).

We consider Datasets I, II, and III, measured at $V_1 = 0.35$, 2.2, and 1.25 V, respectively. Two-tone spectroscopy reveals features around $\varphi_1 = \pi$ that move towards lower drive frequencies from Dataset I to III [Fig. 5.1]. In Dataset III, the transition reaches the resonator frequency near 6.76 GHz, although the avoided crossing is not resolved in the two-tone spectrum. Within the accessible frequency range, these features are consistent with ABS pair transitions described by the effective short-junction relation in Eq. 1.24, with increasing effective transparency from Dataset I to III.

The corresponding single-tone spectroscopy shows an increasingly pronounced resonator frequency shift $\delta\omega_r$ from Dataset I to II, followed by an avoided-crossing-like response in Dataset III [Fig. 5.2]. To describe this evolution, we compare the measurements with effective single- and two-channel ABS models.

Single-channel model. We first fit the single-channel model introduced in Sec. 1.4 [Eqs. 1.19, 1.22, and 1.23] to the measured frequency shift. We initialize the effective gap Δ_{eff} and transparency τ using the two-tone spectroscopy, and the coupling parameter λ using its geometrical estimate of approximately 0.028. As discussed in Sec. 1.4, the effective short-junction description is best justified near $\varphi_1 = \pi$, where Δ_{eff} is given by Eq. 1.25. We extend it phenomenologically over the full phase range, using Δ_{eff} to account for finite-length effects and, potentially, corrections associated with the superconducting leads and Coulomb interactions

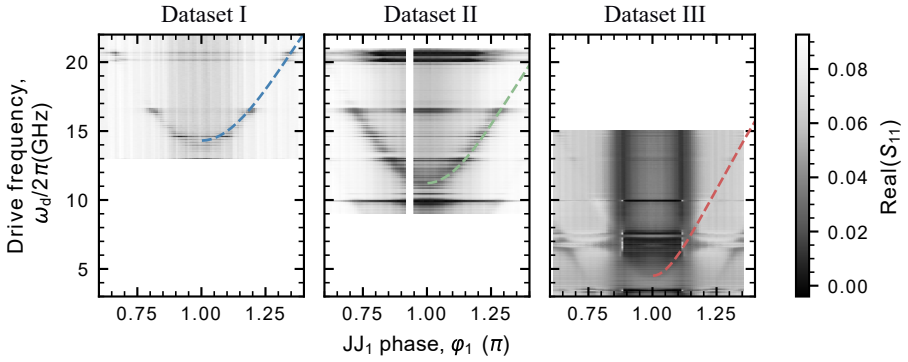


Figure 5.1: Two-tone spectroscopy of JJ_1 for Datasets I, II, and III, measured around $\varphi_1 = \pi$. The dashed lines represent the effective single-ABS pair-transition frequency, $\hbar\omega_{\mathrm{ABS}} = 2\Delta_{\mathrm{eff}}\sqrt{1 - \tau\sin^2(\varphi_1/2)}$, calculated using $\tau = (0.8, 0.86, 0.97)$ and $\Delta_{\mathrm{eff}}/h = (16, 15, 13)$ GHz for Datasets I, II, and III, respectively.

[96, 150, 151]. Likewise, τ describes an effective junction transparency rather than an independently identified channel. Although λ is determined in principle by the resonator geometry, we allow it to vary between datasets to account for limitations of the model. The fitted values remain close to the geometrical estimate. This approach describes Datasets I and II well, but reproduces Dataset III only qualitatively [solid lines in Fig. 5.2]. Extracted parameters are reported in Table 5.1.

Table 5.1: Single-channel model. Effective ABS parameters extracted from the single-channel fits (Eq. 1.22) to JJ_1 (solid lines in Fig. 5.2).

Dataset	Δ_{eff}/h (GHz)	τ	λ
I	16	0.739	0.032
II	15	0.809	0.035
III	9	0.925	0.035

Two-channel model. To describe Dataset III, we extend the model to two independent effective channels, each characterized by a transparency τ_m and an effective gap $\Delta_{\mathrm{eff},m}$[1]. Following Metzger et al. [22], such an extension can also phenomenologically capture contributions from unresolved higher-energy ABSs.

[1] This description differs from that reported in the current version of PAPER IV, where a common effective gap was assumed for both channels. However, we realized that the effective gap phenomenologically accounts for channel-dependent properties, and removed the common-gap constraint here. This modification does not affect the main results or conclusions of PAPER IV or this thesis.

The combined ground-state potential is

$$\varepsilon_{\mathrm{2ABS}}(\varphi) = -\sum_{m=1}^{2} \Delta_{\mathrm{eff},m} \sqrt{1 - \tau_m \sin^2\left(\frac{\varphi}{2}\right)}. \tag{5.1}$$

Neglecting interactions between the channels, the induced resonator frequency shift becomes

$$\delta\omega_{\mathrm{r}}^{(2)}(\varphi) = \sum_{m=1}^{2} \delta\omega_{\mathrm{r}}^{(m)}(\varphi), \tag{5.2}$$

where the contributions are calculated using Eqs. 1.22 and 1.23, with channel-dependent τ_m and $\Delta_{\mathrm{eff},m}$ and a common λ. We fix τ_1 and $\Delta_{\mathrm{eff},1}$ to the estimates from two-tone spectroscopy, and fit τ_2, $\Delta_{\mathrm{eff},2}$, and λ. The second channel produces little change for Datasets I and II, but substantially improves the agreement for Dataset III [dashed lines in Fig. 5.2].

The fitted parameters are summarized in Table 5.2. The effective gaps remain below the aluminum gap, consistent with reduced values reported for other Al/InAs weak links [22, 84]. These results provide the junction parameters used to analyze the nonlinear response in Chapter 6.

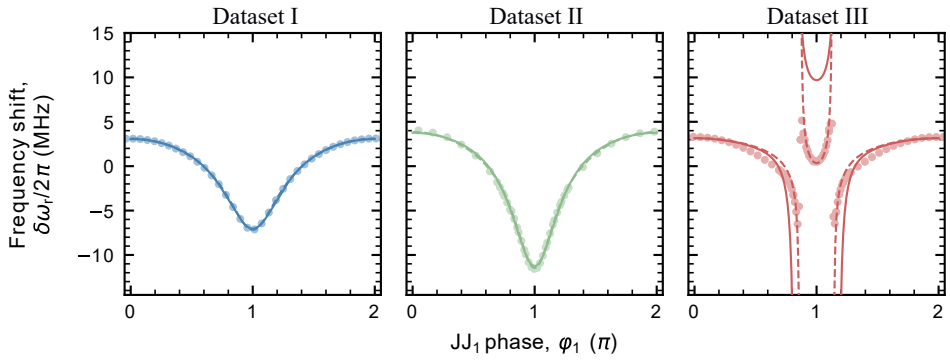


Figure 5.2: Single-tone spectroscopy of JJ_1 for Datasets I, II, and III (left to right), showing the phase-dependent resonator frequency shift relative to its bare value. Solid and dashed curves are the one-channel and two-channel effective ABS models, respectively.

Table 5.2: Two-channel model. Effective ABS parameters extracted from the two-channel fits (Eq. 5.2) to JJ_1 (dashed lines in Fig. 5.2).

Dataset	$\Delta_{\mathrm{eff},1}/h$ (GHz)	τ_1	$\Delta_{\mathrm{eff},2}/h$ (GHz)	τ_2	λ
I	16	0.8	17	0.39	0.025
II	15	0.86	25	0.40	0.027
III	13	0.97	20	0.85	0.020

5.2 Approaching the ultrastrong-coupling regime between an ABS and a microwave resonator

The measurements discussed above yield ABS–resonator coupling strengths of the order of $g_c/2\pi \sim 100$ MHz near $\varphi = \pi$ [Eq. 1.23]. As discussed in Sec. 1.4, increasing the resonator impedance enhances the zero-point phase fluctuations across the shared inductance and, consequently, the coupling strength. Larger coupling facilitates the resolution of ABS transitions and may enable faster resonator-mediated operations. When g_c becomes a significant fraction of the bare resonator frequency, conventionally $g_c/\omega_r \gtrsim 0.1$, the system approaches the ultrastrong-coupling regime. This regime is of interest for fast quantum gates [152], quantum metrology [153], and quantum memories [154].

To explore stronger coupling, PAPER III investigates three devices, labeled Devices 1, 2, and 3, that combine Al/InAs weak links with our high-impedance NbTiN lumped-element resonators. Their weak-link lengths range from 250 to 450 nm, while their differential resonator impedances all exceed 12 kΩ, compared with approximately 290 Ω in PAPER IV. Their main parameters are summarized in Table 5.3.

Table 5.3: Parameters of the three devices investigated in PAPER III. The differential resonator impedance Z_r, coupling parameter $\lambda_{(sim)}$, and weak-link length l_{wl} are estimated from the device geometry and resonator characterization. The effective gap Δ_{eff} and transparency τ are extracted from two-tone spectroscopy, while $\lambda_{(fit)}$ is obtained from single-tone spectroscopy. The maximum coupling $g_c(\pi)$ is calculated from the fitted parameters. To remain consistent with Chapter 1 and PAPER IV, we use the dimensionless coupling parameter $\lambda = 2\pi p\Phi_{zpf}/\Phi_0$ rather than the flux amplitude $p\Phi_{zpf}$ reported in PAPER III.

Device	Z_r (kΩ)	$\lambda_{(sim)}$	l_{wl} (nm)	Δ_{eff}/h (GHz)	τ	$\lambda_{(fit)}$	$g_c(\pi)/2\pi$ (GHz)
1	12.28	0.100	250	25.20	0.99942	0.155	1.95
2	12.76	0.132	320	11.69	0.95690	0.177	0.97
3	13.27	0.094	450	–	–	–	–

Pair transitions

In Device 2, two-tone spectroscopy reveals an ABS pair transition crossing the bare resonator frequency $\omega_r^0/2\pi = 8.619$ GHz [Fig. 5.3a)-c)]. The resulting avoided crossings yield a directly measured coupling of $g_c/2\pi \approx 490$ MHz. The corresponding single-tone spectrum also resolves the hybridized modes, with a splitting of approximately $2g_c/2\pi = 980$ MHz at the crossing [Fig. 5.3b)]. No additional

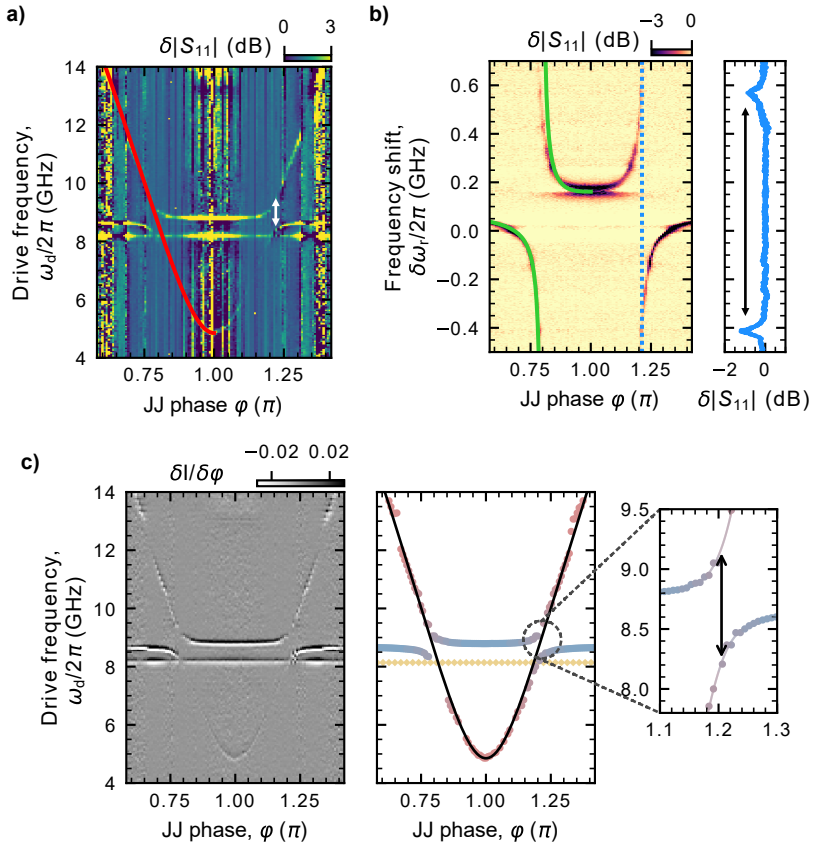


Figure 5.3: Pair-transition spectroscopy of Device 2. **a)** Two-tone spectrum showing the ABS pair transition and its avoided crossings with the resonator mode. The red line represents the effective short-junction transition frequency, $\hbar\omega_{\mathrm{ABS}} = 2\Delta_{\mathrm{eff}}\sqrt{1-\tau\sin^2(\varphi/2)}$, with $\Delta_{\mathrm{eff}}/h = 11.69 \pm 0.03$ GHz and $\tau = 0.9569 \pm 0.0005$. The white double arrow indicates the splitting at one avoided crossing, corresponding to $g_c/2\pi \approx 490$ MHz. **b)** Corresponding single-tone spectroscopy, with the green line representing the fitted resonator frequency shift with $\lambda = 0.177 \pm 0.001$. The right panel shows a vertical line cut at the phase indicated by the blue dashed line, resolving a frequency splitting of approximately $2g_c/2\pi = 980$ MHz, highlighted by the double arrow. **c)** Alternative representation of the two-tone data in panel a). *Left*: Phase derivative of the measured response, highlighting the spectroscopic features. *Center*: Extracted transition frequencies, distinguishing the predominantly ABS-like (red) and resonator-like (blue) branches. The black line represents the effective short-junction fit to the ABS transition, while the yellow data correspond to the resonator even mode, which does not appreciably couple to the ABS. *Right*: Magnified view of one avoided crossing, with the splitting $2g_c/2\pi$ indicated by the double arrow.

transitions are resolved up to a drive frequency of 21 GHz, supporting an effective single-ABS description within the accessible range.

We first fit the effective short-junction model to the pair-transition dispersion, obtaining $\Delta_{\mathrm{eff}}/h = 11.69$ GHz and $\tau = 0.9569$. Keeping these values fixed, we fit Eq. 1.22 to the single-tone frequency shift using λ as the only free parameter

[Fig. 5.3b)]. The model reproduces the observed splitting and predicts a maximum coupling of $g_c/2\pi = 968$ MHz at $\varphi = \pi$ [Eq. 1.23], approximately 11% of the resonator frequency.

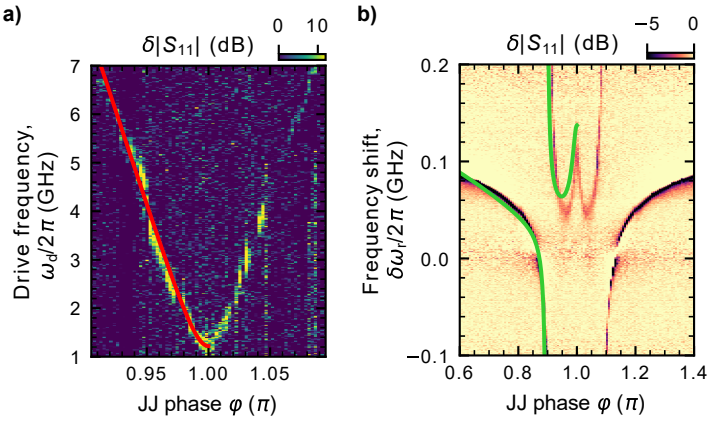


Figure 5.4: Pair-transition spectroscopy of Device 1. **a)** Two-tone spectrum showing the ABS pair transition around $\varphi = \pi$. The red line represents the effective short-junction transition frequency, $\hbar\omega_{\mathrm{ABS}} = 2\Delta_{\mathrm{eff}}\sqrt{1 - \tau\sin^2(\varphi/2)}$, with $\Delta_{\mathrm{eff}}/h = 25.2 \pm 0.2$ GHz and $\tau = 0.99942 \pm 0.00006$. **b)** Corresponding single-tone spectroscopy, showing a sharp feature around $\varphi = \pi$ associated with the highly transparent ABS. The green line represents the fitted resonator frequency shift with $\lambda = 0.155 \pm 0.001$.

In Device 1, no avoided-crossing splitting is directly resolved. We therefore apply the same fitting procedure, extracting $\Delta_{\mathrm{eff}}/h = 25.2$ GHz and $\tau = 0.99942$ from the two-tone spectrum, followed by λ from the single-tone response [Fig. 5.4]. Equation 1.23 then gives an estimated maximum coupling of $g_c/2\pi \approx 1.95$ GHz, approximately 24% of the resonator frequency. At this coupling strength, however, the perturbative treatment is no longer quantitatively reliable. The value should therefore be considered a model-dependent estimate rather than a direct measurement.

Single-quasiparticle transitions with spin-orbit splitting

Besides pair transitions, we observe single-quasiparticle transitions (SQPTs) in Devices 2 and 3, whose longer weak links support multiple spin-orbit-split ABSs. We identify three bundles of spectroscopic lines: bundle A in Device 3 [Fig. 5.5a)] and bundles B and C in Device 2 [Fig. 5.5b)]. Their phase dependence is consistent with transitions between neighboring ABS doublets, which we describe using the finite-length junction model introduced in Sec. 1.4.

We fit Eq. 1.12 with $\Delta/h = 52$ GHz fixed, taking $\Lambda_{1,2}$, x_r, and τ as fitting parameters. Bundle A is described by spin-conserving transitions between the two lowest ABS doublets [$1\uparrow(\downarrow) \rightarrow 2\uparrow(\downarrow)$]. Bundles B and C have an overall upward curvature, consistent with spin-conserving transitions between the second and

third doublets [$2\uparrow(\downarrow) \rightarrow 3\uparrow(\downarrow)$]. We attribute B and C to contributions coming from two independent conduction channels. The fitted parameters are reported in Table 5.4. No spin-flipping transitions are resolved in these measurements.

Although we did not perform time-resolved parity measurements, the SQPT spectra also allow us to estimate the spin-photon coupling through the dispersive resonator shift. Within second-order perturbation theory, the shift $\delta\omega_{\mathrm{r}}^{\mathrm{SQPT}}$ induced by an SQPT is given by [83]:

$$\delta\omega_{\mathrm{r}}^{\mathrm{SQPT}} \approx g_{\mathrm{c}}^2 \frac{2\omega_{\mathrm{SQPT}}}{\omega_{\mathrm{SQPT}}^2 - (\omega_{\mathrm{r}}^0)^2}, \tag{5.3}$$

where ω_{SQPT} is the transition frequency, $\omega_{\mathrm{r}}^0/2\pi = 8.619$ GHz is the bare resonator frequency, and g_{c} is the spin-photon coupling rate. We consider the minimum of the lower SQPT in Device 2 [pink arrow in Fig. 5.5b)], where the driven transition produces a phase shift of approximately 10° in the reflected signal [Fig. 5.5c)]. Using the undriven resonator response to convert this phase shift into a frequency shift [Fig. 5.5d)], we obtain $\delta\omega_{\mathrm{r}}^{\mathrm{SQPT}}/2\pi \approx 770$ kHz. Equation 5.3 then gives $g_{\mathrm{c}}/2\pi \approx 77$ MHz, comparable to values reported in similar systems [83, 155].

Table 5.4: Parameters obtained by fitting the SQPT bundles with Eq. 1.12. Adapted from PAPER III.

	A	B	C
Λ_1	5.7 ± 0.3	2.44 ± 0.07	2.8 ± 0.1
Λ_2	1.5 ± 0.3	3.06 ± 0.09	3.2 ± 0.1
τ	0.35 ± 0.04	0.243 ± 0.009	0.265 ± 0.006
x_{r}	0.489 ± 0.005	0.2615 ± 0.0001	-0.000837

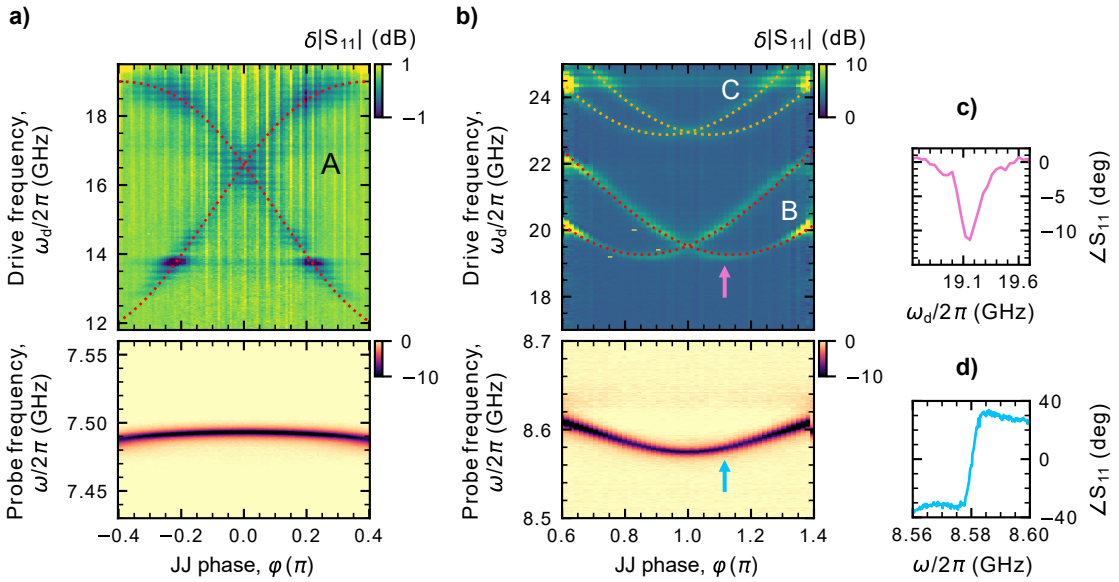


Figure 5.5: Single-quasiparticle spectroscopy of **a)** Device 3 and **b)** Device 2, showing two-tone (top) and corresponding single-tone (bottom) spectra. Three SQPT bundles, labeled A, B, and C, are identified in the two-tone spectra. The dotted lines represent fits of the spin-conserving transitions using Eq. 1.12, with parameters reported in Table 5.4. The pink and blue arrows in panel b) indicate the phase bias considered in panels c) and d), respectively. **c)** Phase shift induced by the single-quasiparticle transition at the phase bias indicated by the pink arrow in panel b). **d)** Corresponding resonator phase measured without the drive tone [see blue arrow in panel b)], used to convert the phase shift in panel c) into the induced resonator frequency shift $\delta\omega_r^{\mathrm{SQPT}}$.

6 Andreev bound state-induced nonlinearities in superconducting resonators

In this chapter, we investigate the nonlinear response of the resonator incorporating two Al/InAs Josephson weak links, as reported in PAPER IV.

6.1 Single-junction configuration

We begin with Datasets I, II, and III in the single-junction configuration, with JJ_1 active and JJ_2 pinched off. Their ABS spectroscopy and resonator frequency shifts are discussed in Chapter 5; here, we examine the corresponding Kerr and cubic nonlinearities.

We extract the Kerr nonlinearity K and cubic nonlinearity g_3 using the procedures described in Sec. 2.3.5. The Kerr response follows a trend approximately opposite to that of the resonator frequency shift [Fig. 6.1a)-b)]. In Datasets I and II, K is weakly negative around $\varphi_1 = 0$ and 2π, and reaches a positive maximum near $\varphi_1 = \pi$. The modulation becomes stronger from Dataset I to II. In Dataset III, the Kerr response instead develops a discontinuous pattern associated with the avoided-crossing-like feature of the frequency shift.

By contrast, $|g_3|$ exhibits two approximately symmetric peaks around $\varphi_1 = \pi$, whose positions and amplitudes depend on the gate voltage [Fig. 6.1c)]. No parametric gain is observed sufficiently close to $\varphi_1 = \pi$, preventing a reliable extraction of $|g_3|$ in that region. The range without measurable gain widens from Dataset I to III. We attribute this trend to the combined effects of stronger Kerr nonlinearity and reduced internal quality factor.

Of particular interest are operating points where K crosses zero while $|g_3|$ remains finite. For Datasets I and II, the zero crossings occur near $\varphi_1 = 0.8\pi$ and 1.2π, where $|g_3|/2\pi$ reaches approximately 35 and 70 kHz, respectively. These points are suitable for three-wave mixing with suppressed Kerr effects.

To interpret these measurements, we use the effective single- and two-channel ABS models developed in Chapter 5. The parameters are fixed to those extracted from two-tone spectroscopy and the resonator frequency shift (Tables 5.1 and 5.2); no additional fitting parameters are introduced for the nonlinear response.

For a single channel, we apply Eqs. 1.35 and 1.33 from Sec. 1.5 [solid lines in Fig. 6.1b)-c)].

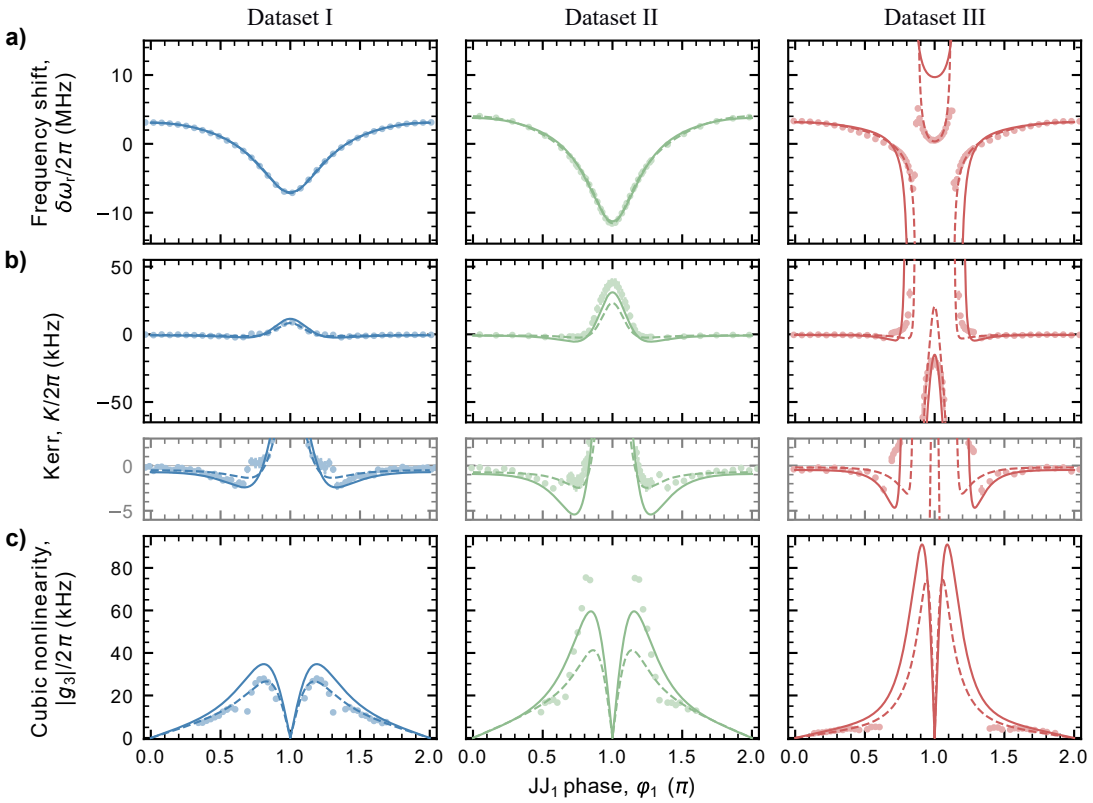


Figure 6.1: Linear and nonlinear response in the single-junction configuration for Datasets I, II, and III. **a)** Resonator frequency shift $\delta\omega_r$ as a function of the superconducting phase difference φ_1. **b)** Kerr nonlinearity K, with an enlarged view around $K = 0$ in the lower panels. **c)** Cubic nonlinearity $|g_3|$ extracted from parametric gain measurements. Experimental data are shown as points, while solid and dashed lines represent the single- and two-channel ABS models, respectively, calculated using the parameters reported in Tables 5.1 and 5.2.

For two independent effective channels, on the other hand, we generalize these equations to

$$\hbar g_3 = \frac{\lambda^3}{6}\tilde{c}_3, \tag{6.1}$$

and

$$\hbar K = \frac{\lambda^4}{2}\left(\tilde{c}_4 - \frac{5\tilde{c}_3^2}{3\tilde{c}_2}\right) + \hbar\sum_{m=1}^{2}\frac{g_{c,m}^4}{\delta_{-,m}^3}, \tag{6.2}$$

where $\tilde{c}_n$ denotes the nth derivative of the total loop potential,

$$U_{\mathrm{loop}}(\varphi) = \left(\frac{\Phi_0}{2\pi}\right)^2 \frac{(\varphi - \varphi_{\mathrm{ext}})^2}{2L_{\mathrm{s}}} + \varepsilon_{\mathrm{2ABS}}(\varphi), \qquad \tilde{c}_n = \left.\frac{\partial^n U_{\mathrm{loop}}}{\partial \varphi^n}\right|_{\varphi_{\mathrm{min}}}, \tag{6.3}$$

with $\varepsilon_{\mathrm{2ABS}}$ defined in Eq. 5.1 and L_{s} approximating the loop inductance, as in Sec. 1.5. The quantities $g_{c,m}$ and $\delta_{-,m}$ are the coupling strength and detuning of the mth effective ABS pair.

Both models capture the main qualitative trends, but their agreement deteriorates from Dataset I to III [Fig. 6.1]. Unlike the frequency-shift analysis, where a second channel is especially useful for Dataset III, its effect on the nonlinearities is less systematic. For Datasets I and II, including the second channel reduces the predicted peaks of both K and $|g_3|$, improving the agreement for Dataset I but worsening it for Dataset II. For Dataset III, the two-channel model improves the description of the lateral Kerr branches, but overestimates the central branch and predicts positive values around $\varphi_1 = \pi$ that are not observed. It also reduces the predicted $|g_3|$ peaks, although the limited gain data prevent a clear comparison. These discrepancies highlight the limitations of the phenomenological model, which neglects terms arising from a full higher-order expansion of the coupled ABS–resonator Hamiltonian. Such terms could become more relevant for the nonlinear response than for the linear frequency shift.

In the complementary single-junction configuration, with JJ_1 pinched off and JJ_2 active, we obtain qualitatively similar results (Datasets IV, V, and VI; see the Supplementary Material of PAPER IV). Here, in addition, Dataset VII[1] [Fig. 6.2] demonstrates that the four Kerr zero crossings predicted by the model for Dataset III are not merely an artifact of our approximation, but can also be observed experimentally. Two-tone spectroscopy reveals an ABS-like transition with a minimum frequency below 4 GHz, consistent with an effective single-channel model with $\Delta_{\mathrm{eff}}/h = 12$ GHz and $\tau = 0.98$ [Fig. 6.2a)], whereas, even in this case, a two-channel model reproduces the measured frequency shift [Fig. 6.2b) and Table 6.1]. Notably, the measured Kerr nonlinearity exhibits four zero crossings, returning to positive values around $\varphi_2 = \pi$ [Fig. 6.2c)]. However, similarly to Dataset III, the model overestimates the magnitude of the Kerr nonlinearity in this region. No cubic nonlinearity data were acquired for this dataset.

Junction	Dataset	$\Delta_{\mathrm{eff},1}/h$ (GHz)	$\Delta_{\mathrm{eff},2}/h$ (GHz)	τ_1	τ_2	λ
JJ_2	VII	12	35	0.98	0.85	0.018

Table 6.1: Effective two-channel parameters describing the frequency shift and Kerr nonlinearity in Dataset VII [Fig. 6.2].

[1] Note that this dataset is not included in PAPER IV.

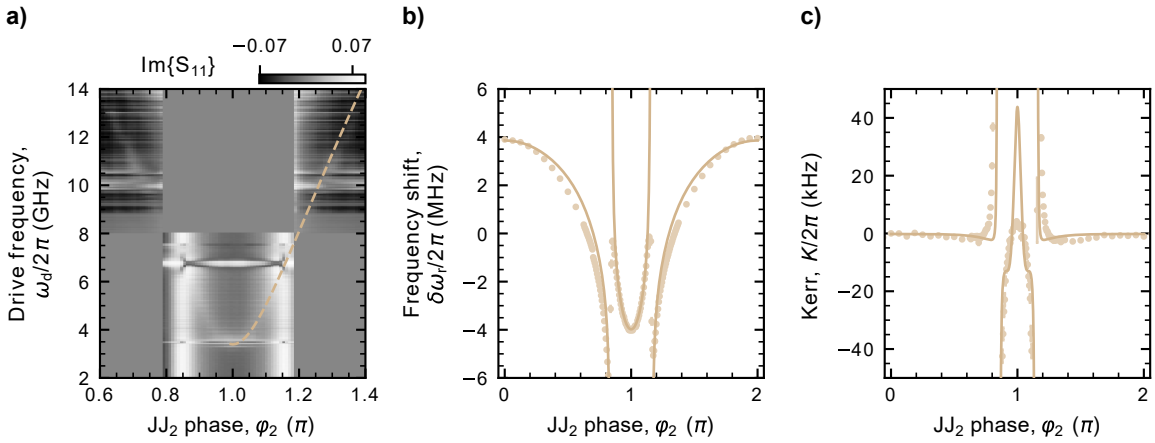


Figure 6.2: Dataset VII, with JJ_2 active and JJ_1 pinched off. **a)** Two-tone spectroscopy as a function of φ_2. The dashed line represents the effective short-junction ABS transition with $\Delta_{\text{eff}}/h = 12$ GHz and $\tau = 0.98$. **b)** Resonator frequency shift $\delta\omega_r$. **c)** Kerr nonlinearity K, exhibiting four zero crossings within one phase period. Solid lines in b)-c) show the corresponding two-channel effective-model predictions with parameters reported in Table 6.1.

6.2 Double-junction configuration

We now investigate the configuration in which both JJ_1 and JJ_2 are active, allowing us to control the resonator nonlinearities through two independent superconducting phase differences, φ_1 and φ_2. We measure K and $|g_3|$ by sweeping the phase across one junction while keeping the other at a fixed bias [Fig. 6.3].

We first characterize $K(\varphi_1)$ and $|g_3(\varphi_1)|$ with $\varphi_2 = 0$ [Fig. 6.3a),c)], identifying suitable φ_1 biases to highlight the interplay between the junctions (colored arrows in the panels). In particular, changing φ_1 from 0 to π introduces an approximately constant offset of -70 kHz in the Kerr nonlinearity measured as a function of φ_2 [Fig. 6.3b)]. Similarly, biasing JJ_1 near either of the two maxima of $|g_3(\varphi_1)|$, at $\varphi_1 = 0.77\pi$ and 1.23π, modifies the amplitude and symmetry of $|g_3(\varphi_2)|$ [Fig. 6.3d)].

We note that, when either junction is biased at zero phase, the nonlinear response follows a trend similar to that observed in the single-junction configuration, allowing us to characterize the individual contributions. We describe these measurements using the effective single-channel short-junction model [gray lines in Fig. 6.3a),c) and salmon lines in Fig. 6.3b),d)], with the parameters reported in Table 6.2.

Neglecting interactions between the two junctions and corrections associated with the loop inductances, we then approximate the total nonlinearities as the sum of the individual contributions,

$$K_{\text{tot}} \simeq K_1(\varphi_1) + K_2(\varphi_2), \qquad g_{3,\text{tot}} \simeq g_{3,1}(\varphi_1) + g_{3,2}(\varphi_2). \tag{6.4}$$

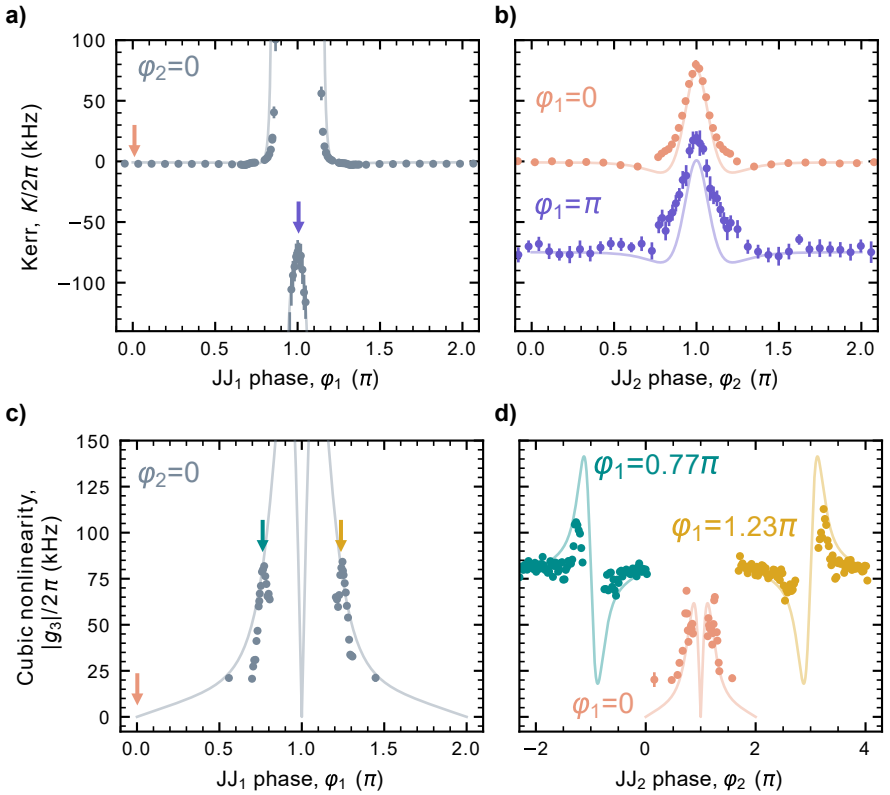


Figure 6.3: Nonlinear response in the double-junction configuration. **a)** Kerr nonlinearity K as a function of φ_1, with $\varphi_2 = 0$. **b)** Kerr nonlinearity versus φ_2, for $\varphi_1 = 0$ and π. Panels a) and b) are measured at $V_1 = 1.58$ V and $V_2 = 1.94$ V. **c)** Cubic nonlinearity $|g_3|$ as a function of φ_1, with $\varphi_2 = 0$. **d)** Cubic nonlinearity versus φ_2, for $\varphi_1 = 0$, 0.77π, and 1.23π. Panels c) and d) are measured at $V_1 = -0.05$ V and $V_2 = 1.15$ V. The three datasets in panel d) are displayed over successive phase periods for clarity. Experimental data are shown as points, while solid lines represent the sum of the individual junction contributions calculated using the effective single-channel short-junction ABS model [Eq. 6.4]. Colored arrows in a) and c) highlight the φ_1 biases used in b) and d).

Dataset	Junction	Δ_{eff}/h (GHz)	τ	λ
K	JJ_1	16	0.88	0.033
	JJ_2	10	0.92	0.023
g_3	JJ_1	17	0.87	0.030
	JJ_2	15	0.93	0.038

Table 6.2: Parameters used to describe the Kerr and cubic nonlinearities in the double-junction configuration [Fig. 6.3], within the effective single-channel short-junction model.

This approximation reproduces the main features of the measured response [solid lines in Fig. 6.3], indicating that the nonlinear contributions of the two

junctions can be treated as approximately independent. The double-junction configuration therefore provides additional flexibility in controlling the resonator nonlinearities. In particular, the contribution of one junction can compensate the Kerr nonlinearity of the other, shifting the operating point where $K_{\mathrm{tot}} \approx 0$. Furthermore, combining the cubic contributions allows us to maintain a sizable $|g_{3,\mathrm{tot}}|$ over a broader range of phase biases.

6.2.1 Three-wave mixing amplification

We also characterize the parametric amplification enabled by the cubic nonlinearity in the double-junction configuration. We select gate voltages $V_1 = 0.25$ V and $V_2 = 0.5$ V, and phase biases $\varphi_1 \approx 0.8\pi$ and $\varphi_2 \approx 0.75\pi$, to obtain a small Kerr nonlinearity while maintaining a sizable g_3. By sweeping the pump power and detuning $\delta_p = \omega_p - 2\omega_r$, we observe a maximum in the on-off gain close to the three-wave-mixing condition $\omega_p = 2\omega_r$ [Fig. 6.4a)]. The gain decreases rapidly as the pump is detuned from this condition, consistently with three-wave mixing parametric amplification.

We select a working point corresponding to optimum pump detuning and power [red star in Fig. 6.4a)] and characterize the amplifier dynamic range by increasing the probe power. We observe a progressive reduction in the peak gain (extracted as described in Sec. 2.3.5), with an estimated 1-dB compression point of -138 dBm [Fig. 6.4b)].

We then characterize the on-off gain and signal-to-noise ratio (SNR) improvement as functions of probe frequency [Fig. 6.4c)]. For each frequency, we record 400 complex samples using the VNA in continuous-wave mode, with the pump on and off. From their mean and variance, we calculate the on-off gain G, as defined in Eq. 2.14, and the SNR improvement as

$$\Delta\mathrm{SNR} = \frac{|\langle S_{11}^{\mathrm{ON}}\rangle|^2 \mathrm{Var}(S_{11}^{\mathrm{OFF}})}{|\langle S_{11}^{\mathrm{OFF}}\rangle|^2 \mathrm{Var}(S_{11}^{\mathrm{ON}})}, \tag{6.5}$$

where $\langle\cdot\rangle$ and Var denote the mean and variance of the complex samples, respectively. We obtain a maximum on-off gain of approximately 25 dB, a bandwidth of approximately 2 MHz, and an SNR improvement reaching 20 dB.

These results can be compared with previous hybrid parametric amplifiers. In planar Al/InAs heterostructures, Phan *et al.* reported 20 dB gain, 4 MHz bandwidth, and a 1-dB compression point of -125.5 dBm [156], while Hao *et al.* achieved over 20 dB gain, 6 MHz bandwidth, and -119 dBm compression power [157]. More recently, Rousset-Zenou *et al.* demonstrated Al/InAs nanowire amplifiers with 20 dB gain, a bandwidth of a few MHz, and a compression point of -137 dBm [158]. Unlike these four-wave-mixing amplifiers, our device exploits cubic nonlinearity, constituting, to our knowledge, the first demonstration

of three-wave-mixing amplification in a superconductor–semiconductor hybrid device.

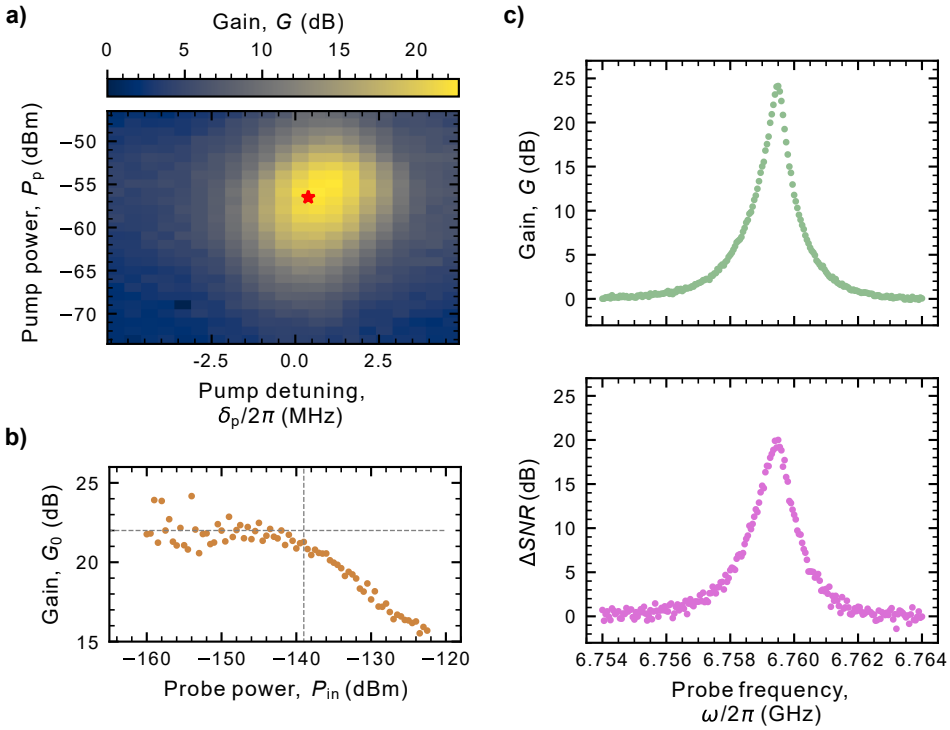


Figure 6.4: Amplifier characterization in the double-junction configuration, at $V_1 = 0.25$ V, $V_2 = 0.5$ V, $\varphi_1 \approx 0.8\pi$, and $\varphi_2 \approx 0.75\pi$. **a)** Peak on-off gain versus pump power and detuning $\delta_p = \omega_p - 2\omega_r$. The red star marks the operating point selected for the subsequent measurements. **b)** Peak on-off gain versus probe power, showing the estimated 1-dB compression point at approximately −138 dBm. **c)** On-off gain (top) and SNR improvement (bottom) versus probe frequency, extracted from repeated continuous-wave measurements.

A well-established example of three-wave-mixing amplification is the SNAIL amplifier [10, 13, 14], which combines sizable cubic nonlinearity with Kerr suppression (see Sec. 1.5). By compensating the Kerr nonlinearity under strong pumping, Sivak *et al.* achieved a 1-dB compression point of −102 dBm and near-quantum-limited noise performance.

Our performance characterization, however, is limited by the absence of a fully calibrated microwave chain and through-reference measurement. Thus, the reported gain and SNR improvement are relative pump-on/off measurements, while the compression point is an estimate subject to input-power calibration uncertainty. Nevertheless, the independent gate and flux control of both junctions offers promising flexibility for optimizing three-wave-mixing amplifiers.

6.2.2 Towards Andreev molecule devices

The approximation of independent junction contributions adopted in our analysis is supported by their separation of approximately 4 μm, significantly exceeding the superconducting coherence length. Furthermore, two-tone spectroscopy with both junctions active reveals spectral features associated with ABS transitions in both junctions (Fig. 6.5), without clear signatures of hybridization, although the broad linewidths prevent us from excluding weak coupling between the ABSs.

Reducing the junction separation to a length comparable to the superconducting coherence length could allow their ABSs to hybridize, forming an Andreev molecule [159]. In this regime, the energy–phase relation depends on the superconducting phases across both junctions, giving rise to a nonlocal Josephson effect in which the supercurrent through one junction can be controlled by the phase across the other. Andreev molecules have been experimentally investigated in InAs nanowires [160] and planar InAs/Al heterostructures [161], revealing hybridized subgap states and nonlocal current–phase relations. Beyond their fundamental interest, these systems offer opportunities for engineering nonlocal superconducting transport, Josephson diode effects, and coupling between Andreev qubits. In our platform, fabricating more closely spaced junctions would allow us to investigate the nonlinear response of Andreev molecules, whose hybridized energy–phase relation could introduce additional contributions to the Kerr and cubic nonlinearities.

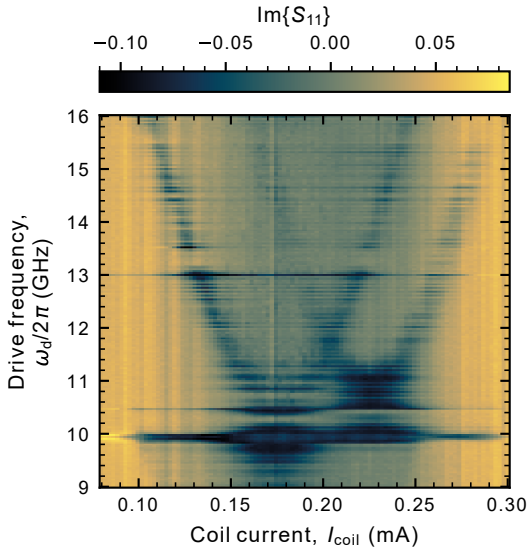


Figure 6.5: Two-tone spectroscopy of Device IV in the double-junction configuration, measured as a function of the current applied to a coil controlling the magnetic flux through both superconducting loops. Spectral features associated with ABS transitions are visible in both junctions, but their broad linewidths prevent any coherent coupling between them from being resolved.

Conclusion

Here we summarize the main results of this thesis and discuss outlook and directions for future experiments.

Summary

The main results of this thesis can be summarized in four points:

- We have demonstrated gate-driven frequency tunability exceeding 90 MHz in a superconducting resonator incorporating an Al/InAs nanowire with a continuous superconducting Al shell, without a semiconducting weak link. This response is accompanied by an approximately 85% reduction in the internal quality factor and a gate leakage current of a few nA. The observed changes in frequency and losses are consistent with the Mattis–Bardeen model using an effective temperature, suggesting an increased quasiparticle population. Furthermore, time-domain and sideband measurements revealed response times down to 35 ns, compatible with quasiparticle recombination dynamics. These results highlight the potential of gate-controlled superconducting elements for fast microwave applications, although the influence of gate-induced losses and leakage current on device performance, particularly noise, requires further investigation.

- We have developed fabrication procedures, cryogenic measurement setups, and two differentially driven NbTiN resonator platforms for the microwave investigation of ABSs in Al/InAs Josephson junctions: a distributed coplanar stripline (CPS) resonator and a compact lumped-element resonator. Using these platforms, we have demonstrated gate and magnetic flux control of the ABS-induced resonator response, observing a behavior consistent with previous experimental reports. We have described this response using effective single- and two-channel short-junction models.

- We have demonstrated strong coupling between ABSs and high-impedance lumped-element NbTiN resonators, observing avoided crossings corresponding to an ABS–resonator coupling strength of $g_c/2\pi \simeq 490$ MHz, with theoretical estimates suggesting maximum coupling strengths approaching 2 GHz.

We also resolved transitions associated with spin-orbit-split ABSs, estimating a spin–photon coupling of 77 MHz. These results demonstrate the potential of high-impedance resonators for approaching the ultrastrong-coupling regime and investigating Andreev spin degrees of freedom.

- We have characterized the Kerr (K) and cubic (g_3) nonlinearities induced by ABSs in Al/InAs Josephson junctions, demonstrating their dependence on both gate voltage and magnetic flux. In particular, we identified operating points where the Kerr nonlinearity approaches zero while the cubic contribution remains sizable. We further demonstrated three-wave mixing parametric amplification with an on-off gain of up to 25 dB, representing, to our knowledge, the first experimental demonstration of this process in a hybrid superconductor–semiconductor device. The measured nonlinearities are qualitatively described by an effective ABS model. These results establish semiconducting Josephson junctions as promising elements for tunable nonlinear microwave circuits, with potential applications in parametric amplification and bosonic-mode manipulation.

Outlook

The demonstration of ABS-induced nonlinearities is arguably the main contribution of this thesis. As already discussed, completing the characterization of our system requires a full fourth-order expansion of the resonator–ABS Hamiltonian to better understand the nonlinearities within the short-junction approximation. Furthermore, a fully calibrated input attenuation and output amplification chain would enable a quantitative characterization of the nonlinearities, particularly the performance of the three-wave mixing amplifier.

Beyond these improvements, two directions are particularly appealing: exploring the role of the spin structure of ABSs in finite-length junctions and investigating the hybridization of ABSs in closely spaced Josephson junctions, forming Andreev molecules. Both effects are known to modify the ABS energy–phase spectrum, potentially altering the nonlinear response of the resonator. Exploring these regimes in future devices could reveal richer nonlinear behavior and offer additional degrees of freedom for engineering superconducting microwave circuits.

Appendices

Appendix A

Fabrication recipes

Glossary

acc: Spin-coater acceleration (rpm/s).

DI: Deionized water.

EBL: Electron-beam lithography.

ICP: Inductively coupled plasma.

IPA: Isopropyl alcohol.

NW: Al/InAs nanowire.

PMMA: Polymethyl methacrylate.

PVD: Physical vapor deposition.

QDR: Quick Dump Rinse.

RIE: Reactive ion etching.

rpm: Revolutions per minute.

SC1: Standard Clean 1.

sccm: Standard cubic centimeters per minute.

SEM: Scanning electron microscopy.

A.1 Auxiliary recipes

Cleaning routines

- **SC1 cleaning:**
  1. Prepare DI H_2O:NH_4OH (25%):H_2O_2 (30%) in a 100:20:20 ml ratio.

2. Immerse at 75–80 °C for 10 min.
3. Rinse using a QDR bath.

- **Cleaning 0:**
  1. Rinse in acetone.
  2. Rinse in IPA.
  3. Dry with N_2.
- **Cleaning 1:**
  1. Sonicate in acetone for 3 min at maximum power.
  2. Sonicate in IPA for 3 min at maximum power.
  3. Dry with N_2.
- **Cleaning 2:**
  1. Soak in acetone at 50 °C for 5 min.
  2. Soak in IPA at 50 °C for 5 min.
  3. Dry with N_2.

Resist coating recipes

- **PMMA A6 (BEK):**
  1. Pre-bake at 180 °C for 3 min.
  2. Spin at 1000 rpm (acc = 500) for 3 s.
  3. Spin at 5000 rpm (acc = 1500) for 60 s.
  4. Bake at 180 °C for 8 min.
- **ma-N2403:**
  1. Pre-bake at 180 °C for 3 min.
  2. Spin at 3000 rpm (acc = 2000) for 60 s.
  3. Bake at 90 °C for 1 min.
- **E-Spacer:**
  1. Spin at 3000 rpm (acc = 2000) for 60 s.
- **AZ1512HS:**
  1. Pre-bake at 180 °C for 2 min.
  2. Spin at 4000 rpm (acc = 1000) for 45 s.
  3. Bake at 110 °C for 1 min.

- **S1813:**
  1. Spin at 3000 rpm (acc = 2000) for 60 s.
  2. Bake at 115 °C for 2 min.

Resist development recipes

- **PMMA A6 + E-Spacer:**
  1. Rinse in DI water for 2 min.
  2. Develop in IPA:DI (4:1) for 5 min.
  3. Dry with N_2.
- **ma-N2403 + E-Spacer:**
  1. Rinse in DI water for 2 min.
  2. Develop in MF319 for 70 s.
  3. Rinse in DI water for 2 min.
  4. Dry with N_2.
- **AZ1512HS:**
  1. Develop in MF-CD-26 for 28 s.
  2. Rinse in DI water for 1 min.
  3. Dry with N_2.

NbTiN sputtering (DCA Cluster)

1. Reactive DC magnetron sputtering.
2. Substrate temperature:
   - Hot: 660 °C, followed by 30 min annealing.
   - Cold: water-cooled sample stage.
3. Ar flow: 60 sccm; N_2 flow: 37 sccm.
4. Operating pressure: 6.7 μbar.
5. Pre-sputter the target for 120 s with the shutter closed.
6. Open the shutter and deposit NbTiN for the duration specified below.

ICP-RIE etching (Oxford Plasmalab 100)

1. Operating pressure: 20 mTorr.
2. Cl_2 flow: 4 sccm; Ar flow: 50 sccm.
3. Etching duration specified below.

A.2 Device fabrication

Substrate preparation

1. SC1 cleaning.
2. Cleaning 0.

Base-layer processing: Device IV

NbTiN deposition

1. NbTiN hot sputtering for 34 s (∼10 nm).
2. Cleaning 1.

Alignment markers

1. Coat PMMA A6 (BEK).
2. Coat E-Spacer.
3. EBL exposure (Raith EBPG 5200):
   - Beam current: 20 nA.
   - Dose: 450 μC/cm^2.
4. Develop PMMA A6 + E-Spacer.
5. O_2 plasma: 50 W, 45 s.
6. Evaporate Ti/Au (Lesker PVD): 6/74 nm.
7. Lift-off:
   a) Soak in mr-Rem 400 overnight.
   b) Heat at 95 °C for 20 min.
   c) Sonicate in mr-Rem 400 for 5 min at maximum power.
   d) Cleaning 1.

Resonator patterning

1. Coat ma-N2403[1].
2. Coat E-Spacer.
3. EBL exposure (Raith EBPG 5200):
   a) Resonator: 40 nA beam and 400 μC/cm^2 dose.
   b) Ground plane: 250 nA beam and 375 μC/cm^2 dose.
4. Develop ma-N2403 + E-Spacer.
5. O_2 plasma: 50 W, 90 s.
6. NbTiN ICP-RIE for approximately 1 min.
7. Rinse in DI water.
8. Resist stripping:
   a) Soak in mr-Rem 700 for approximately 2 h.
   b) Sonicate in mr-Rem 700 at 50 °C for 5 min, 50% power.
   c) Cleaning 1.

Wafer dicing

1. Coat S1813 as a protective layer.
2. Dice the wafer into individual chips (Disco DAD3350).

Base-layer processing: Device III

NbTiN pre-plane fabrication

1. NbTiN cold sputtering for 600 s (∼150 nm).
2. Coat AZ1512HS.
3. UV lithography (MLA150):
   - Dose: 54 mJ/cm^2.
   - Defocus: +2.
   - Optical autofocus.
4. Develop AZ1512HS.

[1] The original process used HSQ [112], which was later replaced by ma-N2403 following a decision by the cleanroom staff to reduce the use of HSQ.

5. O_2 plasma: 50 W, 20 s.
6. NbTiN RIE for approximately 4 min.
7. Immediately rinse in DI water and dry with N_2.
8. O_2 plasma: 50 W, 1 min.
9. Resist stripping: Cleaning 1.

Wafer dicing

1. Coat AZ1512HS as a protective layer.
2. Dice the wafer into individual chips.
3. Cleaning 1.
4. O_2 plasma: 50 W, 1 min.

Resonator fabrication

1. NbTiN cold sputtering for 15 s (∼4 nm).
2. Cleaning 1.
3. Coat ma-N2403.
4. Coat E-Spacer.
5. EBL exposure:
   - Beam current: 3 nA.
   - Dose: 375 μC/cm^2.
6. Develop ma-N2403 + E-Spacer.
7. NbTiN RIE for approximately 80 s.
8. Immediately rinse in DI water.
9. Resist stripping:
   a) Soak in mr-Rem 400 at 80 °C for 10 min, followed by 2 min sonication.
   b) Cleaning 1.

Nanowire transfer

1. Cleaning 1.
2. Transfer NWs onto the chips using the nanomanipulator.
3. Determine NW positions relative to the alignment markers by optical microscopy.

Nanowire processing

Josephson weak-link definition

1. Cleaning 2.
2. Coat PMMA A6 (BEK).
3. Coat E-Spacer.
4. EBL exposure of the etching windows:
   - Beam current: 1 nA.
   - Dose: 450 μC/cm^2.
   - Nominal window length: 180 nm.
5. Develop PMMA A6 + E-Spacer.
6. Al shell etching:
   a) Immerse in MF319 for 55 s.
   b) Rinse in DI water for 10 s.
   c) Rinse in DI water for 30 s.
   d) Soak in DI water bath.
7. Resist stripping: Cleaning 2.
8. Inspect the junctions by SEM and select the NWs for final processing.

Ti/Al contacts and local control lines

1. Coat PMMA A6 (BEK).
2. Coat E-Spacer.
3. EBL exposure:
   - Small structures: 1 nA, 450 μC/cm^2.
   - Large structures: 20 nA, 450 μC/cm^2.

4. Develop PMMA A6 + E-Spacer.
5. O_2 plasma: 50 W, 45 s.
6. Metallization (Lesker):
   a) Ar ion milling for 30 s.
   b) Evaporate Ti/Al: 6/200 nm.
7. Lift-off:
   a) Soak in 1165 overnight.
   b) Heat in 1165 at 95 °C for 20 min.
   c) Cleaning 2.
8. Inspect the completed structures by optical microscopy.

References

[1] A. Blais, S. M. Girvin, and W. D. Oliver, "Quantum information processing and quantum optics with circuit quantum electrodynamics", Nature Physics **16**, 247–256 (2020) (cit. on pp. 1, 5, 19, 22).

[2] A. Wallraff, D. I. Schuster, A. Blais, et al., "Strong coupling of a single photon to a superconducting qubit using circuit quantum electrodynamics", Nature **431**, 162–167 (2004) (cit. on pp. 1, 24).

[3] A. Blais, R.-S. Huang, A. Wallraff, et al., "Cavity quantum electrodynamics for superconducting electrical circuits: An architecture for quantum computation", Physical Review A **69**, 062320 (2004) (cit. on pp. 1, 24).

[4] M. Reagor, W. Pfaff, C. Axline, et al., "Quantum memory with millisecond coherence in circuit QED", Physical Review B **94**, 014506 (2016) (cit. on pp. 1, 24).

[5] M. D. Reed, B. R. Johnson, A. A. Houck, et al., "Fast reset and suppressing spontaneous emission of a superconducting qubit", Applied Physics Letters **96**, 203110 (2010) (cit. on pp. 1, 24).

[6] M. Tinkham, *Introduction to Superconductivity*, 2nd (Dover Publications, 2004) (cit. on pp. 1, 2, 5, 10, 19, 24).

[7] J. Koch, T. M. Yu, J. Gambetta, et al., "Charge-insensitive qubit design derived from the Cooper pair box", Physical Review A **76**, 042319 (2007) (cit. on p. 1).

[8] V. E. Manucharyan, J. Koch, L. I. Glazman, et al., "Fluxonium: Single Cooper-Pair Circuit Free of Charge Offsets", Science **326**, 113–116 (2009) (cit. on p. 1).

[9] A. B. Zorin, "Josephson Traveling-Wave Parametric Amplifier with Three-Wave Mixing", Physical Review Applied **6**, 034006 (2016) (cit. on pp. 1, 25).

[10] N. E. Frattini, U. Vool, S. Shankar, et al., "3-wave mixing Josephson dipole element", Applied Physics Letters **110**, 222603 (2017) (cit. on pp. 1, 25, 26, 89).

[11] P. Krantz, M. Kjaergaard, F. Yan, et al., "A quantum engineer's guide to superconducting qubits", Applied Physics Reviews **6**, 021318 (2019) (cit. on p. 1).

[12] A. Blais, A. L. Grimsmo, S. M. Girvin, et al., "Circuit quantum electrodynamics", Reviews of Modern Physics **93**, 025005 (2021) (cit. on p. 1).

[13] N. E. Frattini, V. V. Sivak, A. Lingenfelter, et al., "Optimizing the Nonlinearity and Dissipation of a SNAIL Parametric Amplifier for Dynamic Range", Physical Review Applied **10**, 054020 (2018) (cit. on pp. 1, 25, 89).

[14] V. V. Sivak, N. E. Frattini, V. R. Joshi, et al., "Kerr-Free Three-Wave Mixing in Superconducting Quantum Circuits", Physical Review Applied **11**, 054060 (2019) (cit. on pp. 1, 25, 61, 89).

[15] A. M. Eriksson, T. Sépulcre, M. Kervinen, et al., "Universal control of a bosonic mode via drive-activated native cubic interactions", Nature Communications **15**, 2512 (2024) (cit. on pp. 1, 25).

[16] A. Maiti, J. W. O. Garmon, Y. Lu, et al., "Linear Quantum Coupler for Clean Bosonic Control", PRX Quantum **6**, 040326 (2025) (cit. on pp. 1, 25, 26).

[17] P. Krogstrup, N. L. B. Ziino, W. Chang, et al., "Epitaxy of semiconductor-superconductor nanowires", Nature Materials **14**, 400–406 (2015) (cit. on pp. 2, 10, 11).

[18] G. De Simoni, F. Paolucci, P. Solinas, et al., "Metallic supercurrent field-effect transistor", Nature Nanotechnology **13**, 802–805 (2018) (cit. on pp. 2, 13).

[19] L. Ruf, C. Puglia, T. Elalaily, et al., "Gate control of superconducting current: Mechanisms, parameters, and technological potential", Applied Physics Reviews **11**, 041314 (2024) (cit. on pp. 2, 13, 67).

[20] G. Catto, W. Liu, S. Kundu, et al., "Microwave response of a metallic superconductor subject to a high-voltage gate electrode", Scientific Reports **12**, 6822 (2022) (cit. on pp. 2, 13, 15, 67).

[21] Y. Ryu, J. Jeong, J. Suh, et al., "Utilizing Gate-Controlled Supercurrent for All-Metallic Tunable Superconducting Microwave Resonators", Nano Letters **24**, 1223–1230 (2024) (cit. on pp. 2, 13, 15, 64, 67).

[22] C. Metzger, S. Park, L. Tosi, et al., "Circuit-QED with phase-biased Josephson weak links", Physical Review Research **3**, 013036 (2021) (cit. on pp. 2, 16, 17, 19, 21, 23, 49, 76, 77).

[23] L. Tosi, C. Metzger, M. F. Goffman, et al., "Spin-Orbit Splitting of Andreev States Revealed by Microwave Spectroscopy", Physical Review X **9**, 011010 (2019) (cit. on pp. 2, 12, 16–19, 23).

[24] C. Janvier, L. Tosi, L. Bretheau, et al., "Coherent manipulation of Andreev states in superconducting atomic contacts", Science **349**, 1199–1202 (2015) (cit. on pp. 2, 16).

[25] M. Hays, V. Fatemi, D. Bouman, et al., "Coherent manipulation of an Andreev spin qubit", Science **373**, 430–433 (2021) (cit. on pp. 2, 11, 16).

[26] C. Schrade and V. Fatemi, "Dissipationless nonlinearity in quantum material Josephson diodes", Physical Review Applied **21**, 064029 (2024) (cit. on pp. 2, 27).

[27] A. J. Annunziata, D. F. Santavicca, L. Frunzio, et al., "Tunable superconducting nanoinductors", Nanotechnology **21**, 445202 (2010) (cit. on p. 5).

[28] J. Gao, M. Daal, A. Vayonakis, et al., "Experimental evidence for a surface distribution of two-level systems in superconducting lithographed microwave resonators", Applied Physics Letters **92**, 152505 (2008) (cit. on pp. 7, 70).

[29] J. Wenner, R. Barends, R. C. Bialczak, et al., "Surface loss simulations of superconducting coplanar waveguide resonators", Applied Physics Letters **99**, 113513 (2011) (cit. on p. 7).

[30] D. M. Pozar, *Microwave Engineering*, 4th (John Wiley & Sons, Hoboken, NJ, 2012) (cit. on pp. 7, 44, 45).

[31] M. S. Khalil, M. J. A. Stoutimore, F. C. Wellstood, et al., "An analysis method for asymmetric resonator transmission applied to superconducting devices", Journal of Applied Physics **111**, 054510 (2012) (cit. on pp. 8, 49).

[32] M. Kudra, J. Biznárová, A. Fadavi Roudsari, et al., "High quality three-dimensional aluminum microwave cavities", Applied Physics Letters **117**, 070601 (2020) (cit. on pp. 8, 49).

[33] U. Vool and M. Devoret, "Introduction to quantum electromagnetic circuits", International Journal of Circuit Theory and Applications **45**, 897–934 (2017) (cit. on p. 8).

[34] S. E. Rasmussen, K. S. Christensen, S. P. Pedersen, et al., "Superconducting Circuit Companion—an Introduction with Worked Examples", PRX Quantum **2**, 040204 (2021) (cit. on p. 8).

[35] S. M. Sze and K. K. Ng, *Physics of Semiconductor Devices*, 3rd ed. (John Wiley & Sons, 2007) (cit. on pp. 10, 13).

[36] R. Hanson, L. P. Kouwenhoven, J. R. Petta, et al., "Spins in Few-Electron Quantum Dots", Rev. Mod. Phys. **79**, 1217–1265 (2007) (cit. on p. 10).

[37] M. H. Devoret and R. J. Schoelkopf, "Superconducting Circuits for Quantum Information: An Outlook", Science **339**, 1169–1174 (2013) (cit. on p. 10).

[38] T. D. Clark, R. J. Prance, and A. D. C. Grassie, "Feasibility of Hybrid Josephson Field Effect Transistors", J. Appl. Phys. **51**, 2736–2743 (1980) (cit. on p. 10).

[39] Y.-J. Doh, J. A. van Dam, A. L. Roest, et al., "Tunable Supercurrent Through Semiconductor Nanowires", Science **309**, 272–275 (2005) (cit. on p. 10).

[40] J. Xiang, A. Vidan, M. Tinkham, et al., "Ge/Si nanowire mesoscopic Josephson junctions", Nature Nanotechnology **1**, 208–213 (2006) (cit. on p. 10).

[41] H. A. Nilsson, P. Samuelsson, P. Caroff, et al., "Supercurrent and Multiple Andreev Reflections in an InSb Nanowire Josephson Junction", Nano Letters **12**, 228–233 (2012) (cit. on p. 10).

[42] K. Gharavi, G. W. Holloway, R. R. LaPierre, et al., "Nb/InAs nanowire proximity junctions from Josephson to quantum dot regimes", Nanotechnology **28**, 085202 (2017) (cit. on p. 10).

[43] Ö. Gül, H. Zhang, F. K. de Vries, et al., "Hard Superconducting Gap in InSb Nanowires", Nano Letters **17**, 2690–2696 (2017) (cit. on p. 10).

[44] P. A. Barnes and A. Y. Cho, "Nonalloyed Ohmic contacts to n-GaAs by molecular beam epitaxy", Applied Physics Letters **33**, 651–653 (1978) (cit. on p. 10).

[45] S. De Franceschi, F. Beltram, C. Marinelli, et al., "Truly ohmic contacts in engineered Al/Si/InGaAs (001) diodes", Applied Physics Letters **72**, 1996–1998 (1998) (cit. on p. 10).

[46] S. De Franceschi, F. Giazotto, F. Beltram, et al., "Andreev reflection in Si-engineered Al/InGaAs hybrid junctions", Applied Physics Letters **73**, 3890–3892 (1998) (cit. on p. 10).

[47] W. Chang, S. M. Albrecht, T. S. Jespersen, et al., "Hard gap in epitaxial semiconductor–superconductor nanowires", Nature Nanotechnology **10**, 232–236 (2015) (cit. on pp. 10, 11).

[48] J. Shabani, M. Kjaergaard, H. J. Suominen, et al., "Two-dimensional epitaxial superconductor-semiconductor heterostructures: A platform for topological superconducting networks", Physical Review B **93**, 155402 (2016) (cit. on p. 10).

[49] M. Pendharkar, B. Zhang, H. Wu, et al., "Parity-preserving and magnetic field–resilient superconductivity in InSb nanowires with Sn shells", Science **372**, 508–511 (2021) (cit. on p. 11).

[50] T. Kanne, M. Marnauza, D. Olsteins, et al., "Epitaxial Pb on InAs nanowires for quantum devices", Nature Nanotechnology **16**, 776–781 (2021) (cit. on p. 11).

[51] M. Pita-Vidal, R. Seoane Souto, S. Goswami, et al., "Novel qubits in hybrid semiconductor-superconductor nanostructures", (2025), arXiv:2512.23336 (cit. on pp. 11, 21).

[52] A. E. Antipov, A. Bargerbos, G. W. Winkler, et al., "Effects of Gate-Induced Electric Fields on Semiconductor Majorana Nanowires", Physical Review X **8**, 031041 (2018) (cit. on p. 12).

[53] J. D. S. Bommer, H. Zhang, Ö. Gül, et al., "Spin-Orbit Protection of Induced Superconductivity in Majorana Nanowires", Physical Review Letters **122**, 187702 (2019) (cit. on p. 12).

[54] S. Vaitiekėnas, G. W. Winkler, B. van Heck, et al., "Flux-induced topological superconductivity in full-shell nanowires", Science **367**, eaav3392 (2020) (cit. on p. 12).

[55] E. Prada, P. San-Jose, M. W. A. de Moor, et al., "From Andreev to Majorana bound states in hybrid superconductor–semiconductor nanowires", Nature Reviews Physics **2**, 575–594 (2020) (cit. on pp. 12, 19).

[56] N. Trnjanin, "Probing Unconventional Superconductivity in Hybrid Josephson Junctions", Doctoral thesis (Chalmers University of Technology, 2026) (cit. on pp. 12, 42).

[57] M. Hays, "Realizing an Andreev Spin Qubit: Exploring Sub-gap Structure in Josephson Nanowires Using Circuit QED", PhD thesis (Yale University, New Haven, CT, USA, 2021) (cit. on pp. 12, 16–18, 23).

[58] A. I. Braginski, "Superconductor Electronics: Status and Outlook", Journal of Superconductivity and Novel Magnetism **32**, 23–44 (2019) (cit. on p. 13).

[59] F. Paolucci, G. De Simoni, E. Strambini, et al., "Ultra-Efficient Superconducting Dayem Bridge Field-Effect Transistor", Nano Letters **18**, 4195–4199 (2018) (cit. on p. 13).

[60] F. Paolucci, F. Vischi, G. De Simoni, et al., "Field-Effect Controllable Metallic Josephson Interferometer", Nano Letters **19**, 6263–6269 (2019) (cit. on p. 13).

[61] C. Puglia, G. De Simoni, and F. Giazotto, "Electrostatic Control of Phase Slips in Ti Josephson Nanotransistors", Physical Review Applied **13**, 054026 (2020) (cit. on p. 13).

[62] I. Golokolenov, A. Guthrie, S. Kafanov, et al., "On the origin of the controversial electrostatic field effect in superconductors", Nature Communications **12**, 2747 (2021) (cit. on pp. 13, 15, 67).

[63] T. Elalaily, O. Kürtössy, Z. Scherübl, et al., "Gate-Controlled Supercurrent in Epitaxial Al/InAs Nanowires", Nano Letters **21**, 9684–9690 (2021) (cit. on p. 13).

[64] M. Ritter, A. Fuhrer, D. Haxell, et al., "A superconducting switch actuated by injection of high-energy electrons", Nature Communications **12**, 1266 (2021) (cit. on p. 13).

[65] M. Ritter, N. Crescini, D. Haxell, et al., "Out-of-equilibrium phonons in gated superconducting switches", Nature Electronics **5**, 71–77 (2022) (cit. on p. 13).

[66] L. Ruf, T. Elalaily, C. Puglia, et al., "Effects of fabrication routes and material parameters on the control of superconducting currents by gate voltage", APL Materials **11**, 091113 (2023) (cit. on p. 13).

[67] T. Elalaily, M. Berke, M. Kedves, et al., "Signatures of Gate-Driven Out-of-Equilibrium Superconductivity in Ta/InAs Nanowires", ACS Nano **17**, 5528–5535 (2023) (cit. on p. 13).

[68] S. Yu, L. Chen, Y. Pan, et al., "Gate-Tunable Critical Current of the Three-Dimensional Niobium Nanobridge Josephson Junction", Nano Letters **23**, 8043–8049 (2023) (cit. on p. 13).

[69] T. Elalaily, M. Berke, I. Lija, et al., "Switching dynamics in Al/InAs nanowire-based gate-controlled superconducting switch", Nature Communications **15**, 9157 (2024) (cit. on pp. 13, 14).

[70] F. Joint, K. Amin, I. Cools, et al., "Dynamics of gate-controlled superconducting Dayem bridges", Applied Physics Letters **125**, 092602 (2024) (cit. on pp. 13, 15, 67).

[71] A. Iorio, "Superconducting circuits with metallic and semiconducting weak-links", PhD thesis (Scuola Normale Superiore, 2023) (cit. on p. 13).

[72] M. Göppl, A. Fragner, M. Baur, et al., "Coplanar Waveguide Resonators for Circuit Quantum Electrodynamics", Journal of Applied Physics **104**, 113904 (2008) (cit. on p. 14).

[73] A. A. Golubov, M. Y. Kupriyanov, and E. Il'ichev, "The current-phase relation in Josephson junctions", Reviews of Modern Physics **76**, 411–469 (2004) (cit. on p. 16).

[74] C. W. J. Beenakker and H. van Houten, "Quantum Transport in Semiconductor Nanostructures", Solid State Physics **44**, 1–228 (1991) (cit. on pp. 16, 18).

[75] L. Bretheau, Ç. Ö. Girit, H. Pothier, et al., "Exciting Andreev pairs in a superconducting atomic contact", Nature **499**, 312–315 (2013) (cit. on p. 16).

[76] L. Bretheau, Ç. Ö. Girit, C. Urbina, et al., "Supercurrent Spectroscopy of Andreev States", Physical Review X **3**, 041034 (2013) (cit. on p. 16).

[77] J.-D. Pillet, C. H. L. Quay, P. Morfin, et al., "Andreev bound states in supercurrent-carrying carbon nanotubes revealed", Nature Physics **6**, 965–969 (2010) (cit. on p. 16).

[78] H. Riechert, S. Annabi, A. Peugeot, et al., "The carbon nanotube gatemon qubit", Nature Communications **16**, 7197 (2025) (cit. on p. 16).

[79] L. Bretheau, J. I.-J. Wang, R. Pisoni, et al., "Tunnelling spectroscopy of Andreev states in graphene", Nature Physics **13**, 756–760 (2017) (cit. on pp. 16, 19).

[80] R. Haller, G. Fülöp, D. Indolese, et al., "Phase-dependent microwave response of a graphene Josephson junction", Physical Review Research **4**, 013198 (2022) (cit. on p. 16).

[81] D. J. van Woerkom, A. Proutski, B. van Heck, et al., "Microwave spectroscopy of spinful Andreev bound states in ballistic semiconductor Josephson junctions", Nature Physics **13**, 876–881 (2017) (cit. on pp. 16, 19).

[82] M. Hays, G. de Lange, K. Serniak, et al., "Direct Microwave Measurement of Andreev-Bound-State Dynamics in a Semiconductor-Nanowire Josephson Junction", Physical Review Letters **121**, 047001 (2018) (cit. on p. 16).

[83] M. Hays, V. Fatemi, K. Serniak, et al., "Continuous monitoring of a trapped superconducting spin", Nature Physics **16**, 1103–1107 (2020) (cit. on pp. 16, 81).

[84] P. Zellekens, R. S. Deacon, P. Perla, et al., "Microwave spectroscopy of Andreev states in InAs nanowire-based hybrid junctions using a flip-chip layout", Communications Physics **5**, 267 (2022) (cit. on pp. 16, 23, 77).

[85] A. Bargerbos, M. Pita-Vidal, R. Zitko, et al., "Spectroscopy of Spin-Split Andreev Levels in a Quantum Dot with Superconducting Leads", Physical Review Letters **131**, 097001 (2023) (cit. on p. 16).

[86] M. Pita-Vidal, A. Bargerbos, R. Zitko, et al., "Direct manipulation of a superconducting spin qubit strongly coupled to a transmon qubit", Nature Physics **19**, 1110–1115 (2023) (cit. on p. 16).

[87] M. Governale and U. Zülicke, "Spin accumulation in quantum wires with strong Rashba spin-orbit coupling", Phys. Rev. B **66**, 073311 (2002) (cit. on p. 18).

[88] D. Willsch, D. Rieger, P. Winkel, et al., "Observation of Josephson harmonics in tunnel junctions", Nature Physics **20**, 815–821 (2024) (cit. on p. 18).

[89] L. Bretheau, Ç. Ö. Girit, M. Houzet, et al., "Theory of microwave spectroscopy of Andreev bound states with a Josephson junction", Physical Review B **90**, 134506 (2014) (cit. on p. 19).

[90] V. Mourik, K. Zuo, S. M. Frolov, et al., "Signatures of Majorana Fermions in Hybrid Superconductor-Semiconductor Nanowire Devices", Science **336**, 1003–1007 (2012) (cit. on p. 19).

[91] S. Park, C. Metzger, L. Tosi, et al., "From Adiabatic to Dispersive Readout of Quantum Circuits", Physical Review Letters **125**, 077701 (2020) (cit. on pp. 19, 21, 75).

[92] L. Tosi, I. Lobato, M. F. Goffman, et al., "Effects of measurement power on state discrimination and dynamics in a circuit-QED experiment", Physical Review Research **6**, 023299 (2024) (cit. on pp. 21, 27).

[93] M. Hinderling, D. Sabonis, S. Paredes, et al., "Flip-Chip-Based Microwave Spectroscopy of Andreev Bound States in a Planar Josephson Junction", Physical Review Applied **19**, 054026 (2023) (cit. on p. 23).

[94] M. Hinderling, S. C. ten Kate, M. Coraiola, et al., "Direct Microwave Spectroscopy of Andreev Bound States in Planar Ge Josephson Junctions", PRX Quantum **5**, 030357 (2024) (cit. on p. 23).

[95] I. C. Iglesias, F. J. Matute-Cañadas, G. O. Steffensen, et al., "Ultrastrong Coupling and Coherent Dynamics in a Gate-Tunable Transmon Qubit", 2026, arXiv:2603.19438 (cit. on p. 23).

[96] C. Metzger, "Spin and charge effects in Andreev Bound States", PhD thesis (Université Paris-Saclay, 2022) (cit. on pp. 23, 72, 76).

[97] M. Malnou, "Synthesis of artificial transmission lines tailored for traveling-wave parametric processes", Physical Review Applied **25**, 054016 (2026) (cit. on p. 24).

[98] L. J. Swenson, P. K. Day, B. H. Eom, et al., "Operation of a titanium nitride superconducting microresonator detector in the nonlinear regime", Journal of Applied Physics **113**, 104501 (2013) (cit. on p. 24).

[99] L. J. Splitthoff, J. Wesdorp, M. Pita-Vidal, et al., "Gate-tunable kinetic inductance parametric amplifier", Physical Review Applied **21**, 014052 (2024) (cit. on p. 24).

[100] N. Frattini, "Three-wave Mixing in Superconducting Circuits: Stabilizing Cats with SNAILs", PhD thesis (Yale University, 2021) (cit. on p. 24).

[101] A. Miano, V. R. Joshi, G. Liu, et al., "Hamiltonian Extrema of an Arbitrary Flux-Biased Josephson Circuit", PRX Quantum **4**, 030324 (2023) (cit. on p. 24).

[102] B. Yurke, L. R. Corruccini, P. G. Kaminsky, et al., "Observation of parametric amplification and deamplification in a Josephson parametric amplifier", Physical Review A **39**, 2519 (1989) (cit. on p. 25).

[103] T. Yamamoto, K. Inomata, M. Watanabe, et al., "Flux-driven Josephson parametric amplifier", Applied Physics Letters **93**, 042510 (2008) (cit. on p. 25).

[104] M. A. Castellanos-Beltran, K. D. Irwin, G. C. Hilton, et al., "Amplification and squeezing of quantum noise with a tunable Josephson metamaterial", Nature Physics **4**, 929–931 (2008) (cit. on p. 25).

[105] S. Puri, S. Boutin, and A. Blais, "Engineering the quantum states of light in a Kerr-nonlinear resonator by two-photon driving", npj Quantum Information **3**, 18 (2017) (cit. on p. 25).

[106] R. Lescanne, M. Villiers, T. Peronnin, et al., "Exponential suppression of bit-flips in a qubit encoded in an oscillator", Nature Physics **16**, 509–513 (2020) (cit. on pp. 25, 26).

[107] W.-L. Ma, S. Puri, R. J. Schoelkopf, et al., "Quantum control of bosonic modes with superconducting circuits", Science Bulletin **66**, 1789 (2021) (cit. on p. 25).

[108] D. Iyama, T. Kamiya, S. Fujii, et al., "Observation and manipulation of quantum interference in a superconducting Kerr parametric oscillator", Nature Communications **15**, 86 (2024) (cit. on p. 25).

[109] B. J. Chapman, S. J. de Graaf, S. H. Xue, et al., "High-On-Off-Ratio Beam-Splitter Interaction for Gates on Bosonically Encoded Qubits", PRX Quantum **4**, 020355 (2023) (cit. on p. 25).

[110] Y. Ye, K. Peng, M. Naghiloo, et al., "Engineering Purely Nonlinear Coupling between Superconducting Qubits Using a Quarton", Physical Review Letters **127**, 050502 (2021) (cit. on p. 25).

[111] M. Elliott, J. Joo, and E. Ginossar, "Designing Kerr interactions using multiple superconducting qubit types in a single circuit", New Journal of Physics **20**, 023037 (2018) (cit. on p. 27).

[112] I. Cools, "Superconducting Resonators for Hybrid Semiconducting and Magnetic Quantum Systems", PhD thesis (Chalmers University of Technology, Gothenburg, Sweden, 2026) (cit. on pp. 31, 48, 99).

[113] W. Kern, "The Evolution of Silicon Wafer Cleaning Technology", Journal of The Electrochemical Society **137**, 1887–1892 (1990) (cit. on p. 31).

[114] K. Kirby, K. Shanmugasundaram, V. Bojan, et al., "Interactions of Sapphire Surfaces with Standard Cleaning Solutions", ECS Transactions **11**, 343–349 (2007) (cit. on p. 31).

[115] D. Zhang, Y. Wang, and Y. Gan, "Characterization of Critically Cleaned Sapphire Single-Crystal Substrates by Atomic Force Microscopy, XPS and Contact Angle Measurements", Applied Surface Science **274**, 405–417 (2013) (cit. on p. 31).

[116] 202Q-Lab, "202Q-Lab – Research Group Website", `https://202q-lab.se/`, Accessed: 2026-10-11 (cit. on p. 37).

[117] 202Q-Lab, "OQTO", `https://github.com/202Q-lab/OQTO`, Accessed: 2026-10-12 (cit. on p. 37).

[118] M. O. Tholén, R. Borgani, G. R. Di Carlo, et al., "Measurement and control of a superconducting quantum processor with a fully integrated radio-frequency system on a chip", Review of Scientific Instruments **93**, 104711 (2022) (cit. on p. 37).

[119] L. Andersson, B. Olsson, S. Gasparinetti, et al., "Co-Designed Reflective and Leaky-Waveguide Low-Pass Filter for Superconducting Circuits", IEEE Transactions on Microwave Theory and Techniques **74**, 1708–1714 (2026) (cit. on p. 39).

[120] SPI Rack, "SPI Rack Documentation", `https://qtwork.tudelft.nl/~mtiggelman/`, Accessed: 2026-10-12 (cit. on p. 40).

[121] J. M. Martinis, M. Ansmann, and J. Aumentado, "Energy Decay in Superconducting Josephson-Junction Qubits from Nonequilibrium Quasiparticle Excitations", Physical Review Letters **103**, 097002 (2009) (cit. on pp. 43, 66).

[122] K. Bladh, D. Gunnarsson, E. Hürfeld, et al., "Comparison of cryogenic filters for use in single electronics experiments", Review of Scientific Instruments **74**, 1323–1327 (2003) (cit. on p. 43).

[123] M. Thalmann, H.-F. Pernau, C. Strunk, et al., "Comparison of cryogenic low-pass filters", Review of Scientific Instruments **88**, 114703 (2017) (cit. on p. 43).

[124] W. B. Weir, "Automatic measurement of complex dielectric constant and permeability at microwave frequencies", Proceedings of the IEEE **62**, 33–36 (1974) (cit. on p. 45).

[125] N. E. Frost and P. B. McGrath, "Permittivity and loss tangent of copper filled epoxy", in Proceedings of the 1996 IEEE Conference on Electrical Insulation and Dielectric Phenomena (1996), pp. 303–306 (cit. on p. 45).

[126] F. Mueller, R. N. Schouten, M. Brauns, et al., "Printed circuit board metal powder filters for low electron temperatures", Review of Scientific Instruments **84**, 044706 (2013) (cit. on p. 46).

[127] F. Pobell, *Matter and Methods at Low Temperatures*, 3rd ed. (Springer, Berlin, Heidelberg, 2007) (cit. on p. 46).

[128] A. A. Clerk, M. H. Devoret, S. M. Girvin, et al., "Introduction to quantum noise, measurement, and amplification", Reviews of Modern Physics **82**, 1155–1208 (2010) (cit. on p. 47).

[129] S. Probst, F. B. Song, P. A. Bushev, et al., "Efficient and robust analysis of complex scattering data under noise in microwave resonators", Review of Scientific Instruments **86**, 024706 (2015) (cit. on p. 49).

[130] J. Burnett, A. Bengtsson, D. Niepce, et al., "Noise and loss of superconducting aluminium resonators at single photon energies", Journal of Physics: Conference Series **969**, 012131 (2018) (cit. on pp. 50, 70).

[131] A. V. Oppenheim, A. S. Willsky, and S. H. Nawab, *Signals & Systems*, 2nd ed. (Prentice Hall) (cit. on p. 54).

[132] M. Aspelmeyer, T. J. Kippenberg, and F. Marquardt, "Cavity optomechanics", Reviews of Modern Physics **86**, 1391 (2014) (cit. on p. 61).

[133] D. C. Mattis and J. Bardeen, "Theory of the Anomalous Skin Effect in Normal and Superconducting Metals", Physical Review **111**, 412–417 (1958) (cit. on p. 64).

[134] C. S. Owen and D. Scalapino, "Superconducting State under the Influence of External Dynamic Pair Breaking", Physical Review Letters **28**, 1559 (1972) (cit. on p. 64).

[135] J. Gao, J. Zmuidzinas, A. Vayonakis, et al., "Equivalence of the Effects on the Complex Conductivity of Superconductor due to Temperature Change and External Pair Breaking", Journal of Low Temperature Physics **151**, 557–563 (2008) (cit. on p. 64).

[136] J. Hu, J. Matin, P. Nicaise, et al., "Investigation of quasi-particle relaxation in strongly disordered superconductor resonators", Superconductor Science and Technology **37**, 055014 (2024) (cit. on p. 64).

[137] P. Chubov, V. V. Eremenko, and Y. A. Plipenko, "Dependence of the critical temperature and energy gap on the thickness of superconducting aluminum films", Soviet Physics JETP **28**, 389 (1969) (cit. on p. 64).

[138] R. Meservey and P. M. Tedrow, "Properties of Very Thin Aluminum Films", Journal of Applied Physics **42**, 51–53 (1971) (cit. on p. 64).

[139] L. J. Splitthoff, "Gate-tunable kinetic inductances for superconducting circuits", PhD thesis (Delft University of Technology, 2024) (cit. on p. 64).

[140] V. Chandrasekhar, "Thermal transport in superconductor/normal-metal structures", Superconductor Science and Technology **22**, 083001 (2009) (cit. on p. 64).

[141] D. Zhang, X. Zheng, and M. D. Ventra, "Local temperatures out of equilibrium", Physics Reports **830**, 1–66 (2019) (cit. on p. 64).

[142] C. N. Thomas, S. Withington, and D. J. Goldie, "Electrothermal model of kinetic inductance detectors", Superconductor Science and Technology **28**, 045012 (2015) (cit. on p. 64).

[143] P. P. Budoyo, J. B. Hertzberg, C. J. Ballard, et al., "Effects of nonequilibrium quasiparticles in a thin-film superconducting microwave resonator under optical illumination", Physical Review B **93**, 024514 (2016) (cit. on p. 64).

[144] P. J. de Visser, "Quasiparticle dynamics in aluminium superconducting microwave resonators", PhD thesis (Delft University of Technology, 2014) (cit. on pp. 65, 66).

[145] S. B. Kaplan, C. C. Chi, D. N. Langenberg, et al., "Quasiparticle and phonon lifetimes in superconductors", Physical Review B **15**, 3567 (1977) (cit. on p. 66).

[146] C. C. Chi and J. Clarke, "Quasiparticle branch mixing rates in superconducting aluminum", Physical Review B **19**, 4495 (1979) (cit. on p. 66).

[147] D. J. Goldie and S. Withington, "Non-equilibrium superconductivity in quantum-sensing superconducting resonators", Superconductor Science and Technology **26**, 015004 (2013) (cit. on p. 66).

[148] J. Burnett, L. Faoro, and T. Lindström, "Analysis of high quality superconducting resonators: consequences for TLS properties in amorphous oxides", Superconductor Science and Technology **29**, 044008 (2016) (cit. on p. 70).

[149] L. Nulens, N. Lejeune, J. Caeyers, et al., "Catastrophic magnetic flux avalanches in NbTiN superconducting resonators", Communications Physics **6**, 267 (2023) (cit. on p. 71).

[150] P. D. Kurilovich, V. D. Kurilovich, V. Fatemi, et al., "Microwave response of an Andreev bound state", Physical Review B **104**, 174517 (2021) (cit. on p. 76).

[151] V. Fatemi, P. D. Kurilovich, M. Hays, et al., "Microwave Susceptibility Observation of Interacting Many-Body Andreev States", Physical Review Letters **129**, 227701 (2022) (cit. on p. 76).

[152] G. Romero, D. Ballester, Y. M. Wang, et al., "Ultrafast Quantum Gates in Circuit QED", Physical Review Letters **108**, 120501 (2012) (cit. on p. 78).

[153] C. Hotter, A. Miranowicz, and K. Gietka, "Quantum Metrology in the Ultrastrong Coupling Regime of Light-Matter Interactions: Leveraging Virtual Excitations without Extracting Them", Physical Review Letters **135**, 100802 (2025) (cit. on p. 78).

[154] R. Stassi and F. Nori, "Long-lasting quantum memories: Extending the coherence time of superconducting artificial atoms in the ultrastrong-coupling regime", Physical Review A **97**, 033823 (2018) (cit. on p. 78).

[155] J. H. Ungerer, A. Pally, A. Kononov, et al., "Strong coupling between a microwave photon and a singlet-triplet qubit", Nature Communications **15**, 1068 (2024) (cit. on p. 81).

[156] D. Phan, P. Falthansl-Scheinecker, U. Mishra, et al., "Gate-Tunable Superconductor -Semiconductor Parametric Amplifier", Physical Review Applied **19**, 064032 (2023) (cit. on p. 88).

[157] Z. Hao, T. Shaw, M. Hatefipour, et al., "Kerr nonlinearity and parametric amplification with an Al-InAs superconductor–semiconductor Josephson junction", Applied Physics Letters **124**, 254003 (2024) (cit. on p. 88).

[158] R. Rousset-Zenou, N. Aparicio, S. Messelot, et al., "Gate-Tunable Josephson Parametric Amplifiers Based on Semiconductor Nanowires", arXiv:2510.00305 (cit. on p. 88).

[159] J.-D. Pillet, V. Benzoni, J. Griesmar, et al., "Nonlocal Josephson Effect in Andreev Molecules", Nano Letters **19**, 7138–7143 (2019) (cit. on p. 90).

[160] O. Kürtössy, Z. Scherübl, G. Fülöp, et al., "Andreev Molecule in Parallel InAs Nanowires", Nano Letters **21**, 7929–7937 (2021) (cit. on p. 90).

[161] D. Z. Haxell, M. Coraiola, M. Hinderling, et al., "Demonstration of the Nonlocal Josephson Effect in Andreev Molecules", Nano Letters **23**, 7532–7538 (2023) (cit. on p. 90).

Appended Papers

PAPER I

Microwave dynamics of gated Al/InAs superconducting nanowires

Vittorio Buccheri, François Joint, Kazi Rafsanjani Amin, Tosson Elalaily, Olivér Kürtössy, Zoltán Scherübl, Gergő Fülöp, Thomas Kanne, Jesper Nygård, Péter Makk, Szabolcs Csonka, and Simone Gasparinetti

Applied Physics Letters **126**, 232602 (2025)

Contribution: The candidate was primarily responsible for the measurements, data analysis, and modeling. He wrote the manuscript.

Applied Physics Letters

RESEARCH ARTICLE | JUNE 10 2025

Microwave dynamics of gated Al/InAs superconducting nanowires

Vittorio Buccheri ; François Joint ; Kazi Rafsanjani Amin ; Tosson Elalaily ; Olivér Kürtössy ; Zoltán Scherübl ; Gergő Fülöp ; Thomas Kanne ; Jesper Nygård ; Péter Makk ; Szabolcs Csonka ; Simone Gasparinetti

Check for updates

Appl. Phys. Lett. 126, 232602 (2025)
https://doi.org/10.1063/5.0267684

View Online
Export Citation

27 May 2026 07:52:08

AIP Advances
Why Publish With Us?
21DAYS average time to 1st decision
OVER 4 MILLION views in the last year
INCLUSIVE scope
Learn More
AIP Publishing

AIP Publishing

Applied Physics Letters ARTICLE pubs.aip.org/aip/apl

Microwave dynamics of gated Al/InAs superconducting nanowires

Cite as: Appl. Phys. Lett. **126**, 232602 (2025); doi: 10.1063/5.0267684
Submitted: 25 February 2025 · Accepted: 27 May 2025 ·
Published Online: 10 June 2025

View Online Export Citation CrossMark

Vittorio Buccheri,[1,a] François Joint,[1,b] Kazi Rafsanjani Amin,[1] Tosson Elalaily,[2,3,4] Olivér Kürtössy,[2,3] Zoltán Scherübl,[2,3] Gergő Fülöp,[2,3] Thomas Kanne,[5] Jesper Nygård,[5] Péter Makk,[2,6] Szabolcs Csonka,[2,3,7] and Simone Gasparinetti[1,c]

AFFILIATIONS

[1]Department of Microtechnology and Nanoscience, Chalmers University of Technology, 41296 Gothenburg, Sweden
[2]Department of Physics, Institute of Physics, Budapest University of Technology and Economics, Műegyetem rkp. 3., H-1111 Budapest, Hungary
[3]MTA-BME Superconducting Nanoelectronics Momentum Research Group, Műegyetem rkp. 3., H-1111 Budapest, Hungary
[4]Low-Temperature Laboratory, Department of Applied Physics, Aalto University School of Science, P.O. Box 15100, FI-00076 Aalto, Finland
[5]Center for Quantum Devices, Niels Bohr Institute, University of Copenhagen, Universitetsparken 5, DK-2100 Copenhagen, Denmark
[6]MTA-BME Correlated van der Waals Structures Momentum Research Group, Műegyetem rkp. 3., H-1111 Budapest, Hungary
[7]Institute of Technical Physics and Materials Science, HUN-REN Centre for Energy Research, Konkoly-Thege Miklós út 29-33, H-1121 Budapest, Hungary

[a]**Author to whom correspondence should be addressed:** buccheri@chalmers.se
[b]**Current address:** Group for Advances Receiver Development (GARD), Department of Space, Earth and Environment, Chalmers University of Technology, 41296 Gothenburg, Sweden.
[c]**Electronic mail:** simoneg@chalmers.se

27 May 2026 07:52:08

ABSTRACT

Several experiments have recently reported on gate-tunable superconducting properties in metallic devices, holding promise for the realization of cryogenic switches, tunable resonators, and superconducting logic. In particular, the suppression of the critical current as a function of the gate voltage has been widely investigated. However, time domain studies are discussed only in a few cases. In this paper, we present a microwave characterization of a gate-controlled Al-capped InAs nanowire embedded in a $\lambda/4$ coplanar waveguide resonator. We observe a shift in the resonator frequency and an increase in its internal losses as a function of the gate voltage, which we relate to a change in the imaginary and real components of the nanowire impedance, respectively. We demonstrate that these changes are described by the Mattis–Bardeen model with an effective temperature. We further study the resonator response to fast-varying gate signals and measure characteristic response times of the order of 40 ns, both in time domain and parametric modulation experiments. Our study elucidates the impact of the gate on the complex impedance of the nanowire in the superconducting state, as well as its dynamic performance, providing a foundation for the design of gate-controlled superconducting devices.

© *2025 Author(s). All article content, except where otherwise noted, is licensed under a Creative Commons Attribution-NonCommercial-NoDerivs 4.0 International (CC BY-NC-ND) license (https://creativecommons.org/licenses/by-nc-nd/4.0/).* https://doi.org/10.1063/5.0267684

Superconductors, thanks to their low energy losses and the Josephson effect, are widely used in cryoelectronics and quantum information processing.[1,2] In these applications, device-design considerations require a specific optimization of superconducting properties such as transition temperature, kinetic inductance, and critical current. For example, kinetic inductance affects the resonant frequency of superconducting resonators,[3] and the spacing of energy levels in transmon qubits depends on the critical current of Josephson junctions.[4]

Although these properties are partially limited by material and geometry,[3] there are strategies to tune them locally and in real time. In superconducting quantum interference devices, for example, a magnetic field is used to control the critical current in one or more Josephson junctions arranged in a superconducting loop.[5,6] On the

© Author(s) 2025

other hand, hybrid superconducting-semiconducting systems take advantage of the low carrier density in the semiconducting channel to tune the critical current with an electric field.[7,8]

Recently, several experiments[9–18] have reported electrostatic gate control even in fully superconducting devices. The mechanism behind such findings, which was originally explained as a field effect,[9–11] is still under debate.[14–20] Nonetheless, gate-controlled superconducting devices promise the same flexibility of semiconductor-based technology in terms of local and real-time control. In fact, compared to magnetic field-controlled devices, gate lines are more compact than flux lines and can be designed to affect only a small portion of the sample. Furthermore, both active region and gate can be made of the same metal—the superconductor—which significantly simplifies the fabrication compared to the hybrid semiconducting-superconducting systems. These advantages make gate-controlled superconducting devices appealing for cryoelectronics applications such as superconducting switches,[21] tunable resonators,[22] and fast superconducting electronics.[19,23] A review summarizing the findings, outstanding questions, and possible application of this phenomenon is given in Ref. 24.

One of the systems in which the gate control has been investigated is the indium arsenide (InAs) nanowire with a full-shell of epitaxial aluminum (Al).[17,19] These studies demonstrate the gate effect on highly crystalline superconductors[25] and are valuable for the possible application of the effect in more complex quantum devices. In fact, hybrid Al/InAs nanowires are a promising platform for implementing gatemon[26] and Andreev qubits,[27,28] in which the gate tunability could be an additional experimental control knob. Moreover, a recent experiment[29] on Al/InAs nanowires shows superconducting-normal state switching dynamics on a nanosecond timescale. These findings motivate further investigation of these systems in the microwave regime.

In this paper, we investigate an InAs nanowire—of the same type discussed in Refs. 17, 19, and 29—with the microwave techniques used in Ref. 23. Our device is based on a hybrid semiconducting-superconducting nanowire with impedance Z_{NW}, consisting of a 150 nm diameter InAs core, which is covered with a 20 nm Al full shell [see Fig. 1(a)]. Since the thickness of the Al shell is orders of magnitude larger than the Thomas–Fermi length in Al, the InAs core is screened from the electric field and does not play any role in the gate response of the nanowire,[19] contrary to other configurations.[30] The nanowire is embedded in the current antinode of a $\lambda/4$ coplanar waveguide resonator and gated in a finger-type configuration. The resonator is capacitively coupled to the feedline we use for the readout. We perform our measurements in a dilution cryostat with 10 mK base temperature.

We measure the feedline transmission parameter, S_{21}, with a vector network analyzer (VNA) as a function of the frequency f and DC gate voltage V_g applied to the gate. We observe a dip in $|S_{21}|$, corresponding to the resonator mode, which shifts as a function of V_g [see the heat map in Fig. 1(b)]. In particular, the resonator mode shows a sign-symmetric gate response with an onset around ± 16 V, together with a rise of gate leakage current up to a few nA [see the purple dashed line and the right axis of Fig. 1(a)]. We extract by fit[31] [see supplementary material Figs. S2(b) and S2(c)] resonant frequency f_{res} and internal quality factor Q_i from the resonator trace for each V_g [see Figs. 1(c) and 1(d)]. Both f_{res} and Q_i decrease monotonically, from $f_{res} = 6.84$ GHz and $Q_i = 1000$ at zero gate to $f_{res} = 6.75$ GHz, $Q_i = 100$ around $V_g = \pm 30$ V.

We interpret our result as a consequence of quasiparticle generation in the gated nanowire due to Cooper pair breaking. An increase in the quasiparticle density n_{qp} has a double effect on Z_{NW}: it increases the kinetic inductance L_k, causing a resonant frequency shift, δf_{res}, and introduces a parallel dissipative channel, i.e., a conductance G, which causes an internal quality factor shift, δQ_i.[3] Note that we assume the nanowire fully contributes to the kinetic component of the device inductance [see supplementary material Fig. S2(a)].

By translating the shift in Z_{NW} in terms of a shift in the complex conductivity $\sigma = \sigma_1 + i\sigma_2$, we apply the generalized Mattis–Bardeen model[32,33] and rewrite the shift in f_{res}, Q_i as

$$\frac{\delta f_{res}}{f_{res}} = \frac{\alpha}{2}\frac{\delta \sigma_2}{\sigma_2} \tag{1}$$

and

$$\delta\left(\frac{1}{Q_i}\right) = \alpha\frac{\delta \sigma_1}{\sigma_2}, \tag{2}$$

respectively, where α is the participation ratio between the gate-affected kinetic inductance and the total inductance of the resonator.[22,34,35] A detailed derivation of Eqs. (1) and (2) can be found in Refs. 36 and 37. Here, assuming thermal equilibrium, real and imaginary parts $\sigma_{1,2}$ are functions of temperature T and critical temperature T_c, i.e., $\sigma_i = \sigma_i(T, T_c)$ [supplementary material Eqs. (S1) and (S2)].

In order to obtain T_c and α, we measure δf_{res} and $\delta(1/Q_i)$ in a temperature-driven experiment where $V_g = 0$ V, and the increase in n_{qp} is due to the temperature rise in the cryostat. We fit Eqs. (1) and (2) to our temperature-driven data [see Fig. 1(e)] and obtain $\alpha = 0.14$ and $T_c = 1.31$ K, compatible with aluminum thin films.[38,39]

Then we apply the same model to our gate-driven data, using an effective-temperature approach. The concept of effective temperature is introduced in mesoscopic physics to characterize systems driven out-of-equilibrium.[40–42] This method has been successful in describing the quasiparticles dynamics in superconducting resonators used as kinetic inductance detectors. For example, the effective temperature has been indirectly measured from the quality factor of the resonator[35] or obtained as a fitting parameter of a thermal model.[43] In our case, after obtaining T_c and α from the temperature-driven experiment, we use Eq. (2) to estimate the effective temperature T_{eff} from the measured internal losses $\delta(1/Q_i)$. In turn, by using the obtained α, T_c, and T_{eff}, we find that Eq. (1) describes the gate-driven shift in frequency [see black dashed line following the red data points in Fig. 1(f)], which validates our analysis. Similar experiments about gate-effect on superconductors in the microwave regime are reported in Refs. 16 and 22. However, in Ref. 16, the Mattis–Bardeen model is used to estimate resonator inductance and resistance from material properties, geometry, and temperature, which then feed a simulation that predicts resonant frequency and quality factor. On the other hand, Ref. 22 applies Eqs. (1) and (2) for a remote-gate configuration calculating an effective quasiparticle density and assuming the temperature to be constant. In this case, the model slightly deviates from the experimental data, which the authors attribute to a heating effect.

To summarize this section, the frequency domain characterization of our device shows a gate-driven frequency tunability in excess of 90 MHz, with a contextual $\sim$85% decrease in internal quality factor, both related to a rise in the leakage current from the gate. Furthermore, we can describe the gate-driven relation between δf_{res}

27 May 2026 07:52:08

© Author(s) 2025

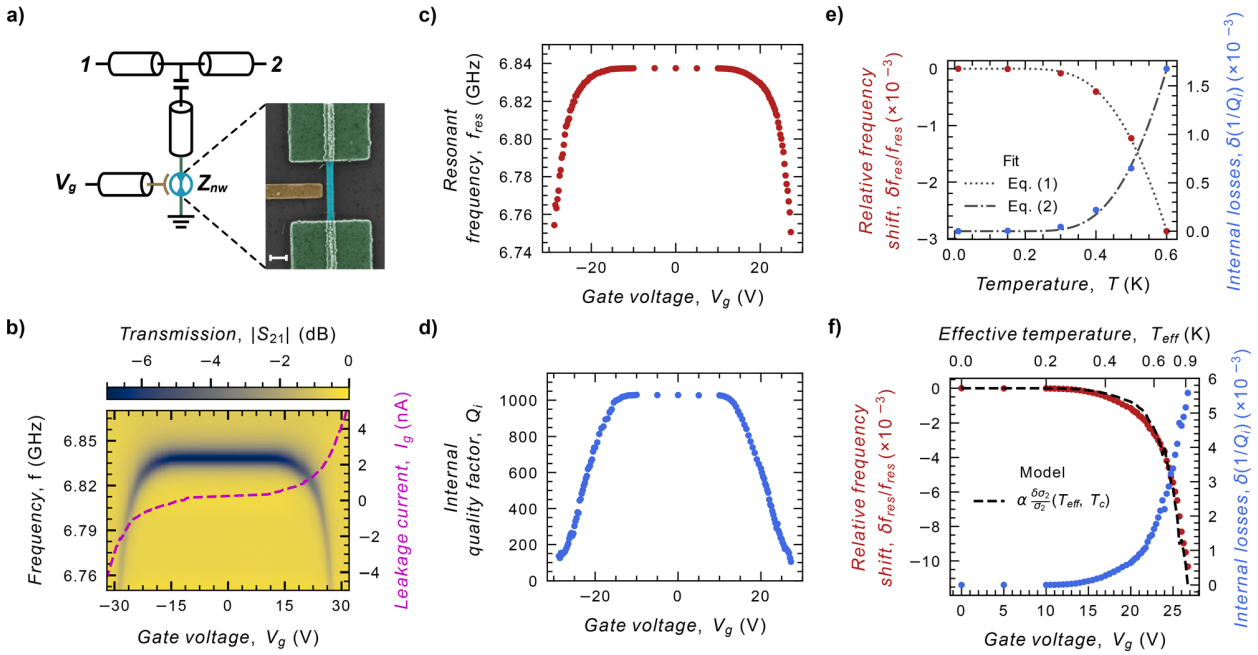


FIG. 1. Device spectroscopy. (a) Simplified schematic of the device. *Zoom-out*: scanning-electron micrograph of the nanowire (scale bar: 300 nm). (b) Heat map of the feedline transmission spectrum, $|S_{21}|$, vs gate voltage, V_g, and frequency, f. On the right axis, we plot the leakage current I_g vs V_g. (c) and (d) Resonant frequency f_{res} and internal quality factor Q_i as a function of V_g. (e) Temperature-driven data with $V_g = 0$: relative frequency shift $\delta f_{res}/f_{res}$ (left axis) and inverse quality factor $\delta(1/Q_i)$ (right axis) are plotted vs temperature. Equations (1) and (2) are globally fitted to the data, according to Mattis–Bardeen model. Fit results: $\alpha = (0.14 \pm 0.04)$ and $T_c = (1.31 \pm 0.05)$ K. (f) Gate-driven data for $T = 10$ mK: $\delta f_{res}/f_{res}$ (left axis) and $\delta(1/Q_i)$ (right axis) vs V_g (bottom axis). For each data point in $\delta(1/Q_i)$, we obtain an effective temperature T_{eff} (top axis), assuming that the gate effect is equivalent to an increase in temperature and using Eq. (2). The predicted $\delta f_{res}/f_{res}$, based on Eq. (1), with the parameter obtained from the fit in panel (e), and $T = T_{eff}$ is plotted as a dashed line.

and $\delta(1/Q_i)$ with an effective temperature in the framework of the Mattis–Bardeen model, which indicates the local heating of the nanowire caused by the leakage current.

We now investigate the dynamic response of our system. We discuss two different techniques for such a measurement: pulsed and continuous gate excitation. In both cases, we send our gate excitation on top of a DC working point V_g, which is above the onset of the gate effect. Excitation and DC signals are combined to the same gate line at the mixing chamber level via a bias-tee [see supplementary material Fig. S6(a)].

Pulsed measurements consist of three pulses: a trigger pulse, a readout pulse, and a gate pulse [see Fig. 2(a)]. We generate all pulses with a microwave digital transceiver, Presto.[44] The trigger pulse defines the time span during which we record the output signal s_{out} from the feedline. While the trigger is on, we send a readout pulse with frequency f_{ro} to the feedline input and a square pulse with amplitude A_g and duration τ_g to the gate line. We average s_{out} over $10^5 - 10^6$ repetition of the triggered sequence and repeat the measurement for different f_{ro}, obtaining a 2D map $s_{out}(t, f_{ro})$ [see Fig. 2(b)].

When $f_{ro} \sim f_{res}$, the readout signal excites the resonator, leaving a signature of the resonant frequency and bandwidth in s_{out}. Consequently, the data at a given time, $s_{out}(t = t_x, f_{ro})$, provides a "snapshot" of the resonator's spectroscopy at time t_x [see $s_{out}(t, f_{ro})$ vertical linecuts on the left side of Fig. 2(c)]. In particular, we fit Lorentzian functions to these frequency traces [see supplementary material Fig. S3(a)], from which we obtain the instantaneous f_{res} and loaded quality factor Q_L. By comparing δf_{res} due to the gate pulse at steady-state with the VNA measurements discussed in the previous section [see left side of Fig. 2(c) vs Fig. 1(c)], we calibrate the attenuation of the RF line we use to drive the gate, obtaining the effective pulse amplitude.

On the other hand, individual time traces $s_{out}(t, f_{ro} \sim f_{res})$ describe the dynamics of our system, namely the resonator ring-up spike around $t = 0.6\,\mu s$ and the gate response around $t = 2\,\mu s$ [see the $s_{out}(t, f_{ro})$ horizontal linecut on the right side of Fig. 2(c)]. The ring-up decays exponentially to a steady-state level with a characteristic time that defines the resonator response time.[45] From an exponential fit [see supplementary material Fig. S3(b)], we obtain $\tau_{res} = 10$ ns, which is compatible with $Q_L/(2\pi f_{res}) = 16$ ns obtained from the Lorentzian fits.

We then fix $f_{ro} \sim f_{res}$ and choose $A_g = 250$ mV, which induces a variation in $|s_{out}|$ up to a few percents while still leaving the system in the linear response regime. Furthermore, we set $500\text{ ns} \leq \tau_g \leq 800$ ns, which is long enough to allow $|s_{out}|$ to saturate to a steady value during the pulse excitation but short enough to avoid distortions due to the bias-tee. With these pulse settings, we investigate the characteristic time of the gate response in the resonator time trace as a function of V_g and cryostat base temperature T. In particular, for each V_g or T, we measure the response for both positive and negative pulse ($\pm A_g$). We fit exponential functions to the rising and falling edges of the positive

27 May 2026 07:52:08

© Author(s) 2025

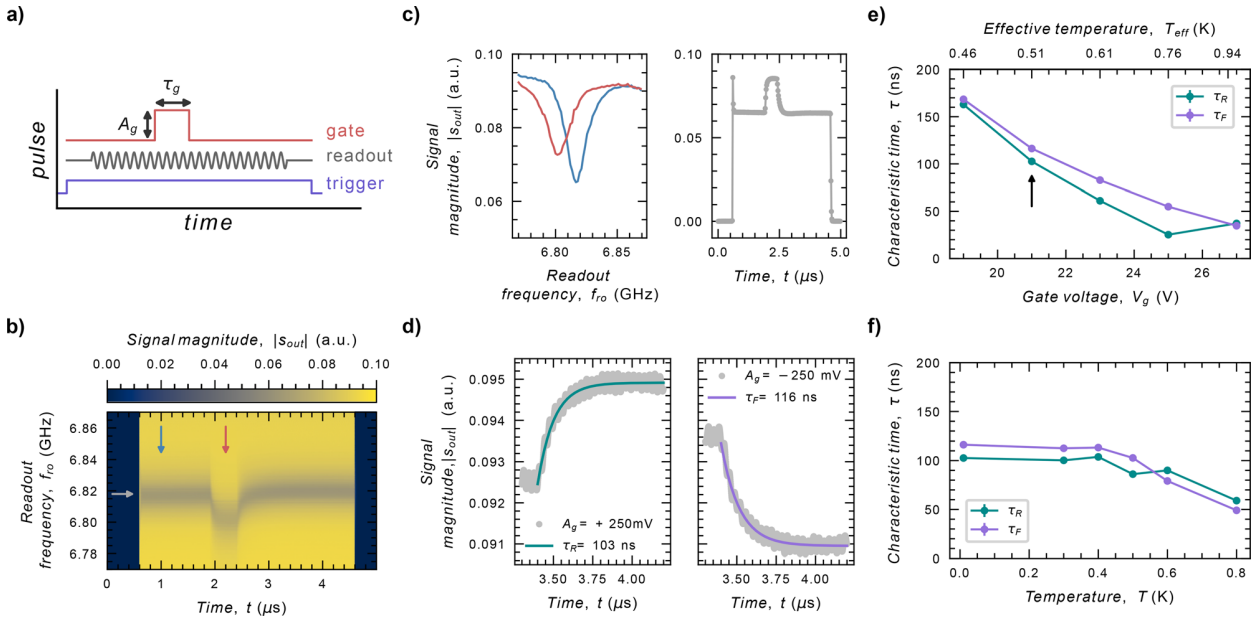


FIG. 2. Device dynamics: time domain spectroscopy. (a) Pulse sequence used for the time-domain measurements. (b) Heat map of resonator time traces recorded for different readout pulse frequencies f_{ro} at gate voltage $V_g = 23.5$ V. With reference to the scheme in panel (a), the trigger period is 5 μs, a 4 μs long readout pulse starts at 0.6 μs and a gate pulse with $A_g = 1.5$ V and $\tau_g = 500$ ns starts around 2 μs. Arrows indicate line cuts discussed in panel (c). (c) Line cuts from panel (b). *Left*: vertical line cuts at 1 μs (blue) and 2.2 μs (red) showing the resonator shift due to the gate pulse. *Right*: horizontal line cut at 6.815 GHz showing resonator ring-up and gate response in time domain. (d) Time traces at $V_g = 21$ V showing resonator rising (left) and falling (right) response under positive and negative gate pulses, respectively. Gate parameters are $|A_g| = 250$ mV and $\tau_g = 800$ ns. Rising (cyan line) and falling (purple line) exponential function are fitted to the gate response, obtaining characteristic time τ_R and τ_F, respectively. (e) Rising and falling time as a function of V_g and effective temperature T_{eff}. The black arrow indicates the gate working point used for the temperature-driven data reported in panel (f). (f) Rising and falling time as a function of the temperature at a fixed $V_g = 21$ V.

and negative pulse-response shape, respectively, obtaining rising and falling characteristic times, $\tau_{R,F}$ [see Fig. 2(d)]. We discard the falling (rising) part of the positive (negative) pulse response, which are affected by the bias-tee in the gate line [see supplementary material Fig. S3(d)].

Since we work in linear regime, we find no clear difference between τ_R and τ_F: they both decrease monotonically with increasing V_g [see Fig. 2(e)], ranging from 170 ns at $V_g = 19$ V to 35 ns at $V_g = 27$ V. We then fix $V_g = 21$ V and measure the characteristic times by stepping the temperature up to 800 mK. We do not observe any clear different behavior between τ_R and τ_F in this case, either: they remain constant at around 130 ns up to 500 mK, then monotonically decrease to 50 ns at 800 mK [see Fig. 2(f)]. Even in time domain, temperature-driven results are compatible with the effective temperature approach. In fact, as discussed in the previous section, $V_g = 21$ V corresponds to $T_{eff} = 510$ mK, which is compatible with the onset in the temperature-induced decrease in $\tau_{R,F}$ for $T \gtrsim 500$ mK.

We compare our data with the expected quasiparticle recombination time, $\tau_{qp} \sim \tau_0/n_{qp}$, where τ_0 is the electron–phonon interaction time in Al.[46] By using the thermal equilibrium $n_{qp}(T_c, T)$, with the critical temperature, T_c, obtained from the temperature-driven frequency spectroscopy, we find that $\tau_0 = 30$ ns leads to a τ_{qp} ranging from 100 ns at $T = 500$ mK to 10 ns at $T = 1$ K (see the supplementary material), which is compatible with the characteristic times we obtain in our experiment as a function of T_{eff}. Whereas τ_0 is often measured to be on the order of 450 ns in aluminum,[46–48] 30 ns is still within the reported range of values for high concentration of aluminum oxide impurities film.[49] On the other hand, also an increase in phonon or quasiparticle density due to nonequilibrium process can effectively decrease τ_0 and τ_{qp}.[46,49,50]

We now perform a continuous gate excitation around $V_g = 27$ V by swapping our pulses with continuous tones. In particular, we send a resonant tone f_r to the feedline input and a tone f_g to the gate, which modulates the device impedance and, consequently, the resonator response. This configuration is equivalent to a mixer where f_r and f_g play the role of local oscillator and intermediate frequency, respectively [see Fig. 3(a)].

We observe sidebands at $f_r \pm f_g$ in the feedline output signal for $f_g = 2$ MHz [see Fig. 3(b)], which proves that f_g modulates f_r. The amplitude of the sideband peaks decreases monotonically with increasing f_g [see Fig. 3(c)]: it ranges from −50 dBm at low frequency to −68 dBm at $f_{g,max} = 25$ MHz with a −3 dB point $f_{g,-3dB} = 3$ MHz, from which we estimate to be an equivalent characteristic response time of $(2\pi f_{g,-3dB})^{-1} = 50$ ns,[51] on the same order of what was obtained in the time domain. Sideband result, which is not limited by bias-tee (bias-tee cutoff is 40 kHz $< f_g$), validates time domain experiments (see the supplementary material for sideband spectroscopy at different V_g and power).

In summary, we discuss the gate response of a Al-capped InAs nanowire embedded in a quarter-wavelength microwave resonator. Spectroscopy characterization of such a system shows a frequency

27 May 2026 07:52:08

© Author(s) 2025

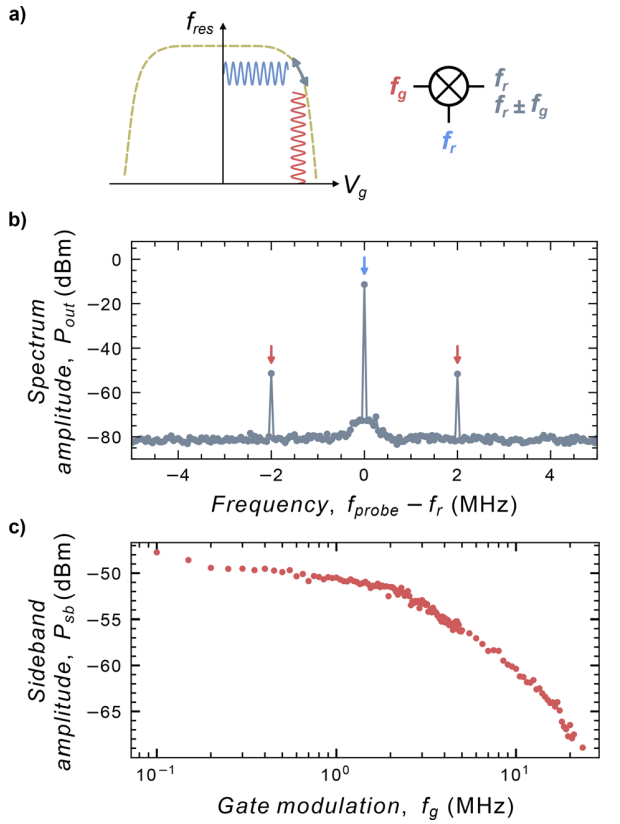


FIG. 3. Device dynamics: sideband spectroscopy. (a) Schematic of the measurement. *Left:* continuous gate excitation modulates the resonator response due to the gate-dependence of the resonator frequency, $f_{res}(V_g)$. *Right:* mixer-equivalent circuit of our system under continuous modulation. (b) Sideband excitation for $V_g = 27$ V, $f_g = 2$ MHz, and $P_g = -5$ dBm. Resonator and sideband peaks are indicated with blue and red arrows, respectively. (c) Averaged upper and lower sideband amplitude [see red arrows in panel (b)] as a function of gate modulation.

tunability on the order of 90 MHz at the price of a degradation in Q_i from 1000 to 100. The onset of the gate response coincides with a rise of the leakage current up to a few nA. We describe the system by the Mattis–Bardeen model with an effective temperature approach, suggesting that the gate response in our device is explained by a heating effect. We note, however, that our use of an effective temperature to model the change in the nanowire impedance does not imply that the quasiparticle population is in thermal equilibrium. In fact, other studies suggest that gating effects on superconductors are related to out-of-equilibrium processes.[14,15,18,19] We study the dynamic response of the resonator under both pulsed and continuous gate excitation. Pulsed excitation is performed in time domain, and it shows a gate-dependent response time down to 35 ns. Even in this experiment, a comparison with temperature-driven measurements suggests that the effect is related to a temperature increase. Continuous excitation confirms the values obtained in time domain, showing sidebands with a −3 dB point at 3 MHz, which gives a characteristic modulation time of 50 ns. Comparison with the expected quasiparticle recombination time suggests that our time domain results agree with the quasiparticle dynamics if we take into account oxygen contamination in our aluminum film or nonequilibrium effects.

Our findings, together with Ref. 23, demonstrate gate-response performances down to tens of nanoseconds, which makes gate-controlled superconducting devices a promising candidate for superconducting switch (see the supplementary material) and cryoelectronics.[24] Moreover, further investigation of the gate dynamics in materials with lower electron–phonon characteristic time and higher critical temperature, such as tantalum (Ta), titanium-nitride (TiN), and niobium-titanium-nitride (NbTiN),[35,46,52,53] could potentially improve the response time.

See the supplementary material for additional information about device fabrication and measurement setup. It also includes supporting data and extended methodologies regarding frequency domain spectroscopy, time domain spectroscopy, and sideband spectroscopy.

The discussed device was partially fabricated in the Chalmers Myfab cleanroom facility. This work was financially supported by the European Research Council via Grant No. 964398 SuperGate, OTKA K138433, ERC project Twistrain, and EIC Pathfinder Challenge QuKiT (No. 101115315). This paper was supported by the János Bolyai Research Scholarship of the Hungarian Academy of Sciences and by the EKÖP-24-4-II-BME-95 University Research Scholarship Program of the Ministry for Culture and Innovation from the source of the National Research, Development, and Innovation Fun. This research was also supported by the Ministry of Culture and Innovation and the National Research, Development and Innovation Office within the Quantum Information National Laboratory of Hungary (Grant No. 2022-2.1.1-NL-2022-00004), and Novo Nordisk Foundation SolidQ. This work was supported by the Knut and Alice Wallenberg Foundation via the Wallenberg Centre for Quantum Technology (WACQT). S.G. acknowledges financial support from the European Research Council via Grant No. 101041744 ESQuAT.

AUTHOR DECLARATIONS

Conflict of Interest

The authors have no conflicts to disclose.

Author Contributions

Vittorio Buccheri: Data curation (equal); Formal analysis (equal); Investigation (equal); Methodology (equal); Software (equal); Visualization (equal); Writing – original draft (equal); Writing – review & editing (equal). **François Joint:** Conceptualization (equal); Methodology (equal); Resources (equal); Writing – review & editing (equal). **Kazi Rafsanjani Amin:** Investigation (supporting); Software (equal). **Tosson Elalaily:** Resources (equal); Writing – review & editing (equal). **Olivér Kürtössy:** Resources (equal). **Zoltán Scherübl:** Supervision (supporting); Writing – review & editing (equal). **Gergő Fülöp:** Supervision (supporting); Writing – review & editing (equal). **Thomas Kanne:** Resources (equal). **Jesper Nygård:** Resources (equal); Writing – review & editing (supporting). **Péter Makk:** Conceptualization (equal); Funding acquisition (equal); Supervision (supporting); Writing – review & editing (equal). **Szabolcs Csonka:** Conceptualization (equal); Funding acquisition (equal); Supervision

27 May 2026 07:52:08

© Author(s) 2025

(supporting); Writing – review & editing (equal). **Simone Gasparinetti:** Conceptualization (equal); Funding acquisition (equal); Methodology (equal); Project administration (equal); Supervision (equal); Writing – original draft (equal); Writing – review & editing (equal).

DATA AVAILABILITY

The data that support the findings of this study are available from the corresponding author upon reasonable request.

REFERENCES

[1]A. I. Braginski, "Superconductor electronics: Status and outlook," J. Supercond. Nov. Magn. **32**, 23–44 (2019).
[2]M. Kjaergaard, M. E. Schwartz, J. Braumüller *et al.*, "Superconducting qubits: Current state of play," Annu. Rev. Condens. Matter Phys. **11**, 369–395 (2020).
[3]M. Tinkham, *Introduction to Superconductivity*, 2nd ed. (Dover Publication, 2004).
[4]J. Koch, T. M. Yu, J. Gambetta *et al.*, "Charge-insensitive qubit design derived from the Cooper pair box," Phys. Rev. A **76**, 042319 (2007).
[5]R. L. Fagaly, "Superconducting quantum interference device instruments and applications," Rev. Sci. Instrum. **77**, 101101 (2006).
[6]J. Li, P. Barry, T. Cecil *et al.*, "Flux-coupled tunable superconducting resonator," Phys. Rev. Appl. **22**, 014080 (2024).
[7]Y. Chen, D. van Driel, C. Lampadaris *et al.*, "Gate-tunable superconductivity in hybrid InSb–Pb nanowires," Appl. Phys. Lett. **123**, 082601 (2023).
[8]G. Burkard, M. J. Gullans, X. Mi, and J. R. Petta, "Superconductor–semiconductor hybrid-circuit quantum electrodynamics," Nat. Rev. Phys. **2**, 129–140 (2020).
[9]G. De Simoni, F. Paolucci, P. Solinas *et al.*, "Metallic supercurrent field-effect transistor," Nat. Nanotechnol. **13**, 802–805 (2018).
[10]F. Paolucci, G. De Simoni, E. Strambini *et al.*, "Ultra-efficient superconducting Dayem bridge field-effect transistor," Nano Lett. **18**(7), 4195–4199 (2018).
[11]F. Paolucci, F. Vischi, G. De Simoni *et al.*, "Field-effect controllable metallic Josephson interferometer," Nano Lett. **19**(9), 6263–6269 (2019).
[12]C. Puglia, G. De Simoni, and F. Giazotto, "Electrostatic control of phase slips in Ti Josephson nanotransistors," Phys. Rev. Appl. **13**, 054026 (2020).
[13]S. Yu, L. Chen, Y. Pan *et al.*, "Gate-tunable critical current of the three-dimensional niobium nanobridge Josephson junction," Nano Lett. **23**(17), 8043–8049 (2023).
[14]I. Golokolenov, A. Guthrie, S. Kafanov *et al.*, "On the origin of the controversial electrostatic field effect in superconductors," Nat. Commun. **12**, 2747 (2021).
[15]M. F. Ritter, N. Crescini, D. Z. Haxell *et al.*, "Out-of-equilibrium phonons in gated superconducting switches," Nat. Electron. **5**, 71–77 (2022).
[16]G. Catto, W. Liu, S. Kundu *et al.*, "Microwave response of a metallic superconductor subject to a high-voltage gate electrode," Sci. Rep. **12**, 6822 (2022).
[17]T. Elalaily, O. Kürtössy, Z. Scherübl *et al.*, "Gate-controlled supercurrent in epitaxial Al/InAs nanowires," Nano Lett. **21**(22), 9684–9690 (2021).
[18]T. Elalaily, M. Berke, M. Kedves *et al.*, "Signatures of gate-driven out-of-equilibrium superconductivity in Ta/InAs nanowires," ACS Nano **17**(6), 5528–5535 (2023).
[19]T. Elalaily, M. Berke, I. Lija *et al.*, "Switching dynamics in Al/InAs nanowire-based gate-controlled superconducting switch," Nat. Commun. **15**, 9157 (2024).
[20]L. Ruf, T. Elalaily, C. Puglia *et al.*, "Effects of fabrication routes and material parameters on the control of superconducting currents by gate voltage," APL Mater. **11**, 091113 (2023).
[21]M. F. Ritter, A. Fuhrer, D. Z. Haxell *et al.*, "A superconducting switch actuated by injection of high-energy electrons," Nat. Commun. **12**, 1266 (2021).
[22]Y. Ryu, J. Jeong, J. Suh *et al.*, "Utilizing gate-controlled supercurrent for all-metallic tunable superconducting microwave resonators," Nano Lett. **24**(4), 1223–1230 (2024).
[23]F. Joint, K. R. Amin, I. P. C. Cools, and S. Gasparinetti, "Dynamics of gate-controlled superconducting Dayem bridges," Appl. Phys. Lett. **125**, 092602 (2024).
[24]L. Ruf, C. Puglia, T. Elalaily *et al.*, "Gate control of superconducting current: Mechanisms, parameters, and technological potential," Appl. Phys. Rev. **11**, 041314 (2024).
[25]P. Krogstrup, N. L. B. Ziino, W. Chang *et al.*, "Epitaxy of semiconductor–superconductor nanowires," Nat. Mater. **14**, 400–406 (2015).
[26]T. W. Larsen, K. D. Petersson, F. Kuemmeth *et al.*, "Semiconductor-nanowire-based superconducting qubit," Phys. Rev. Lett. **115**, 127001 (2015).
[27]M. Hays, G. de Lange, K. Serniak *et al.*, "Direct microwave measurement of Andreev-bound-state dynamics in a semiconductor-nanowire Josephson junction," Phys. Rev. Lett. **121**, 047001 (2018).
[28]M. Hays, V. Fatemi, D. Bouman *et al.*, "Coherent manipulation of an Andreev spin qubit," Science **373**, 430–433 (2021).
[29]Z. Scherübl, M. Kocsis, T. Elalalily *et al.*, "Multimode operation of a superconducting nanowire switch in the nanosecond regime," arXiv:2502.17980 (2025).
[30]L. J. Splitthoff, J. J. Wesdorp, M. Pita-Vidal *et al.*, "Gate-tunable kinetic inductance parametric amplifier," Phys. Rev. Appl. **21**, 014052 (2024).
[31]S. Probst, F. B. Song, P. A. Bushev *et al.*, "Efficient and robust analysis of complex scattering data under noise in microwave resonators," Rev. Sci. Instrum. **86**, 024706 (2015).
[32]D. C. Mattis and J. Bardeen, "Theory of the anomalous skin effect in normal and superconducting metals," Phys. Rev. **111**, 412 (1958).
[33]C. S. Owen and D. J. Scalapino, "Superconducting state under the influence of external dynamic pair breaking," Phys. Rev. Lett. **28**, 1559 (1972).
[34]J. Gao, J. Zmuidzinas, A. Vayonakis *et al.*, "Equivalence of the effects on the complex conductivity of superconductor due to temperature change and external pair breaking," J. Low Temp. Phys. **151**, 557–563 (2008).
[35]J. Hu, J. Matin, P. Nicaise *et al.*, "Investigation of quasi-particle relaxation in strongly disordered superconductor resonators," Supercond. Sci. Technol. **37**, 055014 (2024).
[36]P. K. Day, H. G. LeDuc, B. A. Mazin *et al.*, "A broadband superconducting detector suitable for use in large arrays," Nature **425**, 817–821 (2003).
[37]B. A. Mazin, "Microwave kinetic inductance detectors," Ph.D. thesis (California Institute of Technology, 2005).
[38]P. N. Chubov, V. V. Eremenko, and Y. A. Plipenko, "Dependence of the critical temperature and energy gap on the thickness of superconducting aluminum films," Sov. Phys. JETP **28**, 389 (1969).
[39]R. Meservey and P. M. Tedrow, "Properties of very thin aluminum films," J. Appl. Phys. **42**, 51–53 (1971).
[40]V. Chandrasekhar, "Thermal transport in superconductor/normal-metal structures," Supercond. Sci. Technol. **22**, 083001 (2009).
[41]D. Zhang, X. Zheng, and M. Di Ventra, "Local temperatures out of equilibrium," Phys. Rep. **830**, 1–66 (2019).
[42]C. N. Thomas, S. Withington, and D. J. Goldie, "Electrothermal model of kinetic inductance detectors," Supercond. Sci. Technol. **28**, 045012 (2015).
[43]P. P. Budoyo, J. B. Hertzberg, C. J. Ballard *et al.*, "Effects of nonequilibrium quasiparticles in a thin-film superconducting microwave resonator under optical illumination," Phys. Rev. B **93**, 024514 (2016).
[44]M. O. Tholén, R. Borgani, G. R. Di Carlo *et al.*, "Measurement and control of a superconducting quantum processor with a fully integrated radio-frequency system on a chip," Rev. Sci. Instrum. **93**, 104711 (2022).
[45]P. Heidler, C. M. F. Scheider, K. Kustura *et al.*, "Non-Markovian effects of two-level systems in a niobium coaxial resonator with a single-photon lifetime of 10 milliseconds," Phys. Rev. Appl. **16**, 034024 (2021).
[46]P. J. De Visser, "Quasiparticle dynamics in aluminium superconducting microwave resonators," Ph.D. thesis (De Visser, P.J., 2014).
[47]S. B. Kaplan, C. C. Chi, D. N. Langenberg *et al.*, "Quasiparticle and phonon lifetimes in superconductors," Phys. Rev. B **15**, 3567 (1977).
[48]J. M. Martinis, M. Ansmann, and J. Aumentado, "Energy decay in superconducting Josephson-junction qubits from nonequilibrium quasiparticle excitations," Phys. Rev. Lett. **103**, 097002 (2009).
[49]C. C. Chi and J. Clarke, "Quasiparticle branch mixing rates in superconducting aluminum," Phys. Rev. B **19**, 4495 (1979).

27 May 2026 07:52:08

© Author(s) 2025

[50]D. J. Goldie and S. Withington, "Non-equilibrium superconductivity in quantum-sensing superconducting resonators," Supercond. Sci. Technol. **26**, 015004 (2013).
[51]A. V. Oppenheim and A. S. Willsky, *Signals & Systems*, Signal Processing Series, 2nd ed. (Prentice Hall, 1996), Chap. 6, pp. 448–450.
[52]C. M. Wilson and D. E. Prober, "Quasiparticle number fluctuations in superconductors," Phys. Rev. B **69**, 094524 (2004).
[53]S. A. H. de Rooij, J. J. A. Baselmans, V. Murugesan *et al.*, "Strong reduction of quasiparticle fluctuations in a superconductor due to decoupling of the quasiparticle number and lifetime," Phys. Rev. B **104**, L180506 (2021).

27 May 2026 07:52:08

© Author(s) 2025

Supplementary material for "Microwave dynamics of gated Al/InAs superconducting nanowires"

Vittorio Buccheri[1*], François Joint[1†], Kazi Rafsamjani Amin[1], Tosson Elalaily[2,3,4], Olivér Kürtössy[2,3], Zoltán Scherübl[2,3], Gergő Fülöp[2,3], Thomas Kanne[5], Jesper Nygård[5], Péter Makk[2,6], Szabolcs Csonka[2,3,7], Simone Gasparinetti[1‡]

[1] *Department of Microtechnology and Nanoscience, Chalmers University of Technology, 41296 Gothemburg, Sweden.*

[2] *Department of Physics, Institute of Physics, Budapest University of Technology and Economics, Műegyetem rkp. 3., H-1111 Budapest, Hungary.*

[3] *MTA-BME Superconducting Nanoelectronics Momentum Research Group, Műegyetem rkp. 3., H-1111 Budapest, Hungary.*

[4] *Low-Temperature Laboratory, Department of Applied Physics, Aalto University School of Science, P.O. Box 15100, FI-00076 Aalto, Finland.*

[5] *Center for Quantum Devices, Niels Bohr Institute, University of Copenhagen, Universitetsparken 5, DK-2100 Copenhagen, Denmark.*

[6] *MTA-BME Correlated van der Waals Structures Momentum Research Group, Műegyetem rkp. 3., H-1111 Budapest, Hungary.*

[7] *Institute of Technical Physics and Materials Science, HUN-REN Centre for Energy Research, Konkoly-Thege Miklós út 29-33, H-1121 Budapest, Hungary.*

A. Device

The device discussed in the main text is part of a 7x7 mm^2 chip [see Fig. S1a)]. The chip hosts four resonator-gate devices and we name them D1, D2, D3 and D4. Device D2 is a reference resonator without nanowire (NW) [see Fig. S1b)], while for D1, D3 and D4 the resonator is shunted to ground via a NW [see Fig. S1c) and d)]. The sample is fabricated on a Si substrate [see Fig. S1e)]. First, we thermally grow a 200 nm-thick oxide layer on a 2-inch high-resistivity silicon wafer using a furnace. Next, we evaporate a 150 nm-thick aluminum film across the entire wafer. Using a maskless UV lithography system, we pattern the microwave circuits, including feedlines, gate lines, and resonators. The patterns are transferred to the aluminum layer by immersing the wafer in an aluminum etchant solution for approximately two minutes. Subsequently, we pattern alignment markers using e-beam lithography, followed by the lift-off of a 25 nm-thick gold layer. This step prepares the wafer for the deposition and integration of nanowires with the existing circuitry. We deposit the NWs on the sample with a nano-manipulator and then embedded in the cQED structure with 100 nm of Ti-Al contacts. We obtain the contact via lif-off process and patterned with EBL. Before evaporation, we clean the pattern with Ar milling to reduce contact resistance.

B. Setup

After fabrication, we wire-bond our sample to a PCB with Al wires and close it inside a light-tight RF box. The box is thermally anchored to the mixing chamber plate of a dilution cryostat with base temperature of 10 mK [see Fig. S6a)]. Gate lines, DC and RF, are combined with a bias-tee with 40 kHz cutoff. Both the input line and the gate lines are attenuated and filtered through the cryostat stages; the output signal is amplified both at 4K and at room temperature. We characterize the sample in multiple cooldowns. Initially, we connect all the gate lines to the same bias-tee via a switch installed at the mixing chanber lavel. In later cooldowns, we terminate all the gate lines but D1, which is the only one showing showing gate response (see Sec. C). Regarding the measurements:

* buccheri@chalmers.se

† Current address: Group for Advances Receiver Development (GARD), Department of Space, Earth and Environment, Chalmers University of Technology, 41296 Gothenburg, Sweden.

‡ simoneg@chalmers.se

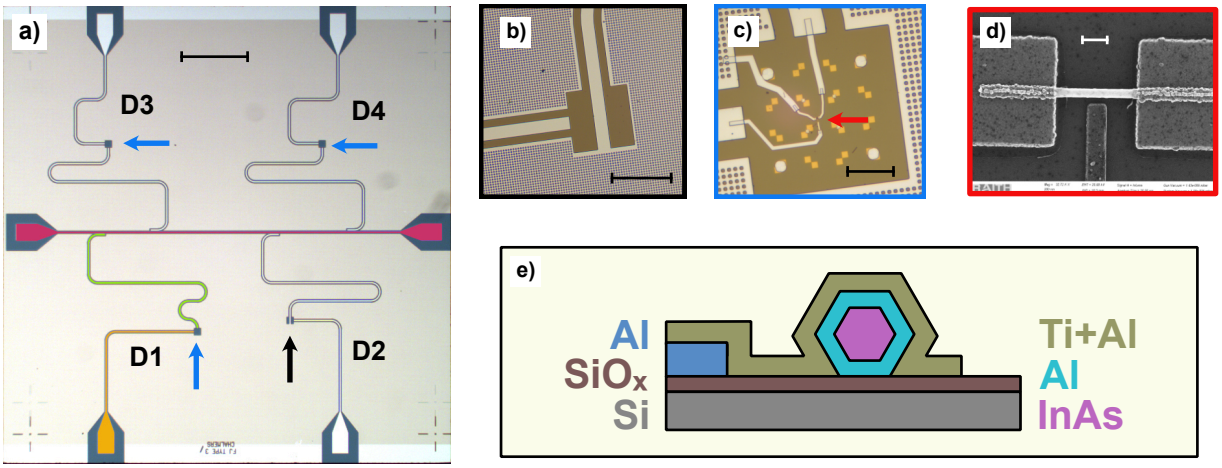


FIG. S1: Device fabrication. **a)** False-colored optical picture of a chip lithographically identical to the one that was used in the experiments. The feedline (red) is capacitively coupled to four devices (D1, D2, D3 and D4) consisting of a $\lambda/4$ CPW resonator and a gate line each. The resonator and gate line are colored in green and yellow, respectively, for the device discussed in the main text, D1. Blue arrows indicate the gating area where NWs are embedded in the resonator line. A black arrow indicates the reference resonator without NW. The scale bar is 1 mm. **b)** Optical zoom-in on the bare resonator. The scale bar is 500 μm. **c)** Optical zoom-in on gating area with showing a NW (red arrow) shunting the resonator line to the ground plane and the gate line tapered towards the NW. The scale bar is 30 μm. **d)** SEM picture of the NW [same as Fig. 1a) in main text]. The scale bar is 400 nm. **e)** Material stack used in the fabrication of the sample.

- DC gate voltage V_g is controlled by a Stanford Research DC205 voltage source and the leakage current is obtained from the voltage drop across a 4.6 kΩ series resistance, measured with a Keithley 2000 Multimeter [see Fig. S6b)].
- Spectroscopy measurement are performed with port 1 and port 2 of a Keysight P5024A VNA with the gate RF line teminated with 50 Ω [see Fig. S6c)].
- Time domain measurements with squared pulse gate-excitation are performed with a digital transceiver with 1 GS/s sampling rate, Presto [1], which generates both readout and gate pulses, and analyses the output signal from the feedline [see Fig. S6d)]. In particular, input (output) readout signals are generated (recorded) by digital up- (down-) conversion with 100-125 MHz intermediate frequency. Down-converted output signal is then demodulated and filtered, to eliminate spurious modes. The resulting time limitation from the instrument is 8 ns. Room temperature gate-pulse amplifier has 2 ns response-time.
- Sidebands are measured with Keysight P5024A. On the one hand, port 1 and port 3 are in continuous wave (CW) mode and generate readout tone and gate excitation, respectively. On the other hand, port 2 is in spectrum analyzer mode (SA) and analyses the output signal.

C. Spectroscopy measurements

A broad scan of the transmission S_{21} versus frequency at different temperatures shows three modes shifting towards lower frequency for $T > 300$ mK (6.3 GHz, 6.8 GHz and 7.2 GHz) and a stable mode at 6.6 GHz [see Fig. S2a)]. The latter corresponds to D2, the bare resonator, while the formers correspond to the NW-loaded ones, D1, D3 and D4. Since the frequency shift as a function of temperature is due to the kinetic inductance [2], we can conclude that in our devices the kinetic contribution of the inductance is in the NWs, while the resonator lines give geometric contribution. This is expected also from the different thicknesses between CPW Al layer (150 nm) and NW Al layer (20 nm) [2]. The measured resonant frequencies for D1, D3 and D4, are compatible with Sonnet simulations of our resonators in which we assume $\sim$ 250 pH contribution form the NWs, on the same order of what reported in [3] for

similar NWs. We obtain resonant frequency and quality factors for the D1 resonator by using the "circle-fit" method [4] [see Fig S2b)-c)].

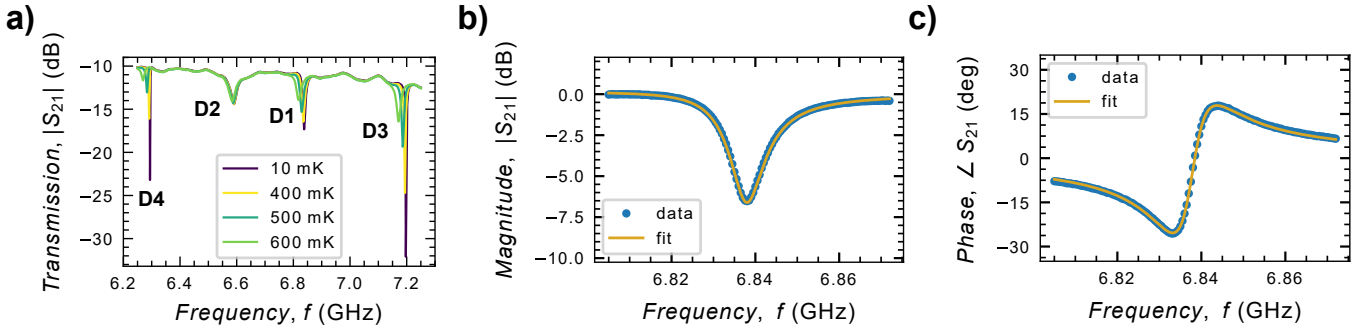


FIG. S2: Frequency spectroscopy. **a)**: Wide frequency-span feedline transmission spectra S_{21} for different temperatures at $V_g = 0$ V. **b)-c)** We show D1 resonator amplitude and phase at 10 mK for $V_g = 0$ V. We perform the fit following Ref. [4], obtaining $f_{res} = 6.837$ GHz, $Q_i = 980$ and $Q_c = 828$.

D. Mattis-Bardeen model

Regarding our analysis of δf_{res} and $\delta(1/Q_i)$ within the Mattis-Bardeen model, equations 1 and 2 in the main text require an expression for σ_i. At low temperature T and small frequency ω, i.e. $k_BT << \Delta$ and $\hbar\omega << \Delta$, with Δ being the superconducting gap and k_B, $\hbar$ being the Boltzmann and reduced Plank constants, respectively, $\sigma_{1,2}$ can be written as [5]

$$\frac{\sigma_1}{\sigma_n} = \frac{2\Delta_0}{\hbar\omega}\frac{n_{qp}}{N_0\sqrt{2\pi k_B T\Delta_0}}\sinh(\xi)K_0(\xi), \tag{S1}$$

and

$$\frac{\sigma_2}{\sigma_n} = \frac{\pi\Delta_0}{\hbar\omega}\left[1 - \frac{n_{qp}}{2N_0\Delta_0}\left(1 + \sqrt{\frac{2\Delta_0}{\pi k_B T}}e^{-\xi}I_0(\xi)\right)\right], \tag{S2}$$

where σ_n is the normal state conductivity, N_0 is the electrons density of states at the Fermi level, $\Delta_0 = 1.764 k_B T_c$ is the superconducting gap at $T = 0$ K, $\xi = \hbar\omega/2k_BT$ and K_0, I_0 are the Bessel function of first and second order, respectively.

Equations S1, S2 take into account an increase in the quasi-particles density due to generic pair-breaking. In case of thermal excitation we can substitute n_{qp} with

$$n_{qp} = 2N_0\sqrt{2\pi k_B T\Delta_0}\,\exp\left(-\frac{\Delta_0}{k_BT}\right). \tag{S3}$$

E. Time-domain measurements

We fit Lorentzian functions to the resonant curves obtained from time domain measurements [see Fig. S3a)]:

$$s_{out}(f) = \beta\frac{\gamma^2}{(f - f^*_{res})^2 + \gamma^2} + \theta, \tag{S4}$$

where f_{res} is the resonant frequency, γ is the FWHM of the curve, i.e. $Q_L = f_{res}/\gamma$, β is the amplitude of the dip and θ is the offset of the baseline. We fit exponential decay functions to the resonator ring-up [see Fig. S3 b)] and rising/falling parts of the gate response [see Fig. S3 d)]:

$$s_{out}(t) = A + (B - A)e^{(t-t_0)/\tau}, \tag{S5}$$

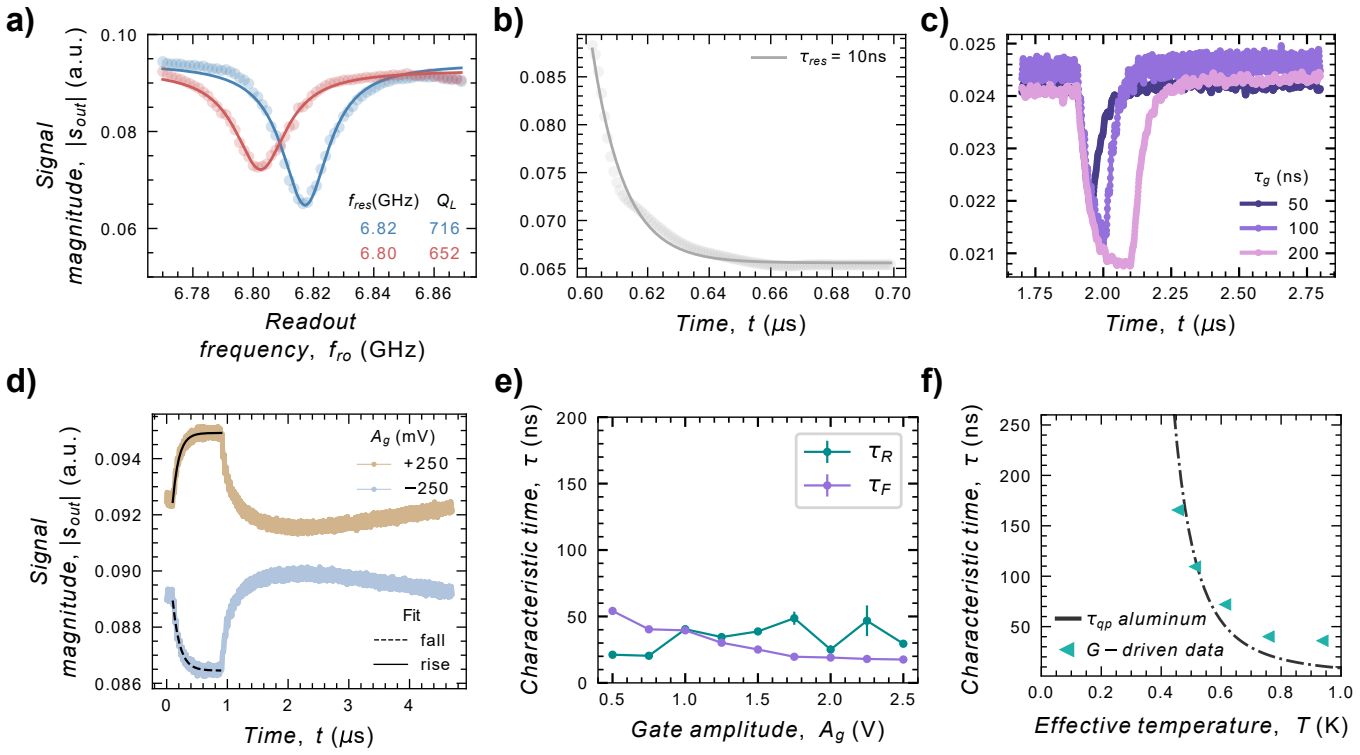


FIG. S3: Time domain: preliminary measurements and comparison with quasiparticle recombination time. **a)** Lorentzian fits [Eq. S4] of resonant frequencies obtained with time domain spectroscopy [see left-side of Fig. 2c) in the main text]. **b)** Exponential fit [Eq. S5] of resonator ring-up [see right-side of Fig. 2c) in the main text]. **c)** Comparison of gate response for different gate pulse duration τ_g. **d)** Comparison of gate response positive ($+A_g$) and negative ($-A_g$) amplitude showing the long-time response of the resonator after the gate pulse. Curves are vertically shifted for clarity. Exponential fit of the rising and falling parts of the gate response are shown in continuous and dashed lines, respectively. Considered and discarded fit results are shown in black and gray, respectively. In this measurement we are at base temperature, 10 mK, and $V_g = 21$ V. **e)** Characteristic times for $V_g \sim 27$ V as a function of the gate pulse amplitude A_g. **f)** Comparison with the quasiparticle recombination time: seagreen data points represent average characteristic times $(\tau_R + \tau_F)/2$ obtained at 10 mK as a function of DC working point, V_g. The voltage has been converted to effective temperature, as explained in the main text. The gray dash-dot line represents the expected quasiparticle recombination time obtained from Eq. S7 with $\tau_0 = 30$ ns.

where A, B are the initial, final value of the exponential, respectively, t_0 if the offset on the starting time and τ is the characteristic decay time. B and τ are used as fit parameters.

For our test pulse, we choose the gate duration such that 200 ns $< \tau_g \leq 1$ μs, which ensures a pulse long enough to saturate the gate response [see Fig. S3c)] and short enough not to be affected by the bias-tee. The falling (rising) part of the positive (negative) pulse triggers a slow response of the output signal [see Fig. S3d)] that we attribute to the frequency-dependent response of the gate line. To avoid the slow-response influence, we discuss results from the rising and falling edges of the positive and negative pulse, respectively, disregarding the others two edges. Note that, as discussed in the main text, $A_g = \pm 250$ mV gives a symmetric gate response, $\delta s_{\rm out}(+A_g) \sim -\delta s_{\rm out}(-A_g)$ [see Fig. S3d)], confirming that the perturbation induced by the gate pulse is in the linear response regime. By increasing A_g, the symmetry between positive and negative gate-response disappears. However, we see that up to 2.5 V-high pulse, the obtained characteristic times remain on the same order of what has been obtained in linear response [see Fig. S3e)], which is also in agreement with what has been reported in Ref. [7].

The expected quasiparticle recombination time can be written as [6]:

$$\tau_{\rm qp} = \frac{\tau_0}{n_{\rm qp}} \frac{N_0 (k_B T_c)^3}{2\Delta_0^2}, \tag{S6}$$

where τ_0 is the material-dependent electron-phonon interaction time. In case of thermal equilibrium, we can substitute

$n_{\rm qp}$ with Eq. S3 and obtain:

$$\tau_{\rm qp} = \frac{\tau_0}{\sqrt{\pi}} \left(\frac{k_B T_{\rm c}}{2\Delta_0} \right)^{5/2} \sqrt{\frac{T_{\rm c}}{T}} e^{\Delta_0/k_B T}. \tag{S7}$$

We find that Eq. S7 with $\tau_0 = 30$ ns is in agreement with measured characteristic times [see Fig. S3f)].

As discussed in the main text, response time down to tens of nanoseconds are promising for the realization cryogenic switches. We show that, within the resonator linewidth, a 50% signal contrast can be reached with $A_g = 1.5$ V [see Fig. 2b)-c) in the main text], which still shows a time response < 50 ns [see Fig. S3e)]. These findings suggest that our system could be implemented in a narrow-band RF switch. In principle, a wide-band switch implementation could be obtained with a more complex RF circuitry where more active elements play a role [8].

F. Sidebands

We compare the characteristic response time, $\tau_{\rm sb}$, obtained from the -3 dB point of the sidebands amplitude at three different V_g values. Compatibly with the time domain results, we find that $\tau_{\rm sb}$ decreases as $V_{\rm g}$ increases, ranging from 150 ns at $V_{\rm g} = 23$ V to 40 ns at $V_{\rm g} = 29$ V [see Fig. S4]. According to the time domain analysis [see Sec. E], we assume that the sidebands spectroscopy is also limited by the quasiparticles recombination time and the bandwidth or response time of the system could be improved by choosing a superconductor with smaller τ_0 [see Eq. S6]. In fact, in Ref. [7], in which sidebands spectroscopy was performed on a Nb Dayem bridge, the -3dB point was observed up to tens of MHz, corresponding to a few ns response time.

Moreover, by keeping $V_{\rm g} = 27$ V, as in the main text, we perform sidebands spectroscopy by changing both the readout power of the carrier signal, $P_{\rm ro}$, and the gate modulation power, $P_{\rm g}$. With $P_{\rm g} = 10$ dBm and $P_{\rm ro} = -20$ dBm, we excite sidebands up to the fourth order [see Fig. S5c)]. The amplitude of the sidebands decreases as a function of the modulation frequency for all orders [see Fig S5d)]. Whereas the maximum modulation at which the first order sideband is excited increases with $P_{\rm g}$, going from 20 MHz for $P_{\rm g} = -5$ dBm to almost 100 MHz for $P_{\rm g} = 10$ dBm [compare Fig. 3c) in the main text with Fig. S5d)] the -3 dB point remains almost constant around 3 MHz. The higher-order sideband excitation is a sign of the non-linearity of the system, which increases as a function of power. In fact, we find that the sidebands order depends on both $P_{\rm g}$ and $P_{\rm ro}$ [see Fig. S5c)-d)].

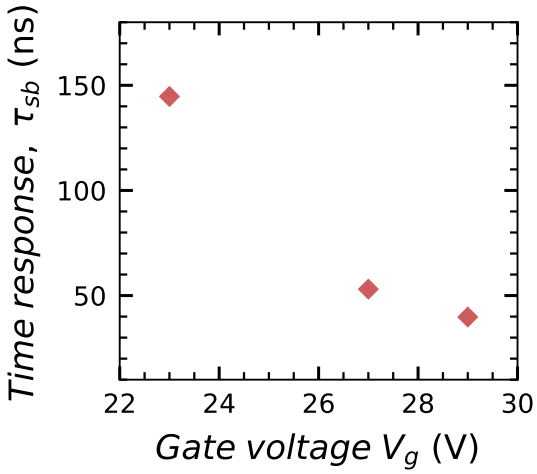


FIG. S4: Sidebands spectroscopy: gate voltage dependence. Time response obtained from the -3 dB point of the sidebands amplitude for different $V_{\rm g}$.

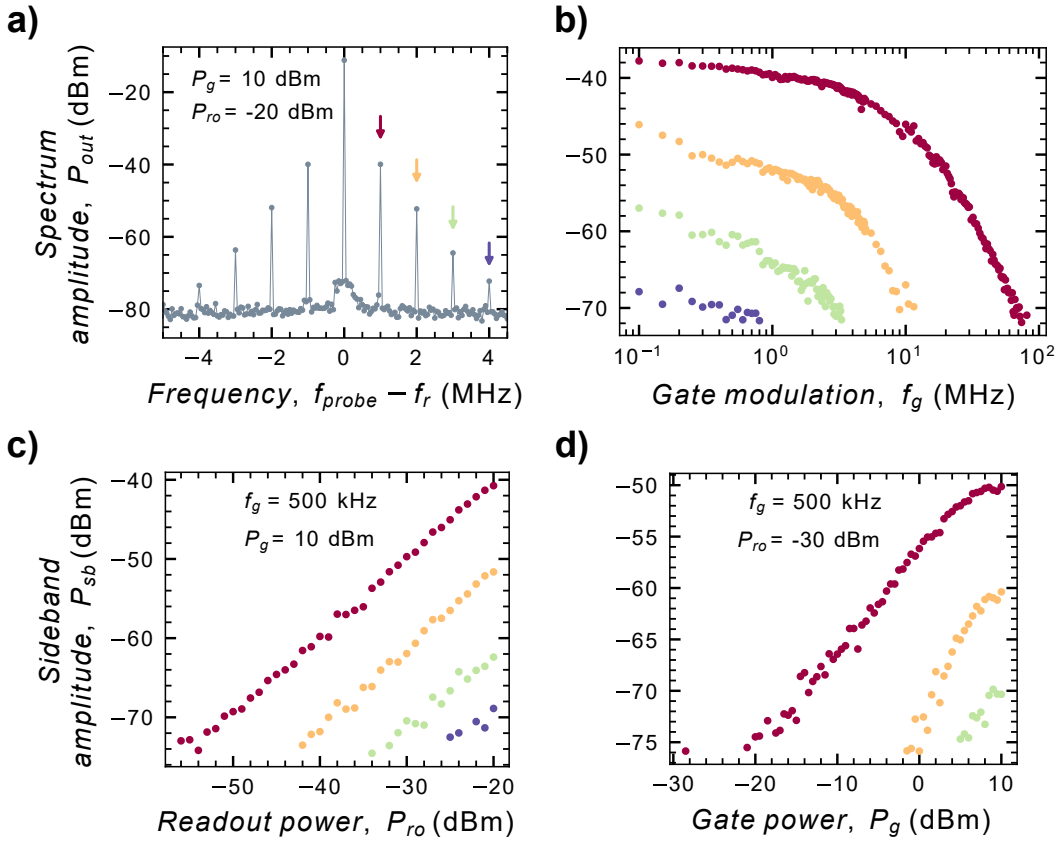


FIG. S5: Sidebands spectroscopy: power dependence. **a)** Multiple sidebands excitation for $V_g = 27$ V and $f_g = 1$ MHz. Upper sideband peaks from the first to the fourth order are indicated with red, yellow, green and violet arrows, respectively. The same color code is used for the other panels in the figure. **b)** Sidebands amplitude as a function of the gate modulation f_g. **c)** Sidebands amplitude as a function of readout power P_{ro}. **d)** Sideband amplitude as a function of gate power P_g.

[1] M. O. Tholén, R. Borgani, G. R. Di Carlo, et al., *Measurement and control of a superconducting quantum processor with a fully integrated radio-frequency system on a chip*, Rev. Sci. Instrum. 93, 104711 (2022).

[2] M. Tinkham, "Introduction to Superconductivity" (2nd ed.), Dover Publication.

[3] L. J. Splitthoff, J.J. Wesdorp, M. Pita-Vidal et al., *Gate-tunable kinetic inductance parametric amplifier*, Phys. Rev. Applied 21, 014052 (2024).

[4] S. Probst, F. B. Song, P. A. Bushev et al., *Efficient and robust analysis of complex scattering data under noise in microwave resonators*, Rev. Sci. Instrum. 86, 024706 (2015).

[5] Y. Ryu, J. Jeong, J. Suh et al, *Utilizing Gate-Controlled Supercurrent for All-Metallic Tunable Superconducting Microwave Resonators*, Nano Lett. 24, 4, 12231230 (2024).

[6] P. J. De Visser, *Quasiparticle dynamics in aluminium superconducting microwave resonators*, PhD Thesis.

[7] F. Joint, K.R. Amin, I.P.C. Cools and S. Gasparinetti, *Dynamics of gate-controlled superconducting Dayem bridges*, Appl. Phys. Lett. 125, 092602 (2024).

[8] C. F. Campbell and D. C. Dumka, *Wideband high power GaN on SiC SPDT switch MMICs*, 2010 IEEE MTT-S International Microwave Symposium, Anaheim, CA, USA, 2010, pp. 145-148.

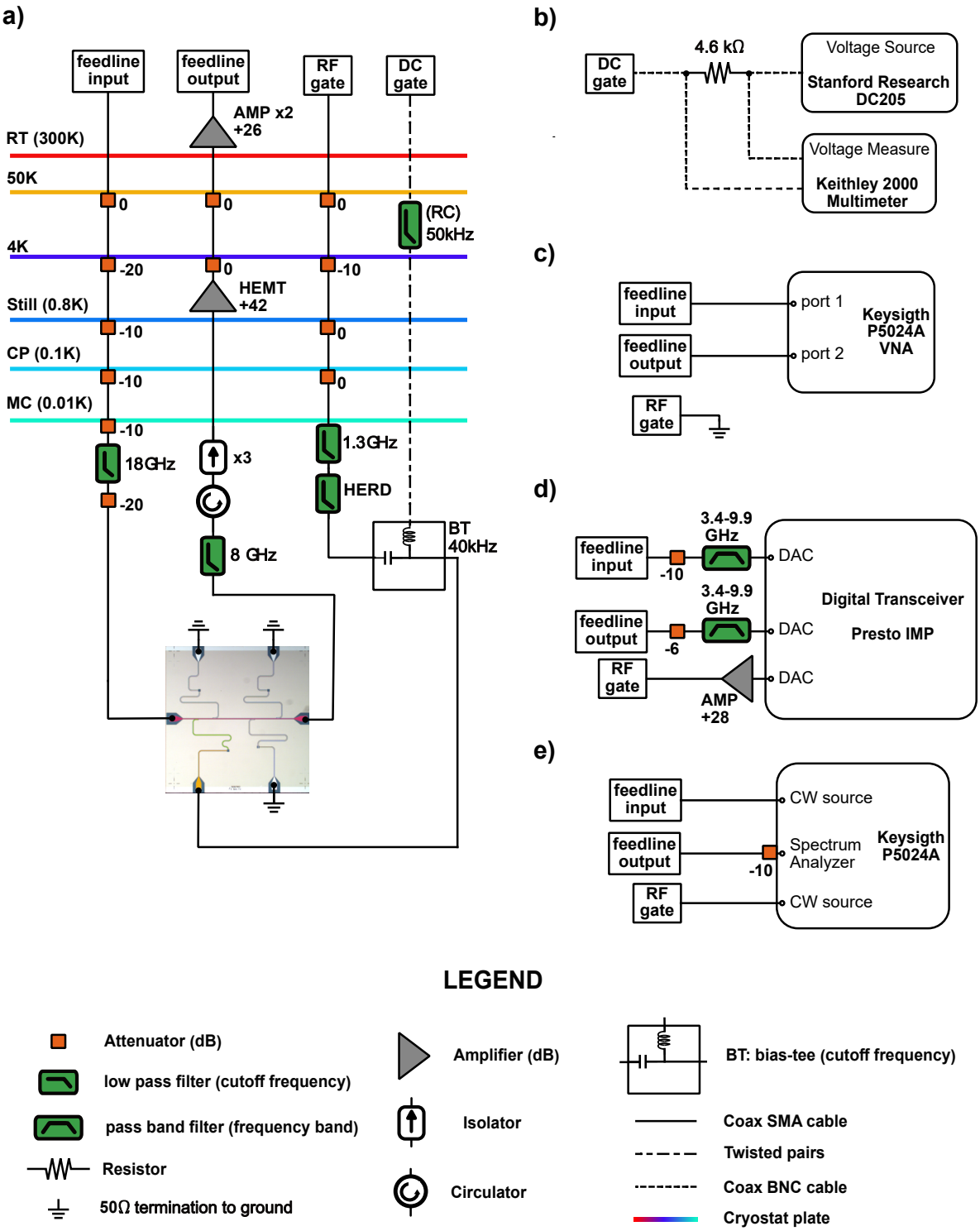


FIG. S6: Experimental setup. **a)** Simplified schematic of the of the cryostat where we perform the measurements. **b)** Scheme of the DC gate source and leakage current measurement. **c)** Scheme of the spectroscopy experiment. **d)** Scheme of the the time domain experiment. **e)** Scheme of the sideband experiments.

PAPER II

Losses in magnetic field resilient coplanar stripline resonators

Ivo P. C. Cools, Rodrigo M. López-Báez, **Vittorio Buccheri**, Oleg Shvetsov, Nermin Trnjanin, Emil Hogedal, and Saroj P. Dash

Journal of Physics D: Applied Physics **58**, 255102 (2025)

Contribution: The candidate contributed to setting up the dilution refrigerators for magnetic-field measurements and performing the magnetic characterization of the resonators. He fabricated the copper-powder filters used in this experiment.

Journal of Physics D:
Applied Physics

PURPOSE-LED PUBLISHING™

PAPER • **OPEN ACCESS**

Losses in magnetic field resilient coplanar stripline resonators

To cite this article: Ivo P C Cools *et al* 2025 *J. Phys. D: Appl. Phys.* **58** 255102

View the article online for updates and enhancements.

You may also like

- Effects of device geometry and material properties on dielectric losses in superconducting coplanar-waveguide resonators
V Lahtinen and M Möttönen
- Tunable superconducting resonators via on-chip control of local magnetic field
Chen-Guang Wang, , Wen-Cheng Yue et al.
- Substrate and process dependent losses in superconducting thin film resonators
Wei Chen, Douglas A Bennett, Vijay Patel et al.

This content was downloaded from IP address 129.16.75.216 on 27/05/2026 at 07:51

OPEN ACCESS
IOP Publishing
Journal of Physics D: Applied Physics
J. Phys. D: Appl. Phys. **58** (2025) 255102 (12pp)
https://doi.org/10.1088/1361-6463/added5

Losses in magnetic field resilient coplanar stripline resonators

Ivo P C Cools*, Rodrigo M López-Báez, Vittorio Buccheri, Oleg Shvetsov, Nermin Trnjanin, Emil Hogedal and Saroj P Dash

Department of Microtechnology and Nanoscience, Chalmers University of Technology, SE-41296 Gothenburg, Sweden

E-mail: Cools@chalmers.se

Received 26 February 2025, revised 23 May 2025
Accepted for publication 30 May 2025
Published 11 June 2025

Abstract

Coplanar waveguide (CPW) resonators have shown considerable success in circuit quantum electrodynamics research. However, their susceptibility to an external magnetic field limits their general functionality. In addition, electrical voltage gating for devices coupled to a CPW resonator necessitates alterations to the ground plane, changing the resonator characteristics. To avoid these problems, we fabricated and measured quarter wavelength differentially driven coplanar stripline (CPS) resonators made of NbTiN. We measured multiple devices with varying geometrical parameters in these novel resonators and analyse changes in their internal quality factor and two-level system losses. Furthermore, we establish the resilience of the resonators to an applied magnetic field by tracking the resonance frequency shift, without optimisation of the resonator geometry. Due to their flexible design and high magnetic field resilience, CPS resonators are particularly well-suited to study superconductor-semiconductor heterophysics where voltage gating or a magnetic field are necessary.

Keywords: resonator, quantum computing, Andreev bound states, superconductor, quantum information

1. Introduction

In recent years, superconducting microwave resonators have garnered significant attention in the field of circuit quantum electrodynamics (cQEDs) for their ability to enable precise readout and manipulation of qubits [1–3]. Among the various geometries used in this field, coplanar waveguide (CPW) resonators have emerged as the workhorse due to their ease of fabrication and high internal quality factors (Q_i) [4, 5]. These distributed element resonators consist of a single central conducting transmission line, separated from a ground plane carrying a return current, and are usually fabricated from a superconducting material (e.g. Al, Nb, NbTiN…). In cQED, the coupling strength between resonator and the dipolar moment of hybrid superconductor-semiconductor structures, such as electrons in single or double quantum dots [6–8], electronic spins [9, 10] or quasiparticles in semiconductors [11] can be tunable. It is mediated by the zero point voltage fluctuations $V_{ZPF} \sim \omega_R \sqrt{Z_R}$ in the resonator, where ω_R is the angular fundamental resonance frequency and $Z_R = \sqrt{\frac{L_R}{C_R}}$ is the characteristic impedance of the resonator as defined by the resonator's inductance, L_R, and capacitance, C_R. Hence, to achieve the strong coupling regime it is typically necessary to fabricate the device from a superconducting material with high kinetic inductance. Such applications often require electrostatic gating, which necessitates the interruption of the ground plane particularly when gating multiple devices per resonator.

* Author to whom any correspondence should be addressed.

Original Content from this work may be used under the terms of the Creative Commons Attribution 4.0 licence. Any further distribution of this work must maintain attribution to the author(s) and the title of the work, journal citation and DOI.

© 2025 The Author(s). Published by IOP Publishing Ltd

This alteration changes the characteristics of a CPW as it disturbs the return current flowing through the ground plane [12, 13], which requires significant alterations to the microwave environment or design [14]. Moreover, this introduces electromagnetic interference problems, such as the appearance of parasitic slotmodes [15]. Additionally, applications frequently require an externally applied magnetic field, which leads to the formation of vortices in the ground plane, resulting in energy dissipation [4, 16, 17].

A native approach to avoid these problems is to omit the interfering ground plane altogether and use a coplanar stripline (CPS) geometry. In this regard, we fabricated and measured differentially driven $\lambda/4$ CPS resonators made from 10 nm thick sputtered NbTiN (with kinetic inductance $L_K \cong 10$ pH/□). We start this paper by demonstrating the consistency of this novel type of resonator, shown by corresponding measurement and simulation results. We study in detail the different microwave loss mechanisms by varying geometrical parameters of the resonators. Both dependence on the width of the resonator prongs and the evolution of loss under an increasing prong-spacing are investigated. These geometrical parameters determine partially the losses in the resonator [18]. By examination of the power dependence of Q_i of each resonator together with a temperature dependence of the resonance frequency, insight is provided into the spectral distribution of two-level system (TLS) losses. This large variation in parameter space allows us to characterise resonators with impedances ranging from 81 to 681Ω, using a film with a relatively low kinetic inductance compared to similar measurements from high-impedance resonators in literature [19–21]. Finally, from the behaviour of the resonators in magnetic field, film parameters such as the electronic diffusion coefficient are determined.

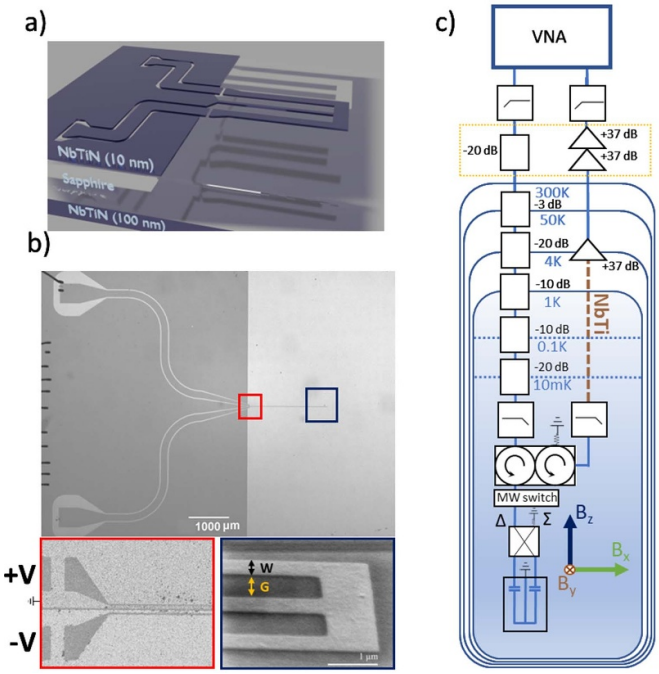


Figure 1. Experimental setup and sample specifics. (a) Schematic view of the sample stack. (b) Optical image of one resonator. Inset are SEM images of the capacitative gap coupler (red) and the resonator's end (dark blue), the latter visualising the definition of lead width *W* and gap *G*. (c) The dilution refrigerator and room-temperature microwave setup for the experiments. Elements enclosed in the yellow-dashed lines are only used for low-power measurements (below -30 dBm applied VNA power) to avoid resonator bifurcation at high powers.

2. Fabrication

The resonators are fabricated on double side polished 430±25 μm thick C-plane Al_2O_3 wafers. In a first step, these wafers are cleaned using a standard 5:1:1 RCA process of respectively deionised water, ammonia water and H_2O_2, heated to 80 °C for 10 min [22]. Subsequently both sides of the wafer are covered by sputtering on a target of $Nb_{81.9}Ti_{18.1}N$ in a near-UHV sputter system from DCA instruments [23], using an Ar:N_2 partial gas pressure ratio of 60:37. On the wafer's backside, approximately 100 nm of NbTiN is sputtered. During this stage of the fabrication process, the wafer is actively cooled with a cooling element. After a brief, *ex-situ* cleaning step with isopropyl alcohol, NbTiN is deposited on the sample-side of the sapphire: first, the wafer is pre-annealed at 660 °C for 30 min and then sputtered with NbTiN for 34 s. Subsequently, the CPS resonators are patterned on the sample side via e-beam lithography using a HSQ negative resist mask, pre-baked at 90 °C. An e-spacer 300Z conduction layer is applied to mitigate substrate charging. After development for 60 s in MF319, an Ar/Cl (4:50 sccm) ICP plasma etches the unwritten part of the metal [24, 25]. Finally, the HSQ is removed by a 30 s dip in a 2% HF solution. The final stack is shown in figure 1(a). After dicing, the sample is pasted using standard silver paint to the bottom of an oxygen free copper box, used for its high thermal conductivity at low temperatures [26]. Finally, it is bonded using Al/Si bondwires to a PCB.

3. Methods

Shown in figure 1(b) is an optical image of one of the resonators. A CPW feedline is used to route the signal from the PCB to the CPS resonator to minimise impedance mismatch. The CPS is connected to this feedline via standard in-plane gap coupling capacitors (bottom left inset in figure 1(b). We stress here that our CPS geometry does not involve a coplanar ground plane. This enables the potential use of gating structures near the resonator without significantly altering its characteristics, an area typically reserved for the groundplane in a CPW geometry. Furthermore, due to the differential drive of the CPS, a grounding strip line at zero-point DC voltage can be implemented to DC-ground coupled electrostatically sensitive structures. The presently shown resonators include this ground line to more accurately mimic a realistic measurement

scenario. To keep the fundamental odd resonance frequency at 6 GHz, the total length of each resonator is adjusted following simulation in Sonnet, necessitated by the variations in geometrical parameters (resonator lead width W and lead spacing G, as illustrated in a scanning electroscope image 1(b), bottom right inset). Via similar simulations, we estimate the external quality factor Q_C by estimations of the resonance frequency bandwidth using a lossless dielectric [4].

The devices are measured in a BlueFors LD dilution refrigerator, with base temperature $\sim$10 mK, using a setup as shown in figure 1(c). The VNA, a Keysight P5004A, is protected from DC signals by a high-pass filter (Mini-Circuits BLKD-183-S+ DC block) on both input and output sides. The probing signal is attenuated at the different temperature stages to achieve an upper bound of 10^{-3} noise photon number at the mixing chamber plate [27]. Besides the cryogenic attenuators, we assume an extra 6 dB attenuation from the CuNi coaxial microwave cabling [27, 28]. To further minimise stray infrared radiation causing quasiparticle generation [29], two in-house fabricated copper powder filters [30, 31] are mounted at the mixing chamber plate, both on the input and output side, with cut-off frequency at $\sim$18 GHz. A dual circulator-isolator (LNF-CIISC4_12A) routes the signal first to through a six-port microwave switch (Radiall Cryogenic SP6T switch) to the Δ-port of a 180°-hybrid (Krytar 4060 200) which splits the signal, allowing to differentially drive the resonator through two short phase-matched SMA cables between hybrid and sample. The reflected signal from the resonating sample is routed to an output line where a cryogenic low noise amplifier (LNF-LNC4_16B mounted at the 4 K stage) and two room-temperature HEMT low noise amplifiers (LNF-LNR4_14B) amplify the outgoing signal. Physically the resulting measurement is between ports 1 and 2 of the VNA (S_{21}-spectrum), yet due to the presence of the circulator in the measurement setup has to be seen as a reflection measurement of the resonator (S_{11}-spectrum). Magnetic field reliant data is measured in a similar dilution refrigerator but containing a vector magnet (AMI Cryogen-free MAxes Vector Magnet).

We use this setup to investigate the effect of varying W and G on the resonator losses in both power and temperature. Figures 2(a) and (b) show representative data in a small frequency window around the resonance frequency f_R of the resonator with $W = 1\,\mu$m and $G = 10\,\mu$m. Both a representative normalised $|S_{11}|$ plot and the normalised data represented in the IQ-plane are shown. Reflection data is fitted around the fundamental odd resonance using the diameter-correction method [32, 33], taking into account the fact that the resonators are purely reflectively measured (and thus not hanger-type). In that case, we describe S_{11} as [34]:

$$S_{11} = a e^{i\alpha} e^{-2\pi i f_R \tau} \left(1 - \frac{2Q_l}{\widetilde{Q_c}} \frac{1}{1 - 2iQ_l\left(\frac{f_R - f}{f_R}\right)}\right). \quad (1)$$

Here, the prefactor $a e^{i\alpha} e^{-2\pi i f_R \tau}$ is due to the resonator's environment: a is the attenuation factor of the signal, $e^{i\alpha}$ acts as a phase prefactor and $e^{-2\pi i f_R \tau}$ is due to the electrical delay

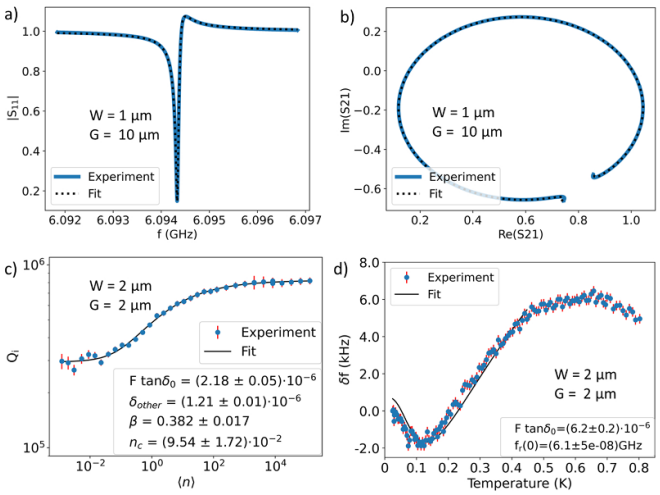


Figure 2. Representative fits and plots of the losses of coplanar stripline resonators. (a) Normalised $|S_{11}|$ versus frequency for the resonator with width $W = 1\,\mu$m and gap $G = 10\,\mu m$. Experimental data (blue) is fitted to equation (5) (black dashed line). (b) The resonator of (a), plotted in the IQ-plane, showing the effect of the impedance miss-match near the off-resonance point. (c) A representative power-dependent evolution of the internal quality factor of the resonator with $W = 2\,\mu$m and $G = 2\,\mu$m. The experimentally determined internal quality factor Q_i values (blue), including error bar (red), are fitted to equation (5) (black). (d) Low-temperature dependent resonance shift at zero magnetic field at high average internal photon level. The experimentally determined frequency shift δf values (blue), including error bar (red), are fitted to equation (6) (black).

in the refrigerator's microwave lines. Furthermore, Q_l is the total quality factor, combining both Q_i, the internal and the complex external quality factor $\widetilde{Q_c} = |Q_c|\exp(-i\phi)$ as $Q_l^{-1} = Q_i^{-1} + Q_c^{-1}$. This complex Q_c describes the asymmetry in the Lorentzian line shape of $|S_{11}|$ and is attributed to either an impedance mismatch [4], an extra series inductance from the wire bond connections [35, 36] or even reflections in the resonator's feedline [37]. For the data in the IQ-plane, the mismatch exhibits itself as non-circular behaviour near the off-resonance point. Simulation in the open-source software package QUCS [38] hints towards a phase-mismatch of the cables after the hybrid as a potential source of this ϕ-factor (appendix D). For the dataset shown in figures 2(a) and (b), the mismatch is $\phi = -0.43$. Fitting scripts are available on the group's GitHub page [39].

To verify whether standard CPW resonator routines (e.g. simulation) work for differentially driven CPS resonators, we present the data in figure 3. When fabricating a sample, we measure the DC sheet resistance of the NbTiN film which allows us to estimate the kinetic inductance via equation [40] 2:

$$L_k\,(\mathrm{T} = 0\mathrm{K}) = \frac{\hbar R_N}{\pi \Delta_0}, \quad (2)$$

where we use the superconducting energy gap of NbTiN via the BCS theory for extremely dirty superconductors: $\Delta_0 =$

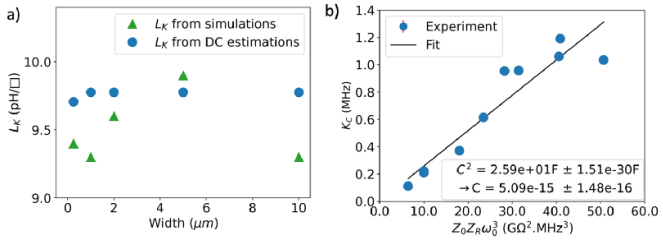


Figure 3. (a) The estimated kinetic inductance L_K of each sample from DC measurement of bulk films at room temperature, compared to the estimated kinetic inductance from simulations of the resonance in the mK regime. Green triangles are the simulated L_K, blue circles are the estimated L_K from DC measurements. (b) Validity test of the simulation and fitting procedures. The external quality factor Q_c is plotted versus the rescaled simulated impedance of the resonators. A fit is performed using equation (3).

$1.764 k_B T_c$ [41–43]. The critical temperature T_c is estimated from previous DC measurements on NbTiN films of the same thickness (15.2 K), while the normal state resistance R_N is ideally measured right above T_c. As the resistance of disordered metals does not change appreciably with temperature, we estimate it from measurements at room temperature. All DC parameters of a representative film are shown in appendix A. We correspond the resulting inductance value to the kinetic inductance we obtain from a comparison between a simulated resonance frequency in Sonnet to the fitted resonance frequency from measurements [21]. This data is shown in figure 3(a). We attribute deviations to fabrication tolerances, a slight non-uniformity of the film thickness and the crude estimation of the kinetic inductance using only the room-temperature sheet resistance. A second check of simulations versus measurements is shown in figure 3(b). From fitting resonator data we obtain the external quality factor Q_c while from resonator simulations we obtain its impedance Z_R. The relation between Q_c and Z_R is (derived in appendix B)

$$Q_c = \frac{\pi}{4\left(2\pi f_R\right)^2 C_c^2 Z_0 Z_R}. \tag{3}$$

This allows us to derive the coupling capacitance C_c. In the resonator designs, this capacitance was kept approximately constant. However, deviations cause discrepancies between data and fit, e.g. due to the increasing width of the conductor which changes C_c but was unaccounted for. Furthermore, a constant f_R was assumed, but here a natural variation due to slightly differing kinetic inductances was also observed. Finally, at smaller resonator conductor width, fabrication errors become relatively more pronounced (i.e. at higher Z_R). We use equation (3) to do a linear fit to the coupling rate $\kappa_c = \frac{2\pi f_R}{Q_c}$ in function of $Z_R f_R \times Z_0 f_R^2$ to obtain the coupling capacitance directly, and we get a reasonable value of $C_c = (5.09 \pm 0.148) \times 10^{-15}$ F. We find the correspondence enough to conclude that standard industry CPW simulation and fitting routines are applicable to CPS resonators.

4. Losses

To understand the behaviour of TLS losses on the resonator, the evolution of Q_i on input power is studied at base refrigerator temperature. As input power varies depending on the exact attenuation, the unitless quantity of average photon number $\langle n \rangle$ is used instead, defined as [44, 45]:

$$\langle n \rangle = \frac{4}{2\pi h f_R^2} \frac{Z_0}{Z_R} \frac{Q_l^2}{Q_c} P_{IN} \tag{4}$$

where both the characteristic impedance of the input feedline, Z_0, as that of the resonator Z_R play a role as well as the input power P_{IN} at the resonator's feedline. At low temperature, we fit the power-dependent Q_i to [45, 46]:

$$\frac{1}{Q_i} = \frac{F \tan\left(\delta_{tls}^0\right)}{\left(1 + \frac{\langle n \rangle}{n_c}\right)^\beta} + \delta_{other} \tag{5}$$

where F is a material dependent filling factor of the electric field [45], $\tan(\delta_{tls}^0)$ the intrinsic TLS loss tangent of the same material, and δ_{other} is usually dominated by the next-largest loss channel of the resonator. Furthermore, the amount of photons needed to saturate the TLS is given by n_c, while β is determined by the interacting strength between individual TLS. For non-interacting TLS [47], β equals 0.5 . We neglect the effect of quasiparticles with increasing μw-power [12, 48] due to the comparatively low kinetic inductance fraction in these resonators [49] and the presence of low-pass copper powder filters filtering away high energy radiation. A representative fit is shown in figure 2(c). In this plot, the difference between high and low power saturation values is attributed to the TLS losses. Since this power-dependence approach only probes a narrow window of TLS around the resonance, they are called the *narrow-band TLS losses*. [50, 51]. At higher power, the intrinsic kinetic inductance of the resonator causes a bifurcation, likely a Duffing non-linearity [52], complicating the fitting procedure. We do not include these points in our fit, as a full description is outside the scope of this paper.

On the other side, the *wide band TLS losses* are uncovered by the temperature dependence of the real part of the dielectric constant, usually measured via the shift in relative resonance frequency up until ~1 K [47, 53]:

$$\delta f = \frac{\Delta f}{f_0} = \frac{k}{\pi}\left(\mathrm{Re}\left[\Psi\left(\frac{1}{2} + \frac{1}{2\pi i}\frac{h f_R(T)}{k_B T}\right)\right] - \ln\left(\frac{h f_R(T)}{k_B T}\right)\right). \tag{6}$$

Here is $\Delta f = f_R(T) - f_0$ the temperature-dependent resonance frequency referenced at low temperature (in our data at 10 mK) while Ψ is the complex digamma function. The factor $k = F\delta_{tls}^{0,i}$ contains the intrinsic temperature dependent TLS-loss component, $\delta_{tls}^{0,i}$, which is sensitive to thermally varying TLS for a wide spectrum [24].

As these off-resonant TLS are not saturated, the frequency shift is nearly power independent and it is possible to gather data at higher powers which speeds up measurements. We used

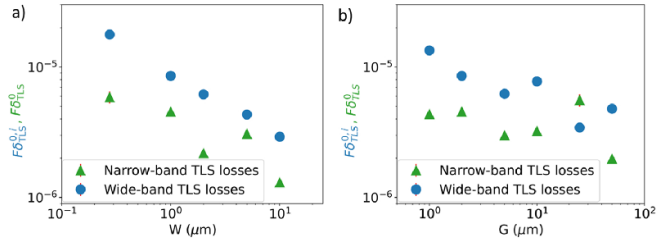


Figure 4. The evolution of the geometrically dependent loss tangent of the narrow-band losses $F\delta^0_{\rm tls}$ (green triangles) and the wide-bands losses $F\delta^{0,i}_{\rm tls}$ (blue circles) (a) decreases with increased width W of the resonator leads (for constant gap spacing $G = 2\,\mu$m) and (b) decreases with an increasing G of the leads (for constant $W = 1\,\mu$m).

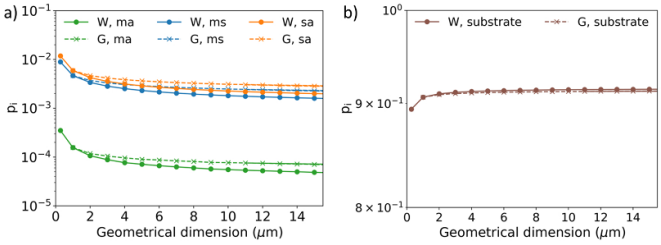


Figure 5. Simulation of the participation ratios of different dielectric volumes of the resonators. (a) Simulation of the metal-air (ma), metal-surface (ms) and surface-air (sa) interfaces, threaded by the electric field and their evolution with geometrical parameter (resp. W, width, in full line and circle, and G, the gap, in dashed line and cross). (b) Simulation of the participation ratio of the substrate and its evolution with geometrical parameter.

$\langle n\rangle = 1\text{e}5$, which for each resonator is in the high-power saturated regime [51]. At higher temperatures, the onset of quasiparticles dominates the resonator's frequency shift and losses [21, 54]. For this reason we constrained our fits to data up to 450 mK, still well below the superconducting energy gap of NbTiN. A representative fit of the temperature dependent frequency shift is shown in figure 2(d). The presence of a universal dip in the relative frequency shift at $T \approx \frac{\hbar\omega_{\rm R}}{2k_{\rm B}}$ supports the validity of equation (6) for these resonators, and confirms that quasiparticle loss is not a dominant factor in the total loss of the resonator [49, 55]. The observed discrepancy between fit and experimental data at very low temperatures has similarly been observed for TLS-dominated CPW resonators [56, 57] .

Using the established fitting and simulation procedure, we quantify the losses depending on resonator lead geometry using the aforementioned methods (power and temperature dependence, with fits to resp. Equations (5) and (6). As shown in figure 4, we observe decreasing losses with both W-dependence of the lead as with G, which is on the same order of magnitude as results of similar geometric dependences of CPW resonators [4, 53, 58, 59]. We report the data of all devices numerically in appendix C. We explain the geometric behaviour by the fact that the current density (and hence electric field) is highest on the inner edges of the differentially driven resonators [60, 61]. This means that the interaction of the field with the TLS is enhanced there and thus TLS losses are higher for resonators with a relatively larger contribution of conductor-edge to total-resonator-surface. These are the narrower resonators, as the data shows. In a similar vein, an increased gap to lead-width ratio decreases the current density at the inner edge and improves the TLS losses.

We support this conclusion by the simulations of interface participation ratios $p_{\rm i}$ shown in figure 5(a). This entity describes how much of the electrical field is threaded through each individual volume in the resonator. As electric field couples to the dipolar TLS, a higher participation ratio leads to a relatively larger loss for a given volume. We describe these ratios by the penetrating of the field through four dielectric regions: metal-air (ma), metal-substrate (ms), substrate-air (sa) and substrate. Here, we neglect the influence of the participation ratio of the perfect vacuum volume. More details on the simulation are given in appendix F. The metal-air interface has two orders of magnitude less contribution to loss participation than both the ms and the sa interfaces, including at higher dimensions of both width and gap. As the participation ratio of the lossy dielectric interfaces drop for larger geometrical dimension, the relative contribution of the substrate related losses increase as shown in figure 5(b). This is because the total electrical field penetrating the ms and ma interfaces scale as approximately respectively W or G while the total field in the substrate scales as approximately W^2 and G^2. Since the losses of bulk sapphire are negligible compared to those in the resonator surfaces (the bulk average losses of sapphire are in the range of $10^{-7} - 10^{-9}$, while those of the resonator surfaces are around $10^{-3} - 10^{-4}$), the overall internal quality factor decreases with increasing width and gap as observed [62, 63].

5. Magnetic field dependence

The behaviour of the resonance frequency to a magnetic field is shown in figure 6. These measurements were taken at an average photon number of $\langle n\rangle \sim 10^4$. The thick substrate effectively shields the resonator current distribution from the effect of vortex nucleation on the superconducting plane on the sample's backside [60]. Hence, the magnetic field behaviour is fully due to the currents circulating in the resonator leads. In general, the relative frequency shift due to the supercurrent depairing by a parallel magnetic field is well approximated by a quadratic relation of the form

$$\frac{\Delta f_{\rm R}(B)}{f_{\rm R,0}} = -k_{\parallel}B_{\parallel}^2 \tag{7}$$

$$= \frac{-\pi}{48}\frac{De^2}{\hbar k_{\rm B}T_{\rm c}(0)}B_{\parallel}^2 t^2, \tag{8}$$

valid for thin films where the t is much smaller than the *effective* London penetration depth, $\lambda_{\rm eff} = \lambda(1 + \frac{\xi_0}{l})^{\frac{1}{2}}$, around 1 μm for these films [43, 64–67]. Here, λ, ξ_0 and l are respectively the London penetration depth, the coherence length of NbTiN and the elastic electron mean free path, for which representative values are shown in appendix A.

We extend this formalism to a perpendicular magnetic field. In that case [68], as $t \ll \lambda_{\rm eff}$, the screening distance

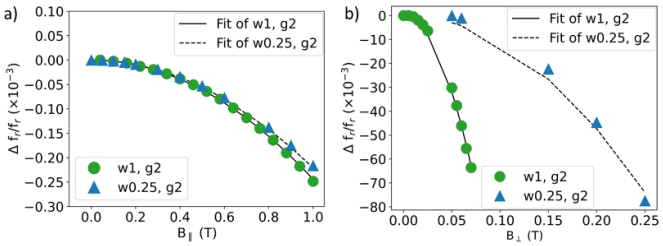


Figure 6. The relative shift of the resonance frequency of the resonator with width $W = 0.25\,\mu$m and 1 μm (gap spacing $G = 2\,\mu$m) when sweeping an external magnetic field. Error bars are smaller than the data points. (a) and (b) Evolution of the frequency shift under an in-plane (perpendicular) applied field. Data is fit to $\frac{\Delta f_R}{f_R} = -k_{\parallel(\perp)}B^2_{\parallel(\perp)}$.

takes the form of $\lambda_\perp = \frac{\lambda^2_{\rm eff}}{t} \approx 100\,\mu{\rm m} \gg W$. This validates our approach to use W instead of t for perpendicular fields in equation (8). For the data shown in figure 6, we get $k_{0.25\mu{\rm m},\perp} = 1.18 \pm 4.81 \times 10^{-2}\ {\rm T}^{-2}$ and $k_{1\mu{\rm m},\perp} = 1.28e1 \pm 1.37 \times 10^{-1}\ {\rm T}^{-2}$. In this approximation, we can derive directly the electron diffusion coefficient D of the NbTiN films. We obtain diffusion coefficients of $D_{1\mu{\rm m}} = 1.55\,{\rm cm}^2\ {\rm s}^{-1}$ and $D_{0.25\mu{\rm m}} = 2.29\,{\rm cm}^2{\rm s}^{-1}$ from the perpendicular field data, which is in line with earlier reported results on NbTiN [19, 20, 65, 69].

We use these derived diffusion coefficients of the material to recreate the effective electronic thickness of the film. For this, we determine the k-values of the devices under an in-plane applied magnetic field parallel to the resonator direction with equation (8). We extract respective k-values of $k_{0.25\mu{\rm m},\parallel} = 2.23 \times 10^{-4} \pm 4.0 \times 10^{-7}\,{\rm T}^{-2}$ and $k_{1\mu{\rm m},\parallel} = 2.47 \times 10^{-4} \pm 3.74 \times 10^{-7}\,{\rm T}^{-2}$, which results in calculated electronic film thicknesses of 4.39 nm and 3.44 nm for the 1 μm and 250 nm wide resonators, respectively. We attribute the difference to the physical layer thickness to rough granular structure of the NbTiN, especially near the substrate surface, and the suppression of shielding currents within one coherence length from the surfaces. Finally, we stress the resonator's reliability in magnetic field from the consistent and low relative resonance frequency shift up to 1 T for a parallel field and up to 250 mT for a perpendicular field.

6. Summary

In conclusion, this paper presented the fabrication and characterisation of differentially driven CPS superconducting resonators with varying geometrical parameters, made from a 10 pH/□ NbTiN layer. By varying the width of the conductor leads and the spacing between the conductor pair, we achieved impedances ranging from 81 to 681 Ω. This stresses the flexibility of the CPS as its impedance is proportional to the coupling strength with a dipolar moment of e.g. Andreev bound states in semiconducting nanowires [70]. Moreover, the lack of groundplane makes these resonators an ideal platform for the next generation of superconductor-semiconductor heterostructure coupled devices, as they enable electrostatic gating without compromising resonator characteristics. Through the use of standard fitting techniques, we determined that losses are dominated by TLS in the zero-field regime. Furthermore, magnetic field indicates a high electronic diffusion constant of the NbTiN films, suggesting a high film quality. The films are especially resilient to parallel magnetic fields, which are paramount for cQED Majorana research. Future work includes incorporating semiconductor nanostructures into these resonators to directly measure the spectrum of an Andreev molecule.

Data availability statement

The data cannot be made publicly available upon publication because they are not available in a format that is sufficiently accessible or reusable by other researchers. The data that support the findings of this study are available upon reasonable request from the authors.

Acknowledgments

Devices were fabricated in the Myfab cleanroom Chalmers, and we acknowledge the help we got from Nanofabrication Laboratory engineers. We have gained a lot from useful discussions with V Fatemi, T Connolly, S Mahashabde, F Joint, D Winkler and B Dalelkhan. L Jönsson's help was invaluable to fabricate sample boxes and in other mechanical help. I P C C, V B and N T acknowledge support by the European Union's H2020 research and innovation program, grant no. 804988 (SiMS) and 828948 (AndQC). We gracefully acknowledge A Geresdi in obtaining this funding.

Conflict of interest

The authors have no conflicts to disclose.

Appendix A. DC characterisation

We performed DC characterisations of our NbTiN films in a four-point Hall bar geometry, with channel width 10 μm, length 595 μm and specifically fabricated out of the same film as the resonator with both width and gap 2 μm. All DC results are summarised in figure 7. We first measure the critical temperature T_c of the nominally $d = 10$ nm thick film. In figure 7(a), we show the $R(T)$ plot taken by cooling the sample from room temperature (bias 100 nA) to base temperature (2 K) in a Quantum Design DynaCool PPMS. From the data we obtain $R_n = 98.3\ \Omega/\square$ (near T_c) and a critical temperature of 15.2 K. To estimate this T_c we use a 1 $\Omega/\square$ cut-off. Subsequently, shown in figure 7(b), we perform Hall measurements. This happens at 30 K to avoid potential interference of superconducting current screening. We again use a current-biased four-point measurement scheme with $I = 25\,\mu$A to measure the Hall-voltage $V_H(B)$. Furthermore, we account for a small voltage offset of 1.2 μV, likely due to fabrication errors in the Hall bar (misalignment of the arms). A linear fit to the

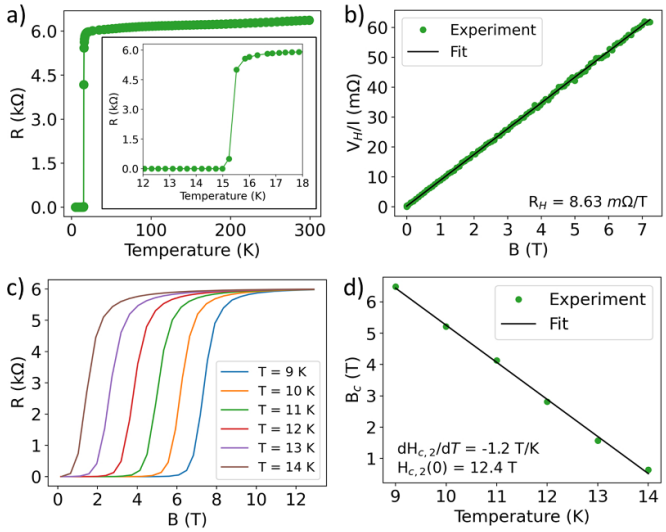


Figure 7. DC measurement data of our nominally 10 nm thick NbTiN films. (a) $R(T)$ plot, taken in decreasing temperature, with the insert showing a finer scan (increasing temperature) around $T_c = 15.2$ K. (b) Current biased (25 μA) Hall measurement to extract the Hall-coefficient. Via a linear fit we extract $R_H = 8.62\,\mathrm{m\Omega\,T^{-1}}$. (c) Small subset of the B(T)-phase diagram for the film. We use a 1 $\Omega/\square$ cut-off to estimate the critical magnetic field B_c at every fixed temperature. (d) The estimated critical fields in function of the temperature near T_c. A fit to equation (A1) data generates $H_{c,2}(0) = 12.4\,\mathrm{T}$ and $\frac{dH_{c,2}}{dT} = -1.2\,\mathrm{T\,K^{-1}}$.

data gives a Hall coefficient of $R_H = 8.63\,\mathrm{m\Omega\,T^{-1}}$. This coefficient is also defined as $R_H = \frac{1}{n_e e d}$; hence we obtain consecutively the electron carrier density $n_e = 7.23 \times 10^{28}\,\mathrm{m^{-3}}$ and the Fermi wave vector $k_F = (3\pi^2 n_e)^{\frac{1}{3}} = 12.9\,\mathrm{nm^{-1}}$ from the Hall measurement. Finally, we derive the elastic electron mean free path $l_e = \frac{\hbar k_F}{n_e e^2 R_n d} = 0.74\,\mathrm{nm}$, a value similar to other NbTiN films reported in literature [65].

To extract the NbTiN coherence length, we first measure a $B(T)$ diagram under a constant applied current bias of 25 nA, shown in figure 7(c). By scanning the magnetic field at fixed temperatures, we obtain the critical magnetic field B_c for each. Again, we use a 1 $\Omega/\square$ cut-of criterion. The close-to-T_c tail-end of the B_c's is shown in figure 7(d). Here, we can extract the critical field at 0 K for a type-II superconductor from fitting the data to the Werthamer-Helfand-Hohenberg formula [71]

$$B_{c,2}(0) = -\ln(2)\, T_c \left(\frac{dB_{c,2}}{dT}\right)_{T=T_c}. \tag{A1}$$

Using our initially measured $T_c = 15.2$ K, this gives $B_{c,2} = 12.4$ T. As the last step, we derive the Ginzburg–Landau coherence length as $\xi(0) = \sqrt{\frac{\phi_0}{2\pi B_{c,2}(0)}}$, giving $\xi(0) = 5.1$ nm.

Appendix B. Qc in Zr derivation

To derive equation (3), we followed the same procedure as [20], but adapted to pure reflection type $\lambda/4$-resonators. The input impedance of a shorted $\lambda/4$ line is given by [72]

$$Z_{in} = \frac{2Z_R}{\frac{\pi}{2Q_i} + \frac{i\pi\Delta\omega_0}{\omega_0}} \tag{B1}$$

where Z_R is the resonator's characteristic impedance and $\Delta\omega_0$, the drive frequency ω offset to the bare resonator resonance frequency ω_0. Coupling the resonator to the environment is usually done via a coupling capacitance C_c. This changes both the impedance,

$$\begin{aligned} Z_{tot} &= Z_{in} + \frac{1}{i\omega C} \\ &= 2Z_R \frac{\frac{2Q_i}{\pi} - i\left[\frac{4Q_i^2}{\pi}\frac{\Delta\omega_0}{\omega_0} + \frac{1}{2\omega Z_R C_c}\left(1 + 4Q_i^2\left(\frac{\Delta\omega_0}{\omega_0}\right)^2\right)\right]}{1 + 4Q_i^2\left(\frac{\Delta\omega_0}{\omega_0}\right)^2}, \end{aligned} \tag{B2}$$

and the resonance frequency to a new value, ω_R:

$$\frac{\Delta\omega_0}{\omega_0} = \frac{2}{\pi}\omega_R Z_R C_c. \tag{B3}$$

Here, we used the fact that $\mathrm{Im}(Z_{tot}) = 0$ at resonance and the assumption that $\frac{Q_i^2}{\pi^2} \gg \frac{1}{4\omega_R^2 C_c^2 Z_R^2}$ which is valid for most resonators with $Q_i \gtrsim 1\mathrm{e}5$. Under this assumption, the total impedance at resonance becomes:

$$\begin{aligned} Z_{tot} &= \frac{4Z_R Q_i}{\pi}\frac{1}{1 + \frac{1}{\pi^2}16Q_i^2\omega_R^2 Z_R^2 C_c^2} \\ &= \frac{\pi}{4Q_i Z_R \omega_R^2 C_c^2}. \end{aligned} \tag{B4}$$

Equating two general forms of $|S_{11}|$ leads by identification to the desired result [33, 72]:

$$|S_{11}| = \left|\frac{1 - \frac{Z_0}{Z_{tot}}}{1 + \frac{Z_0}{Z_{tot}}}\right| = \left|\frac{1 - \frac{Q_i}{Q_c}}{1 + \frac{Q_i}{Q_c}}\right| \tag{B5}$$

thus

$$Q_c = \frac{\pi}{4Z_0 Z_R \omega_R^2 C_c^2}. \tag{B6}$$

Appendix C. Table of measured resonator parameters

The tabulated values of all measured resonators are shown in table 1. We report the narrow-band (power-dependent) loss tangent $\tan(\delta_P)$, the wide-band (temperature dependent) losses $\tan(\delta_T)$, and the high-power loss tangent (δ_{other}).

Table 1. Measured and inferred values of all resonators data. The device with width $W = 1\,\mu$m and gap $G = 2\,\mu$m are used as the base design. Both the reported internal and external quality factors Q_i and Q_c are extracted at average internal photon number $\langle n\rangle = 1$.

W (μm)	G (μm)	L_K ($\frac{\mathrm{pH}}{\square}$)	f_R (GHz)	Z_R (Ω)	Q_i ($\times 10^4$)	Q_c ($\times 10^4$)	$\tan(\delta_\mathrm{P})$ ($\times 10^{-6}$)	$\tan(\delta_\mathrm{T})$ ($\times 10^{-5}$)	δ_other ($\times 10^{-6}$)
1	1	9.9	5.98	287	40.3	6.09	4.362	13.43	1.33
1	2	9.3	6.19	310	6.35	4.07	4.547	8.564	15.0
1	5	9.8	6.11	359	65.6	4.01	2.996	6.243	0.748
1	10	9.7	6.09	389	7.87	11.3	3.231	7.766	11.3
1	25	8.8	6.36	411	25.8	3.76	5.583	3.437	2.89
1	50	9.5	6.17	454	4.53	3.27	1.983	4.789	21.6
0.275	2	9.4	5.79	681	47.9	3.50	5.870	17.76	1.66
2	2	9.6	6.10	208	46.9	10.3	2.184	6.181	1.21
5	2	9.9	5.96	123	87.8	16.9	3.074	4.326	0.285
10	2	9.3	5.91	81	44.0	33.6	1.303	2.923	1.19

Appendix D. Derivation of $\langle n\rangle$

To derive the average photon number $\langle n\rangle$ that circulates in the resonator due to an applied power P_in, we use the general form of S_{11}, given by equation (B5). Then, the absorbed power by the resonator P_abs is given by [73]:

$$\begin{aligned} P_\mathrm{abs} &= P_{in} - |S_{11}|^2 P_\mathrm{IN} \\ &= \frac{\hbar\omega_\mathrm{R}^2\langle n\rangle}{Q_\mathrm{i}} \end{aligned} \tag{D1}$$

which means that

$$\langle n\rangle = \frac{4Q_l^2}{\hbar\omega_\mathrm{R}^2 Q_\mathrm{c}} P_\mathrm{IN} \tag{D2}$$

as $Q_l = \frac{Q_\mathrm{i}Q_\mathrm{c}}{Q_\mathrm{i}+Q_\mathrm{c}}$. To account for reflections due to impedance mismatch, the final result becomes:

$$\langle n\rangle = \frac{Z_0}{Z_\mathrm{R}}\frac{4Q_l^2}{\hbar\omega_\mathrm{R}^2 Q_\mathrm{c}} P_\mathrm{IN} \tag{D3}$$

We stress that experimentally most of these values are an approximation, and hence $\langle n\rangle$ is approximate as well.

Appendix E. Phi-factor

Some of the data sets presented in this work show a non-ideal Lorentzian behaviour caused by the resonator's environment, leading to a complex Q_c factor in equation (1). To investigate both the cause of this ϕ-factor and the sporadic 'negative' Q_i observed in the resonator magnetic field spectra (not shown), computational simulations were conducted with the open-source circuit simulator QUCS [38] as shown in table 2. Initially, a perfectly matched sample behaviour was modelled to establish a baseline. Subsequently, controlled perturbations were introduced to various parameters to investigate potential sources contributing to the shoulder-like features observed in the Lorentzian profile governing the magnitude spectrum of the resonator. Finally, we attempt to recreate a ϕ-value corresponding to measurement.

The first aspect investigated is the phase mismatch in the transmission lines between hybrid and sample (*H–S leads*). Here, we varied the cable lengths to induce a phase difference (attributable to electrical length) between the signals emerging from the -3 dB ports of the 180° hybrid. Secondly, we assess the impact of an impedance mismatch in the wirebonds (*Wirebonds*, length and impedance). Notably, this introduces a very large shoulder behaviour in the Lorentzian lineshape, as shown in figure 8(a). Then, we model the non-ideal behaviour of the hybrid by directly altering the phase relation between its output ports (*Hybrid a–e*). This modification did not lead to large changes in the ϕ-factor when using realistic values.

Subsequently, to exclude the influence of the internal quality factor, we vary the resonator's R_R (which directly defines Q_i in QUCS simulations). This is shown in *R resonator a–c*. Even over many orders of magnitude, we observe no appreciable difference in ϕ, indicating that non-ideal Lorentzian behaviour primarily stems from the imperfections introduced in the 180° hybrid component or from wirebonding impedance mismatches. However, we observe the occurrence of a negative Q_i for the higher R_R value, indicating that it may be the ratio between Q_i and Q_c that is of importance. This is only valid when imperfections in the system are present, as shown in the *ideal, high* Q_i resonator behaviour.

To verify the effect of changing coupling factor $g = \frac{Q_\mathrm{i}}{Q_\mathrm{c}}$, we altered Q_c of two resonators by changing their coupling capacitances (*Coupling C*(a)–(b), keeping their g consistent with respectively the resonators *R resonator.a* and *R resonator.b*. We conclude that, under similar circumstances, a higher g increases ϕ, which is attributed to a lower coupling to external impedance mismatches. We could not do the same simulations for *R resonator.c* as it is not possible to define a coupling factor for a negative Q_i (which is unphysical). We stress that these negative Q_is are not physical values, but have to be seen as a convolution of environment and resonator. We show the excellent agreement between fit and simulated data in figure 8 for the simulation *Wirebonds.a*. This confirms in part that especially without a well-known background, getting an accurate value of Q_i for pure reflection type resonators is difficult and leads to inaccuracies not present in

Table 2. Tabulated simulation data of various resonators to uncover the cause of the non-ideal Lorentzian shape of some resonator profiles. The parameters f_r, Q_i, Q_c and ϕ are derived from fitting of simulation.

Variation	Hybrid (°)	*H*–*S* leads (mm), (Ω)	Wirebonds (mm), (Ω)	Coupling *C* (fF), (fF)	R_R (MΩ)	f_r (GHz)	Q_i (1×10^{-5})	Q_c (1×10^{-4})	ϕ (rad)
Ideal	180	100, 50	4, 50	5	100	5.964	10.03	1.14	1.54×10^{-6}
		100, 50	4, 50	5					
Ideal, high Q_i	180	100, 50	4, 50	5	10×10^{-3}	5.964	1.003×10^{-3}	1.14	3.948×10^{-08}
		100, 50	4, 50	5					
Phase mismatch	180	98.3, 50	4, 50	5	100	5.964	−968.1	1.13	1.952×10^{-4}
		100, 50	4, 50	5					
Wirebonds.a	180	100, 50	4, 90	5	100	5.964	−4.921	1.16	5.89×10^{-2}
		100, 50	4, 30	5					
Wirebonds.b	180	100, 50	2.3, 50	5	100	5.964	-1.003×10^{-3}	1.13	1.71×10^{-4}
		100, 50	4, 50	5					
Hybrid.a	167.5	100, 50	4, 50	5	100	5.964	−154.1	1.13	2.264×10^{-4}
		100, 50	4, 50	5					
Hybrid.b	167.9	100, 50	4, 50	5	100	5.964	3040	1.13	2.118×10^{-4}
		100, 50	4, 50	5					
Hybrid.c	170	100, 50	4, 50	5	100	5.964	3.103×10^{-6}	1.14	1.443×10^{-4}
		100, 50	4, 50	5					
Hybrid.d	175	100, 50	4, 50	5	100	5.964	1.205	1.14	3.690×10^{-5}
		100, 50	4, 50	5					
Hybrid.e	185	100, 50	4, 50	5	100	5.964	1.025	1.14	3.689×10^{-5}
		100, 50	4, 50	5					
R resonator.a	170	100, 50	4, 50	5	10	5.964	1.076	1.14	1.582×10^{-4}
		100, 50	4, 50	5					
R resonator.b	170	100, 50	4, 50	5	146	5.964	121.9	1.13	1.438×10^{-4}
		100, 50	4, 50	5					
R resonator.c	170	100, 50	4, 50	5	250	5.964	−36.26	1.14	1.434×10^{-4}
		100, 50	4, 50	5					
Coupling C.a	170	100, 50	4, 50	1.575	100	5.983	10.73	11.3	4.671×10^{-5}
		100, 50	4, 50	1.575					
Coupling C.b	170	100, 50	4, 50	6.046	100	5.958	79.72	0.7783	1.736×10^{-4}
		100, 50	4, 50	6.046					
Combination	170	100, 50	7, 10	5	10	5.964	1.511	1.704	6.016×10^{-1}
		100, 50	4, 90	5					

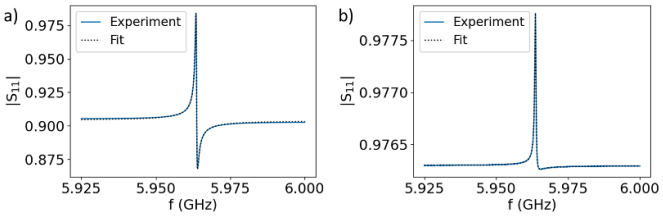


Figure 8. (a) and (b) The simulation of respectively samples *Wirebonds.a* and *Hybrid.a*, showcasing the excellent fit even with a virtual negative internal quality factor.

hanger-mode resonator fitting [4]. The root cause is that with a pure reflection type of resonator, one essentially probes the entire microwave structure in which the resonator is embedded, which can cause constructive interference between the ingoing and outgoing signal. However, since this environment is only minimally power and temperature dependent, we stress that the methodology of using *differences* of Q_i as used in our paper remains valid.

Finally, we combine all potential contributing factors to replicate a similar ϕ as to the measured resonators. Especially the wirebonding impedance mismatch is of prime importance to achieve a realistic result. In practice, such mismatch occurs by e.g. having wirebonds go loose during sample cooldown. Hence, to avoid non-ideal Lorentzian behaviour in these resonators, we suggest to add multiple wirebonds per contact pad. Furthermore, we conclude that the occurrence of a negative Q_i is not directly related to a high ϕ-factor, yet does require a non-symmetric environment. It will only occur at a higher coupling factor.

The custom hybrid S_{11} file, together with the simulation files is available alongside with the data. Note that all the resonator parameters f_r, Q_i, Q_c and ϕ have been obtained from fits to simulation data, using the same fitting algorithm as mentioned in the text [33].

Appendix F. Simulation of the participation ratio

To explain our measured loss spectra, we simulate the participation ratios p_i of the relevant surfaces in the differentially driven co-planar stripline resonators. Generally, there are six interfaces participating in loss-calculations: the metal-air interface (p_ma), the metal-surface interface ($p_\mathrm{substrate}$) , the surface-air interface (p_sa), the substrate (p_air) and the air/vacuum. The total loss tangent of these areas is $\sum_i p_i \tan\delta_i$, where surface type i has a loss tangent δ_i. The participation ratio of a TLS-host volume with relative permittivity ϵ_i is then defined as

$$p_i = \frac{\frac{1}{2}\int_{V_i} \epsilon_i |E|^2 \mathrm{d}V}{\frac{1}{2}\int_V \epsilon |E|^2 \mathrm{d}V}, \tag{F1}$$

where we calculate the ratio between the energy that is stored in the electric field E in a volume V_i, to the total energy of the electric field threading the resonator. Here, ϵ is the effective permittivity of the entire volume V [18, 59]. These simulations were performed in the Ansys HFSS software package.

Table 3. Simulation parameters of the resonator for different interfaces: metal-air, metal-substrate, substrate-air, substrate and air [15, 74, 75].

Property	Thickness (nm)	Dielectric constant ϵ_i
Metal-air	1.2	54
Metal-substrate	3	11.35
Substrate-air	3	11.35
Substrate	280×10^3	11.35
Air/vacuum	10^6	1

We included the effect of the differential drive in simulations. The simulation parameters are shown in table 3.

ORCID iDs

Ivo P C Cools https://orcid.org/0000-0001-8822-1470
Rodrigo M López-Báez https://orcid.org/0000-0002-9304-0460
Vittorio Buccheri https://orcid.org/0009-0009-9354-0869
Oleg Shvetsov https://orcid.org/0000-0001-6824-1386
Nermin Trnjanin https://orcid.org/0009-0006-6911-5182
Emil Hogedal https://orcid.org/0009-0008-1447-5484
Saroj P Dash https://orcid.org/0000-0001-7931-4843

References

[1] Blais A, Huang R-S, Wallraff A, Girvin S M and Schoelkopf R J 2004 Cavity quantum electrodynamics for superconducting electrical circuits: an architecture for quantum computation *Phys. Rev. A* **69** 062320
[2] Wallraff A, Schuster D I, Blais A, Frunzio L, Huang R-S, Majer J, Kumar S, Girvin S M and Schoelkopf R J 2004 Strong coupling of a single photon to a superconducting qubit using circuit quantum electrodynamics *Nature* **431** 162–7
[3] Blais A, Grimsmo A L, Girvin S and Wallraff A 2021 Circuit quantum electrodynamics *Rev. Mod. Phys.* **93** 025005
[4] McRae C R H, Wang H, Gao J, Vissers M R, Brecht T, Dunsworth A, Pappas D P and Mutus J 2020 Materials loss measurements using superconducting microwave resonators *Rev. Sci. Instrum.* **91** 091101
[5] Mazin B A 2009 Microwave kinetic inductance detectors: the first decade *AIP Conf. Proc.* **1185** 135–42
[6] Deng G-W *et al* 2015 Coupling two distant double quantum dots with a microwave resonator *Nano Lett.* **15** 6620–5
[7] Frey T, Leek P J, Beck M, Blais A, Ihn T, Ensslin K and Wallraff A 2012 Dipole coupling of a double quantum dot to a microwave resonator *Phys. Rev. Lett.* **108** 046807
[8] Burkard G, Gullans M J, Mi X and Petta J R 2020 Superconductor-semiconductor hybrid-circuit quantum electrodynamics *Nat. Rev. Phys.* **2** 129–40
[9] Kurizki G, Bertet P, Kubo Y, Mølmer K, Petrosyan D, Rabl P and Schmiedmayer J 2015 Quantum technologies with hybrid systems *Proc. Natl Acad. Sci.* **112** 3866–73
[10] Xiang Z-L, Ashhab S, You J and Nori F 2013 Hybrid quantum circuits: superconducting circuits interacting with other quantum systems *Rev. Mod. Phys.* **85** 623
[11] Hays M, Fatemi V, Serniak K, Bouman D, Diamond S, de Lange G, Krogstrup P, Nygård J, Geresdi A and Devoret M H 2020 Continuous monitoring of a trapped superconducting spin *Nat. Phys.* **16** 1103–7

[12] De Visser P J 2014 Quasiparticle dynamics in aluminium superconducting microwave resonators *PhD Thesis* TUDelft (available at: https://repository.tudelft.nl/islandora/object/uuid%3Aeae4c9fc-f90d-4c12-a878-8428ee4adb4c)
[13] Sage J M, Bolkhovsky V, Oliver W D, Turek B and Welander P B 2011 Study of loss in superconducting coplanar waveguide resonators *J. Appl. Phys.* **109** 063915
[14] de Graaf S E, Davidovikj D, Adamyan A, Kubatkin S E and Danilov A V 2014 Galvanically split superconducting microwave resonators for introducing internal voltage bias *Appl. Phys. Lett.* **104** 052601
[15] Lee J, Lee H, Kim W, Lee J and Kim J 1999 Suppression of coupled-slotline mode on CPW using air-bridges measured by picosecond photoconductive sampling *IEEE Microw. Guid. Wave Lett.* **9** 265–7
[16] Bothner D, Gaber T, Kemmler M, Koelle D and Kleiner R 2011 Improving the performance of superconducting microwave resonators in magnetic fields *Appl. Phys. Lett.* **98** 102504
[17] Nulens L *et al* 2023 Catastrophic magnetic flux avalanches in NbTiN superconducting resonators *Commun. Phys.* **6**
[18] Wenner J *et al* 2011 Surface loss simulations of superconducting coplanar waveguide resonators *Appl. Phys. Lett.* **99** 113513
[19] Samkharadze N, Bruno A, Scarlino P, Zheng G, DiVincenzo D, DiCarlo L and Vandersypen L 2016 High-kinetic-inductance superconducting nanowire resonators for circuit QED in a magnetic field *Phys. Rev. Appl.* **5** 044004
[20] Yu C X *et al* 2021 Magnetic field resilient high kinetic inductance superconducting niobium nitride coplanar waveguide resonators *Appl. Phys. Lett.* **118** 054001
[21] Amin K R, Ladner C, Jourdan G, Hentz S, Roch N and Renard J 2022 Loss mechanisms in tin high impedance superconducting microwave circuits *Appl. Phys. Lett.* **120** 164001
[22] Kirby K W2008 Processing of sapphire surfaces for semiconductor device applications
[23] Burton M C, Beebe M R, Yang K, Lukaszew R A, Valente-Feliciano A-M and Reece C 2016 Superconducting nbtin thin films for superconducting radio frequency accelerator cavity applications *J. Vac. Sci. Technol. A* **34** 021518
[24] Niepce D 2020 Superinductance and fluctuating two-level systems: loss and noise in disordered and non-disordered superconducting quantum devices *PhD Thesis* Chalmers Tekniska Hogskola
[25] Mahashabde S, Otto E, Montemurro D, de Graaf S, Kubatkin S and Danilov A 2020 Fast tunable high-Q-factor superconducting microwave resonators *Phys. Rev. Appl.* **14** 044040
[26] Pobell F 2007 *Matter and Methods at low Temperatures* (Springer Science & Business Media)
[27] Krinner S, Storz S, Kurpiers P, Magnard P, Heinsoo J, Keller R, Lütolf J, Eichler C and Wallraff A 2019 Engineering cryogenic setups for 100-qubit scale superconducting circuit systems *EPJ Quantum Technol.* **6** 1103–7
[28] Kurpiers P, Walter T, Magnard P, Salathe Y and Wallraff A 2017 Characterizing the attenuation of coaxial and rectangular microwave-frequency waveguides at cryogenic temperatures *EPJ Quantum Technol.* **4** 1–15
[29] Barends R *et al* 2011 Minimizing quasiparticle generation from stray infrared light in superconducting quantum circuits *Appl. Phys. Lett.* **99** 113507
[30] Milliken F P, Rozen J R, Keefe G A and Koch R H 2007 50 Ohm characteristic impedance low-pass metal powder filters *Rev. Sci. Instrum.* **78** 024701
[31] Lukashenko A and Ustinov A V 2008 Improved powder filters for qubit measurements *Rev. Sci. Instrum.* **79** 014701
[32] Khalil M S, Stoutimore M, Wellstood F and Osborn K 2012 An analysis method for asymmetric resonator transmission applied to superconducting devices *J. Appl. Phys.* **111** 054510
[33] Probst S, Song F, Bushev P A, Ustinov A V and Weides M 2015 Efficient and robust analysis of complex scattering data under noise in microwave resonators *Rev. Sci. Instrum.* **86** 024706
[34] Kudra M, Biznárová J, Roudsari A F, Burnett J J, Niepce D, Gasparinetti S, Wickman B and Delsing P 2020 High quality three-dimensional aluminum microwave cavities *Appl. Phys. Lett.* **117** 070601
[35] Doyle S, Mauskopf P, Naylon J, Porch A and Duncombe C 2008 LumpeLs *J. Low Temp. Phys.* **151** 530–6
[36] Megrant A *et al* 2012 Planar superconducting resonators with internal quality factors above one million *Appl. Phys. Lett.* **100** 113510
[37] Geerlings K L 2013 Improving coherence of superconducting qubits and resonators *PhD Thesis* Yale University (available at: https://ui.adsabs.harvard.edu/abs/2013PhDT.....252G)
[38] Brinson M, Crozier R, Novak C, Roucaries B, Schreuder F and Torri G B 2015 Qucs: an introduction to the new simulation and compact device modelling features implemented in release 0.0.19/0.0.19 Src2 of the popular GPL circuit simulator 1–46
[39] Cools I 2022 Basic mw analysis fitting and controlling software
[40] Annunziata A J, Santavicca D F, Frunzio L, Catelani G, Rooks M J, Frydman A and Prober D E 2010 Tunable superconducting nanoinductors *Nanotechnology* **21** 445202
[41] Yang X, You L, Zhang L, Lv C, Li H, Liu X, Zhou H and Wang Z 2018 Comparison of superconducting nanowire single-photon detectors made of NbTiN and NbN thin films *IEEE Trans. Appl. Supercond.* **28** 1–6
[42] Zichi J 2019 NbTiN for improved superconducting detectors *PhD Thesis* KTH Royal Institute of Technology
[43] Thoen D J, Bos Boy Gustaaf Cornelis, Haalebos E A F, Klapwijk T M, Baselmans J J A and Endo A 2017 Superconducting NbTin thin films with highly uniform properties over a ∅ 100 mm wafer *IEEE Trans. Appl. Supercond.* **27** 1–5
[44] Weber S J, Murch K W, Slichter D H, Vijay R and Siddiqi I 2011 Single crystal silicon capacitors with low microwave loss in the single photon regime *Appl. Phys. Lett.* **98** 172510
[45] Burnett J, Bengtsson A, Niepce D and Bylander J 2018 Noise and loss of superconducting aluminium resonators at single photon energies *J. Phys.: Conf. Ser.* **969** 012131
[46] Burnett J, Faoro L and Lindström T 2016 Analysis of high quality superconducting resonators: consequences forTLS properties in amorphous oxides *Supercond. Sci. Technol.* **29** 044008
[47] Phillips W A 1987 Two-level states in glasses *Rep. Prog. Phys.* **50** 1657
[48] Nsanzineza I 2016 Vortices and quasiparticles in superconducting microwave resonators *PhD Thesis* Syracuse University
[49] Grünhaupt L, Maleeva N, Skacel S T, Calvo M, Levy-Bertrand F, Ustinov A V, Rotzinger H, Monfardini A, Catelani G and Pop I M 2018 Loss mechanisms and quasiparticle dynamics in superconducting microwave resonators made of thin-film granular aluminum *Phys. Rev. Lett.* **121** 117001
[50] de Graaf S E, Faoro L, Burnett J, Adamyan A A, Tzalenchuk A Y, Kubatkin S E, Lindström T and Danilov A V 2018 Suppression of low-frequency charge

noise in superconducting resonators by surface spin desorption *Nat. Commun.* **9** 1143
[51] Pappas D P, Vissers M R, Wisbey D S, Kline J S and Gao J 2011 Two level system loss in superconducting microwave resonators *IEEE Trans. Appl. Supercond.* **21** 871–4
[52] Abdo B, Segev E, Shtempluck O and Buks E 2006 Nonlinear dynamics in the resonance line shape of NbN superconducting resonators *Phys. Rev. B* **73** 134513
[53] Gao J, Daal M, Vayonakis A, Kumar S, Zmuidzinas J, Sadoulet B, Mazin B A, Day P K and Leduc H G 2008 Experimental evidence for a surface distribution of two-level systems in superconducting lithographed microwave resonators *Appl. Phys. Lett.* **92** 152505
[54] Coumou P C J J 2015 Electrodynamics of strongly disordered superconductors *PhD Thesis* Technische Universiteit Delft (available at: https://repository.tudelft.nl/islandora/object/uuid%3Aad01901d-511f-4496-ae66-301d0db92caa)
[55] Gao J 2008 The physics of superconducting microwave resonators *PhD Thesis* California Institute of Technology
[56] Arzeo M, Lombardi F and Bauch T 2014 Microwave losses in MgO, $LaAlO_3$ and (La0.3Sr0.7)(Al0.65Ta0.35) O3 dielectrics at low power and in the millikelvin temperature range *Appl. Phys. Lett.* **104** 212601
[57] McRae C R H, Béjanin J H, Earnest C T, McConkey T G, Rinehart J R, Deimert C, Thomas J P, Wasilewski Z R and Mariantoni M 2018 Thin film metrology and microwave loss characterization of indium and aluminum/indium superconducting planar resonators *J. Appl. Phys.* **123** 205304
[58] Lahtinen V and Möttönen M 2020 Effects of device geometry and material properties on dielectric losses in superconducting coplanar-waveguide resonators *J. Phys.: Condens. Matter* **32** 405702
[59] Niepce D, Burnett J J, Latorre M G and Bylander J 2020 Geometric scaling of two-level-system loss in superconducting resonators *Supercond. Sci. Technol.* **33** 025013
[60] Vendik I B, Gubina M N, Deleniv A N and Kholodnyak D V 1997 Distribution of current, surface impedance and damping in superconductor coupled microstriplines *Techn. Phys.* **42** 196–201
[61] Deleniv A, Gubina M, Kholodniak D and Vendik I 1998 Model of high-temperature superconducting coupled microstrip lines on anisotropic sapphire substrate *Int. J. RF Microw. Comput.-Aided Eng.* **8** 375–85
[62] Müller M *et al* 2022 Magnetic field robust high quality factor nbtin superconducting microwave resonators *Mater. Quantum Technol.* **2** 015002
[63] Read A P, Chapman B J, Lei C U, Curtis J C, Ganjam S, Krayzman L, Frunzio L and Schoelkopf R J 2023 Precision measurement of the microwave dielectric loss of sapphire in the quantum regime with parts-per-billion sensitivity *Phys. Rev. Appl.* **19** 034064
[64] Tinkham M 2004 *Introduction to Superconductivity Secondedn* 2nd edn (Dover Publications)
[65] Sidorova M, Semenov A D, Hübers H-W, Gyger S, Steinhauer S, Zhang X and Schilling A 2021 Magnetoconductance and photoresponse properties of disordered NbTiN films *Phys. Rev. B* **104** 184514
[66] Mironov A Y, Silevitch D M, Proslier T, Postolova S V, Burdastyh M V, Gutakovskii A K, Rosenbaum T F, Vinokur V V and Baturina T I 2018 Charge Berezinskii-Kosterlitz-Thouless transition in superconducting nbtin films *Sci. Rep.* **8** 4082
[67] Yu L, Newman N and Rowell J 2002 Measurement of the coherence length of sputtered nb/sub 0.62/ti/sub 0.38/n thin films *IEEE Trans. App. Supercond.* **12** 1795–8
[68] Pearl J 1964 Current distribution in superconducting films carrying quantized fluxoids *Appl. Phys. Lett.* **5** 65–66
[69] Kroll J *et al* 2019 Magnetic-field-resilient superconducting coplanar-waveguide resonators for hybrid circuit quantum electrodynamics experiments *Phys. Rev. Appl.* **11** 064053
[70] Shetvsov O, Ankit A, Buccheri V, Cools I P C, Trnjanin N and Geresdi A 2025 Strong coupling between Andreev bound states and a high impedance lumped-element resonator (arXiv:2502.09243)
[71] Werthamer N R, Helfand E and Hohenberg P C 1966 Temperature and purity dependence of the superconducting critical field, III. electron spin and spin-orbit effects *Phys. Rev.* **147** 295–302
[72] Pozar D M 2011 *Microwave Engineering* 4th edn (Wiley)
[73] Bruno A, De Lange G, Asaad S, Enden K L, Langford N and DiCarlo L 2015 Reducing intrinsic loss in superconducting resonators by surface treatment and deep etching of silicon substrates *Appl. Phys. Lett.* **106** 182601
[74] Kaiser C, Skacel S T, Wünsch S, Dolata R, Mackrodt B, Zorin A and Siegel M 2010 Measurement of dielectric losses in amorphous thin films at gigahertz frequencies using superconducting resonators *Supercond. Sci. Technol.* **23** 075008
[75] Clima S, Pourtois G, Hardy A, Van Elshocht S, Van Bael M K, De Gendt S, Wouters D J, Heyns M and Kittl J A 2010 Dielectric response of TaO_5, Nb_2O_5, and $NbTaO_5$ from first-principles investigations *J. Electrochem. Soc.* **157** G20

PAPER III

Approaching the ultrastrong-coupling regime between an Andreev level and a microwave resonator

Oleg O. Shvetsov, Ankit Khola, **Vittorio Buccheri**, Ivo P. C. Cools, Nermin Trnjanin, Attila Geresdi, Thomas Kanne, and Jesper Nygård

Physical Review Applied **24**, 044015 (2025)

Contribution: The candidate contributed to developing the device fabrication recipe, setting up the dilution refrigerators, and establishing the measurement protocols.

Approaching the ultrastrong-coupling regime between an Andreev level and a microwave resonator

O. O. Shvetsov,* A. Khola, V. Buccheri, I. P. C. Cools, N. Trnjanin, and A. Geresdi
Department of Microtechnology and Nanoscience, Chalmers University of Technology, SE-41296 Gothenburg, Sweden

T. Kanne and J. Nygård
Niels Bohr Institute, Center for Quantum Devices, University of Copenhagen, Universitetsparken 5, DK-2100 Copenhagen O, Denmark

(Received 17 February 2025; revised 5 June 2025; accepted 12 September 2025; published 6 October 2025)

Josephson junctions formed in semiconductor nanowires host Andreev bound states and serve as a physical platform to realize Andreev qubits tuned by electrostatic gating. With the Andreev bound state being confined to the nanoscale weak link, it couples to a circuit-QED architecture via the state-dependent supercurrent flowing through the weak link. Thus, increasing this coupling strength is a crucial challenge for this architecture. Here, we demonstrate the fabrication and microwave characterization of a weak link which is defined in an InAs-Al (core-half shell) nanowire and embedded in a superconducting loop with a lumped-element resonator patterned from a thin NbTiN film with high kinetic inductance. We investigate several devices with various weak-link lengths and performed spectroscopy that revealed pair transitions and single-quasiparticle transitions arising from spin-orbit-split Andreev bound states. Our approach offers a compact geometry and a large resonator impedance above 12 kΩ at a resonator frequency of 8 GHz, which facilitates large coupling in the system. For the pair transitions, the experimentally observed energy level splitting demonstrates the coupling to an Andreev level of 490 MHz. We apply a perturbative model that shows good agreement with the experimental data and extract the maximum coupling of 968 MHz. Moreover, we show that the coupling is even stronger to an Andreev level with a higher transmission. In addition, spectroscopy of single-quasiparticle transitions reveals spin-orbit-split Andreev bound states with the extracted spin-photon coupling of 77 MHz.

DOI: 10.1103/f81h-xjcv

I. INTRODUCTION

Circuit-QED (CQED) describes the interaction of photons stored in a superconducting resonator and a two-level system (qubit) [1]. The latter is often based on a single electron spin [2] or collective excitations in various superconducting circuits [3,4]. For quantum information processing, the favorable regime is when the qubit is strongly coupled to the resonator, that is, when they exchange a photon many times before the coherence is lost [4].

A distinct ultrastrong-coupling regime is established when the coupling strength becomes a significant fraction of the bare resonator and qubit frequencies [5–7]. In this case, the common rotating-wave approximation is no longer valid and more comprehensive models are applied [8]. From a practical point of view, the ultrastrong-coupling regime has been proposed to be used, for example, for ultrafast quantum computation [9].

Andreev bound states (ABSs) are discrete fermionic excitations spatially confined in a weak link between two superconductors [10,11]. Atomiclike transitions between these states can be utilized for the realization of two types of qubits, namely Andreev pair qubit [12–16] and Andreev spin qubit [17–23], which can be experimentally investigated by the means of CQED techniques [24–26]. Semiconductor nanowires serve as the preferred platform for such experiments, due to high material quality, gate tunability, and intrinsically strong spin-orbit coupling [27], which opens the way to exploit not only the charge, but also the spin degree of freedom in qubit applications. The possibility of coupling a single quasiparticle spin to macroscopic supercurrents makes Andreev qubits a promising alternative to traditional spin and superconducting qubit platforms [18,28,29].

*Contact author: shvetsov@chalmers.se

Published by the American Physical Society under the terms of the Creative Commons Attribution 4.0 International license. Further distribution of this work must maintain attribution to the author(s) and the published article's title, journal citation, and DOI. Funded by Bibsam.

In conventional superconducting circuits, qubits are formed from quantized energy levels of collective electromagnetic excitations. In contrast, ABSs are localized within the weak link and carry a supercurrent up to the range of 10 nA for the typical geometry of InAs nanowires [30]. This makes it more challenging to reach strong coupling to a microwave resonator. In practice, the coupling is typically realized by embedding a phase-biased weak link in a superconducting loop with a part of the resonator, also referred to as a shared inductance. In this case, the coupling rate g_c is proportional to the zero-point flux (phase) fluctuations across the shared inductance [24], which is in turn proportional to the square root of the resonator impedance Z_r, resulting in $g_c \propto \sqrt{Z_r}$ [31,32]. Thus, an increase in the resonator impedance naturally leads to a stronger coupling, enabling better resolution spectroscopy and making higher-energy states accessible.

In this paper, we investigate several devices that integrate a lumped-element resonator made of a thin NbTiN film and a weak link tailored in an InAs-Al (core-half shell) nanowire. Because of the high kinetic inductance of the NbTiN film, the differential impedance of the resonator reaches values above 12 kΩ. We perform single- and two-tone spectroscopy that revealed pair and single-quasiparticle transitions. The system exhibits large energy splitting at the avoided crossings, which indicates the coupling to an Andreev level of 490 MHz, and the model predicts that the coupling reaches up to 968 MHz. Moreover, we show that coupling to an Andreev level with a higher transmission can reach the value of 1.95 GHz, more than 20% of the bare resonator frequency. Our findings suggest that the system is approaching the ultrastrong-coupling regime. In addition, we demonstrate that the presented geometry can be used to resolve spin-orbit-split ABSs, and we extract the coupling to an Andreev spin of 77 MHz.

II. DEVICE AND SETUP

The devices used in this work consist of a weak link which is defined in an InAs nanowire [27] and embedded in a superconducting loop with a high-impedance lumped-element resonator. We report on fabrication and measurement of three devices, where the resonator geometry and the weak-link length vary. Their parameters are listed in Table I. A representative device (a replica of device 2) is demonstrated in Fig. 1(a) and is described below.

The resonator is patterned on a sapphire substrate with a thin (around 6 nm) sputtered film of a highly disordered NbTiN superconductor. Figure 1(b) represents an electron micrograph of the resonator structure. It consists of a differential pair of 130-nm-wide and 38.3-μm-long symmetric arms, divided by the grounding strip in the middle. Each arm is terminated with a triangular-shaped capacitor plate that is coupled to a 50-Ω feedline. When these feedlines are driven differentially, the microwave signal oscillates in the arms with opposite phase, which is also referred to as the odd mode. In the even mode, on the contrary, microwaves in the two arms oscillate in-phase. Because of the high kinetic inductance of the thin film, $L_{k,\square} \approx 400$ pH, this compact structure with a footprint of $50 \times 50\ \mu\text{m}^2$ realizes a total inductance $L_r \approx 118$ nH and resonates in the odd mode at the frequency $f_r = 8.619$ GHz as a lumped-element resonator. The differential impedance of the resonator reaches $Z_{r,\text{diff}} = 2\sqrt{L_r/C_r} \approx 12.76\ \text{k}\Omega$.

TABLE I. Parameters of the devices, including length, width, and differential impedance of the resonators, thin-film kinetic inductance, bare resonator frequency, zero-point flux fluctuations across the shared inductance, and the weak-link length.

Device	Length[a] (μm)	Width (nm)	$Z_{r,\text{diff}}$ (kΩ)	$L_{k,\square}$[b] (pH)	f_r (GHz)	Φ_{zpf}[c] (Φ_0)	l_{wl} (nm)
1	48.3	130	12.28	320	8.2230	0.016	250
2	38.3	130	12.76	400	8.6190	0.021	320
3	53.3	130	13.27	345	7.4685	0.015	450

[a]Length of one arm of the differential pair.
[b]May vary due to sample aging and slightly different fabrication parameters.
[c]Deduced from the resonator geometry and inductance.

The weak link was defined in a 150-nm-thick MBE-grown InAs nanowire with an *in-situ*-grown epitaxial Al shell covering three of its facets [27]. A 250- to 450-nm-long part of the 27-nm-thick Al shell was removed by wet etching [33]; an example is shown in Fig. 1(c). A small part of the resonator with the shared inductance $2l \approx 12.3$ nH is coupled to the nanowire by incorporating it in a common superconducting loop with Al contacts. The weak link couples to the odd mode of the resonator, because in the even mode the currents through the shared inductance cancel out. In this geometry, the coupling between the ABSs and the resonator is proportional to the zero-point flux fluctuations across the shared inductance $\Phi_{\text{zpf}} = (l/L_r)\sqrt{\hbar Z_{r,\text{diff}}/2} \approx 0.021\Phi_0$, where $\Phi_0 = h/2e$ is the superconducting flux quantum. The shared inductance was intentionally designed to be large, but comparable to the weak-link Josephson inductance, which ensures that the phase across the junction φ is a nonhysteretic function of the applied flux Φ. Moreover, our analysis shows that $\varphi \approx 2\pi\Phi/\Phi_0$ is a reasonable approximation (see Appendix D).

A dc electrostatic side gate is defined at a distance of 150 nm away from the junction to tune the electrochemical potential in the nanowire. The differential drive and the overall symmetric chip layout ensure that, along the mirror line, the ac electric field is essentially zero. To reference the nanowire to the dc ground potential, the nanowire loop is connected to the ground by a metal strip located along

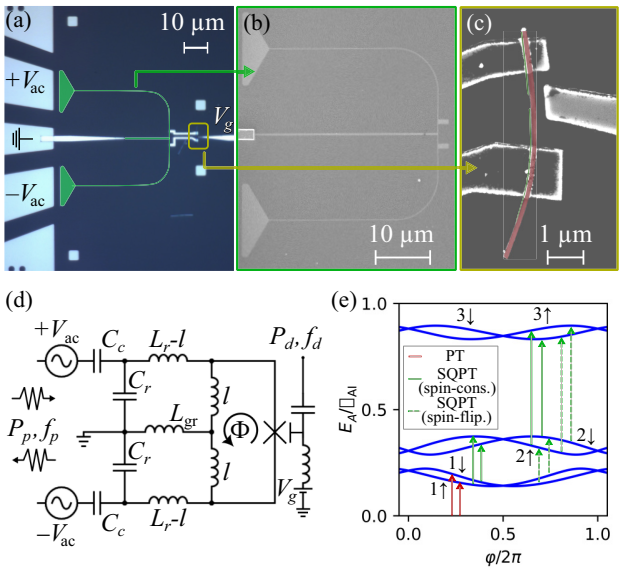


FIG. 1. (a) An optical micrograph of a representative device. The resonator is denoted by a green (false color) U-shaped structure patterned from a thin NbTiN film with high kinetic inductance. The resonator is capacitively coupled to a pair of feedlines. A weak link in an InAs-Al nanowire is defined close to the mirror line of the device and coupled to the resonator by aluminum contacts. (b) Electron micrograph of a test resonator structure fabricated simultaneously with the studied device on the same chip. (c) Electron micrograph of the nanowire (false color) with a weak link, Al leads, and a side gate. (d) Circuit diagram showing an equivalent lumped-element scheme of the device. It consists of a differential pair of resonators with the inductances L_r and capacitances C_r, coupled to the feedlines by the capacitors C_c. The nanowire weak link is embedded in a flux-biased superconducting loop with a small fraction of the resonator with the shared inductance $2l$. To ground the loop, the resonator's middle part is connected with the ground plane. The resonator is probed in reflection with the probe signal of power P_p and frequency f_p. The side gate is used to tune the nanowire's electrochemical potential and to excite the system with a drive signal of power P_d and frequency f_d. (e) Typical excitation spectrum of a long weak link with spin-orbit interaction. Three ABSs are present in the spectrum, each of them being split into a doublet of states with the opposite pseudospin, denoted by ↑ and ↓. Microwave photons can induce pair transitions (PT, red arrows) and single-quasiparticle transitions (SQPT, green arrows), where, for the latter, spin-conserving (solid) and spin-flipping (dashed) processes can be distinguished. The energy scale is normalized to the superconducting gap in Al.

this line, which does not disturb the resonator's odd mode. In such a design, having the nanowire weak link defined at the zero ac voltage line is preferable to mitigate microwave losses through the side gate. A superconducting coil was used to flux-bias the weak link. The circuit diagram of the device is presented in Fig. 1(d).

The odd mode of the resonator is probed in reflection with the signal of power P_p and frequency f_p. A separate microwave tone passes through a bias tee to the side gate to excite the system with a drive signal of power P_d and frequency f_d.

After fabrication, the device chip is wire-bonded to a printed circuit board and embedded in a copper box attached to the mixing chamber of a dilution refrigerator with a base temperature of 10 mK. To screen spurious magnetic fields in the laboratory, an additional aluminum shield wrapped with magnetic shielding foil was installed.

The system represents a typical CQED setup, where microwave photons drive transitions between ABSs, and the state of the system can be detected by the resonator dispersive shift. One of the defining parameters of the ABS spectrum in a weak link is the ratio between the weak-link length $l_{\rm wl}$ and the superconducting coherence length ξ, which is typically several hundred nanometers in InAs nanowires proximized by aluminum. To describe the excitation spectrum in a finite-length weak link with $l_{\rm wl}/\xi \sim 1$, we refer to the model employed in Refs. [19,34]. The minimal model that includes spin-orbit splitting requires two transverse subbands. In this case the energy dispersion $\epsilon = E_A/\Delta_{\rm Al}$ of the ABSs is a solution to the transcendental equation:

$$\tau \cos[(\Lambda_1 - \Lambda_2)\epsilon \mp \varphi] + (1-\tau)\cos[(\Lambda_1 + \Lambda_2)\epsilon x_0] = \cos[2\arccos\epsilon - (\Lambda_1 + \Lambda_2)\epsilon]. \quad (1)$$

Here τ is the channel transmission, $\Delta_{\rm Al}$ is the Al superconducting gap, $x_0 \in [-1,1]$ indicates the position of a barrier in the weak link (normalized to $l_{\rm wl}/2$), and $\Lambda_j = l_{\rm wl}\Delta_{\rm Al}/\hbar v_{Fj}$, where v_{Fj} is the Fermi velocity of the subband $j = 1,2$ in the nanowire.

In a finite-length weak link, multiple ABSs can squeeze into the spectrum; e.g., three levels are shown in a characteristic spectrum illustrated in Fig. 1(e). Spin-orbit interaction lifts the spin degeneracy, splitting each of the states into a doublet with the opposite pseudospin, denoted by ↑ and ↓. The time-reversal symmetry preserves degeneracy only at $\varphi = 0$ and $\varphi = \pi$. We consider two types of transitions: a pair transition (PT, red arrows) takes place when two quasiparticles are excited from the ground state; a single-quasiparticle transition (SQPT, green arrows) occurs when a quasiparticle that is already present in the system is promoted to one of the upper levels. Among SQPTs, spin-conserving (solid) and spin-flipping (dashed) transitions can be distinguished, when the transition is between the levels with the same or opposite pseudospin, respectively.

III. RESULTS AND DISCUSSION

We first present the typical microwave gate response, obtained for device 2. The change in the absolute value of

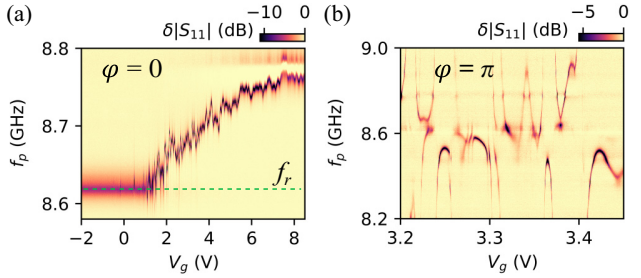


FIG. 2. Change in the absolute value of the resonator reflection $\delta|S_{11}|$ as a function of the probe frequency f_p and gate voltage V_g measured in device 2 at (a) $\varphi = 0$ and (b) $\varphi = \pi$. The line at $f_r = 8.619$ GHz in panel (a) denotes the bare resonator frequency, when the nanowire is fully pinched off. The gate-independent background was subtracted.

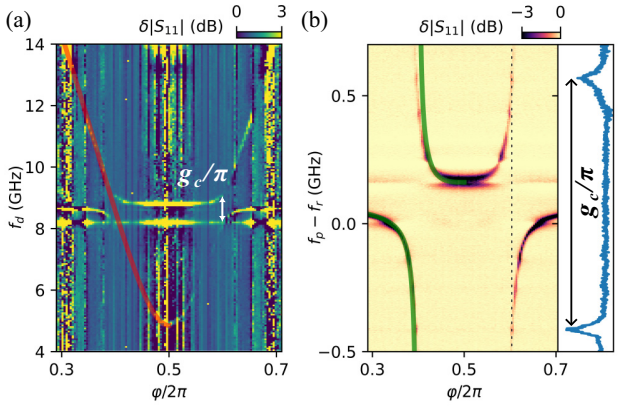


FIG. 3. (a) Two-tone spectrum measured in device 2 at $V_g = 3.39$ V. The fit of the PT frequency as a function of phase is shown by the red line. The spectrum reveals avoided crossings at $\varphi/2\pi = 0.4$ and $\varphi/2\pi = 0.6$ with the coupling at the crossings $g_c/2\pi \approx 490$ MHz, denoted by the white arrow. The flat line seen at around 8.1 GHz corresponds to the resonator's even mode, which is insensitive to the state of the weak link. (b) Corresponding single-tone spectrum. The probe frequency f_p is offset to the bare resonator frequency $f_r = 8.619$ GHz. The green line represents the fit of the resonator shift. The line cut on the right-hand side clearly confirms that $g_c/2\pi \approx 490$ MHz at the avoided crossing [along the gray dotted line in panel (b)].

the resonator reflection $\delta|S_{11}|$ as a function of the probe frequency f_p and side-gate voltage V_g is presented in Fig. 2 (the gate-independent background is subtracted). In Fig. 2(a), the phase across the weak link φ is fixed at zero, while $\varphi = \pi$ in Fig. 2(b). The junction is fully pinched off below $V_g \approx 1$ V, where the resonance approaches the bare resonator frequency $f_r = 8.619$ GHz. The data obtained at $\varphi = \pi$ in Fig. 2(b) demonstrate multiple avoided crossings, signifying that the ABSs are strongly coupled to the resonator mode.

Further, we performed single- and two-tone spectroscopy to characterize the system. To mitigate charge noise and avoid electrostatic drifting, in these measurements we fix the gate voltage V_g at one of the points where the resonator gate response has a local extremum, such as one of those observed in Fig. 2(b). Single-tone spectra are taken by sweeping the probe frequency f_p of power P_p and measuring complex parameters S_{11} at various applied fluxes. The flux-independent background was subtracted in the data plotted. When the two-tone spectra were measured, we first performed a single-tone frequency sweep to define the resonance position at a certain phase (flux). Then, a continuous-wave probe tone was fixed at this frequency and S_{11} was measured as a function of the drive tone with frequency f_d and power P_d. To reference the signal measured in two-tone spectra, we subtracted a drive-frequency-independent background.

A. Spectroscopy of pair transitions

Figure 3 presents the spectroscopy data for device 2. Data were acquired at $V_g = 3.39$ V and at the nominal powers $P_p \approx -130$ dBm and $P_d \approx -100$ dBm. Figure 3(a) illustrates the two-tone spectrum, which reveals a PT arising from a highly transmissive ABS. It crosses the odd mode of the resonator, forming a pair of avoided crossings at $\varphi/2\pi = 0.4$ and $\varphi/2\pi = 0.6$, where the coupling can be directly extracted from the level splitting on resonance $g_c/2\pi \approx 490$ MHz.

In the vicinity of $\varphi = \pi$, the PT frequency can be fitted to the dispersion relation valid for a short weak link,

$$hf_{\mathrm{PT}} = 2E_A = 2\Delta'\sqrt{1 - \tau \sin^2(\varphi/2)}, \tag{2}$$

respecting the fact that the effective gap value in a finite-length weak link is smaller than the gap in aluminum, $\Delta' < \Delta_{\mathrm{Al}}$ (see Appendix C for details). The least-squares method yields $\Delta'/h = 11.69 \pm 0.03$ GHz and $\tau = 0.9569 \pm 0.0005$. The resulting fit is represented as a red line in Fig. 3(a).

Figure 3(b) shows the corresponding single-tone spectrum. The coupling at the avoided crossing $g_c/2\pi \approx 490$ MHz can be directly extracted from the line cut along the gray dotted line (see the right-hand side of the plot). The green line denotes the fit that was obtained from the model described in Appendix C. The fit relies on a single ABS observed in the two-tone spectrum in Fig. 3(a). We confirmed that no higher-energy states are observed up to $f_d = 21$ GHz (see Appendix F). In the fit, the zero-point flux fluctuation across the shared inductance is the only fitting parameter. The least-squares fit to the experimental data yields $\Phi_{\mathrm{zpf}} = (0.0282 \pm 0.0002)\Phi_0$, which slightly overshoots the value obtained from the geometry analysis (see Table I). To validate the fit, we extract the magnitude of the coupling at the avoided crossing $g_c/2\pi = 495 \pm 4$ MHz,

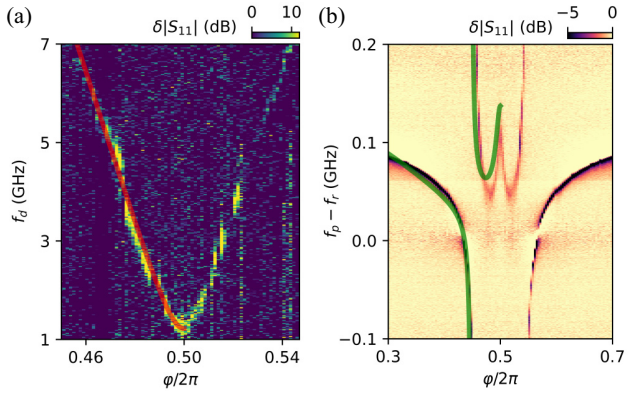


FIG. 4. (a) Two-tone spectrum measured in device 1 at $V_g = 14.5$ V. The PT frequency fit plotted as a function of phase is denoted by the red line. (b) Corresponding single-tone spectrum. The probe frequency f_p is offset to the bare resonator frequency $f_r = 8.223$ GHz. The green line denotes the fit of the resonator shift.

which is in good agreement with the observed energy splitting. The maximum coupling can be extracted at $\varphi = \pi$: $g_c/2\pi = 968 \pm 7$ MHz.

Figure 4 provides the spectroscopy data obtained for device 1 with the shortest 250-nm weak link at $P_p \approx -130$ dBm and $P_d \approx -100$ dBm, and at $V_g = 14.5$ V (this device required a higher gate voltage due to the longer distance to the gate). Here, we were following a similar fitting routine. The two-tone spectrum in Fig. 4(a) is fitted by Eq. (2) describing a PT arising from a single high-transmission channel. The best fit reveals $\tau = 0.99942 \pm 0.00006$ and $\Delta'/h = 25.2 \pm 0.2$ GHz. The manifestation of ABS with a very large transmission in single-tone spectroscopy in Fig. 4(b) is a sharp peak at $\varphi = \pi$ [24]. This feature is well described within the presented model with $\Phi_{\mathrm{zpf}} = (0.0247 \pm 0.0002)\Phi_0$ as the only fitting parameter, and we extract the maximum coupling $g_c/2\pi = 1.95 \pm 0.02$ GHz at $\varphi = \pi$. We note that the extracted coupling indicates that the system is beyond the applicability of the perturbative approach. This explains a noticeable fit deviation in Fig. 4(b). At this level of consideration, the extracted coupling should be perceived as an approximate value.

B. Spectroscopy of single-quasiparticle transitions

SQPTs associated with spin-orbit-split ABSs were routinely observed for devices 2 and 3 with longer weak links.

Figures 5(a)–5(d) provide the spectroscopy data obtained for device 3 at $V_g = 1.498$ V and for device 2 at $V_g = 2.44$ V around the degeneracy points $\varphi = 0$ and $\varphi = \pi$, respectively. Figures 5(a) and 5(b) illustrate two-tone spectroscopy data that reveal bundles of four lines, which we assign to spin-conserving SQPTs [see Fig. 1(e)].

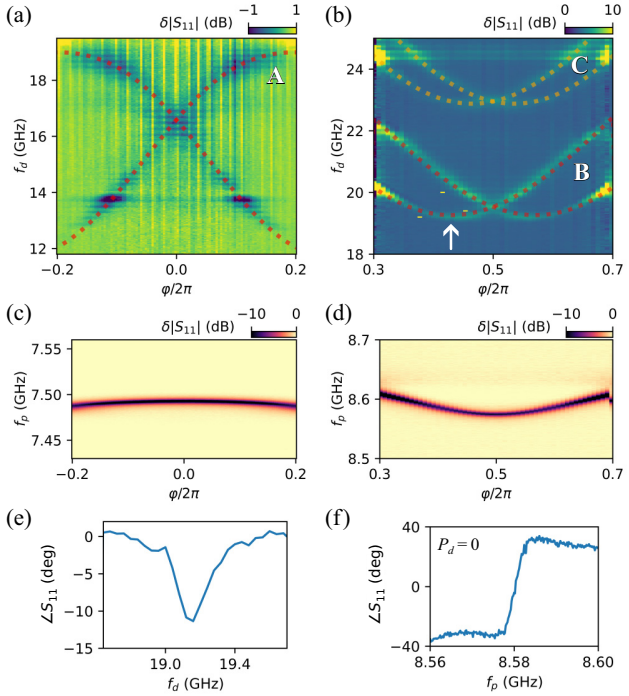


FIG. 5. (a)–(d) Spectroscopy data obtained for (a),(c) device 3 at $V_g = 1.498$ V and (b),(d) device 2 at $V_g = 2.44$ V. (a),(b) In two-tone spectra, bundles of SQPTs are observed, with crossings at the degeneracy points. SQPT frequency fits are denoted by the dotted lines and labeled as A, B, and C. The fit parameters are listed in Table II. (c),(d) The corresponding single-tone spectra. (e) Phase of the reflected signal as a function of the drive frequency at a minimum of the lower SQPT [see the white arrow in panel (b)]. (f) The corresponding resonator response when the system is not excited.

The spectroscopic lines in Fig. 5(a) can be fitted with the transitions between the two lowest Andreev doublets ($1\uparrow \Rightarrow 2\uparrow$ and $1\downarrow \Rightarrow 2\downarrow$). Parameters which provide the best fit were obtained by the least-squares method applied to transitions between the ABSs given by Eq. (1); see Appendix C for details. These parameters are listed in Table II, column A. The fit is shown by the red dotted line.

In Fig. 5(b), two bundles of lines are observed. Each of those take place at relatively large frequencies above 19 GHz and have an upward curved shape, implying that

TABLE II. A table of parameters for the SQPT fits in Figs. 5(a) and 5(b). The Δ_{Al}/h value is fixed at 52 GHz. See main text for meaning of column headings.

	A	B	C
Λ_1	5.7 ± 0.3	2.44 ± 0.07	2.8 ± 0.1
Λ_2	1.5 ± 0.3	3.06 ± 0.09	3.2 ± 0.1
τ	0.35 ± 0.04	0.243 ± 0.009	0.265 ± 0.006
x_0	0.489 ± 0.005	0.2615 ± 0.0001	-0.000837

the transitions occur between the upper doublets ($2\uparrow \Rightarrow 3\uparrow$ and $2\downarrow \Rightarrow 3\downarrow$). The parameters provided by the least-squares method are listed in Table II, where B corresponds to the red dotted line, and C to the orange one in Fig. 5(b), respectively.

The coupling between the resonator and a spinful ABS can be estimated from the line shape of an SQPT. Figure 5(e) shows the phase of the reflected signal as a function of the drive frequency at a minimum of the lower SQPT in Fig. 5(b) (marked by an arrow). The phase shift induced by this transition is $\delta(\angle S_{11}) \approx 10^\circ$. Based on the corresponding resonance line shape of a nonexcited system [Fig. 5(f)], the phase shift can be converted to the resonator frequency shift $\delta f_r^{\mathrm{SQPT}} \approx 770$ kHz. It can be described by second-order perturbation theory [21] as

$$\delta f_r^{\mathrm{SQPT}} \approx \left(\frac{g_c}{2\pi}\right)^2 \frac{2f_{\mathrm{SQPT}}}{f_{\mathrm{SQPT}}^2 - f_r^2},$$

from which we extract the spin-photon coupling $g_c/2\pi \approx 77$ MHz. This value is comparable to the recently reported strong coupling between a high-impedance resonator and a singlet-triplet spin qubit [35] and to the previously reported spin-photon coupling in InAs nanowire weak links [21].

We note that a more rigorous assessment of the coupling requires measurements of parity-switching dynamics in the system, which is a subject for further investigation. If the nonequilibrium quasiparticle poisoning is weak, the system resides in an odd-parity state [15,24,36,37] for only a small fraction of time, during which an SQPT can be excited. This can reduce the signal obtained in the spectroscopy of spin-orbit-split ABSs.

In our experiment, we repeatedly observed that only spin-conserving SQPTs are clearly visible in the spectra. This is in agreement with the general selection rules: in the presence of transverse symmetry in the nanowire, spin-flipping transitions should be suppressed. However, previous studies showed that spin-flipping transitions can still be excited at elevated drive powers in a realistic nonideal device [19,21]. For example, the gate drive can violate transverse symmetry and unlock spin-flipping transitions [24,38,39]. Although we used the gate drive in our setup, we did not observe spin-flipping SQPTs. This is most likely because we had to operate at sufficiently low drive powers, so that the thin-film resonator is not driven into a nonlinear regime.

IV. CONCLUSION

In conclusion, we have demonstrated a robust approach for achieving a large coupling strength between a high-impedance lumped-element resonator and ABSs residing in an InAs nanowire weak link. Moreover, we have shown that our geometry is suitable for the investigation of spin-orbit-split ABSs and the associated Andreev spin qubits. The presented approach can be further extended to facilitate a strong qubit-qubit coupling in a device comprising multiple Andreev qubits.

ACKNOWLEDGMENTS

This work was financially supported by the European Union's H2020 Research and Innovation Program, Grants No. 804988 (SiMS) and No. 828948 (AndQC), and by the Army Research Office (ARO), Grant No. W911NF2210053. The Center for Quantum Devices is supported by the Danish National Research Foundation, Grant No. DNRF101, by the Novo Nordisk Foundation, project SolidQ, and by the Carlsberg Foundation. The devices were fabricated in the Myfab cleanroom at Chalmers, and technical support from the Nanofabrication Laboratory is gratefully acknowledged. We also thank P. Makk, S. Csonka, G. Fülöp, and V. Fatemi for fruitful discussions.

DATA AVAILABILITY

The data that support the findings of this article are openly available [40].

APPENDIX A: NbTiN THIN-FILM HIGH KINETIC INDUCTANCE AND THE RESONATOR IMPEDANCE

The dc transport characterization of a test resonator structure (a replica of device 1) provides NbTiN thin-film normal-state sheet resistance $R_{N,\square} = 1.46$ kΩ and critical temperature $T_c = 6$ K. With these parameters, we can estimate the sheet kinetic inductance as $L_{k,\square}^{\mathrm{dc}} \approx \hbar R_N/\pi\Delta$ [41], where $\Delta \approx 1.76 k_B T_c$ is the superconducting gap linked to T_c by a standard BCS prediction [42]. This yields $L_{k,\square}^{\mathrm{dc}} \approx 320$ pH.

In addition, for each of the devices, we performed microwave domain simulations for the actual geometries used in the experiment. To simulate a bare resonator, we replaced the weak links with a short break in the film, but all the aluminum structures were included because they contribute to the total stray capacitance of the resonator. We extracted $L_{k,\square}$ from the best fits of the simulated resonator microwave response to the experimental data at low V_g, when the nanowires are fully depleted. The results are listed in Table I in the main text. Since all resonators were picked up from the same batch with the same NbTiN thickness, we attribute the variation in $L_{k,\square}$ to the aging of the sample and slightly different fabrication parameters used during nanowire processing (e.g., it was observed that the resulting $L_{k,\square}$ depends on the baking temperature of the resist).

The total inductance L_r (for one arm of the differential pair) is derived from the geometry and $L_{k,\square}$ is obtained as described above. The bare resonator frequency f_r is obtained experimentally. The differential impedance is defined as $Z_{r,\mathrm{diff}} = 2\sqrt{L_r/C_r} = 4\pi f_r L_r$.

We note that we routinely observed the resonator's even mode, which is insensitive to the weak link's state and positioned at several hundred megahertz below the odd mode, yielding a flat line at around 8.1 GHz in Fig. 3. We confirmed the even-mode frequency by microwave domain simulations. Its frequency is determined by $2\pi f_r^{\mathrm{even}} = 1/\sqrt{(L_r + 2L_{\mathrm{gr}})C_r}$, where $L_{\mathrm{gr}} \approx 10$ nH is the inductance of the grounding strip, which connects the ground plane and the middle part of the resonator [see Figs. 1(a) and 1(d)].

APPENDIX B: MEASUREMENT SETUP

The measurement scheme is similar to the one described in Ref. [43] and depicted in Fig. 6(a). The microwave readout tone passes through an attenuated line and a double circulator located at the mixing chamber stage, and is then routed through a 180° hybrid to differentially drive two on-chip 50-Ω feedlines capacitively coupled to the resonator. The readout tone is reflected off the resonator's odd mode and routed through a series of cryogenic and room-temperature amplifiers. The complex reflection parameter (S_{11}) is measured by a vector network analyzer. A separate microwave tone passes through the gate line to drive the ABS transitions, where a bias tee is used to combine the dc gate voltage and the drive tone.

Figures 6(b) and 6(c) represent the characteristic S_{11} response of one of the devices when the ABSs are far detuned (at zero applied flux). The resonance is fitted by the diameter-correction method [44], which yields the internal quality factor $Q_i \approx 3800$ and the coupling quality factor $Q_c \approx 1000$ when the ABSs are far detuned. We would like to emphasize that, in our setup, the large coupling magnitude results in a significant magnetic flux dependence of the internal quality factor when the Andreev level energy approaches the bare resonator frequency. At $\varphi = \pi$ the nanowire introduces maximum losses to the system, and Q_i usually drops to around 1000.

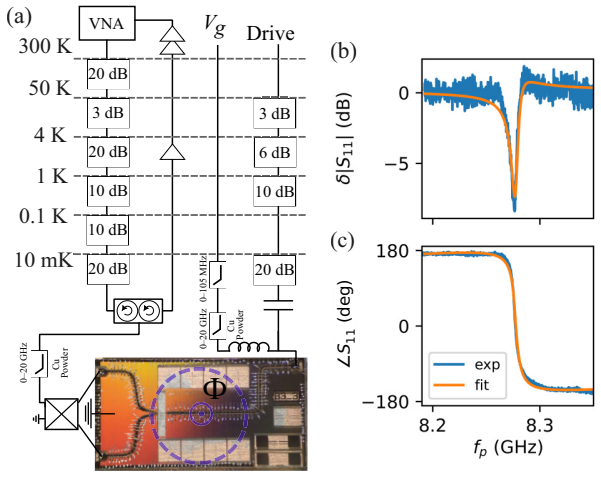


FIG. 6. (a) Experimental setup. (b),(c) Reflected signal amplitude (phase) versus probe tone frequency for one of the devices at zero external flux (the ABSs are far detuned). The blue line shows the experimental data. The orange line represents the fit, revealing that $Q_i \approx 3800$ and $Q_c \approx 1000$.

APPENDIX C: DETAILS OF THE FITTING ROUTINE

1. SQPTs

The SQPT frequency can be found from Eq. (1) in the main text as the difference between the energies of the two neighboring states. In our fitting routine, we first performed manual parameter selection to obtain a reasonable fit. Then, these parameters were used as an initial guess for the least-squares method. We found that the set of parameters is not always unique, which can produce large uncertainties. Furthermore, we frequently observed significant correlations between the parameters, such as the correlation between x_0 and Δ_{Al}, which could reach almost 100%. This is likely because both parameters are responsible for the overall energy scale. In order to mitigate these concerns, we fixed the gap parameter $\Delta_{\mathrm{Al}}/h = 52$ GHz for all the fits depicted in Fig. 5. This appeared to be a satisfactory initial parameter guess for each fit.

2. PTs

The dispersion relation in Eq. (1) can be simplified to describe PTs in a finite-length weak link. For a PT, we detect the average of a spin-split Andreev doublet and we can neglect spin-orbit coupling assuming that $\Lambda_1 = \Lambda_2 = \Lambda$. Expansion of Eq. (1) around $\varphi = \pi$ up to second order in ϵ recovers the short-junction expression

$$E_A(\varphi) \approx \Delta' \sqrt{1 - \tau \sin^2(\varphi/2)}, \tag{C1}$$

with

$$\Delta' = \frac{\Delta_{\mathrm{Al}}}{\sqrt{(1+\Lambda)^2 + (x_0 \Lambda \sqrt{1-\tau})^2}}. \tag{C2}$$

To fit the resonator frequency shift in single-tone spectra, we use the perturbative model developed in Ref. [24]. This model relies on expansion of the Hamiltonian up to second order in $\Phi_{\mathrm{zpf}}/\Phi_0$, which is still applicable to our strongly coupled system. The resonator shift is determined

by the ABSs in the ground state, which is described by

$$\delta f_r = -2\left(\frac{\pi\Phi_{\rm zpf}}{\Phi_0}\right)^2 \frac{\partial^2 f_A}{\partial\varphi} + \left(\frac{g_c(\varphi)}{2\pi}\right)^2 \left(\frac{2}{f_A} - \frac{1}{f_A - f_r} - \frac{1}{f_A + f_r}\right), \quad \text{(C3)}$$

with the phase-dependent coupling rate

$$\frac{g_c(\varphi)}{2\pi} = \frac{\Phi_{\rm zpf}}{\Phi_0}\sqrt{(1-\tau)}\left(-\frac{\partial f_A}{\partial\varphi}\right)\tan(\varphi/2), \quad \text{(C4)}$$

where the pair transition frequency is expressed through its energy as $f_A(\varphi) = 2E_A(\varphi)/h$.

Here, we have introduced a single channel and neglected all the possible higher-energy states, including the continuum of states above the superconducting gap, which is known to contribute to the inductive response of a finite-length weak link [36,45]. We have also neglected the inductive energy of the shared inductance, which is generally true only when the supercurrent in the weak link is sufficiently small. However, this simple model demonstrated good correspondence between the extracted value of the coupling and the one directly observed in spectroscopy (e.g., in Fig. 3 in the main text), which justifies its validity.

In our fits, we used the least-squares method. When the single-tone spectra in Figs. 3(b) and 4(b) were fitted, the data set was multiplied by $f_A - f_r$ to eliminate the divergence in Eq. (C3).

APPENDIX D: RELATION BETWEEN THE PHASE ACROSS THE WEAK LINK AND THE APPLIED FLUX

In our devices, the loop inductance comprises the highly inductive NbTiN film with a total inductance of $2l \approx 10\,\text{nH}$. When external flux is applied, part of the phase drops across the loop inductance, causing the self-screening effect [46],

$$\varphi = \frac{2\pi}{\Phi_0}(\Phi - 2lI_s), \quad \text{(D1)}$$

where the supercurrent through the weak link is given by

$$I_s = \frac{-2e}{\hbar}\sum_p \frac{\partial E_A^p}{\partial\varphi}. \quad \text{(D2)}$$

Here, the sum is taken over all ABSs with dispersions E_A^p. The full spectrum of ABSs residing in the weak link spans up to $2\Delta_{\rm Al}$ and, therefore, is usually not accessible in experiments.

However, it is possible to estimate the self-screening effect in the dispersive regime. Considering the circuit shown in Fig. 1(d) classically, we obtain the resonator frequency shift that arises from shunting the $2l$ part of the resonator inductance with the phase-dependent weak-link inductance $L_{\rm wl}(\varphi)$,

$$\frac{\delta f}{f_r} = -\frac{\delta L}{2(2L_r)}, \quad \text{(D3)}$$

where $2L_r$ is the total resonator inductance and

$$\delta L = 2L_r - 2l + \frac{2lL_{\rm wl}}{2l + L_{\rm wl}} - 2L_r = -\frac{(2l)^2}{2l + L_{\rm wl}}. \quad \text{(D4)}$$

Thus, the weak-link inductance can be directly retrieved from the single-tone spectra in the dispersive regime. The total supercurrent is related to the weak-link inductance as [47]

$$L_{\rm wl}(\varphi)^{-1} = \frac{2\pi}{\Phi_0}\frac{\partial I_s}{\partial\varphi}. \quad \text{(D5)}$$

We analyze the self-screening effect, using the single-tone spectroscopy data obtained for device 3 at $V_g = 1.5034\,\text{V}$ [see Fig. 7(a)]. In this regime, no avoided crossing is observed, but the resonator shift is reasonably large (about 150 MHz), which implies that one or a few ABSs with moderate transmission are present in the weak link, resulting in a relatively large supercurrent. The frequency shift fit is obtained by introducing one channel with

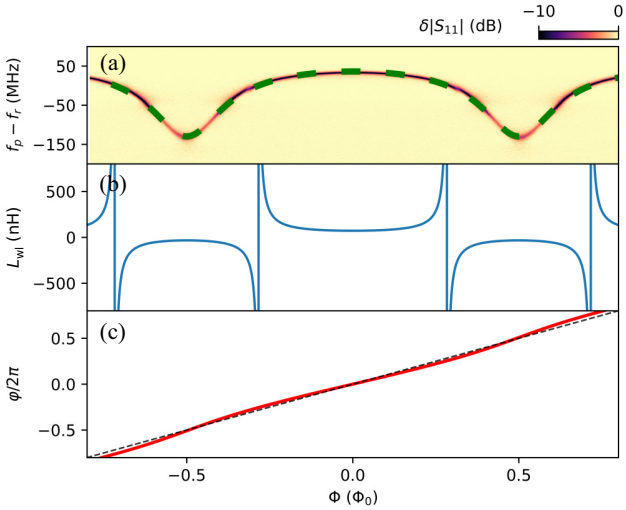


FIG. 7. (a) Single-tone spectrum measured in device 3 at $V_g = 1.5034\,\text{V}$ offset to the bare resonator frequency $f_r = 7.4685$ GHz. The frequency shift fit as a function of applied flux is denoted by the green dashed line. (b) The corresponding weak-link inductance, derived from Eqs. (D3) and (D4). (c) The red line represents the phase across the weak link φ as a function of the applied flux Φ. For comparison, the black dashed line is plotted in the absence of self-screening ($2l = 0$).

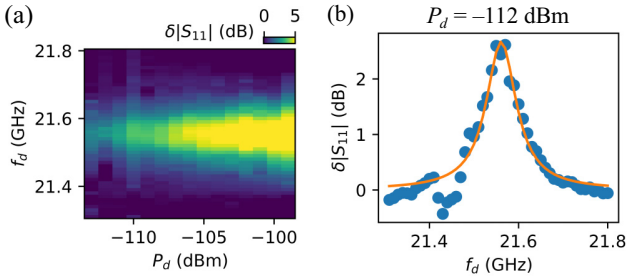


FIG. 8. (a) Power spectrum for device 3 at $V_g = 3.962$ V and $\varphi = 0$. (b) Line cut of panel (a) at low power $P_d = -112$ dBm with a Lorentzian fit.

$\Delta'/h = 17$ GHz, $\tau = 0.68$, and $\Phi_{\rm zpf} = 0.025\Phi_0$. Using Eqs. (D3) and (D4), we extract $L_{\rm wl}$ as a function of the applied flux [see Fig. 7(b)]. Further, under the assumption of negligible self-screening, $\varphi \approx 2\pi\Phi/\Phi_0$, we calculate the supercurrent by integrating Eq. (D5), and plug it into Eq. (D1) to estimate the self-screening. Figure 7(c) shows that $\varphi \approx 2\pi\Phi/\Phi_0$ was indeed a reasonable approximation, and self-screening can be neglected.

APPENDIX E: POWER SPECTRUM

Figure 8(a) represents the power spectrum, obtained for one of the PTs observed in device 2 at $\varphi = 0$. A low-power spectral line can be used to estimate the lower bound of the inhomogeneous dephasing time T_2^* in this device [48]. A line cut at $P_d = -112$ dBm is shown in Fig. 8(b). A Lorentzian fit to the spectral line fit reveals the full width at half maximum, $f_{\rm FWHM} \approx 82$ MHz. We estimate the lower bound of the inhomogeneous dephasing time as $T_2^* \gtrapprox 1/\pi f_{\rm FWHM} \approx 4$ ns, a smaller value compared to that previously reported in Ref. [15].

APPENDIX F: ADDITIONAL SPECTROSCOPY DATA

In this section, further data are provided for the devices.

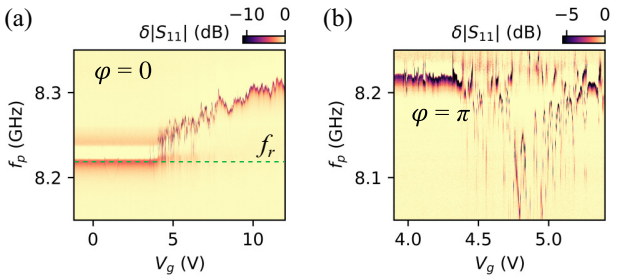


FIG. 9. Gate response measured in device 1 at (a) $\varphi = 0$ and (b) $\varphi = \pi$. The line at $f_r = 8.223$ GHz in panel (a) denotes the bare resonator frequency, when the nanowire is fully pinched off. The gate-independent background was subtracted.

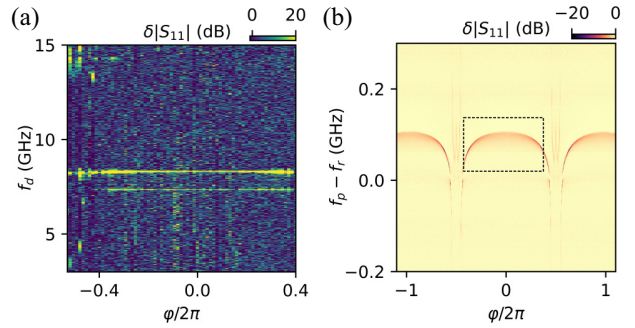


FIG. 10. Supplement to Fig. 4. (a) Two-tone spectrum measured in device 1 at $V_g = 14.5$ V. (b) The single-tone spectrum in a wide range of phase verifies the periodicity. The dashed rectangle denotes the range where panel (a) was measured.

1. Device 1

Figures 9(a) and 9(b) show the gate response of device 1 at $\varphi = 0$ and at $\varphi = \pi$, respectively. Figure 10 is a supplement to Fig. 4. The two-tone spectrum in Fig. 10(a) shows the lack of contributions from other higher-energy transitions, which justifies the use of the single-channel approximation in the fit in Fig. 4(b). The wide-range single-tone spectrum in Fig. 10(b) confirms the periodicity.

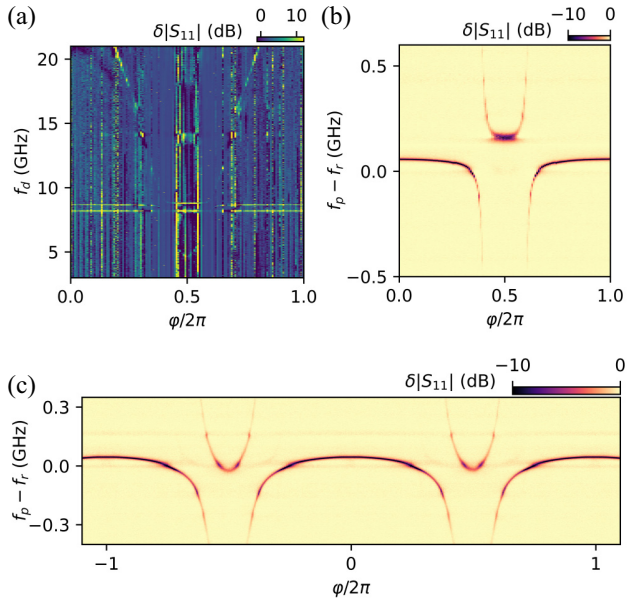


FIG. 11. Supplement to Fig. 3. (a) Two-tone spectrum measured in device 2 at $V_g = 3.39$ V. No higher-energy transitions are observed, which validates the single-channel model used in the fits. (b) The corresponding single-tone spectrum. (c) The single-tone spectrum at $V_g = 3.07$ V demonstrates periodicity.

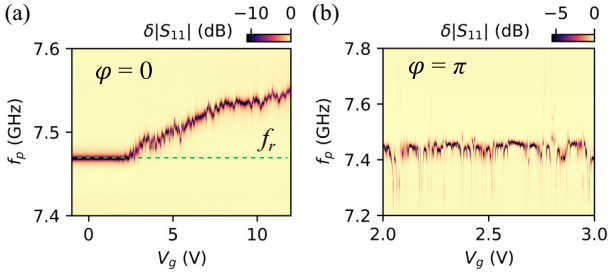


FIG. 12. Gate response measured in device 3 at (a) $\varphi = 0$ and (b) $\varphi = \pi$. The line at $f_r = 7.4685$ GHz in panel (a) denotes the bare resonator frequency, when the nanowire is fully pinched off. The gate-independent background was subtracted.

2. Device 2

Figure 11 is a supplement to Fig. 3. The two-tone spectrum in Fig. 11(a) demonstrates the absence of higher-energy transitions, which justifies the single-channel approximation used in the fit in Fig. 3(b). Figure 11(b) shows the corresponding single-tone spectrum. The wide range spectrum at $V_g = 3.07$ V in Fig. 11(c) confirms the periodicity.

3. Device 3

Figures 12(a) and 12(b) show the gate response of device 3 at $\varphi = 0$ and $\varphi = \pi$, respectively.

[1] A. Blais, A. L. Grimsmo, S. M. Girvin, and A. Wallraff, Circuit quantum electrodynamics, Rev. Mod. Phys. **93**, 025005 (2021).

[2] X. Mi, J. V. Cady, D. M. Zajac, P. W. Deelman, and J. R. Petta, Strong coupling of a single electron in silicon to a microwave photon, Science **355**, 156 (2016).

[3] J. Clarke and F. K. Wilhelm, Superconducting quantum bits, Nature **453**, 1031 (2008).

[4] A. Wallraff, D. I. Schuster, A. Blais, L. Frunzio, R.-S. Huang, J. Majer, S. Kumar, S. M. Girvin, and R. J. Schoelkopf, Strong coupling of a single photon to a superconducting qubit using circuit quantum electrodynamics, Nature **431**, 162 (2004).

[5] P. Forn-Díaz, L. Lamata, E. Rico, J. Kono, and E. Solano, Ultrastrong coupling regimes of light-matter interaction, Rev. Mod. Phys. **91**, 025005 (2019).

[6] A. Frisk Kockum, A. Miranowicz, S. De Liberato, S. Savasta, and F. Nori, Ultrastrong coupling between light and matter, Nat. Rev. Phys. **1**, 19 (2019).

[7] W. Qin, A. F. Kockum, C. S. Muñoz, A. Miranowicz, and F. Nori, Quantum amplification and simulation of strong and ultrastrong coupling of light and matter, Phys. Rep. **1078**, 1 (2024).

[8] T. Niemczyk, F. Deppe, H. Huebl, E. P. Menzel, F. Hocke, M. J. Schwarz, J. J. Garcia-Ripoll, D. Zueco, T. Hümmer, E. Solano, A. Marx, and R. Gross, Circuit quantum electrodynamics in the ultrastrong-coupling regime, Nat. Phys. **6**, 772 (2010).

[9] Y. Wang, C. Guo, G.-Q. Zhang, G. Wang, and C. Wu, Ultrafast quantum computation in ultrastrongly coupled circuit QED systems, Sci. Rep. **7**, 1 (2017).

[10] I. O. Kulik, Macroscopic quantization and the proximity effect in S-N-S junctions, Sov. J. Exp. Theor. Phys. **30**, 944 (1969).

[11] C. W. J. Beenakker and H. van Houten, Josephson current through a superconducting quantum point contact shorter than the coherence length, Phys. Rev. Lett. **66**, 3056 (1991).

[12] M. A. Despósito and A. Levy Yeyati, Controlled dephasing of Andreev states in superconducting quantum point contacts, Phys. Rev. B **64**, 140511(R) (2001).

[13] A. Zazunov, V. S. Shumeiko, E. N. Bratus', J. Lantz, and G. Wendin, Andreev level qubit, Phys. Rev. Lett. **90**, 087003 (2003).

[14] C. Janvier, L. Tosi, L. Bretheau, Ç. Ö. Girit, M. Stern, P. Bertet, P. Joyez, D. Vion, D. Esteve, M. F. Goffman, H. Pothier, and C. Urbina, Coherent manipulation of Andreev states in superconducting atomic contacts, Science **349**, 1199 (2015).

[15] M. Hays, G. de Lange, K. Serniak, D. J. van Woerkom, D. Bouman, P. Krogstrup, J. Nygård, A. Geresdi, and M. H. Devoret, Direct microwave measurement of Andreev-bound-state dynamics in a semiconductor-nanowire Josephson junction, Phys. Rev. Lett. **121**, 047001 (2018).

[16] P. Zellekens, R. S. Deacon, P. Perla, D. Grützmacher, M. I. Lepsa, T. Schäpers, and K. Ishibashi, Microwave spectroscopy of Andreev states in InAs nanowire-based hybrid junctions using a flip-chip layout, Commun. Phys. **5**, 1 (2022).

[17] N. M. Chtchelkatchev and Yu. V. Nazarov, Andreev quantum dots for spin manipulation, Phys. Rev. Lett. **90**, 226806 (2003).

[18] C. Padurariu and Yu. V. Nazarov, Theoretical proposal for superconducting spin qubits, Phys. Rev. B **81**, 144519 (2010).

[19] L. Tosi, C. Metzger, M. F. Goffman, C. Urbina, H. Pothier, S. Park, A. L. Yeyati, J. Nygård, and P. Krogstrup, Spin-orbit splitting of Andreev states revealed by microwave spectroscopy, Phys. Rev. X **9**, 011010 (2019).

[20] M. Hays, V. Fatemi, D. Bouman, J. Cerrillo, S. Diamond, K. Serniak, T. Connolly, P. Krogstrup, J. Nygård, A. L. Yeyati, A. Geresdi, and M. H. Devoret, Coherent manipulation of an Andreev spin qubit, Science **373**, 430 (2021).

[21] M. Hays, V. Fatemi, K. Serniak, D. Bouman, S. Diamond, G. de Lange, P. Krogstrup, J. Nygård, A. Geresdi, and M. H. Devoret, Continuous monitoring of a trapped superconducting spin, Nat. Phys. **16**, 1103 (2020).

[22] A. Bargerbos, M. Pita-Vidal, R. Žitko, L. J. Splitthoff, L. Grünhaupt, J. J. Wesdorp, Y. Liu, L. P. Kouwenhoven, R. Aguado, C. K. Andersen, A. Kou, and B. van Heck, Spectroscopy of spin-split Andreev levels in a quantum dot with superconducting leads, Phys. Rev. Lett. **131**, 097001 (2023).

[23] M. Pita-Vidal, A. Bargerbos, R. Žitko, L. J. Splitthoff, L. Grünhaupt, J. J. Wesdorp, Y. Liu, L. P. Kouwenhoven, R. Aguado, B. van Heck, A. Kou, and C. K. Andersen, Direct

manipulation of a superconducting spin qubit strongly coupled to a transmon qubit, Nat. Phys. **19**, 1110 (2023).

[24] C. Metzger, S. Park, L. Tosi, C. Janvier, A. A. Reynoso, M. F. Goffman, C. Urbina, A. Levy Yeyati, and H. Pothier, Circuit-QED with phase-biased Josephson weak links, Phys. Rev. Res. **3**, 013036 (2021).

[25] F. J. Matute-Cañadas, C. Metzger, S. Park, L. Tosi, P. Krogstrup, J. Nygård, M. F. Goffman, C. Urbina, H. Pothier, and A. L. Yeyati, Signatures of interactions in the Andreev spectrum of nanowire Josephson junctions, Phys. Rev. Lett. **128**, 197702 (2022).

[26] J. J. Wesdorp, F. J. Matute-Cañadas, A. Vaartjes, L. Grünhaupt, T. Laeven, S. Roelofs, L. J. Splitthoff, M. Pita-Vidal, A. Bargerbos, D. J. van Woerkom, P. Krogstrup, L. P. Kouwenhoven, C. K. Andersen, A. L. Yeyati, B. van Heck, and G. de Lange, Microwave spectroscopy of interacting Andreev spins, Phys. Rev. B **109**, 045302 (2024).

[27] P. Krogstrup, N. L. B. Ziino, W. Chang, S. M. Albrecht, M. H. Madsen, E. Johnson, J. Nygård, C. M. Marcus, and T. S. Jespersen, Epitaxy of semiconductor–superconductor nanowires, Nat. Mater. **14**, 400 (2015).

[28] M. Pita-Vidal, J. J. Wesdorp, and C. K. Andersen, Blueprint for all-to-all-connected superconducting spin qubits, PRX Quantum **6**, 010308 (2025).

[29] H. Lu, I. A. Day, A. R. Akhmerov, B. van Heck, and V. Fatemi, Kramers-protected hardware-efficient error correction with Andreev spin qubits, ArXiv:2412.16116 [quant-ph].

[30] S. Abay, D. Persson, H. Nilsson, F. Wu, H. Q. Xu, M. Fogelström, V. Shumeiko, and P. Delsing, Charge transport in InAs nanowire Josephson junctions, Phys. Rev. B **89**, 214508 (2014).

[31] M. H. Devoret, S. Girvin, and R. Schoelkopf, Circuit-QED: How strong can the coupling between a Josephson junction atom and a transmission line resonator be? Ann. Phys. **519**, 767 (2007).

[32] A. Stockklauser, P. Scarlino, J. V. Koski, S. Gasparinetti, C. K. Andersen, C. Reichl, W. Wegscheider, T. Ihn, K. Ensslin, and A. Wallraff, Strong coupling cavity QED with gate-defined double quantum dots enabled by a high impedance resonator, Phys. Rev. X **7**, 011030 (2017).

[33] J. E. Sestoft, M. Marnauza, D. Olsteins, T. Kanne, R. D. Schlosser, I.-J. Chen, K. Grove-rasmussen, and J. Nygård, Shadowed versus etched superconductor–semiconductor junctions in Al/InAs nanowires, Nano Lett. **24**, 8394 (2024).

[34] S. Park and A. L. Yeyati, Andreev spin qubits in multichannel Rashba nanowires, Phys. Rev. B **96**, 125416 (2017).

[35] J. H. Ungerer, A. Pally, A. Kononov, S. Lehmann, J. Ridderbos, P. P. Potts, C. Thelander, K. A. Dick, V. F. Maisi, P. Scarlino, A. Baumgartner, and C. Schönenberger, Strong coupling between a microwave photon and a singlet-triplet qubit, Nat. Commun. **15**, 1 (2024).

[36] V. Fatemi, P. D. Kurilovich, M. Hays, D. Bouman, T. Connolly, S. Diamond, N. E. Frattini, V. D. Kurilovich, P. Krogstrup, J. Nygård, A. Geresdi, L. I. Glazman, and M. H. Devoret, Microwave susceptibility observation of interacting many-body Andreev states, Phys. Rev. Lett. **129**, 227701 (2022).

[37] M. R. Sahu, F. J. Matute-Cañadas, M. Benito, P. Krogstrup, J. Nygård, M. F. Goffman, C. Urbina, A. L. Yeyati, and H. Pothier, Ground-state phase diagram and parity-flipping microwave transitions in a gate-tunable Josephson junction, Phys. Rev. B **109**, 134506 (2024).

[38] C. Metzger, Spin & charge effects in Andreev bound states, Ph.D. thesis, Service de physique de l'état condensé, France, Quantronics Group, France, Saclay, 2022.

[39] H. Lu, D. F. Bofill, Z. Sun, T. Kanne, J. Nygård, M. Kjaergaard, and V. Fatemi, Andreev spin relaxation time in a shadow-evaporated InAs weak link, Phys. Rev. Appl. **24**, 024046 (2025).

[40] O. Shvetsov, A. Khola, V. Buccheri, I. Cools, N. Trnjanin, T. Kanne, J. Nygård, and A. Geresdi, Dataset for "Approaching the ultrastrong coupling regime between an Andreev level and a microwave resonator", https://zenodo.org/records/17117780 (2025).

[41] A. J. Annunziata, D. F. Santavicca, L. Frunzio, G. Catelani, M. J. Rooks, A. Frydman, and D. E. Prober, Tunable superconducting nanoinductors, Nanotechnology **21**, 445202 (2010).

[42] J. Bardeen, L. N. Cooper, and J. R. Schrieffer, Theory of superconductivity, Phys. Rev. **108**, 1175 (1957).

[43] I. P. C. Cools, R. M. López-Báez, V. Buccheri, O. Shvetsov, N. Trnjanin, E. Hogedal, and S. P. Dash, Losses in magnetic field resilient coplanar stripline resonators, J. Phys. D: Appl. Phys. **58**, 255102 (2025).

[44] S. Probst, F. B. Song, P. A. Bushev, A. V. Ustinov, and M. Weides, Efficient and robust analysis of complex scattering data under noise in microwave resonators, Review of Scientific Instruments **86**, 024706 (2015).

[45] P. D. Kurilovich, V. D. Kurilovich, V. Fatemi, M. H. Devoret, and L. I. Glazman, Microwave response of an Andreev bound state, Phys. Rev. B **104**, 174517 (2021).

[46] P. Jung, S. Butz, S. V. Shitov, and A. V. Ustinov, Low-loss tunable metamaterials using superconducting circuits with Josephson junctions, Appl. Phys. Lett. **102**, 062601 (2013).

[47] A. Paila, D. Gunnarsson, J. Sarkar, M. A. Sillanpää, and P. J. Hakonen, Current-phase relation and Josephson inductance in a superconducting Cooper-pair transistor, Phys. Rev. B **80**, 144520 (2009).

[48] K. D. Petersson, J. R. Petta, H. Lu, and A. C. Gossard, Quantum coherence in a one-electron semiconductor charge qubit, Phys. Rev. Lett. **105**, 246804 (2010).

PAPER IV

Kerr nonlinearity and three-wave mixing in superconducting resonators hosting Al-InAs weak links

Vittorio Buccheri, Ivo P. C. Cools, Nermin Trnjanin, Ankit Khola, Oleg Shvetsov, Thomas Kanne, Jesper Nygård, Attila Geresdi, and Simone Gasparinetti

Manuscript under review. arXiv:2608.28428

Contribution: The candidate was primarily responsible for the device fabrication, measurements, data analysis, and modeling. He wrote the manuscript.

Kerr nonlinearity and three-wave mixing in superconducting resonators hosting Al-InAs weak links

Vittorio Buccheri[1*], Ivo P. C. Cools[1], Nermin Trnjanin[1], Ankit Khola[1], Oleg Shvetsov[1], Thomas Kanne[2], Jesper Nygård[2], Attila Geresdi[1], Simone Gasparinetti[1†]

[1] *Department of Microtechnology and Nanoscience, Chalmers University of Technology, 41296 Gothemburg, Sweden.*

[2] *Center for Quantum Devices, Niels Bohr Institute, University of Copenhagen, Universitetsparken 5, DK-2100 Copenhagen, Denmark.*

Nonlinear microwave resonators are a versatile tool in quantum information processing, enabling parametric amplification, continuous variable quantum computing, and engineered mode interactions. Many of these applications especially benefit from cubic nonlinearities enabling three-wave mixing; at the same time, they are limited by quartic nonlinearities giving rise to undesired Kerr effects. A recurrent challenge is therefore to engineer resonators with a finite cubic nonlinearity while suppressing quartic terms. Here, we investigate a superconducting resonator hosting two weak links fabricated from an aluminum-capped indium arsenide nanowire. We characterize the Kerr nonlinearity as a function of magnetic flux and gate bias, showing that it can be tuned to zero with either control parameter. Furthermore, we experimentally demonstrate three-wave mixing in a semiconductor-superconductor hybrid device, establishing nonzero cubic nonlinearity. An effective model based on Andreev bound states qualitatively captures the observed trends. Our results validate semiconductor-superconductor hybrid devices as a promising platform for tunable nonlinear superconducting circuits, with applications in parametric amplification, quantum control of bosonic modes, and engineering interactions between microwave modes.

Superconducting microwave resonators with engineered nonlinearities are a key component in quantum information processing. Their nonlinear response enables a broad range of applications, including parametric amplification [1–7], bosonic-mode quantum computing [8–12], and both linear [13, 14] and nonlinear [15] coupling schemes.

Many of these applications rely on the cubic nonlinearity, which enables three-wave mixing for parametric amplification [4–7], non-Gaussian interactions [12], and beamsplitter coupling between bosonic modes [13]. By contrast, the Kerr nonlinearity is often detrimental, limiting the dynamic range of the amplifiers and degrading the fidelity of bosonic-mode operations. Engineering resonators with a nonzero cubic nonlinearity while suppressing the Kerr term is therefore a recurrent challenge in superconducting quantum circuits.

Nonlinearity is introduced into superconducting resonators either through the current-dependent kinetic inductance of a superconducting film [16–19] or through Josephson-junction-based elements. Devices such as the radio-frequency superconducting quantum interference device (rf-SQUID) [4], the superconducting nonlinear asymmetric inductive element (SNAIL) [5], the asymmetrically threaded SQUID (ATS) [9], and the linear inductive coupler (LINC) [14] exploit the nonlinear Josephson potential, whose effective shape can be engineered by arranging one or more junctions in superconducting loops. Appropriate choices of the junction parameters and external magnetic flux then allow independent control of the cubic and quartic nonlinearities.

Another strategy for realizing tunable nonlinearity relies on semiconducting weak links. In the short-junction limit, a single conducting-channel semiconducting weak link hosts a spin-degenerate pair of Andreev bound states (ABSs) with potential $\pm U_{\mathrm{ABS}}(\varphi) = \pm\Delta\sqrt{1-\tau\sin^2(\varphi/2)}$, where Δ is the superconducting gap of the junction leads and τ is the junction transparency [20–22]. In contrast to tunnel junction-based technologies, τ can be tuned via electrostatic gating, providing an additional control parameter alongside magnetic flux.

The ABSs phenomenology has been widely investigated, including coherent manipulation of both charge [23–25] and spin [26–31] degrees of freedom. However, the dependence of ABS-induced nonlinearities in superconducting resonators on the electrostatic gating and external magnetic flux has not yet been investigated experimentally. This behavior has only been discussed theoretically [32], while experimental studies have been limited to power-dependent state discrimination [33]. Moreover, although parametric amplification based on four-wave mixing has already been demonstrated in aluminum (Al)-indium arsenide (InAs) hybrid devices, both in pla-

*buccheri@chalmers.se
†simoneg@chalmers.se

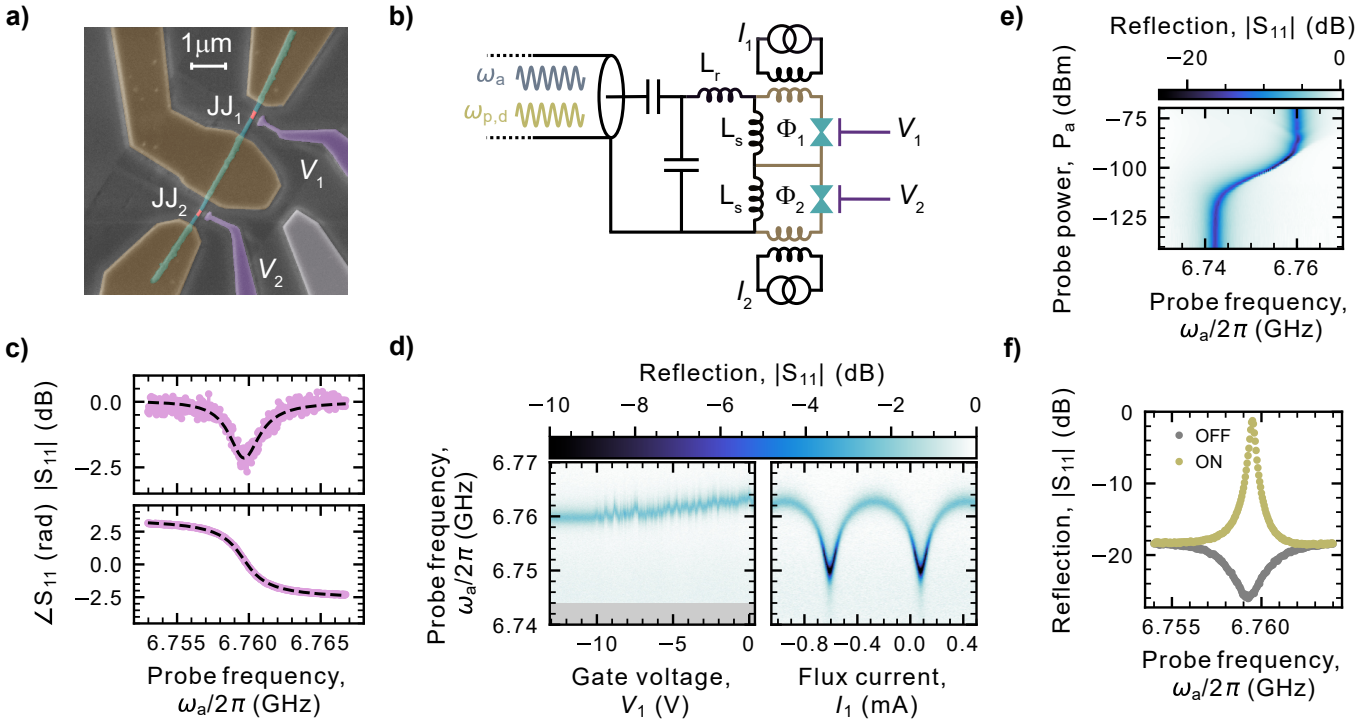


FIG. 1: Device and characterization. **a)** False-colored scanning electron micrograph showing two InAs junctions (red), JJ_1 and JJ_2, defined by selectively etching a 250-nm section of the Al shell (green) covering the nanowire. The nanowire is embedded in the resonator structure (made of NbTiN, not shown) via Ti-Al contacts (yellow) obtained from a standard lift-off process, together with the gate lines V_1 and V_2 (purple), and a ground screening line (light gray) separating the two gates. **b)** Simplified circuit diagram. An LC resonator with total inductance $L_r + 2L_s$ shares two equal inductive sections L_s with two gate-tunable weak links arranged in superconducting loops. The magnetic fluxes through the loops, Φ_1 and Φ_2, are controlled by the currents I_1 and I_2. The resonator is capacitively coupled to a feedline used for both probe tone, ω_a, and pump(drive) tone, $\omega_{p(d)}$. **c)** Magnitude (top) and phase (bottom) of the reflection coefficient, S_{11}, in a gate configuration where both junctions are pinched-off. Black dashed lines represent a circle-fit model [41] with resonant frequency $\omega_r^0/2\pi = 6.759$ GHz, internal quality factor $Q_i^0 = 2.1 \times 10^4$ and external quality factor $Q_c^0 = 2.5 \times 10^3$. **d)** Single-tone spectroscopy showing S_{11} as a function of ω_a and V_1 for $I_1 = -0.25$ mA (left), displaying the activation of JJ_1 for $V_1 > -10$ V, and as a function of ω_a and I_1 for $V_1 = -2$ V (right), displaying a periodic flux modulation. In both cases JJ_2 is pinched-off ($V_2 < -8$ V). **e)** Single-tone spectroscopy versus probe power P_a with both junctions active ($V_1 = V_2 = -1$ V). **f)** Low-power resonator spectra measured with (yellow) and without (gray) an additional pump tone at $\omega_p/2\pi = 13.518$ GHz and power -56 dBm with both junctions active ($V_{1(2)} = 0.5(0.3)$ V).

nar heterostructures [34, 35] and nanowire platforms [36], the three-wave-mixing amplification has not yet been reported.

In this work, we investigate a superconducting resonator incorporating two Al-InAs weak links. We study how these weak links induce both a linear and nonlinear response in the resonator, including the resonance-frequency shift, the Kerr nonlinearity, and the first realization of three-wave mixing parametric amplification. We show that these properties can be tuned through the electrostatic gates controlling the junction transparencies and through the external magnetic flux setting the superconducting phase difference across the weak links. Furthermore, we demonstrate that the observed behavior is qualitatively captured by an effective model based on the ABSs phenomenology. Our results establish hybrid semiconductor-superconductor weak links as versatile nonlinear elements for applications in parametric amplification, bosonic-mode manipulation, and engineered coupling schemes.

The core of our device consists of an Al-capped InAs nanowire [37] hosting two Josephson junctions [see Fig. 1a)]. The junctions are approximately 250 nm long and separated by 4 μm. The nanowire is embedded in a niobium-titanium-nitride (NbTiN) resonator structure [see Supplementary for details on the exact resonator topology and coupling scheme]. An equivalent circuit representation of the device consists of an LC resonator where two portions, L_s, of the total inductance are shared with the junctions, JJ_1 and JJ_2, forming a double rf-

SQUID configuration [see Fig. 1b)]. The resonator is capacitively coupled to a feedline and is probed in reflection; the same feedline is used for drive and pump tones. The electrochemical potentials of the semiconducting junctions are controlled by two gate lines, while two flux lines set the superconducting phase across them. The resonator used in this work has been discussed in [38], and similar devices designed for single junction studies have been employed in [24, 27, 28, 31]. We perform our experiments in a dilution cryostat down to 10 mK. To characterize the device, we compensate for the crosstalk between the flux and gate lines, enabling independent control of the magnetic flux and the electrostatic potential of each junction.

The gate voltages define four distinct operating regimes. When both gate voltages are below their respective pinch-off thresholds, $\tilde{V}_1 = -10$ V and $\tilde{V}_2 = -8$ V, the semiconducting weak links are fully depleted, suppressing transport through both junctions. Here, the junctions effectively behave as open circuits, and the resonator response is independent of both gate voltage and magnetic flux. In this regime we extract the bare resonant frequency, $\omega_{\rm r}^0$, and the internal(external) quality factor, $Q_{\rm i(c)}^0$ [Fig. 1c)]. Increasing only one gate voltage, namely $V_1(V_2) \gg \tilde{V}_1(\tilde{V}_2)$ while keeping $V_2(V_1) < \tilde{V}_2(\tilde{V}_1)$, activates a single-junction configuration and, finally, increasing both gate voltages above pinch-off activates both junctions, bringing the device into the double-junction regime.

Activating a junction opens several conduction channels, whose number and transparency are strongly gate dependent. Consequently, the resonance frequency exhibits an irregular dependence on gate voltage [Fig. 1d), left], consistent with previous observations [26, 31]. An active junction acquires a phase-dependent Josephson inductance resulting in the periodic modulation of the resonance frequency $\omega_{\rm r}(I_1)$, characteristic of a SQUID-like circuit [Fig. 1d), right]. The resonator quality factor is also modulated, as evidenced by changes in the signal intensity. Near the maximum of $\omega_{\rm r}(I_1)$, the resonator remains overcoupled and close to its bare parameters, whereas near the minimum, the resonance shifts to lower frequencies and the losses increase, bringing the resonator close to critical coupling.

Beyond shifting the resonance frequency, both the single- and double-junction configurations introduce nonlinearities, including Kerr nonlinearity and three-wave mixing [5, 7]. The Kerr nonlinearity manifests as a power-dependent shift of the resonance frequency, $\delta\omega_{\rm kerr}(P_{\rm a})$, defined with respect to its low-power value [Fig. 1e)], whereas the three-wave mixing enables energy transfer from a pump tone at $\omega_{\rm p}$ to signal and idler tones at $\omega_{\rm s}$ and $\omega_{\rm i}$ satisfying $\omega_{\rm p} = \omega_{\rm s} + \omega_{\rm i}$. In the degenerate case, $\omega_{\rm s} = \omega_{\rm i}$, yielding $\omega_{\rm p} = 2\omega_{\rm s}$. By comparing two probe-frequency sweeps around $\omega_{\rm r}/2\pi = 6.759$ GHz with and without a pump tone at $\omega_{\rm p}/2\pi = 13.518$ GHz, we observe an on-off gain exceeding 20 dB [Fig. 1f)], which demonstrates three-wave mixing in our system. From the ratio between the on and off traces we extract the on-off gain G, as the amplitude of the Lorentzian fitted to the gain profile (see Supplementary).

We now measure the linear $[\delta\omega_{\rm r} = \omega_{\rm r}(I_1) - \omega_{\rm r}^0]$ and nonlinear $(\delta\omega_{\rm kerr}, G)$ response of the resonator by varying both the flux current and gate voltage.

We first consider the single-junction configuration with $\rm JJ_2$ pinched-off. After converting I_1 into the superconducting phase φ_1 (see Supplementary), we measure a full oscillation $\delta\omega_{\rm r}(\varphi_1)$ for three representative gate voltages, $V_1 = (0.35, 2.2, 1.25)$ V, corresponding to Dataset I, II, and III, respectively [Fig. 2a)]. We find that $\delta\omega_{\rm r}$ exhibits a larger dip when going from I to II and eventually shows an avoided-crossing pattern in III.

These observations are compatible with tuning the transparency of ABS pairs. In the short-junction limit, a semiconducting weak link supporting a single conduction channel is described by a pair of ABSs with energies $\pm U_{\rm ABS}$ [Fig. 2b), top] [21, 22]. Assuming $\hbar = 1$, the corresponding excitation frequency, $\omega_{\rm ABS} = 2U_{\rm ABS}$, reaches its maximum value, 2Δ, at $\varphi = 0$ and 2π, and its minimum value, $2\Delta\sqrt{1-\tau}$, at $\varphi = \pi$ [Fig. 2b), bottom]. Since τ is gate-dependent, the minimum excitation frequency is tuned by the gate voltage. Consequently, the interaction between the resonator and the ABS transition depends strongly on both φ and τ, evolving from a strongly detuned regime to dispersive and eventually resonant coupling around $\varphi = \pi$ as the ABS transparency increases. This interpretation is further supported by two-tone spectroscopy measurements around $\varphi_1 = \pi$, which reveal spectroscopic signatures consistent with ABS transitions [Fig. 2c) and Fig. S6].

We write the frequency shift $\delta\omega_{\rm r}$ induced by a single ABS pair as [21, 22]:

$$\delta\omega_r = -\lambda^2 c_2 + g_{\rm c}^2 \left(\frac{2}{\omega_{\rm ABS}} - \frac{1}{\delta_-} - \frac{1}{\delta_+} \right), \qquad (1)$$

where λ is a dimensionless participation ratio, $c_2 = d^2U_{\rm ABS}/d\varphi^2$, $\delta_\pm = \omega_{\rm ABS} \pm \omega_{\rm r}^0$ and $g_{\rm c} = \lambda\sqrt{1-\tau}\,(dU_{\rm ABS}/d\varphi)\tan(\varphi/2)$ is the phase-dependent coupling rate. The first term in Eq. 1 is the contribution coming from the curvature of the ABS ground state potential, which is dominant at low τ, whereas the second term takes into account the exchange of virtual photons between the resonator and the ABS pair, which is dominant at high τ.

The short-junction limit in InAs nanowire has been proven accurate up to $\sim$ 100 nm-long junctions [39].

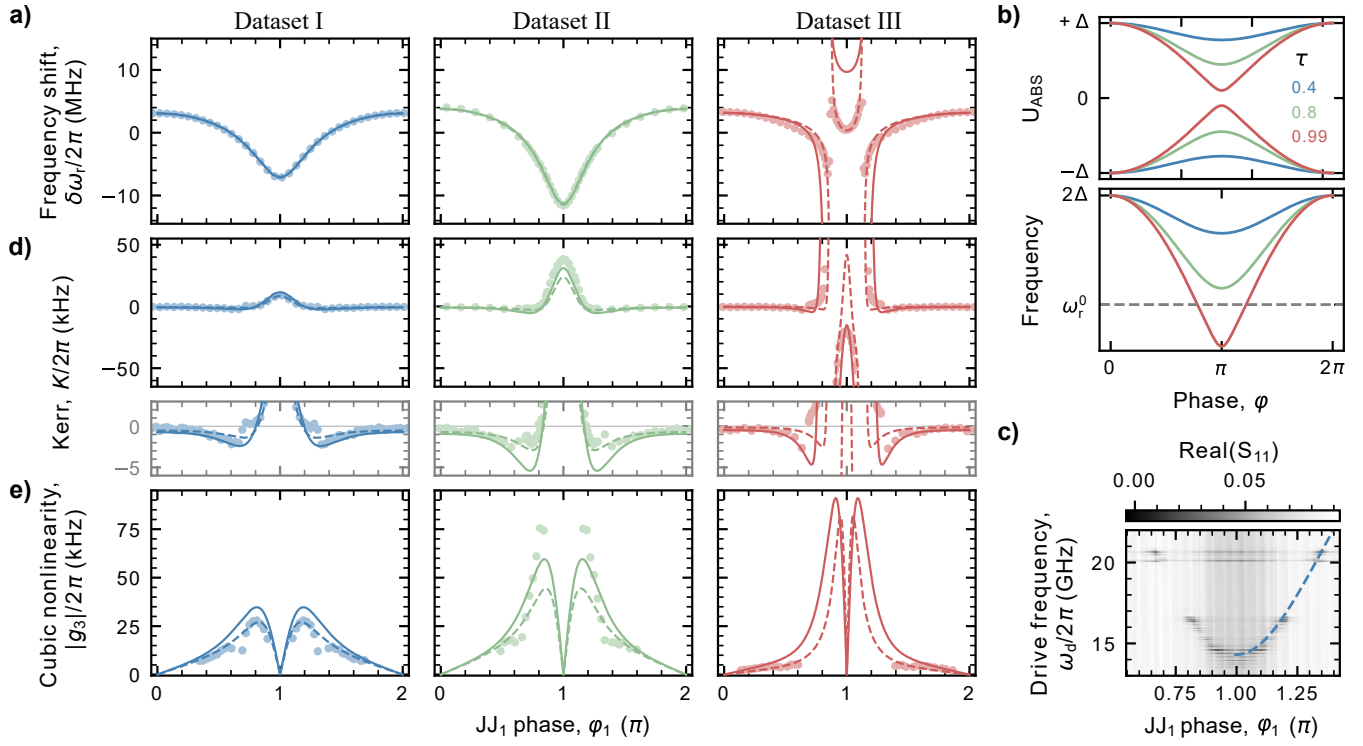


FIG. 2: Single-junction configuration (JJ$_1$ active, JJ$_2$ pinched-off). **a)** Measured frequency shift, $\delta\omega_r$, as a function of the phase across JJ$_1$, φ_1, for Dataset I (left, $V_1 = 0.35$ V), II (center, $V_1 = 2.2$ V) and III (right, $V_1 = 1.25$ V). Solid and dashed lines reproduce single- (Eq. 1) and double-channel (Eq. S8) model, respectively, with the parameters given in Tab.S1. **b)** Single Andreev bound state (ABS) model for three representative transparencies τ. *Top*: Ground- and excited-state ABS energies versus superconducting phase, $\pm U_{ABS}(\varphi)$. *Bottom*: Corresponding ABS excitation frequency $2U_{ABS}(\varphi)$. The horizontal dashed line indicates the bare resonator frequency ω_r^0. **c)** Two-tone spectroscopy measured around $\varphi_1 = \pi$ for the same gate configuration of Dataset I, revealing a spectroscopic feature consistent with an ABS transition coupled to the resonator mode. The blue dashed line shows the expected ω_{ABS}, calculated using $\Delta/2\pi = 16$ GHz and $\tau = 0.8$. **d, e)** Kerr nonlinearity K and cubic nonlinearity $|g_3|$ measured as function of φ_1 for Datasets I, II and III. For K (panel d), both the full range (top row) and a zoom around $K/2\pi = 0$ (bottom row) are shown. Horizontal gridlines on the bottom row of panel d highlight $K/2\pi = 0$. Experimentally, K and $|g_3|$ are obtained from $\delta\omega_{kerr}$ and gain G as explained in the main text and in the Supplementary. Solid and dashed lines represent single- (Eqs. 2 and 3) and double-channel (Eqs. S9 and S10) model, respectively, with the parameters given in Tab.S1.

Even if our junctions are more than twice as long, following Refs. [22, 31, 40], we use the short-junction results as an effective phenomenological description, where finite junction length effects and multichannel transport are modeled through a gate-dependent effective gap $\Delta(V_g) < \Delta_{Al}$, whereas τ represents an average transparency of all the channels present in the junction.

We fit Eq. 1 to $\delta\omega_r(\varphi_1)$ data for Dataset I, II and III [solid lines in Fig. 2a)], extracting the junction parameters $\tau(V_1)$ and $\Delta(V_1)$ (Tab. S1). Using L_s together with the resonator impedance and total inductance obtained from material characterization and electromagnetic simulations, we estimate $\lambda = 0.028$. However, we find that our data are best described by the model when including λ as an additional fit parameter, obtaining values ranging from 0.020 to 0.035. The single-channel model captures $\delta\omega_r(\varphi_1)$ for Dataset I and II, while it fails to reproduce Dataset III around $\varphi_1 = \pi$. We observe that generalizing Eq. 1 for a two-channel ABS model (see Supplementary) solves the discrepancy for Dataset III without producing appreciable changes for Dataset I and II [dashed lines in Fig. 2a)].

We extract the Kerr nonlinearity from the linear dependence of the low-power induced frequency shift, $K \approx \delta\omega_{kerr}/\bar{n}$, where $\bar{n}$ is the average probe photon number in the resonator, and the cubic nonlinearity from the on-off gain as $g_3 \approx G/\sqrt{\bar{n}_p}$, where $\bar{n}_p$ is the average pump photon number in the resonator, as a function of φ_1 for the same datasets discussed above [Fig. 2d)-e)]. Note that the probe and pump powers at the device are estimated

from the nominal line attenuation and are therefore subject to an uncertainty of a few dB.

The Kerr nonlinearity follows a trend opposite to that of $\delta\omega_r$, remaining weakly negative around $\varphi_1 = 0, 2\pi$, and reaching a maximum near $\varphi_1 = \pi$. Its amplitude increases from Dataset I to II and develops a discontinuous pattern in III, following the corresponding avoided crossing in $\delta\omega_r$. In contrast, $|g_3|$ exhibits two peaks symmetric about $\varphi = \pi$, whose amplitude and position depend on the junction transparency. No gain is observed around $\varphi_1 = \pi$, over a phase range that increases from Dataset I to III, preventing the extraction of $|g_3|$ in this region. We attribute this behavior to the combination of an increasing Kerr nonlinearity and a reduced internal quality factor.

Notably, K changes sign, and can therefore be tuned to zero, by either gate or flux control. In particular, for Datasets I and II we find $K/2\pi \approx 0$ kHz around $\varphi_1 = 0.8\pi, 1.2\pi$, where $|g_3|$ reaches approximately 35 kHz and 70 kHz, respectively.

A fourth-order expansion in λ of the Hamiltonian of our system including the ABS pair degrees of freedom, necessary to describe K and g_3, is beyond the scope of the present work. Instead, by combining the ABS ground state contribution calculated in Ref. [32], with the dispersive term discussed in Refs. [33, 42], we approximate the nonlinear parameters as

$$g_3 = \frac{\lambda^3}{6} c_3 \tag{2}$$

and

$$K = \frac{\lambda^4}{2}\left(c_4 - \frac{5c_3^2}{3\tilde{c}_2}\right) + \frac{g_c^4}{\delta_-^3}, \tag{3}$$

where $c_{3(4)} = d^{3(4)}U_{\mathrm{ABS}}/d\varphi^{3(4)}$ and $\tilde{c}_2 = (\Phi_0/2\pi)^2/L_s + c_2$. By using the parameters extracted from $\delta\omega_r$, we find that Eqs. 2 and 3 are in qualitative agreement with the nonlinear data for all three datasets [solid lines in Fig. 2d)-e)]. Generalizing Eqs. 2 and 3 to the two-channel case (see Supplementary) maintains the qualitative agreement for g_3, and for K in Dataset I and II [dashed lines in Fig. 2d)-e)]. For Dataset III, however, including the contribution of the second channel to K worsens the agreement with the data, especially around $\varphi_1 = \pi$, in contrast to the improved description of the linear response. This discrepancy may originate from additional terms arising from a full fourth-order expansion of the Hamiltonian or from inter-channel coupling effects that becomes relevant at higher orders while remaining negligible for the linear response.

With both junctions active, we measure $K(\varphi_{2(1)})$ and $g_3(\varphi_{2(1)})$ at different $\varphi_{1(2)}$ biases [Fig. 3]. At $\varphi_{1(2)} = 0$,

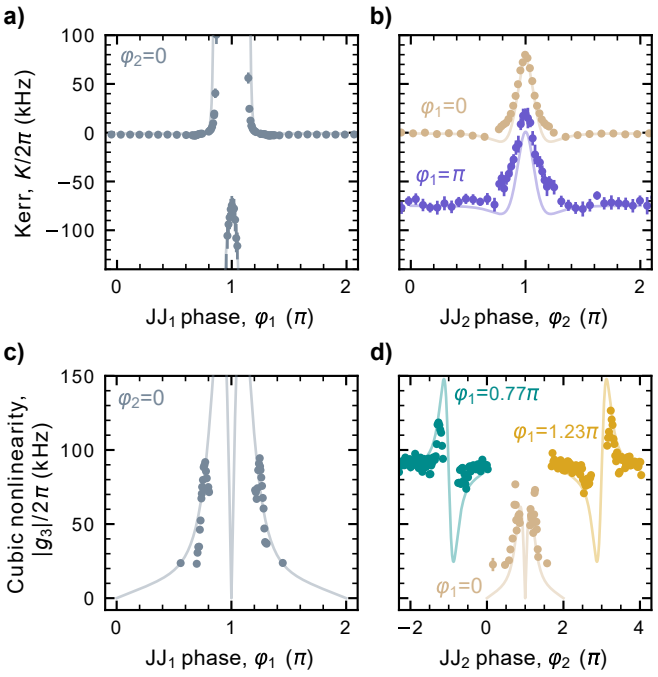


FIG. 3: Two-junction configuration. Kerr nonlinearity K measured at gate voltages $V_1 = 1.58$ V and $V_2 = 1.94$ V, **a)** versus φ_1 with $\varphi_2 = 0$, and **b)** versus φ_2 with $\varphi_1 = 0$ (sand) and $\varphi_1 = \pi$ (violet). Solid lines show $K(\varphi_1) + K(\varphi_2)$ calculated from Eq. 3. Cubic nonlinearity g_3 measured at gate voltages $V_1 = -0.05$ V and $V_2 = 1.15$ V, **c)** versus φ_1 with $\varphi_2 = 0$, and **d)** versus φ_2 with $\varphi_1 = 0$ (sand), $\varphi_1 = 0.77\pi$ (teal) and $\varphi_1 = 1.23\pi$ (gold). The three datasets in d) are displayed over successive phase periods for clarity. Solid lines show $|g_3(\varphi_1) + g_3(\varphi_2)|$ calculated from Eq. 2. Model parameters are listed in Tab. S2.

both quantities behave as in the single junction configuration, which allows the extraction of the system parameters [Tab. S2]. On the other hand, biasing $\varphi_1 = \pi$ shifts $K(\varphi_2)$ vertically by $K(\varphi_1 = \pi) = -70$ kHz [Fig. 3a-b)]. Similarly, biasing $g_3(\varphi_1)$ to either peak shifts $g_3(\varphi_2)$ by the corresponding peak value and alters its symmetry [Fig. 3c-d)]. Neglecting both the interaction between the junctions and the loop inductance, we find that the measurements are well described by the sum of the individual junction contributions.

The double-junction configuration therefore provides an additional degree of control over the resonator nonlinearities. In particular, varying φ_1 shifts the $K(\varphi_2) = 0$ operating point, although the accessible range is limited by flux noise and the steep phase dependence of $K(\varphi_1)$ near π. Furthermore, biasing JJ_1 close to the maxima of $|g_3(\varphi_1)|$ maintains a large cubic nonlinearity over a broad range of φ_2, enabling amplification across a wider frequency range while reducing the pump power required to reach a given gain. After maximizing g_3 and minimiz-

ing K, in the double junction configuration, we obtain an on-off gain of 25 dB and a -1 dB compression point of -138 dBm. A quantitative assessment of the amplifier performance is currently limited by the lack of a calibrated input attenuation and amplification chain (see Supplementary). Further studies will therefore be required to optimize the amplifier performance and identify its limiting factors.

In conclusion, we have characterized the linear and nonlinear response of a superconducting resonator coupled to two semiconducting Josephson junctions which we can control independently. We have shown how the Kerr nonlinearity K and the cubic nonlinearity g_3 depend on both flux and gate voltage, finding an operating point at which K is negligible and g_3 is sizable. To our knowledge, this constitutes the first experimental demonstration of a nonzero cubic nonlinearity in superconductor-semiconductor hybrid devices. A model based on Andreev bound state pairs shows qualitative agreement with our data. We further observed that the double-junction configuration is well described by the sum of the single-junction contributions.

No Andreev molecule phenomenology [43] was observed in our device, consistently with the junction separation (~ 4 μm) significantly exceeding the superconducting coherence length (hundreds of nm). However, investigating future devices with much closer junctions, as in Refs. [44, 45], would allow measurement of the nonlinearities induced by the Andreev molecule potential.

Our findings open new pathways for semiconducting Josephson junctions to be deployed in three-wave mixing-based amplifiers, quantum control of bosonic modes, and coupling schemes such as beamsplitter interaction.

Acknowledgments

We thank V. Fatemi, M. Jirlow, T. Abad, F. J. Matute-Cañadas and A. Levy Yeyati for fruitful discussions. This work was financially supported by the European Unions H2020 Research and Innovation Program, Grants No. 804988 (SiMS) and No. 828948 (AndQC), by the Army Research Office (ARO), Grant No. W911NF2210053, by the Novo Nordisk Foundation, project SolidQ, and by the Carlsberg Foundation. The device discussed in this work was fabricated at the Chalmers Myfab cleanroom facility. S.G. acknowledges financial support from the European Research Council (Grant No. 101041744 ESQuAT), and from the Knut and Alice Wallenberg Foundation through the Wallenberg Centre for Quantum Technology (WACQT). External interest disclosure: S.G. is a co-founder and equity holder in Sweden Quantum AB.

[1] B. Yurke, L. R. Corruccini, P. G. Kaminsky et al., *Observation of parametric amplification and deamplification in a Josephson parametric amplifier*, Phys. Rev. A 39, 2519 (1989).

[2] T. Yamamoto, K. Inomata, M. Watanabe et al., *Flux-driven Josephson parametric amplifier*, Appl. Phys. Lett. 93, 042510 (2008).

[3] M. A. Castellanos-Beltran, K. D. Irwin, G. C. Hilton et al., *Amplification and squeezing of quantum noise with a tunable Josephson metamaterial*, Nature Physics volume 4, 929931 (2008).

[4] A. B. Zorin, *Josephson Traveling-Wave Parametric Amplifier with Three-Wave Mixing*, Appl. Rev. Applied. 6, 034006 (2016).

[5] N. E. Frattini, U. Vool, S. Shankar et al., *3-wave mixing Josephson dipole element*, Appl. Phys. Lett. 110, 222603 (2017).

[6] N. E. Frattini, V. V. Sivak, A. Lingenfelter et al., *Optimizing the Nonlinearity and Dissipation of a SNAIL Parametric Amplifier for Dynamic Range*, Phys. Rev. Applied 10, 054020 (2018).

[7] V. V. Sivak, N. E. Frattini, V. R. Joshi et al., *Kerr-Free Three-Wave Mixing in Superconducting Quantum Circuits*, Phys. Rev. Applied 11, 054060 (2019).

[8] S. Puri, S. Boutin and A. Blais, *Engineering the quantum states of light in a Kerr-nonlinear resonator by two-photon driving*, npj Quantum Inf 3, 18 (2017).

[9] R. Lescanne, M. Villiers, T. Peronnin et al., *Exponential suppression of bit-flips in a qubit encoded in an oscillator*, Nature Physics volume 16, 509513 (2020).

[10] W.-L. Ma, S. Puri, R. J. Schoelkopf et al., *Quantum control of bosonic modes with superconducting circuits*, Sci. Bull. 66, 1789 (2021).

[11] D. Iyama, T. Kamiya, S. Fujii et al., *Observation and manipulation of quantum interference in a superconducting Kerr parametric oscillator*, Nat Commun 15, 86 (2024).

[12] A. M. Eriksson, T. Sépulcre, M. Kervinen et al., *Universal control of a bosonic mode via drive-activated native cubic interactions*, Nat Commun 15, 2512 (2024).

[13] B. J. Chapman, S. J. de Graaf, S. H. Xue, et al., *High-On-Off-Ratio Beam-Splitter Interaction for Gates on Bosonically Encoded Qubits*, PRX Quantum 4, 020355 (2023).

[14] A. Maiti, J. W. O. Garmon, Y. Lu et al., *Linear Quantum Coupler for Clean Bosonic Control*, PRX Quantum 6, 040326 (2025).

[15] Y. Ye, K. Peng, M. Naghiloo et al., *Engineering Purely Nonlinear Coupling between Superconducting Qubits Using a Quarton*, Phys. Rev. Lett. 127, 050502 (2021).

[16] E. A. Tholén, A. Ergül, E. M. Doherty et al., *Nonlinearities and parametric amplification in superconducting coplanar waveguide resonators*, Appl. Phys. Lett. 90, 253509 (2007).

[17] M. Malnou, *Synthesis of artificial transmission lines tailored for traveling-wave parametric processes*, Phys. Rev. Applied 25, 054016 (2026).

[18] L. J. Splitthoff, J.J. Wesdorp, M. Pita-Vidal et al., *Gate-tunable kinetic inductance parametric amplifier*, Phys. Rev. Applied 21, 014052 (2024).

[19] V. Buccheri, F. Joint, K. R. Amin et al., *Microwave dynamics of gated Al/InAs superconducting nanowires*, Appl. Phys. Lett. 126, 232602 (2025).

[20] C. W. J. Beenakker and H. van Houten, *Josephson current through a superconducting quantum point contact shorter than the coherence length*, Phys. Rev. Lett. 66, 3056 (1991).

[21] S. Park, C. Metzger, L. Tosi et al., *From Adiabatic to Dispersive Readout of Quantum Circuits*, Phys. Rev. Lett. 125, 077701 (2020).

[22] C. Metzger, S. Park, L. Tosi et al., *Circuit-QED with phase-biased Josephson weak links*, Phys. Rev. Research 3, 013036 (2021).

[23] C. Janvier, L. Tosi, L. Bretheau et al., *Coherent manipulation of Andreev states in superconducting atomic contacts*, Science 349, 1199-1202 (2015).

[24] M. Hays, G. de Lange, K. Seriniak et al., *Direct Microwave Measurement of Andreev-Bound-State Dynamics in a Semiconductor-Nanowire Josephson Junction*, Phys. Rev. Lett. 121, 047001 (2018).

[25] P. Zellekens, R. S. Deacon, P. Perla et al., *Microwave spectroscopy of Andreev states in InAs nanowire-based hybrid junctions using a flip-chip layout*, Commun Phys 5, 267 (2022).

[26] L. Tosi, C. Metzger, M. F. Goffman et al., *Spin-Orbit Splitting of Andreev States Revealed by Microwave Spectroscopy*, Phys. Rev. X 9, 011010 (2019).

[27] M. Hays, V. Fatemi, K. Serniak et al., *Continuous monitoring of a trapped superconducting spin*, Nat. Phys. 16, 11031107 (2020).

[28] M. Hays, V. Fatemi, D. Bouman et al., *Coherent manipulation of an Andreev spin qubit*, Science 373, 430-433 (2021).

[29] A. Bargerbos, M. Pita-Vidal, R. Zitko et al., *Spectroscopy of Spin-Split Andreev Levels in a Quantum Dot with Superconducting Leads*, Phys. Rev. Lett. 131, 097001 (2023).

[30] M. Pita-Vidal, A. Bargerbos, R. Zitko et al., *Direct manipulation of a superconducting spin qubit strongly coupled to a transmon qubit*, Nat. Phys. 19, 11101115 (2023).

[31] O. O. Shvetsov, A. Khola, V. Buccheri et al., *Approaching the ultrastrong-coupling regime between an Andreev level and a microwave resonator*, Phys. Rev. Applied 24, 044015 (2025).

[32] C. Schrade and V. Fatemi, *Dissipationless nonlinearity in quantum material Josephson diodes*, Phys. Rev. Applied 21, 064029 (2024).

[33] L. Tosi, I. Lobato. M. F. Goffman et al., *Effects of measurement power on state discrimination and dynamics in a circuit-QED experiment*, Phys. Rev. Research 6, 023299 (2024).

[34] D. Phan, P. Falthansl-Scheinecker, U. Mishra et al., *Gate-Tunable Superconductor-Semiconductor Parametric Amplifier*, Phys. Rev. Applied 19, 064032 (2023).

[35] Z. Hao, T. Shaw, M. Hatefipour et al., *Kerr nonlinearity and parametric amplification with an Al-InAs superconductorsemiconductor Josephson junction*, Appl. Phys. Lett. 124, 254003 (2024).

[36] R. Rousset-Zenou, N. Aparicio, S. Messelot et al., *Gate-tunable Josephson parametric amplifiers based onsemiconductor nanowires*, arXiv:2510.00305.

[37] P. Krogstrup, N. L. B. Ziino, W. Chang et al, *Epitaxy of semiconductorsuperconductor nanowires*, Nature Mater 14, 400406 (2015).

[38] I. P. C. Cools, R. M. López-Báez, V. Buccheri, et al., *Losses in magnetic field resilient coplanar stripline resonators*, J. Phys. D: Appl. Phys. 58 255102 (2025).

[39] S. Abay, D. Persson, H. Nilsson et al., *Charge transport in InAs nanowire Josephson junctions*, Phys. Rev. B 89, 214508 (2014).

[40] I. C. Iglesias, F. J. Matute-Cañadas, G. O. Steffensen, et al., *Ultrastrong Coupling and Coherent Dynamics in a Gate-Tunable Transmon Qubit*, arXiv:2603.19438.

[41] S. Probst, F. B. Song, P. A. Bushev et al., *Efficient and robust analysis of complex scattering data under noise in microwave resonators*, Rev. Sci. Instrum. 86, 024706 (2015).

[42] M. Elliott, J. Joo and E. Ginossar, *Designing Kerr interactions using multiple superconducting qubit types in a single circuit*, New J. Phys. 20, 023037 (2018).

[43] J.-D. Pillet, V. Benzoni, J. Griesmar, et al., *Nonlocal Josephson Effect in Andreev Molecules*, Nano Lett. 19 (10): 71387143 (2019).

[44] D. Z. Haxell, M. Coraiola, M. Hinderling, et al., *Demonstration of the Nonlocal Josephson Effect in Andreev Molecules*, Nano Lett. 23 (16): 75327538 (2023).

[45] O. Kürtössy, Z. Scherübl, G. Fülöp, et al., *Andreev Molecule in Parallel InAs Nanowires*, Nano Lett. 21 (19): 79297937 (2021).

Supplementary Material

A. Device

We fabricate the devices on single-side polished, 430-μm-thick sapphire substrates cleaned using a standard SC-1 process. After heating the substrate to 660 °C, we deposit approximately 10 nm thick NbTiN film by reactive sputtering. The resulting film has a kinetic inductance of $L_k \approx 10$ pH/□ and a critical temperature of $T_c \approx 15$ K. We define alignment markers by electron-beam lithography (EBL) and lift-off of an 80 nm thick evaporated Ti/Au layer. We subsequently pattern the NbTiN film by negative EBL process using ma-N2403 resist and etch the metal by inductively coupled plasma reactive ion etching in a Cl_2/Ar (4/50 sccm) plasma, defining the resonator, microwave feedlines, and the coarse gate and flux-line circuitry. Additional details on the fabrication process and resonator design can be found in Ref. [1].

We dice the wafer into 10×5 mm^2 chips. We then deposit several hybrid Al/InAs nanowires near the resonator voltage node using a nanomanipulator. The weak links are defined by selectively removing the Al shell using an MF319 wet etch. The etch windows are patterned by standard positive EBL process. Following scan electron microscopy (SEM) inspection, we select the most promising nanowire on each chip for the final step of the fabrication. We fabricate the fine circuitry, including the ohmic contacts connecting the nanowire to the resonator as well as the gate and flux lines, by lift-off of a 250 nm thick evaporated Ti/Al layer. Immediately before metal deposition, a 30 s Ar ion milling step is performed to remove the native oxide from the epitaxial Al shell and improve the contact transparency between the nanowire and the evaporated Ti/Al contacts. The chip is then ready for measurements [see Fig. S1].

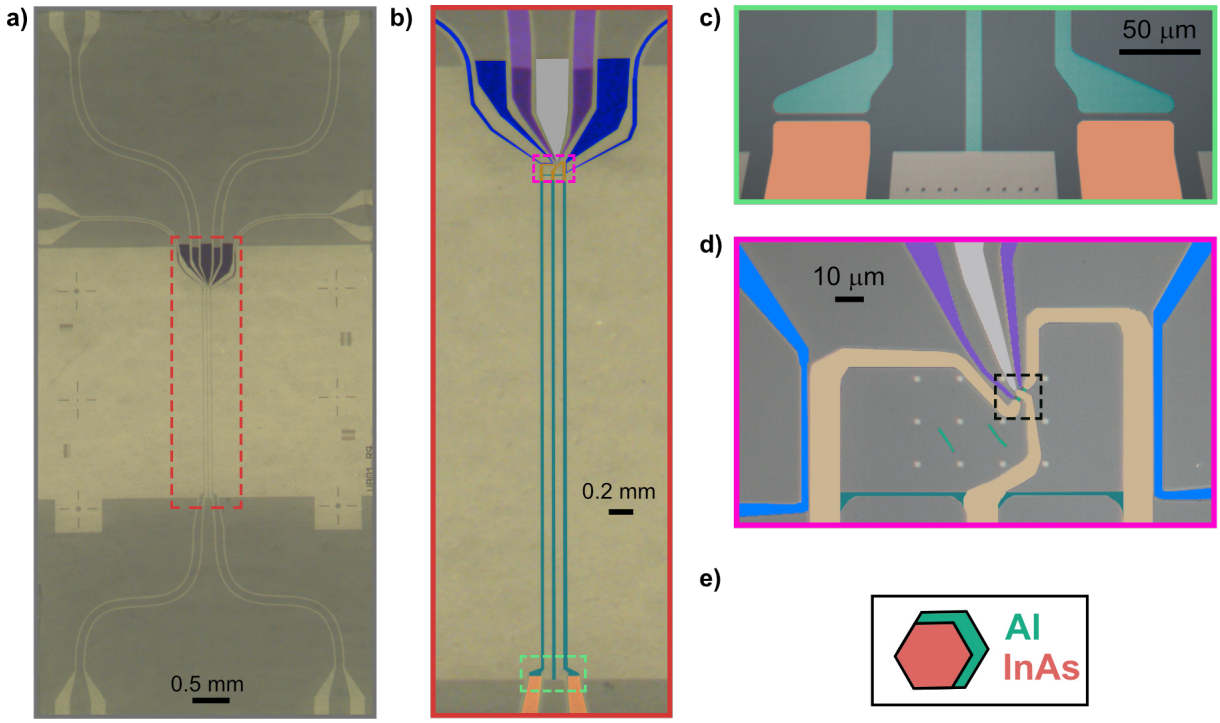


FIG. S1: Device. **a)** Optical micrograph of the device. The region outlined in red is magnified in b). **b)** False-colored optical micrograph showing the resonator structure (cyan), the differential feedlines (orange), the gate lines (purple) with their ground-shielding line (grey), the flux lines (blue) and the loops embedding the nanowire near the resonator voltage node (yellow). The ground plane and the substrate are left uncolored. The regions outlined in green and pink are magnified in c) and d), respectively. **c)** False-colored optical micrograph showing the coupling capacitors between the resonator and the feedlines. The color code is the same as panel in b). **d)** False-colored optical micrograph of the nanowire region located near the resonator voltage node. The nanowires are shown in green, while the rest of the circuitry follows the same color code as in b). The region enclosed by the black rectangle is shown in the SEM image in Fig. 1a). **e)**: Schematic cross-section of the nanowire. The Al shell is 27 nm thick and the total diameter is approximately 180 nm.

B. Experimental Setup

We perform the experiment in a Bluefors dilution cryostat with 10 mK base temperature [see Fig. S2a)]. The resonator is differentially driven, and readout in reflection. The Cu powder filters are fabricated in-house and, unless otherwise specified in the schematic, have a cut-off frequency of approximately 4 GHz. The room temperature setup used for the readout of the resonator [see Fig. S2b)] consists of a vector network analyzer (VNA, Keysight P5004A), and additional filtering and amplification stages for the output line. On the other hand, the pump/drive line control [see Fig. S2c)] consists of a signal source generator (Rohde & Schwarz SGS100A) equipped with an upconverter (Rohde & Schwarz SGU100A).

Specification about the modular control system SPI-rack used for the gate and flux lines [see Fig. S2d)] can be found in Ref. [2]. The π filters at room temperature absorb noise in the range 10 MHz-10 GHz. Specification for the infrared-blocking filter HERD2 can be found in Ref. [3].

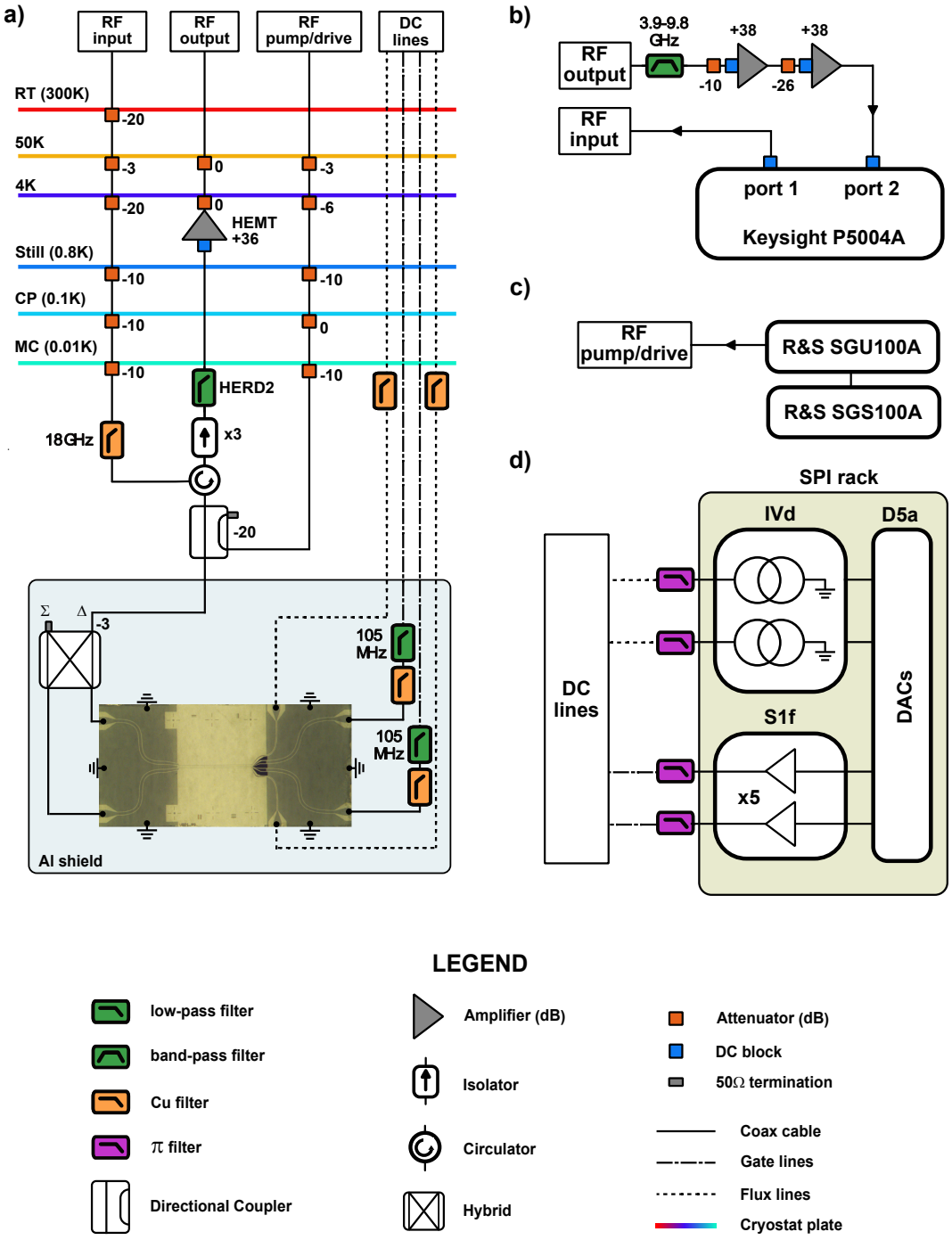


FIG. S2: Experimental setup. **a)** Cryostat schematic. **b)** Room temperature setup for the resonator readout. **c)** Room temperature setup for the pump/drive signal source. **d)** Room temperature setup for the gate (D5a + S1f modules) and flux (D5a + IVd modules) signal generation. The DC lines are twisted pairs from the π-filter to the mixing chamber plate. The flux lines are superconducting below the 4K plate.

C. Extended gate and flux spectroscopy

Flux and gate lines crosstalk is compensated by applying the following linear transformation:

$$\begin{pmatrix} I_1 \\ I_2 \end{pmatrix} = \begin{pmatrix} 1 & -0.11 \\ -0.22 & 1 \end{pmatrix} \begin{pmatrix} I_1^0 \\ I_2^0 \end{pmatrix} \quad \text{and} \quad \begin{pmatrix} \mathrm{V}_1 \\ \mathrm{V}_2 \end{pmatrix} = \begin{pmatrix} 1 & -0.042 \\ -0.03 & 1 \end{pmatrix} \begin{pmatrix} V_1^0 \\ V_2^0 \end{pmatrix}, \tag{S1}$$

where $I_i(V_i)$ and $I_i^0(V_i^0)$ are the actual and effective current(voltage) values sent to the device, respectively.

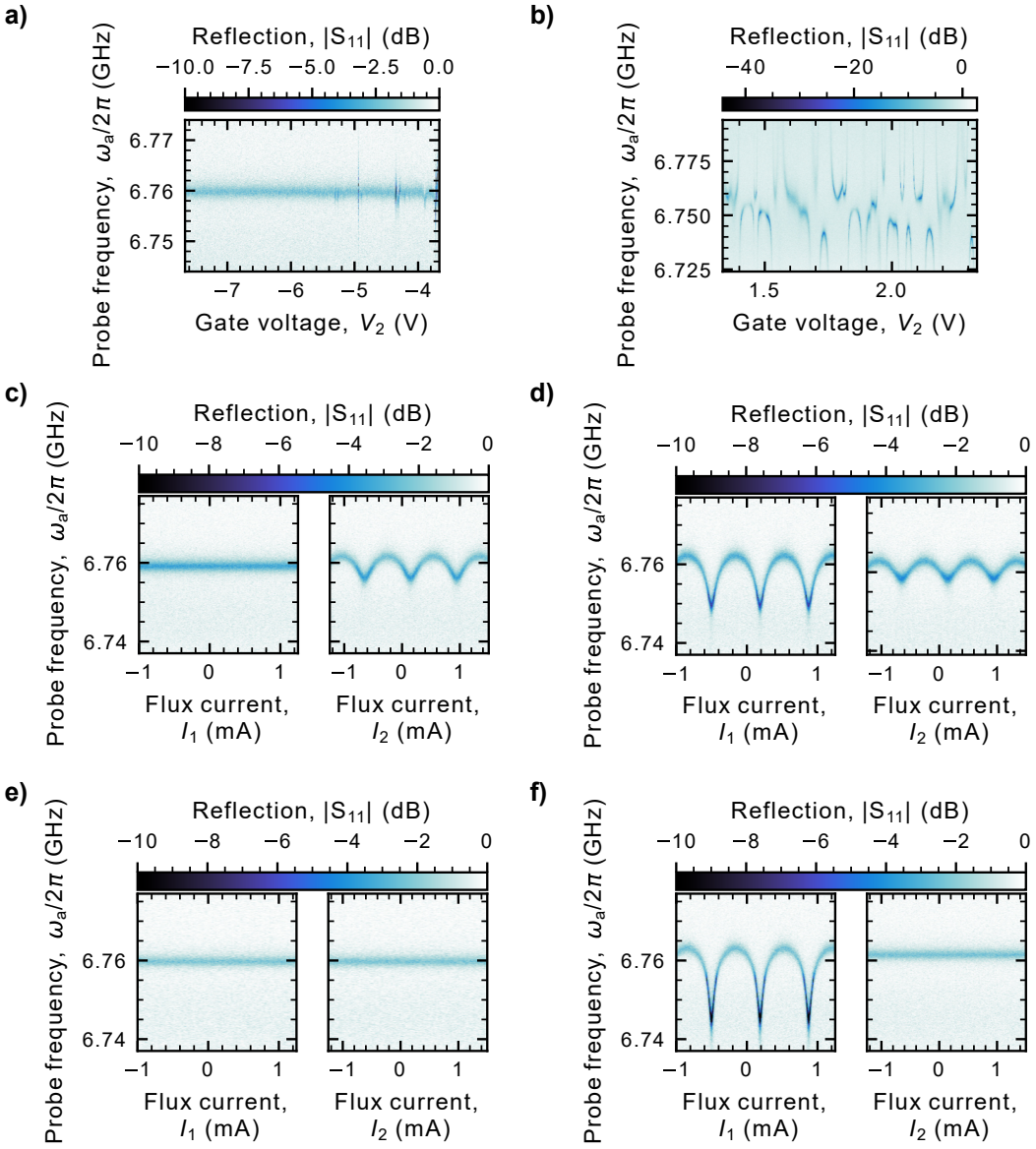


FIG. S3: Gate and Flux spectroscopy. **a)** Single-tone spectroscopy as a function of V_2 with JJ_1 piched-off, showing that JJ_2 enters in a pinch-off region for $V_2 < -7$V. **b)** Single-tone spectroscopy as a function of V_2 in the active junction regime with $\varphi_2 = \pi$, showing several avoided crossing patterns related to tuning of the conduction channels. **c-d-e-f)** Single-tone spectroscopy as a function of I_1 (left panels) and I_2 (right panels) for four different gate regimes: single-junction regime [JJ_1 off(on) and JJ_2 on(off) in c(f)), respectively], double-junction regime in d) and both junctions pinched off in e).

The flux and gate crosstalk compensation enable independent junction control [see Fig. 1c) and Fig. S3]. Following results for high-impedance resonator in Ref. [4], we neglect the loop inductance, so that the flux current I_i is converted

in superconducting phase across the junction φ_i by linear transformation, $\varphi_\mathrm{i} = 2\pi(I_\mathrm{i} - \delta_\mathrm{i})/\vartheta_\mathrm{i}$, where δ_i is the current corresponding to a minimum of the $f_\mathrm{r}(I_\mathrm{i})$ oscillation and $\vartheta_{1(2)} = 0.138(0.158)$ mA is the oscillation period.

D. Nonlinear data extraction

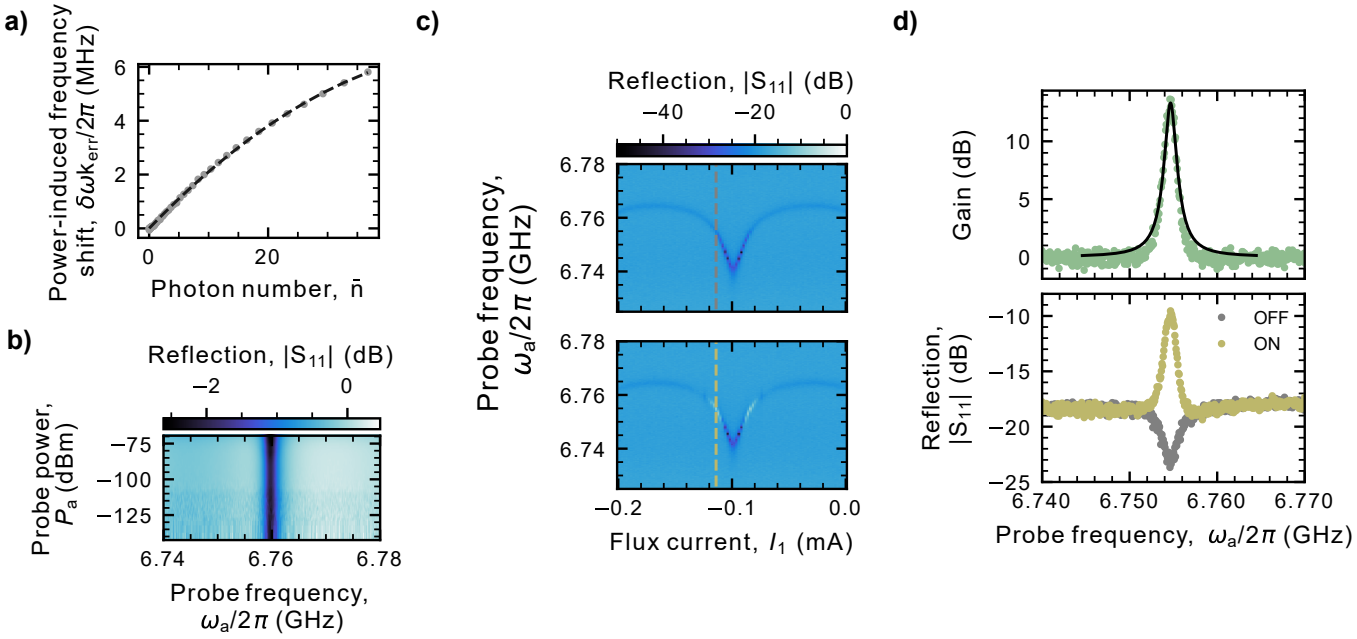


FIG. S4: Nonlinear data extraction. **a)** Power-induced frequency shift, $\delta\omega_\mathrm{kerr}$, as a function of the average probe photon number in the resonator, $\bar{n}$, for the same dataset shown in Fig. 1 e). The dashed black line represents the function $\delta\omega_\mathrm{kerr} = 2K\bar{n} + K'\bar{n}^2$ fitted to the data. Fitting parameters are $K/2\pi = 230$ kHz and $K'/2\pi = 2$ kHz. **b)** Single-tone spectroscopy as a function of probe power P_a with both junction pinched-off. **c)** Single-tone spectroscopy as a function of flux current I_1 without (top) and with (bottom) a pump tone at $\omega_\mathrm{p} = 2\omega_\mathrm{r}$. The gate configuration is the same as Dataset II in Fig. 2. The dashed vertical lines highlight the traces shown in panel d). **d)** Line cuts from panel c). *Bottom*: low-power resonator traces measured with (yellow) and without (gray) the pump tone at $\omega_\mathrm{p}/2\pi = 13.518$ GHz. *Top*: gain profile (green) obtained from the difference between the ON and OFF reflection traces shown below. The black line is a Lorentzian fit (Eq. S4) from which the on-off gain G_0 is extracted.

The resonator Kerr K is related to the power-induced frequency shift $\delta\omega_\mathrm{kerr}$ as a function of the average photon number $\bar{n}$ at the resonant frequency ω_r in the cavity. We convert the probe power at the resonator, P_a, estimated from the VNA output, the nominal input line attenuation and an additional -6 dB attenuation accounting for cables losses, into $\bar{n}$ using [1]:

$$\bar{n} = \frac{4Q_\mathrm{l}^2}{Q_\mathrm{c}} \frac{P_\mathrm{a}}{2\pi\hbar\omega_\mathrm{r}} \frac{Z_0}{Z_\mathrm{r}}, \tag{S2}$$

where Q_l is the loaded quality factor of the resonator, $Z_0 = 50\ \Omega$ is the feedline impedance, $Z_\mathrm{r} = 290\ \Omega$ is the characteristic impedance of the resonator as extracted from simulation and h is the Plank constant. For sufficient low $\bar{n}$, $\delta\omega_\mathrm{kerr}(\bar{n})$ shows a quadratic behavior [see Fig. S4a)] that can be described by the following expression [5]:

$$\delta\omega_\mathrm{kerr} = 2K\bar{n} + K'\bar{n}^2, \tag{S3}$$

where K represents the Kerr of the resonator. A power sweep of the bare resonator (i.e., with both junctions pinched-off) shows no power-induced frequency shift in the considered range of P_a [see Fig. S4b)], from which we conclude that the Kerr data do not include any effects due to the kinetic inductance of the NbTiN or Al.

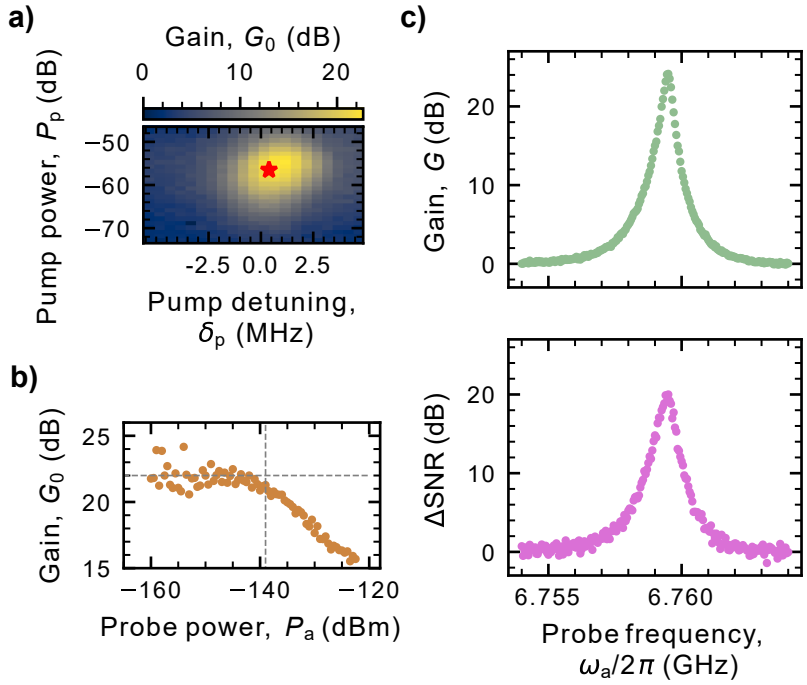


FIG. S5: Amplification performance. **a)** Heat-map showing the on-off amplification gain G_0 versus pump power P_p and pump detuning $\delta_p = \omega_\mathrm{p} - 2\omega_\mathrm{r}$. Gate voltages are $V_1 = 0.25$ V and $V_2 = 0.5$ V. Phase biases are $\varphi_1 \approx 0.8\pi$ and $\varphi_2 \approx 0.75\pi$. The red stars marks the operating point used in b) and c). **b)** Gain G_0 versus probe power P_a. The dashed lines highlight the -1dB compression point at -138 dBm. **c)** On-off amplification gain G (top) and corresponding signal-to-noise-ration improvement ΔSNR (bottom) as a function of probe frequency ω_a. The on-off gain shown in a,b) is extracted following the procedure described in Sec. D, whereas the data discussed in panel c) are obtained as described in Sec. E.

To measure the three-wave mixing gain as a function of φ, we perform single-tone spectroscopy as a function of flux current with and without a pump tone applied at $\omega_\mathrm{p}(\varphi) = 2\omega_\mathrm{r}(\varphi)$ [Fig. S4c)] from which we can extract ON and OFF traces, whose difference in amplitude gives the gain profile $G(\omega)$ [Fig. S4d)]. For each flux bias, the on-off gain G_0 is approximated by the amplitude of a Lorentzian function fitted to the gain profile in linear scale and around its maximum:

$$G(\omega_\mathrm{a}) = 1 + \frac{G_0}{1 + \left(\frac{\omega_\mathrm{a} - \omega_0}{\Gamma}\right)^2}, \tag{S4}$$

where ω_0 is the frequency at which the gain is maximum and Γ is the half-width at half-maximum. The cubic nonlinearity g_3 is then extracted from G_0 by solving [6]

$$G_0 = 1 + \frac{4\kappa^2 |2g_3\sqrt{\bar{n}_\mathrm{p}}|^2}{\left(\delta_\mathrm{p}^2 + \kappa^2/4 - 4|2g_3\sqrt{\bar{n}_\mathrm{p}}|^2\right)^2}, \tag{S5}$$

where $2\pi\kappa = \omega_\mathrm{r}/Q_\mathrm{l}$, $\delta_\mathrm{p} = \omega_\mathrm{p} - 2\omega_\mathrm{r}$ and $\bar{n}_\mathrm{p}$ is the intracavity photon number at the pump frequency given by a generalization of Eq. S2 [7]:

$$\bar{n}_\mathrm{p} = \frac{\kappa_\mathrm{e}}{\left(\omega_\mathrm{p} - \omega_\mathrm{r}\right)^2 + \left(\kappa/2\right)^2} \frac{P_\mathrm{p}}{\hbar\omega_\mathrm{p}}, \tag{S6}$$

with $2\pi\kappa_\mathrm{e} = \omega_\mathrm{r}/Q_\mathrm{c}$, and P_p pump power at the resonator estimated from the signal generator output, nominal pump-line attenuation and an additional -6 dB attenuation accounting for the cables losses [1].

This method has been used to extract G_0 and then g_3 both in single [Figs. 2e), S7] and double [Figs. 3c,d)] junction configuration. In these cases, P_p was chosen to get a around 10 dB amplification or lower, in order to avoid large-gain correction in Eq. S5.

E. Parametric amplifier performance

We characterize the parametric amplification in the double-junction configuration. After choosing gate voltages and flux biases in order to minimize K and maximize g_3, we sweep the pump power P_p and detuning δ_p for maximum gain [Fig. S5a)]. Using these optimized parameters, we characterize the amplifier dynamic range by measuring the maximum gain as a function of the probe power P_a, obtaining a -1-dB compression point of -138 dBm [Fig. S5b)].

With the optimized pump parameters and for probe powers below the compression point, we obtain a maximum on-off gain of 25 dB with a bandwidth of approximately 2 MHz and a signal-to-noise improvement of $\Delta\mathrm{SNR} = 20$ dB [Fig. S5b)]. In this case, the amplitude $|S_{11}^{\mathrm{ON(OFF)}}|$ and noise $\langle S_{11}^{\mathrm{ON(OFF)}}\rangle$ data are obtained at each frequency as average and variance over 400 data-points measured with the VNA in continuous-wave mode, respectively. Gain and $\Delta\mathrm{SNR}$ are then obtained as $G = |S_{11}^{\mathrm{ON}}|/|S_{11}^{\mathrm{OFF}}|$ and $\Delta\mathrm{SNR} = (|\mathrm{S}_{11}^{\mathrm{ON}}|^2\langle \mathrm{S}_{11}^{\mathrm{OFF}}\rangle)/(|\mathrm{S}_{11}^{\mathrm{OFF}}|^2\langle \mathrm{S}_{11}^{\mathrm{ON}}\rangle)$.

The fact that G_0 decreases and eventually disappears for large pump detuning [Fig. S5a)], i.e. when the three-wave-mixing condition $\omega_\mathrm{p} = 2\omega_\mathrm{r}$ is not satisfied, excludes that our results are dominated by two-level systems saturation.

F. Effective Andreev bound state pairs model

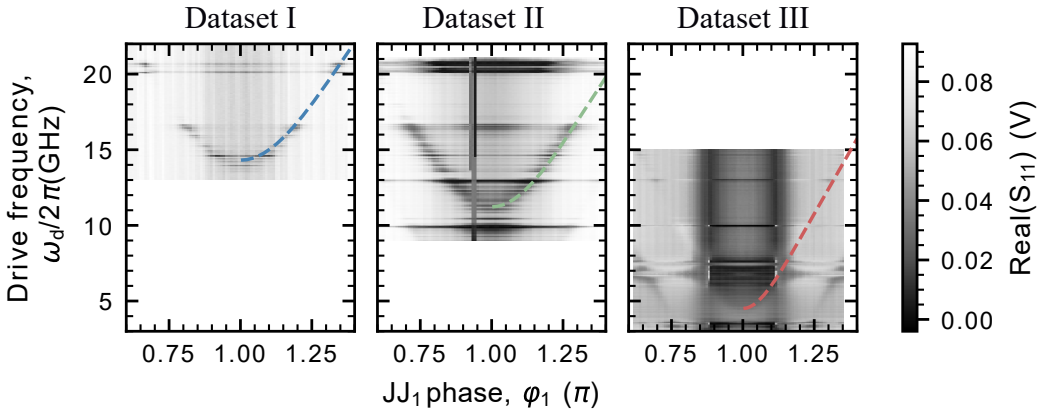


FIG. S6: Two tone spectroscopy corresponding to Dataset I (left), II (center) and III (right) in Fig. 2a), where the dashed line represent $\hbar\omega_\mathrm{ABS} = 2\Delta\sqrt{1-\tau\sin^2(\varphi/2)}$ with $\tau = (0.8, 0.86, 0.97)$ and $\Delta = (16, 15, 13)$ GHz for Datasets I, II and III.

From a two-tone spectroscopy around $\varphi_1 = \pi$ [see Fig. S6] we get a first estimation of τ and Δ for the gate configuration explored in the main text for JJ_1 [Fig. 2a)]. These values are then used as initial guesses when fitting Eq. 1 (main text) to the $\delta\omega_\mathrm{r}$ data. In particular, the fitting parameters are τ and λ, while Δ is kept fixed.

The parameter λ is the product between the participation ratio $p = L_\mathrm{s}/(L_\mathrm{r} + 2L_\mathrm{s})$ and the reduced zero-point-fluctuation $2\pi\Phi_\mathrm{zpf}/\Phi_0$ [8], where $\Phi_\mathrm{zpf} = \sqrt{\hbar Z_\mathrm{r}/2}$ is the resonator zero-point fluctuation, $Z_\mathrm{r} = 290\ \Omega$ is the characteristic impedance of the resonator as extracted from simulation, $\hbar$ is the reduced Plank constant and Φ_0 is the flux quantum.

We can generalize the phenomenological ABS model taking into account a second channel by following Ref. [9]. Considering two channels with transparency τ_1 and τ_2, the effective ABS potential reads

$$U_\mathrm{2ABS} = \Delta_\mathrm{eff}\left(\sqrt{1-\tau_1\sin^2\left(\frac{\varphi}{2}\right)} + \sqrt{1-\tau_2\sin^2\left(\frac{\varphi}{2}\right)}\right) = U_\mathrm{ABS}^{(1)} + U_\mathrm{ABS}^{(2)}. \tag{S7}$$

The induced frequency shift then becomes (as in the main text, $\hbar = 1$):

$$\delta\omega_r = \sum_{m=1}^{2}\left(-\lambda^2 c_2^{(m)} + \left(g_\mathrm{c}^{(m)}\right)^2\left(\frac{2}{\omega_\mathrm{ABS}^{(m)}} - \frac{1}{\delta_-^{(m)}} - \frac{1}{\delta_+^{(m)}}\right)\right), \tag{S8}$$

where $c_2^{(m)} = d^2U_\mathrm{ABS}^{(m)}/d\varphi^2$, $\omega_\mathrm{ABS}^{(m)} = 2U_\mathrm{ABS}^{(m)}$, $\delta_\pm^{(m)} = \omega_\mathrm{ABS}^{(m)} \pm \omega_\mathrm{r}^0$ and $g_\mathrm{c}^{(m)} = \lambda\sqrt{1-\tau_m}\left(dU_\mathrm{ABS}^{(m)}/d\varphi\right)\tan(\varphi/2)$. We note that in Eq. S8 we consider the two channels to be uncoupled.

Similarly, we generalize the cubic and Kerr nonlinearity:

$$g_3 = \frac{\lambda^3}{6}\tilde{c}_3 \tag{S9}$$

and

$$K = \frac{\lambda^4}{2}\left(\tilde{c}_4 - \frac{5\tilde{c}_3^2}{3\tilde{c}_2}\right) + \sum_{m=1}^{2} \frac{\left(g_c^{(m)}\right)^4}{\left(\delta_-^{(m)}\right)^3}, \tag{S10}$$

where $\tilde{c}_n = d^n\tilde{U}_{\mathrm{ABS}}/d\varphi^n$, with

$$\tilde{U}_{\mathrm{ABS}} = \left(\frac{\Phi_0}{2\pi}\right)^2 \frac{\left(\varphi - \varphi_{\mathrm{ext}}\right)^2}{2L_{\mathrm{loop}}} - U_{\mathrm{ABS}}^{(1)} - U_{\mathrm{ABS}}^{(2)}. \tag{S11}$$

As for the double junctions configuration, Eqs. 3 and 2 (main text) are fitted to the K and $|g_3|$ data for $\mathrm{JJ}_1(\mathrm{JJ}_2)$ while $\varphi_2(\varphi_1) = 0$ [Fig. 3]. Obtained parameters are listed in Tab. S2.

Junction	Dataset	Δ (GHz)	τ	τ_2	λ
JJ_1	I	16	0.739	-	0.032
		16	0.797	0.379	0.026
	II	15	0.809	-	0.035
		15	0.851	0.483	0.028
	III	9	0.925	-	0.035
		13	0.975	0.850	0.020
JJ_2	IV	18	0.736	-	0.024
		18	0.752	0.071	0.023
	V	15	0.863	-	0.029
		13	0.865	0.328	0.027
	VI	9.5	0.900	-	0.035
		12.8	0.955	0.400	0.025

TABLE S1: Parameter describing single-junction configuration data for JJ_1 [Fig. 2] and JJ_2 [Fig. S7]. For each Dataset we list both the one-channel and two-channel parameters.

Dataset	Junction	Δ (GHz)	τ	λ
K	JJ_1	16	0.88	0.033
	JJ_2	10	0.92	0.023
g_3	JJ_1	17	0.87	0.03
	JJ_2	15	0.93	0.038

TABLE S2: Parameter describing double-junction configuration data [see Fig. 3].

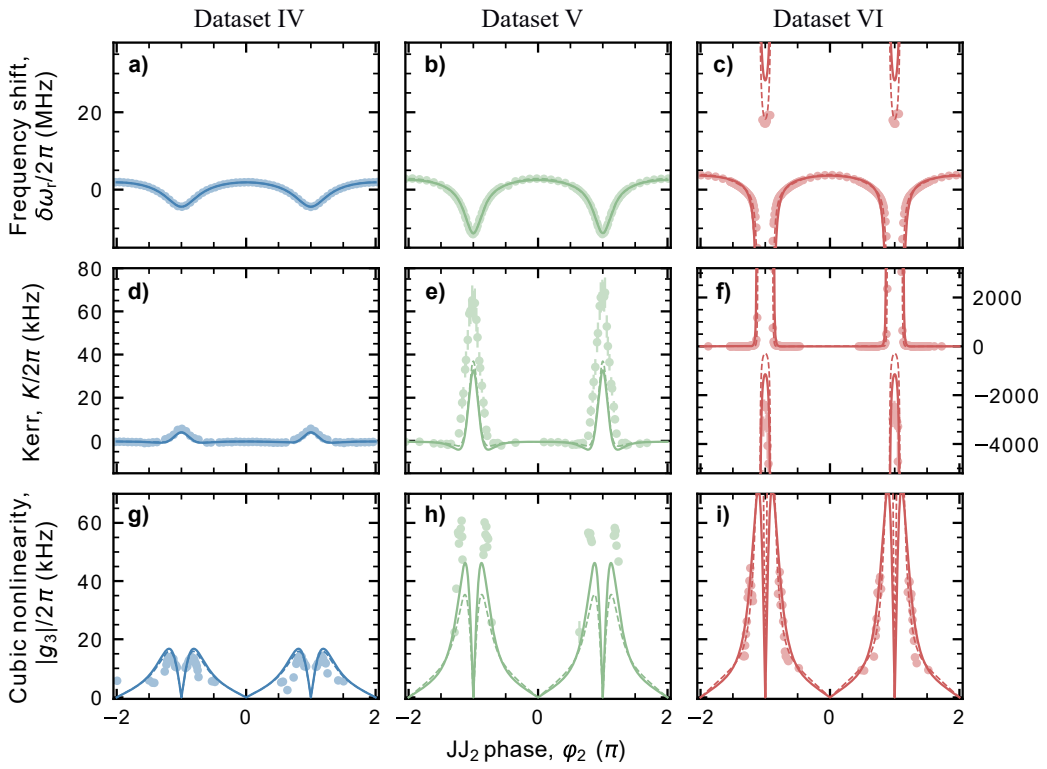


FIG. S7: Linear ($\delta\omega_r$) and nonlinear (K, g_3) data for the single-junction regime where JJ_1 is pinched-off and JJ_2 is active measured versus φ_2, for Dataset IV (left, $V_2 = -0.55$ V), V (center, $V_2 = 0.65$ V) and VI (right, $V_2 = 1.8$ V). Solid and dashed lines represent one-channel and two-channel model, respectively. Parameters are listed in Tab. S1.

[1] I. P. C. Cools, R. M. López-Báez, V. Buccheri et al., *Losses in magnetic field resilient coplanar stripline resonators*, J. Phys. D: Appl. Phys. 58 255102 (2025).

[2] SPI rack website.

[3] L. Andersson, B. Olsson, S. Gasparinetti et al., *Co-Designed Reflective and Leaky-Waveguide Low-Pass Filter for Superconducting Circuits*, IEEE Transactions on Microwave Theory and Techniques 17 (2025).

[4] O. O. Shvetsov, A. Khola, V. Buccheri et al., *Approaching the ultrastrong-coupling regime between an Andreev level and a microwave resonator*, Phys. Rev. Applied 24, 044015 (2025).

[5] N. Frattini, *Three-wave Mixing in Superconducting Circuits: Stabilizing Cats with SNAILs*, PhD Thesis, 2021.

[6] V. V. Sivak, N. E. Frattini, V. R. Joshi et al., *Kerr-Free Three-Wave Mixing in Superconducting Quantum Circuits*, Phys. Rev. Applied 11, 054060 (2019)

[7] M. Aspelmeyer, T. J. Kippenberg and F. Marquardt, *Cavity optomechanics*, Rev. Mod. Phys. 86, 1391 (2014)

[8] S. Park, C. Metzger, L. Tosi et al., *From Adiabatic to Dispersive Readout of Quantum Circuits*, Phys. Rev. Lett. 125, 077701 (2020).

[9] C. Metzger, S. Park, L. Tosi et al., *Circuit-QED with phase-biased Josephson weak links*, Phys. Rev. Research 3, 013036 (2021).